

Strengthening mechanisms in dilute and random solid solution high-entropy BCC alloys

Présentée le 21 juin 2022

Faculté des sciences et techniques de l'ingénieur
Laboratoire de modélisation mécanique multi-échelle
Programme doctoral en mécanique

pour l'obtention du grade de Docteur ès Sciences

par

Alireza GHAFAROLLAHI

Acceptée sur proposition du jury

Prof. B. T. A. Lecampion, président du jury
Prof. W. Curtin, directeur de thèse
Prof. J. Marian, rapporteur
Dr S. Rao, rapporteur
Prof. A. Natarajan, rapporteur

Acknowledgements

The present thesis is an outcome of my rewarding stay as a Ph.D. student in Laboratory for Multi-scale Mechanics Modeling (LAMMM) at École Polytechnique Fédérale de Lausanne (EPFL). Financial support was provided by the Swiss National Science Foundation through a grant for the project entitled 'Harnessing atomic-scale randomness: design and optimization of mechanical performance in High Entropy Alloys', Project"200021_18198/1". At the end of this very interesting and life-changing scientific journey, I would like to address a few words of thanks.

First and foremost, I wish to express my deepest gratitude to my thesis advisor, Professor Bill Curtin, for his continual guidance, trust, and inspiration throughout my study. Without his mentorship and encouragement, I would not have been able to continue my academic journey. It has truly been a pleasure and an honor to work with him.

I would also like to thank the jury members for being willing to participate in my PhD exam. I am also thankful to the current and former members of LAMMM: Till Junge, Mostafa Khosrownejad, Francesco Maresca, Wolfram Nöhring, Max Hodapp, Ali Tehrani, Markus Stricker, Binglun Yin, Predrag Andric, Xiao Zhou, Carolina Baruffi, Manura Liyanage, You Rao, Rasool Ahmad, Ali Falsafi, Ankit Gupta, Yi Hu, Eleanor Mak, Daniel Marchand, Shankha Nag, Ekin Kubilay, Xin Liu, Terrence Moran, and Masoud Rahbarniazi. Furthermore, many thanks to always smiling LAMMM secretary, Ms. Géraldine Palaj, for her assistance with everyday issues. It has been a wonderful experience working with such a great group of people.

I am grateful to Prof. Francesco Maresca for introducing me to basic concepts of plasticity in BCC metals and alloys. Thank you Rasool Ahmad and Shankha Nag for fruitful discussions about fundamentals and statistics of solute strengthening theories. Moreover, I am thankful to Terrence Moran for proofreading the first few chapters of my thesis.

I express my deepest thanks to my parents, Rasool and Zahra, and my siblings, Mohammad, Narges, Nasrin and Saeed, for their love and encouragement during my whole life. I also thank to my parents in law, Hamid and Maryam, for their great hospitality when I was in Iran.

Finally, I would like to dedicate this work to my wife Niloufar, the most important person in my life. She was always with me, in good and hard times, giving me an unconditional support, love, and assistance in innumerable ways. I am sure that without her patient and encouragement this thesis would have never been written.

Lausanne, April 11, 2022

A. G.

Abstract

Tuning the mechanical properties of metals, including strength, through adjusting the type and/or concentration of added solute elements, has been recognized as an effective way to design and produce materials with desired or optimized mechanical properties. Developing predictive models that connect the material properties at atomic level to the macroscopic strength is thus crucial for theory-guided design of new materials with superior mechanical performance.

Solute strengthening refers to the additional strength which arises from the totality of the interaction energies between the solutes and an individual dislocation. Prevailing theories for strengthening in body-centered cubic (BCC) alloys consider only solute interactions in the core of the screw dislocation while computations suggest longer-range interactions. In this work, we define the proper solute/screw interaction energy parameter relevant for strengthening of screw dislocations in random bcc alloys from dilute binary alloys to high-entropy alloys.

Solute could be added in small amounts to the pure base metal to form substitutional dilute alloys. It is well-established that the plastic deformation in dilute BCC alloys is controlled by motion of screw dislocations through thermally-activated double-kink nucleation and migration processes. However, the effect of solutes on these processes is not well-established. Here, we develop theoretical models to predict the barrier associated with each of these processes which ultimately enable us to compute the strength of the alloy without any fitting parameters.

High-entropy alloys (HEAs) are a new class of random multi-component alloys with impressive mechanical properties. Recent theory suggested that the underlying mechanisms involving the screw dislocation motion in BCC non-dilute and HEAs differs fundamentally from that of dilute alloys and is controlled by a combination of Peierls-like motion, kink migration, and cross-kink failure. Existing kink migration models, in spite of successes in capturing some experiments, are based on several invalid assumptions. Here, a new theory for the kink migration in HEAs is developed based on our recent understanding in dilute alloys, leading to a fully derived analytical model for the kink migration energy barrier.

The BCC refractory HEAs composed of the family of Mo-W-V-Nb-Ta are of particular interest due to their high-temperature strength retention. Very recent theoretical and experimental studies have proposed that yield strength in these and other BCC HEAs is controlled by edge dislocation. In this study, the very high energy barriers hindering the edge dislocation is analyzed using atomistic simulations, leading to high strengths and high strength retention at elevated temperatures.

Introduction

Many BCC refractory HEAs show a distinct plateau in strength versus temperature at intermediate temperatures. In the last part of this thesis, we examine one possible mechanism for the intermediate-T strength plateau: the dynamic strain aging (DSA) process of solute diffusion immediately across the core of an edge dislocation. An analytic model is developed which captures the major dependencies in terms of underlying material properties, and can thus be applied to other alloys.

The predictive theoretical models developed in this thesis pave the way for theory-guided design of novel high-performance materials with excellent or even unprecedented mechanical properties.

Keywords: BCC alloys, high entropy alloys, dilute alloys, solute strengthening, screw dislocation, edge dislocation, double-kink nucleation, kink migration, dynamic strain aging, cross-core diffusion, NEB, atomistic simulations

Zusammenfassung

Die Anpassung der mechanischen Eigenschaften von Metallen, einschließlich ihrer Festigkeit, durch Abstimmung der Art und/oder Konzentration zugesetzter Lösungsatome ist allgemein als effektive Methode zum Design und zur Herstellung von Materialien mit gewünschten oder optimalen mechanischen Eigenschaften anerkannt. Die Entwicklung von Vorhersagemodellen, die eine Verbindung zwischen den Materialeigenschaften auf atomarer Ebene und der makroskopischen Festigkeit herstellen, ist daher von entscheidender Bedeutung für die theoriegeleitete Entwicklung neuer Materialien mit überlegenen mechanischen Eigenschaften.

Mischkristallhärtung bedeutet die zusätzliche Festigkeit, die sich aus der Gesamtheit der Wechselwirkungsenergien zwischen den Lösungsatomen und einer einzelnen Versetzung ergibt. Die vorherrschenden Theorien zur Verfestigung in krz-Legierungen berücksichtigen nur Wechselwirkungen mit Lösungsatomen im Kern der Schraubenversetzung, obwohl Berechnungen Wechselwirkungen mit größerer Reichweite nahelegen. In dieser Arbeit haben wir den für die Verfestigung von Schraubenversetzungen in krz-Mischkristallen, von verdünnten Lösungen bis hin zu Hochentropie-Legierungen, maßgeblichen Parameter der Wechselwirkungsenergie zwischen Lösungsatomen und Versetzungen definiert.

Lösungsatome können dem reinen Metall in kleinen Mengen zugesetzt werden, um verdünnte Mischkristalle bilden. Es ist bekannt, dass die plastische Verformung in verdünnten krz-Legierungen durch die Bewegung von Schraubenversetzungen, über Nukleation von Doppelkinken und Migrationsprozesse, gesteuert wird. Hier haben wir theoretische Modelle zur Vorhersage der mit jedem dieser Prozesse verbundenen Barriere entwickelt, die es uns letztendlich ermöglichen, die Festigkeit der Legierung ohne jegliche Fitting-Parameter zu berechnen.

Hochentropie-Legierungen (High Entropy Alloys, HEAs) sind eine neue Klasse von Mehrkomponenten-Legierungen mit beeindruckenden mechanischen Eigenschaften. Jüngste Theorien deuten darauf hin, dass sich die zugrundeliegenden Mechanismen der Bewegung von Schraubenversetzungen in nicht verdünnten krz- und HEA-Legierungen grundlegend von jenen in verdünnten Legierungen unterscheiden und durch eine Kombination aus Peierls-artiger Bewegung, Migration von Kinken und Zerfall von Kreuz-Kinken kontrolliert werden. Wenn sie auch einige Experimente erfolgreich beschreiben, so basieren bestehende Experimente doch auf verschiedenen ungültigen Annahmen. Hier wird, ausgehend von unseren jüngsten Erkenntnissen im Bereich der verdünnten Legierungen, eine neue Theorie der Kinkenmigration in HEAs entwickelt, die zu einem vollständig hergeleiteten analytischen Modell der Energiebarriere für Kinkenmigration führt.

Die hochtemperaturbeständigen krz-HEAs aus der Mo-W-V-Nb-Ta-Familie sind von besonderem Interesse, weil sie ihre Festigkeit bei hohen Temperaturen beibehalten. Jüngste theoretische und experimentelle Studien haben ergeben, dass die Streckgrenze in diesen und anderen krz-HEAs durch Stufenversetzungen kontrolliert wird. In dieser Studie haben wir die sehr hohen Energiebarrieren analysiert, die die Stufenversetzung behindern und zu hohen Festigkeiten und hoher Beibehaltung der Festigkeit bei erhöhten Temperaturen führen.

Viele hochtemperaturbeständige krz-HEAs weisen im Festigkeits-Temperatur-Diagramm bei mittleren Temperaturen ein deutliches Plateau auf. Im letzten Teil dieser Arbeit wird ein möglicher Mechanismus für das Festigkeitsplateau bei mittleren Temperaturen untersucht: der Prozess der dynamischen Reckalterung (Dynamic Strain Aging, DSA), bei dem Lösungsatome unmittelbar durch den Kern einer Stufenversetzung diffundieren. Es wird ein analytisches Modell entwickelt, das die wichtigsten Abhängigkeiten von den zugrundeliegenden Materialeigenschaften erfasst und somit auf andere Legierungen angewendet werden kann.

Die in dieser Arbeit entwickelten theoretischen Vorhersagemodelle ebnen den Weg für die theoriegeleitete Entwicklung neuartiger Hochleistungswerkstoffe mit exzellenten oder sogar noch nie dagewesenen mechanischen Eigenschaften.

Stichworte: krz-Legierungen, Hochentropie-Legierungen, verdünnte Legierungen, Mischkristallhärtung, Schraubenversetzung, Stufenversetzung, Kreuzkinkennukleation, Kreuzkinkenmigration, dynamische Reckalterung, Versetzungskerndiffusion, NEB, atomistische Simulationen

Contents

Acknowledgements	i
Introduction	iii
List of Figures	xi
List of Tables	xiv
I Introduction, Background, Computational Methods, and Interaction energy parameter	1
1 Introduction and Background	3
Introduction	3
1.1 Strength of materials	3
1.2 Dislocations in BCC materials	7
1.3 Solute strengthening theories for BCC materials	9
1.4 Scope and structure of the thesis	11
2 Computational Methods	15
2.1 Molecular statics simulations	15
2.1.1 Embedded atom method	17
2.1.2 Average-atom approximation of random alloys	18
2.2 Transition state theory	21
2.3 Nudged Elastic Band method	22
2.4 Atomistic simulations of screw dislocations	24
2.4.1 Screw dislocation core structure	25
2.4.2 Peierls potential	26
3 Solute/Screw Dislocation Interaction Energy Parameter	29
3.1 Solute/Screw Interaction Energy Parameter	32
3.2 Molecular Static Simulations	34
3.3 Results	36
3.3.1 Full results and convergence	36
3.3.2 Suzuki approximation	37
	vii

3.3.3	Correlation with solute/USF interaction energy	38
3.3.4	Polarized cores	39
3.4	Discussion and Summary	40
II	Strengthening mechanisms in dilute BCC alloys	43
4	Double-kink nucleation in dilute BCC alloys	45
4.1	Solute effects on the double-kink nucleation barrier	47
4.1.1	Basic quantities	47
4.1.2	Solute/double-kink interaction energy	50
4.1.3	Model for solute softening in dilute alloys	51
4.2	Solute effects in the very dilute limit	54
4.3	Validation against atomistic simulations using a model Fe-Si alloy	56
4.3.1	Very dilute limit: the single solute	58
4.3.2	Validation of solute/double-kink interaction energies	58
4.3.3	Double-kink nucleation in model dilute Fe-Si random alloys	60
4.4	Applications and implications	63
4.4.1	Application to Fe-Si alloys	65
4.4.2	Application to W-Ta and W-Re alloys	68
4.4.3	Implications for spontaneous kinking in the non-dilute regime	72
5	Kink migration in dilute BCC alloys	75
5.1	Solute effects on the kink migration barrier	77
5.1.1	Solute/kink interaction energy	77
5.1.2	Energy landscape models for kink glide	79
5.2	Validation using an atomistic model Fe-Si alloy	80
5.2.1	Simulation Details	81
5.2.2	Validation of solute/kink interaction energies	82
5.2.3	Validation of Kink Migration Models	82
5.3	Kink migration under stress	85
5.3.1	Kink migration under stress: a Wiener Process	86
5.4	Applications	90
5.4.1	Fe-Si alloys	93
5.4.2	W-Re alloys	96
5.5	Discussion	97
III	Strengthening mechanisms in high-entropy BCC alloys	101
6	Screw-controlled strength of BCC non-dilute and High-Entropy alloys	103
6.1	Maresca-Curtin model for screw strengthening in non-dilute alloys	105
6.2	New theory for kink migration in non-dilute alloys	109
6.2.1	Energy landscape for kink migration in a random solute environment	109

6.2.2	Kink migration in a non-dilute random alloy	110
6.2.3	Analytic model for kink migration	112
6.3	Applications of the theory	116
6.4	Discussion	118
6.5	Current vs. existing theories	119
7	Analysis of high energy barriers for edge dislocation motion in BCC high-entropy alloys	123
7.1	Solute strengthening theory	124
7.2	Material properties	126
7.3	Computational method	126
7.4	Results from NEB simulations	128
7.5	Application to real alloys	135
8	Model of Dynamic Strain Aging in BCC High-Entropy Alloys	139
8.1	Cross-core diffusion: mechanism and energetics	141
8.1.1	Solute strengthening	141
8.1.2	Cross-core diffusion	142
8.1.3	Cross-core energetics	143
8.1.4	Validation of the cross-core energy barrier model	145
8.1.5	Kinetic model of cross-core diffusion	147
8.1.6	Yield strength versus temperature	149
8.2	Dynamic strain aging in MoNbTaW	150
8.3	Discussion and Conclusions	152
9	Conclusion	155
A	Appendix	159
A.1	Standard deviation of the potential energy change	159
A.2	Double-kink nucleation rate	161
A.3	Simulation details of NEB calculations for double-kink nucleation	162
A.3.1	Periodic array of dislocations (PAD) configuration	162
A.3.2	Nudged elastic band (NEB) calculations	162
A.4	Activation volume of kink-migration process	163
A.5	Simulation details of NEB calculations for kink migration	164
A.6	Simulation details of the solute/edge interaction energies	164
A.7	Average waiting time	165
	Bibliography	167
	Curriculum Vitae	183

List of Figures

1.1	Tensile stress-strain curves of Mo single crystals at various temperatures.	4
1.2	Yield stress versus temperature and strain rate for six pure BCC metals.	4
1.3	Application of Niobium in aerospace industry.	5
1.4	Temperature and concentration-dependent experimental flow stress in BCC pure metal and dilute alloys.	6
1.5	Yield stress versus temperature for various BCC multicomponent alloys.	6
1.6	Schematic of screw and edge dislocations gliding on a slip plane of a crystalline material.	7
1.7	Schematic illustration of the preferential glide plane and glide direction in BCC crystal.	8
1.8	Plastic deformation in pure BCC metals and dilute alloys by thermally-activated double-kink nucleation and kink propagation processes.	9
1.9	Schematic of cross-kink formation as a result of the collision of kinks propagating on different glide planes.	11
2.1	Schematic illustration of a 3N-dimensional potential energy surface.	16
2.2	Average-alloy method for solute-dislocation interaction energy.	20
2.3	Schematic of a thermally activated process from an initial metastable state A to final metastable state B in a potential energy surface.	21
2.4	Schematic of force components involved in NEB calculation for the MEP between initial (A) and final (B) metastable states in a two dimensional potential energy surface.	24
2.5	Pristine BCC crystal structure viewd as a collection of atomic rows along [111] direction.	25
2.6	Differential displacement maps at the dislocation core for two compositions of TiZrNb ternary alloys.	26
2.7	Peierls potential for different BCC metals computed by DFT.	27
2.8	Peierls potential for screw dislocation in pure Fe computed by EAM potentials and DFT.	28
3.1	Suzuki's estimation of the solute/screw interaction energy	30
3.2	Solute/screw dislocation interaction energy map.	31
3.3	Average alloy method for solute-screw dislocation interactions.	33

List of Figures

3.4	Sucessive shells of atomic sites around the compact dislocation core.	37
3.5	Interaction energy parameter $\Delta\tilde{E}_p(a)$ versus alloy composition.	38
3.6	Examination of correlation of solute/screw interaction energies with solute/USF interaction energy.	40
3.7	Interaction energy parameter $\Delta\tilde{E}_p(a)$ for BCC Ti-Zr-Nb ternary alloys.	41
4.1	Schematic of double-kink nucleation in the presence of a single solute.	46
4.2	Solute/screw dislocation interaction energy map.	48
4.3	Stress-dependent transition state configurations in pure Fe.	49
4.4	Schematic of the very dilute and dilute solute regimes around a double-kink nucleation.	55
4.5	Single-solute effect on the double-kink nucleation barrier.	59
4.6	Validation of the model for solute/double-kink interaction energies.	60
4.7	NEB and predicted results for zero-stress double-kink nucleation barrier in random field of solutes.	62
4.8	NEB and predicted results of double-kink nucleation barrier versus applied stress.	63
4.9	Generic prediction of solute softening by double-kink nucleation starting from double-kink nucleation in the pure metal.	64
4.10	Theory predictions for dilute $\text{Fe}_{1-x}\text{Si}_x$ alloys.	67
4.11	Theory predictions for dilute $\text{Fe}_{1-x}\text{Si}_x$ alloys.	69
4.12	Theory predictions for W-Re and W-Ta alloys.	70
4.13	Double-kink nucleation enthalpy barrier and the time required to move a kink over the length ζ_c at room temperature for various non-dilute complex alloys.	73
5.1	Schematic of the models for the kink shape and solute/kink interaction energy and the models developed for determining the energy landscape of single kink migration across a random field of solutes.	78
5.2	Solute/screw interaction energy and energy change for single Si solute in Fe matrix.	81
5.3	Validation of the model for solute/kink interaction energies.	83
5.4	NEB and predicted results for energy landscape of a single kink motion in random field of solutes.	84
5.5	Comparison of the results of the kink migration barriers at zero-stress as obtained by NEB and developed models.	86
5.6	Comparison of the results of the kink migration barriers and activation distances at different applied stress as obtained by NEB and developed models.	87
5.7	Model predictions for single kink migration barrier for long migration distances.	88
5.8	Model predictions for single kink migration barrier for very long migration distances.	91
5.9	Prediction of double-kink and kink migration barriers for W-Re alloys.	94
5.10	Theory predictions for dilute $\text{Fe}_{1-x}\text{Si}_x$ alloys.	95
5.11	Theory predictions for W-Re alloys.	97

6.1	Schematic of the models for the kink shape and solute/kink interaction energy.	104
6.2	Schematic of the models for the kink shape and solute/kink interaction energy.	110
6.3	Energy landscape due to kink migration as computed from stochastic rigid-kink model (SRKM).	112
6.4	Kink migration barrier versus applied stress.	113
6.5	Theory predictions for non-dilute $\text{Fe}_{1-x}\text{-Si}_x$ alloys.	117
6.6	Theory predictions for Nb-based binary alloys.	118
6.7	Comparison of the present theory for the kink migration barrier with the Maresca and Curtin model.	120
6.8	Comparison of the present theory for the kink migration barrier with the Suzuki model.	122
7.1	Solute/edge dislocation interaction energy map in NbTaV and MoNbTaW alloys.	127
7.2	Energy landscape $E(x)$ versus position x for a dislocation moving through one entire simulation cell for NbTaV.	130
7.3	Dislocations at their minimum energy locations on 360 Å portion of the long NbTaV sample.	130
7.4	Energy and shape of an edge dislocation through its minimum energy path in NbTaV.	131
7.5	Energy and shape of an edge dislocation through its minimum energy path in MoNbTaW.	132
7.6	Cumulative probability distribution of energy barriers versus applied shear stresses.	134
7.7	Yield strength edge theory predictions at selected temperatures.	137
8.1	Experimental data of yield stress versus temperature for various BCC HEAs. The experimental data for BCC metals in (a) exhibit a plateau in strength over the temperature range of $\approx 700 < T < \approx 1200$, while those in (b) show a plateau for $\approx 900\text{K} < T < \approx 1300\text{K}$.	140
8.2	Interaction energy map of Nb, Ta, Mo, and W solutes with the edge dislocation in the average-atom MoNbTaW alloy computed by Zhou et al. EAM-type interatomic potentials [203].	142
8.3	Energy difference for different solute-types swaps versus transition paths across the core as numbered in the inset. Only transitions from higher to lower energy states have been considered in these calculations.	144
8.4	NEB results for a sample MoNbTaW random alloy at different cross-core diffusion states ρ .	146
8.5	Average energy barrier versus applied stress over 100 realizations of edge dislocation motion in random NbMoTaW alloy between two adjacent local minimum energy states for different number of solute swaps (diffused density ρ) as obtained by direct NEB simulations and predicted by theoretical model, Eq. (8.6) using an average solute-swap energy change of $\overline{\Delta W} = 200$ meV	147

List of Figures

8.6	Strength versus temperature for MoNbTaW HEA as obtained by the present theory with different vacancy concentrations together with the experimental data and the results of Maresca and Curtin model.	151
A.1	The initial and final screw configurations in pure Fe to be used for subsequent NEB simulations of double-kink nucleation in dilute Fe-Si alloys.	163
A.2	Atomistic modeling of single kink motion.	165

List of Tables

4.1	Parameters describing the transition state configurations for double-kink nucleation of pure Fe at various normalized applied stresses, τ/τ_p . The geometrical factor, $G(\tau/\tau_p)$ is obtained by Eq. (4.6) with $g(z, \tau)$ given by Eq. (4.19) and $N_s = 10$.	57
4.2	The kink formation energy E_k , solute/dislocation interaction energy parameter $\Delta\tilde{E}_p$, characteristic length ζ_c , and the typical energy reduction due to solute fluctuations ($ \Delta\tilde{H}^{\text{sol}} + \bar{\sigma}_{\Delta H^{\text{sol}}}$) at characteristic length $\zeta_c = Nl d_k$, for various non-dilute complex alloys.	73
6.1	Symbols defining all relevant quantities in the theory.	108
6.2	Input parameters to the theory for all alloys studied. Please refer to [94] for more details.	112
7.1	Characteristic length scale and energy barrier, $\text{mean}(\cdot) \pm \text{standard deviation}(\cdot)$ of the corresponding distributions, as measured by direct NEB simulations and as predicted by theory [93] for two model alloys.	129
7.2	Single-element properties used in the reduced edge theory predictions	136

Introduction, Background, Part I

Computational Methods, and

Interaction energy parameter

1 Introduction and Background

1.1 Strength of materials

From a mechanical and materials engineering point of view, the strength of a material can be defined as its ability to resist an applied load without failure or plastic deformation. The strength of the material plays a key role in designing structural materials (e.g. bridges, turbine blades, etc.) and thus exploring and designing different ways to enhance the materials strength has been an active area of research for over a century. The strength of metals can be measured by applying tensile or compressive forces to the test specimens at a specified strain rate $\dot{\epsilon}$, and temperature T , until failure of the material. The outcome of the test is a stress-strain curve, from which the mechanical properties of the material can be extracted. An example of this curve is shown in Figure 1.1 for Mo single crystals. The important mechanical properties which can be extracted from the stress-strain curves include the yield stress, the ultimate stress and the fracture strain. The yield stress (strength) is a material property on the stress-strain curve where the material begins to deform plastically. Since dislocations are well-understood to be responsible for plasticity in crystalline materials, the strength of materials indicates the stress at which dislocations move. A dislocation is a type of defect in crystalline materials which significantly influences its mechanical performance, to include strength as will be discussed further in Section 1.2. In this thesis, we are merely interested in the yield stress of the materials.

The atoms in metallic materials are typically divided into three common crystal structures, namely body-centered cubic (BCC), face-centered cubic (FCC), and hexagonal close-packed (HCP). The variation of strength for various BCC materials versus the temperature and strain rate is shown in Figure 1.2. Generally, the strength of crystalline materials having a BCC structure (e.g. Fe, Mo, W, Nb, Ta, V) are much higher while showing increased low-temperature-dependency compared to those having a FCC structure (e.g. Al, Ni, Cu, Ag). Magnesium, which is known as the lightest structural material has a HCP crystal structure.

A group of BCC metals including Niobium, Molybdenum, Tantalum and Tungsten that possess extraordinary resistance to heat and wear are referred to as refractory metals. Refractory metals have attracted a lot of attention, over the past decades, due to their remarkable properties,

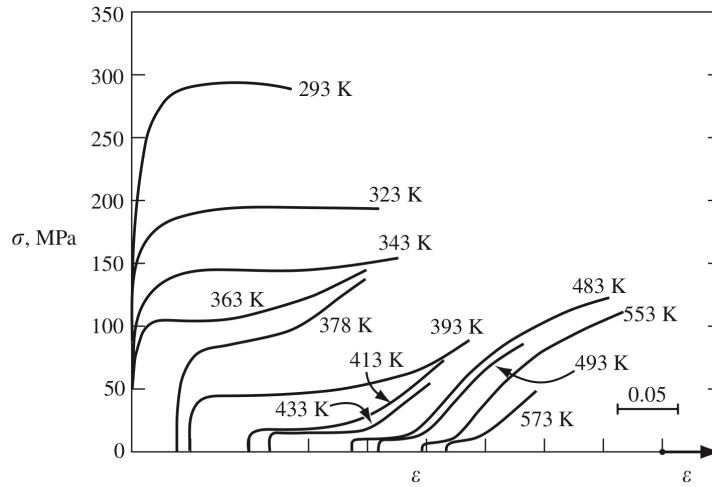


Figure 1.1 – **Tensile stress-strain curves of Mo single crystals at various temperatures.** Experiments performed at a tensile strain rate of $\dot{\epsilon} = 7 \times 10^{-6} \text{s}^{-1}$. From Ref. [5].

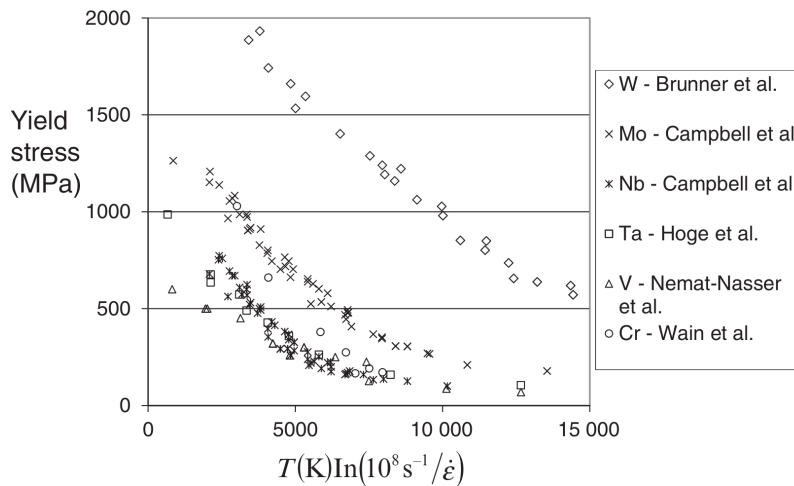


Figure 1.2 – **Yield stress versus temperature and strain rate for six pure BCC metals.** Experimental yield stress versus temperature for pure W [14], Mo [12], Nb [12], Ta [66], V [105], and Cr [180] BCC metals. Adapted from Ref. [43]

especially at high temperatures. The shared key properties between these elements include a melting point above 2000°C , high hardness at room temperature, high mass density, and very high strength at extreme temperatures. These significant properties make refractory metals a very good candidate for applications such as rocket nozzles, weapon projectiles, turbine engines, nuclear power plants, and casting molds. However, one of the shortcomings of refractory metals is their weak low-temperature mechanical behavior in their elemental form. Therefore, different approaches have been proposed in order to enhance their mechanical performance.

A metallurgical practice to improve the performance of the elemental metals is by alloying

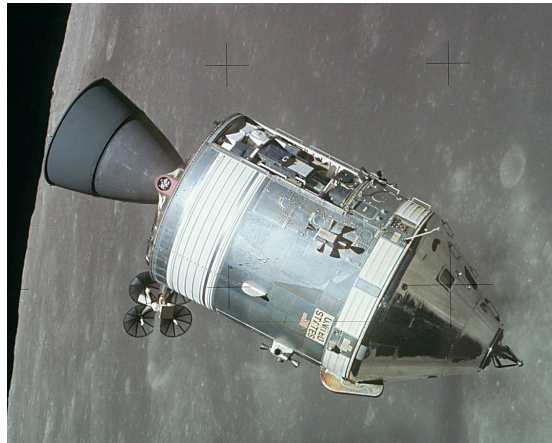


Figure 1.3 – **Application of Niobium in aerospace industry.** The dark rocket nozzle of Apollo command and service module is made from niobium-titanium alloy. From Ref. [62].

through adding dilute concentrations of alloying elements. Alloying is a classical approach that has been used by humans since the Bronze Age to enhance the properties of pure metals. Bronze, formed by adding tin to copper, is known as the oldest alloy, which has been used extensively by ancient civilizations for making sculptures and utensils. The bronze age was followed by the iron age, marked by the advent of steel, an alloy of iron and carbon that is stronger and more durable than bronze. As human civilization has progressed, alloying has been used extensively to produce structural materials with superior mechanical properties such as higher strength and toughness relative to those of the principal pure element.

Alloying was traditionally accomplished by adding relatively small amounts of a secondary element (solutes) to a primary element (host); e.g. Rhenium to Tungsten, Silicon to Iron, Tungsten to Niobium, etc. Solutes enter the host material as substitutionals or interstitials and alter its mechanical properties. In the former, the solutes sit on the lattice sites of the host material, while in the latter the solutes occupy interstitial voids. Figure 1.4(a) and (b) shows the variation of yield stress versus temperature for two substitutional Fe-Si and Nb-Mo BCC binary alloys, respectively. The effect of interstitial oxygen on the yield stress of Nb is also shown in Figure 1.4(c).

The design of metal alloys has recently undergone a paradigm shift with the proposition of a fundamentally new alloying concept, termed high-entropy alloys (HEAs). HEAs are a new class of metal alloys with multiple principal components combined, in relatively high, roughly equiatomic concentrations. HEAs show enhanced mechanical properties that can far exceed those of the constitutive pure elements. Although these alloys have complex compositions, they typically form a single FCC or BCC phase without precipitates. Given that these alloys do not contain a single primary element, as opposed to traditional dilute alloys, all of the atoms can be regarded as solutes within an average matrix serving as the host. In the past few years, refractory HEAs mainly comprised of refractory elements (W, Nb, Mo, Ta) have gained the interest of researchers due to their interesting mechanical properties, e.g. high strength at

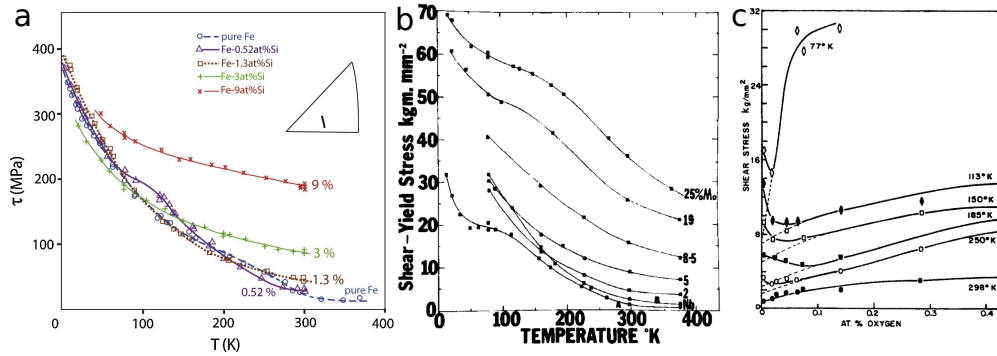


Figure 1.4 – **Temperature-dependent experimental flow stress in BCC pure metal and dilute alloys.** (a) Variation of experimental yield stress versus temperature in (a) Fe-Si substitutional alloys [78], (b) Nb-Mo substitutional alloys ([152]). (c) Yield stress versus interstitial oxygen concentration in Nb-O alloys at various temperatures [125]. Adapted from Refs. [18, 152, 125].

room temperature and exceptional strength retention at elevated temperatures. The plot of the temperature-dependence of yield stress for two NbMoTaW and VNbMoTaW refractory HEAs is shown in Figure 1.5. In addition to very high strength retention of the two refractory HEAs, experimental results exhibit a plateau of strength in the intermediate temperature range of 600°C to 1000°C. In addition, the strength in BCC NbMoTaW and VNbMoTaW refractory HEAs show a smaller temperature dependency as compared to the pure BCC metals.

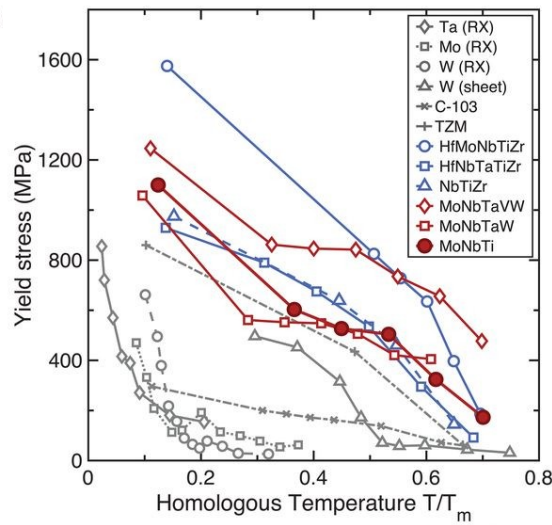


Figure 1.5 – **Yield stress versus temperature for various BCC multicomponent alloys.** The yield stress versus normalized temperature T/T_m is shown for several refractory HEAs [29, 137], where T_m denotes the melting point. For comparison, results for pure BCC metals (Ta, Mo, W) in either recrystallized (RX) or rolled condition (sheet) [9, 133] as well as the commercial dilute alloys, C-103 (a Nb-based alloy) and TZM (a Mo-based alloy, Mo-Ti-Zr), are also included. Adapted from Ref. [181].

The rest of this chapter is organized as follows. First, we provide an overview of screw dislo-

cations in BCC crystalline materials starting with a brief definition of dislocation in Section 1.2. An introduction to existing theories for solute strengthening in BCC dilute to high entropy alloys is given in Section 1.3. We then present the scope and general structure of this thesis in Section 1.4.

1.2 Dislocations in BCC materials

Dislocations are a line defect within a crystalline material which was first introduced in 1934 as a way of explaining the discrepancy between the theoretical estimate and experimentally observed strength of crystalline materials [166, 110, 115]. Dislocations were later directly observed in a crystal in 1956 [65] after the invention of the transmission electron microscope (TEM). The plastic properties of metals and other crystalline materials is primarily controlled by the motion and evolution of these dislocations. Dislocations mark the boundary between the slipped and unslipped parts of the crystalline material, as shown in Figure 1.6. The dislocations can be identified by a line direction ξ and a Burgers vector \mathbf{b} . The Burgers vector indicates the displacement in the crystal caused by the movement of the dislocation. Each crystalline material has its own characteristic Burgers vectors for a given glide plane.

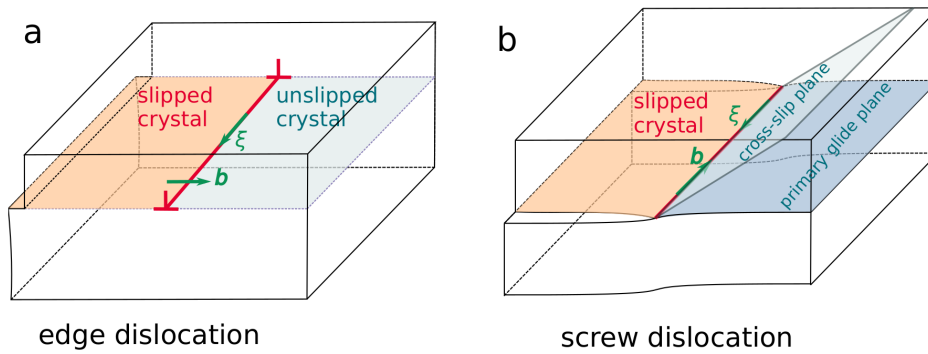


Figure 1.6 – **Schematic of screw and edge dislocations gliding on a slip plane of a crystalline material.** (a) edge and (b) screw dislocation. A dislocation is characterized by its dislocation line ξ and Burgers vector \mathbf{b} . In an edge dislocation ξ and \mathbf{b} are perpendicular to each other, while these two vectors are parallel or anti-parallel in the case of screw dislocation. From Ref. [1].

In general, there are three types of dislocations: screw, edge, and mixed, depending on the angle between the line direction and the Burgers vector. In a screw dislocation, the Burgers vector and line direction are parallel to each other; in an edge dislocation the Burgers vector is perpendicular to the line direction; other intermediate cases are classified as mixed dislocations. The glide plane of a crystal is the plane that contains both vectors ξ and \mathbf{b} . Dislocation motion along its glide plane is the most common type of dislocation motion which merely requires relative slip between atoms on both sides of the glide plane. Non-screw dislocations are constrained to glide on one plane, since their Burgers vector and line direction form a unique glide plane. On the other hand, screw dislocations can glide from one plane

to another, through a process called cross-slip. Cross-slip is a result of the fact that the glide plane is not unique for screw dislocation motion, making it possible for the screw dislocation to change slip planes in response to the applied stress or overcome a barrier caused by an obstacle such as solutes.

In a crystalline material, the combination of slip plane and slip direction define the slip system. The slip system in BCC metals is more complex than metals with FCC structure. Slip is favored on close-packed planes, since lower shear stress for atomic displacement is required. However, unlike FCC, there are no truly close-packed planes in the BCC crystal structure. In BCC crystals, the atoms are closest to each other along the $\langle 111 \rangle$ direction and thus any plane in the BCC crystal that contains this direction is a suitable slip plane. Experiments have shown that slip in BCC metals occurs in the closed pack $\langle 111 \rangle$ direction and the Burgers vector is $a_0/2\langle 111 \rangle$ where a_0 is the lattice constant [24, 22, 165, 58, 186]. Moreover, the most commonly observed glide plane in BCC metals is the $\{110\}$ plane. Figure 1.7(a) shows the $[111]$ direction in the $(1\bar{1}0)$ glide plane. There exists six $\{110\}$ type planes in BCC structure. As shown in Figure 1.7(b), each $\{110\}$ plane has two $\langle 111 \rangle$ type direction, which consequently gives rise to 12 slip systems of this type in a BCC crystal structure.

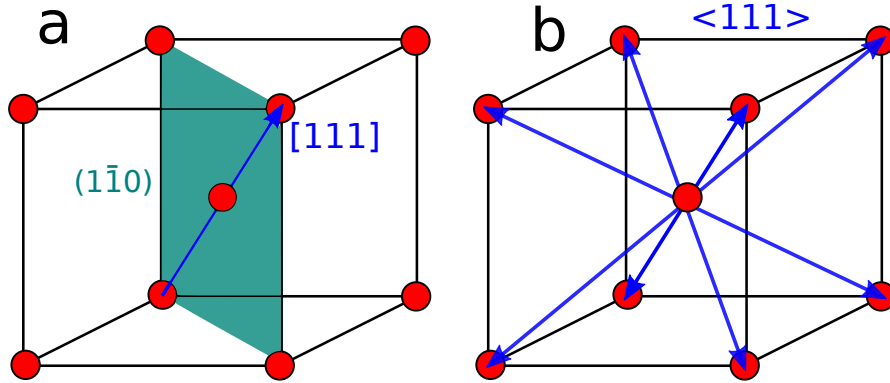


Figure 1.7 – **Schematic illustration of the preferential glide plane and glide direction in BCC crystal.** (a) Schematic of the $[111]$ direction in the $(1\bar{1}0)$ glide plane. (b) Each $\{110\}$ plane has two $\langle 111 \rangle$ type direction.

In the light of above, in this study the Burgers vector and glide plane of both the edge and screw dislocations considered is $b = a_0/2[111]$ and $\{110\}$ -plane respectively. Consequently, the dislocation line is aligned with $\langle 112 \rangle$ and $\langle 111 \rangle$ directions for the edge and screw dislocations, respectively.

The strain and stress fields induced by line defects at regions far from the dislocation line, can be accurately described within the framework of the linear theory of elasticity. However, at regions in the vicinity of the dislocation line elastic theory does not hold, predicting unphysical stress and strain fields. This region around the dislocation line where elasticity cannot be applied is termed the dislocation core and requires special theoretical treatment or atomistic simulations.

1.3 Solute strengthening theories for BCC materials

Depending on the deformation mechanisms dominating the plasticity in BCC materials, the solute strengthening theories can be broadly classified into three categories; (I) screw strengthening theories in dilute alloys, (II) screw strengthening theories in BCC non-dilute and high entropy alloys, and (III) strengthening theories in high entropy alloys where the motion is controlled by edge dislocations. In the following of this section, the overall picture of the dislocation mechanisms in BCC dilute and high entropy alloys along with a brief introduction of the existing solute strengthening theories is presented.

It is well known that in BCC metals and dilute substitutional alloys, the plastic deformation is controlled by the thermally activated two-step motion of the screw dislocations. The first step is the nucleation of a pair of kinks somewhere along an initial long straight screw dislocation, as shown schematically in Fig. 1.8a. The second step is the migration of these kinks along the screw that ultimately advances the entire screw dislocation forward by one Peierls valley (Fig. 1.8b). This motion of screw dislocations by double-kink nucleation and propagation is consistent with the TEM observations of long dislocations in BCC metals and alloys [24, 7, 163, 44].

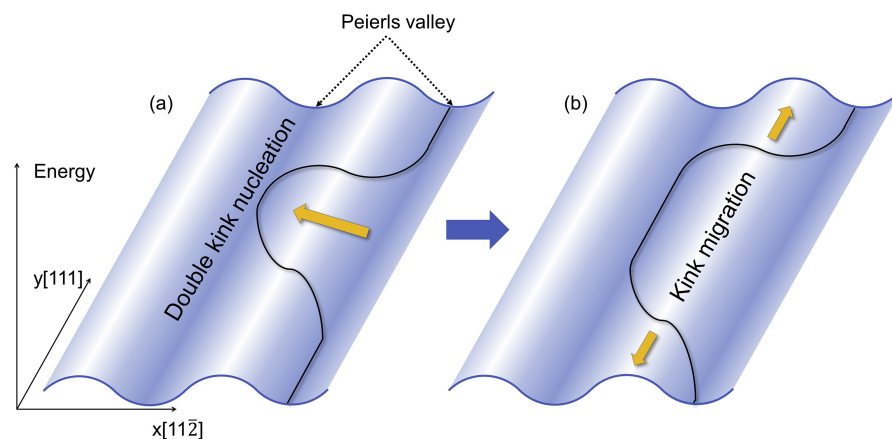


Figure 1.8 – **Plastic deformation in BCC pure metal and dilute alloys by thermally-activated double-kink nucleation and kink propagation processes.** (a) A pair of kinks is first nucleated somewhere along the straight dislocation line. (b) The kinks formed in (a) are then migrated away from each other to finally advance the dislocation to the next Peierls valley.

Plasticity in BCC metals and alloys via double-kink nucleation and kink propagation is thermally activated, i.e. it is temperature-dependent. For instance, as shown in Figure 1.4, the experimentally observed flow stress of pure Fe and Fe-Si alloys [78] as well as Nb and Nb-Mo [152] alloys decrease with increased temperature.

In pure BCC metals, the double-kink nucleation always control the dislocation motion, since there is a negligible barrier against the kink migration. However, when the solutes are added to the pure metal, both the double-kink nucleation and kink migration barriers will be affected by

the interactions between solutes and the screw dislocation. The general understanding is that in BCC dilute alloys, the double-kink nucleation controls the motion at low temperatures, while at higher temperatures the dislocation motion is controlled by kink migration. Furthermore, with increasing solute concentration, the double-kink nucleation barrier is steadily reduced while the kink migration is more inhibited. Therefore, there is a cross-over from double-kink nucleation controlled to kink migration controlled motion which is temperature- and solute-dependent.

From the above, it can be seen that alloying has a significant effect on the strength of the materials which is the stress required to move a dislocation. Therefore, the term "solute strengthening" refers to the increased stress required to move a dislocation in dilute or complex alloys. Solute strengthening arises from the totality of the interaction energies between the solutes and an individual dislocation. Over the past few decades, a great deal of effort has been put into developing theoretical models that predict the strength of alloys as a function of alloying elements and temperature.

One of the main theories rationalizing the strengthening in dilute binary BCC alloys is the Suzuki's theory [158, 15, 61] which accounts for the effects of solutes on double-kink nucleation, kink migration, and cross kink/jog/dipole formation. For a long time, Suzuki's solid strengthening theory has been considered as the only theory applicable to BCC substitutional alloys. The dominant strengthening in the Suzuki model is the inhibition of kink glide along the screw dislocation line due to solutes. Despite its success in predicting the strength of some dilute alloys, Suzuki's theory suffers from some rudimentary approximations on the interaction energy between the solutes and the dislocation. More details of Suzuki's theory with a focus on its elementary approximations are given in Section 3.

The mobility of screw dislocations in BCC alloys have been modeled using kinetic Monte Carlo (KMC) models. KMC models are mesoscale type of models providing time and length scales more suitable for experiments, as compared to molecular dynamics. The KMC models were originally developed for pure and dilute BCC systems [157, 202, 199, 147], and have recently extended to multi-component alloys [204, 205]. Although, the KMC models have been able to predict the softening-to-hardening transition in dilute alloys such as W-Re [202] and Fe-Si [147], they have failed to capture the experimental results, especially at low temperatures. These failures are, however, not due to the flaw in the KMC model itself but rather in the assumed parameters for the barrier and Peierls stress that are based on DFT [202] or EAM potential [147], which have shown to be not realistic.

The impressive mechanical properties of single phase BCC multi-component alloys, including medium and high entropy alloys, has renewed interest in understanding the mechanisms controlling strength in BCC alloys. While the deformation mechanisms of BCC metals and their alloys are relatively well understood, theories that explain the behavior observed in BCC refractory medium entropy alloys have only recently begun to be developed [204]. Retaining the classical view that screw strengthening is the dominant factor, Rao et al. [119, 120, 123]

adapted the Suzuki model to the HEA case. Recent KMC simulations [204] suggest that the strength in Nb-V-Ta BCC alloy is controlled by double-kink nucleation and migration at low temperatures, while the high-temperature strength is controlled by the cross-kinks. The cross-kinks form due to the collision of kinks gliding on different glide planes, as schematically shown in Figure 1.9. The breaking of cross-kinks requires the creation of high-energy-cost point defects, which create high energy barriers to flow.

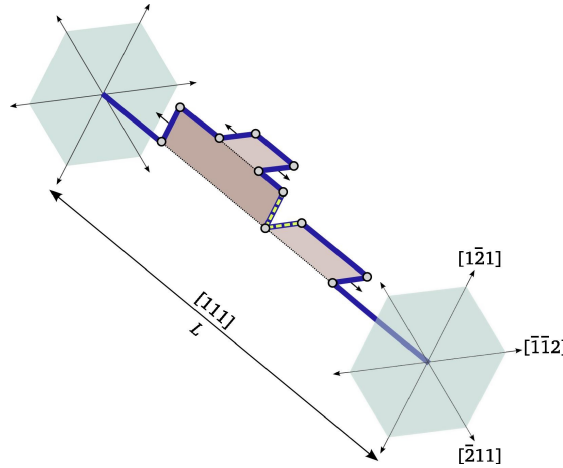


Figure 1.9 – **Schematic of cross-kink formation as a result of the collision of kinks propagating on different glide planes..** Two pair of kinks are nucleated on two different $\{110\}$ planes along the $[111]$ screw dislocation line of length L . The arrows indicate the direction of motion of kinks under an applied stress. A cross-kink, shown by dashed line, is formed at the intersection point of two spreading kinks. From Ref. [157]

Recent theory and simulation of strengthening of screw dislocations in HEAs propose that screw dislocations become spontaneously kinked along their length to lower the total energy due to solute/screw interactions [94]. The screw dislocation motion is then controlled by a combination of Peierls-like motion, lateral kink migration, and cross-kink failure. More details of screw strengthening theory in HEAs will be presented in Section 6.

The BCC refractory HEAs composed of the family of Cr-Mo-W-V-Nb-Ta-Ti-Zr-Hf-Al are of particular interest due to their high-temperature strength retention. Very recent experimental and theoretical studies have proposed that yield strength in these and other BCC HEAs is controlled by edge dislocation[93], rather than the classical view of strengthening controlled by screw dislocations. The high energy barriers against the edge dislocation motion in BCC HEAs will be analyzed in detail in Section 7 using atomistic simulations.

1.4 Scope and structure of the thesis

As described in the preceding sections, the strength of a material is related to the resistance of an individual dislocation against motion. Solute strengthening then refers to the increased strength required to move the dislocation caused by the solute/dislocation interactions. Solute

strengthening theories are aimed to provide a theoretical framework for an accurate estimation of the strength of the material. Developing robust theoretical statistical models for predicting the strength in dilute and high-entropy BCC alloys is the main objective of this thesis. We will approach the problem from an energy-based rather than a force-based perspective.

In order to validate our theoretical models, extensive atomistic simulations are performed in this study. In chapter 2 we briefly review the fundamental principles of the computational methods employed in this research including molecular statics and the nudged-elastic-band (NEB) method. The EAM interatomic potentials, as well as concept of "Average atom" interatomic potential are briefly introduced in this chapter. One of the main issues with the atomistic simulations of screw dislocations is the non-physical behavior that EAM potentials typically show. Therefore, it is crucial to use an EAM potential that is reliable and does not exhibit unphysical behaviors in the atomistic simulations. More specifically, the EAM potentials should be validated in terms of the correct prediction of the screw dislocation properties, namely the core structure and Peierls barrier. As such, a close examination of the widely used EAM potentials for the screw dislocation motion will be given in this chapter. Here an EAM potential is shown to have all the key aspects for screw dislocation in Fe and will be used to perform our atomistic simulations.

The fundamental quantity in every solute strengthening theory is the interaction energy between solutes and the dislocation. To have a proper description of solute interaction energies effect on the dislocation mobility, a full statistical solute/screw interaction energy parameter is introduced in Chapter 3. The parameter is valid for any number of constituent atoms and at any concentrations, thus including the range from dilute binary alloys to high-entropy alloys. This parameter is extensively examined in this chapter via atomistic simulations and will be used in our subsequent developments of solute strengthening theories in dilute and high-entropy BCC alloys.

The next two sections constitute the second part of this thesis and are devoted to the strengthening of screw dislocation in dilute BCC alloys. The energy barrier for thermally activated double-kink nucleation and kink migration processes are influenced by random solutes in dilute BCC alloys. The effect of solutes on the double-kink nucleation and migration barriers are examined in Chapters 4 and 5 respectively. A predictive statistical model is developed based on the energetics of solutes with the double-kink and single-kink structures which are then extensively validated via simulations in model Fe-Si alloys. The theoretical models are applied to real dilute alloys and good agreement is obtained with experiments over a range of concentrations and temperatures with no fitting parameters.

In the third part of this thesis, we then turn our interest to strengthening mechanisms in HEAs where the strength is screw-controlled (chapter 6) or can be controlled by edge dislocations (Chapters 7 and 8). Chapter 6 presents a new theory for the kink migration in screw-controlled HEAs based on our recent understanding in dilute alloys as described in Chapter 5, leading to a fully derived analytical model for the kink migration energy barrier as a function of applied

stress and kink spacing. A revised version of the Maresca-Curtin screw strengthening theory that incorporates the new kink migration model is then compared to experiments on non-dilute Fe-Si, Nb-Mo, and Nb-W alloys and shows broad agreement as a function of temperature and composition, establishing the quantitative accuracy of the new theory.

In chapters 7 and 8 we focus on the strengthening mechanisms in HEAs where the strength is controlled by edge dislocation motion. More specifically, in chapter 7, the energy barriers for edge motion are computed for two model alloys, NbTaV and MoNbTaW as represented by interatomic potentials, using the NEB method and compared to theoretical predictions. A reduced analytic model based on solute misfit volumes is then applied to Hf-Mo-Nb-Ta-Ti-Zr and Mo-Nb-Ta-Ti-V-W alloys, rationalizing the observed significant strength increases at room temperature and 1000°C upon addition of solutes with large misfit into a base alloy.

BCC refractory HEAs show high strength retention at elevated temperatures, including a plateau in strength at the intermediate temperature regime. An example of the strength plateau at intermediate temperatures for the two BCC refractory HEAs, MoNbTaW and VMoNbTaW can be seen in Figure 1.5. In chapter 8, a model for dynamic strain aging via cross core diffusion is presented. Cross-core diffusion occurs when the solute diffuses right at the core of edge dislocation from higher to lower-energy sites, providing an additional barrier against dislocation motion, increasing strength as a consequence. The model is able to predict the additional time-dependent energy barrier and strength in random BCC HEAs. Results for a model MoNbTaW alloy show the general observed behavior, but would require high vacancy concentrations to reach quantitative agreement with experiments.

A summary of the main findings of this thesis is presented in Chapter 9, where several potential directions for future research in the area of solute strengthening in BCC alloys is also discussed.

2 Computational Methods

2.1 Molecular statics simulations

Materials are made of atoms interacting with each other. Consider a system consisting of N interacting atoms represented in a $3N$ -dimensional "configurational space" with a position $\mathbf{R} = (\mathbf{r}_1, \mathbf{r}_2, \dots, \mathbf{r}_N)$, where \mathbf{r}_i represents the position of the i^{th} -atom. Any arbitrary configuration \mathbf{R} has its potential energy on this configurational space. Therefore, the configurational space can be envisioned as a potential energy surface (PES) with some topography and described by a potential energy function $U(\mathbf{R})$. The potential energy function describes the interactions between atoms solely in terms of interatomic distances. A schematic of this potential energy surface is shown in Figure 2.1 comprising a number of valleys and mountains. The valleys (darkest regions) represent the local minima which are the metastable states in the system. The mountains (lightest regions) are the maxima, i.e the points with the highest potential energy. The dashed lines divide the configurational space into regions, each of which corresponds to the set of points yielding the same minimum. The saddle points, denoted by S , are the points on the line connecting two maxima and will be discussed in Section 2.2. The deepest minima in the energy landscape corresponds to defect-free system with crystalline arrangements of the atoms. Defects will influence the energy states, giving rise to minima with somewhat higher energies on the energy landscape, compared to defect-free states. As such, identifying these energy minima are of great interest since they reflect the energetically metastable configurations of the system.

Molecular statics (MS) simulations employ an energy minimization in order to find the atomic configurations corresponding to the local minima (the "relaxed" states) of the potential energy surface. The relaxation of the system starts from an initial guess (the "unrelaxed" states) of the equilibrium structure. Widely used minimization algorithms in MS simulations include gradient methods (e.g. steepest descent, conjugate gradient) and damped dynamics methods (e.g. FIRE [11]). Using these algorithms, the atomic positions are iteratively updated until the force or energy of every atom is less than a specified force or energy tolerance. MS simulations are extremely useful in computing the intrinsic zero temperature, $T=0$ K, material properties (e.g.

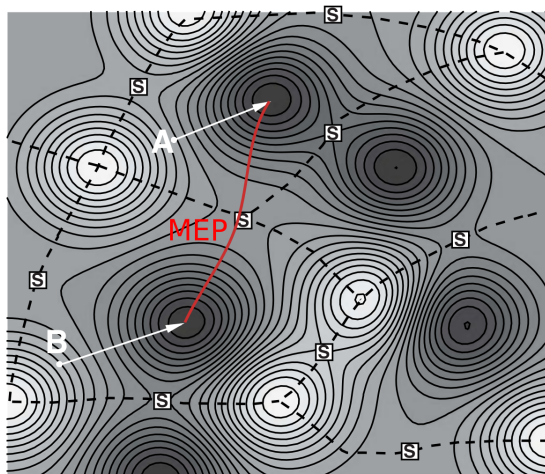


Figure 2.1 – **Schematic illustration of a 3N-dimensional potential energy surface.** Each point on this surface corresponds to a particular configuration \mathbf{R} with a specific potential energy given by the potential energy function $U(\mathbf{R})$. Minima and maxima are the darkest and lightest regions, having the lowest and the highest potential energy, respectively, and "s" denote the saddle points. Solid lines represent contours of constant potential energy. From Ref. [161].

lattice parameter, elastic constants, generalized stacking fault curves, etc.) and identifying the configuration and energetics of dislocations and other crystalline defects. MS simulations can also be used to find transition paths and saddle points in the energy landscape. The transition path is the trajectory connecting two minima with the lowest energies and the saddle point is the point with the maximum energy along the transition path which will be described in Section 2.2.

The critical component in molecular statics simulations is the interatomic potential function $U(\mathbf{r}_1, \mathbf{r}_2, \dots, \mathbf{r}_N)$. The accuracy of the atomistic simulations is controlled by the interatomic potentials. Although, first principle methods, such as Density Functional Theory (DFT), could, in theory, be employed to accurately determine the potential energy of any atomistic configurations, such calculations require an enormous amount of computational resources, even for a small number of atoms, and thus cannot be feasibly used. This is especially true for simulations of dislocation motion in BCC metals and alloys which require simulating tens of thousands of atoms. For instance, a typical configuration for studying the screw dislocation motion in BCC metals consists of at least 4×10^4 atoms which is far beyond the current capacity of DFT calculations. Due to the limitations of first principle calculations, a large effort in the computational research community is devoted to the development of empirical interatomic potentials. These interatomic potentials are essentially functions that map the configuration of atom positions to a corresponding energy. An empirical potential usually takes on a fixed functional form containing several free parameters. These free parameters are obtained by fitting to experiments and/or first-principle calculations such that specific material properties, e.g. lattice or elastic constants, are reproduced in simulation. The embedded atom method

(EAM) is one of the widely used frameworks of empirical potentials to describe metals in MS simulations. We present the details of EAM potentials in the next Section 2.1.1.

As it was alluded to above, the solute strengthening in multi-component alloys is due to the underlying interactions between the solutes and an individual dislocation. Therefore, it is of particular importance for alloy development to understand how solutes interact with such defects. Atomistic simulations can provide us with the means to quantify such solute/dislocation interactions. Typical HEAs have many elemental components at high concentrations and with local structural/compositional disorder. From an atomistic point of view, two approaches can be implemented in order to model these multicomponent random alloys. A straightforward method is to randomly assign an atom type to each atomic site with a probability proportional to the desired atomic concentration and then use the EAM potentials as described above. However, high fluctuations in local atomic chemical environments make the analysis of solute/dislocation interactions in such random systems, difficult and ill-defined. Average-atom approximation is the second approach which can be used to study the complex random alloys. This method has emerged as a powerful way to compute material properties and, more importantly, solute-dislocation interaction energies. In this method, instead of occupying the atomic sites with true random solutes, a fictitious “average” atom (A-atom) type is used to generate an effective “average alloy” which has the same average properties as the true random alloy. In order to model an “average alloy” medium, a corresponding A-atom EAM potential needs to be developed as discussed in Section 2.1.2.

In this research work, all the molecular statics simulations are conducted with the open-source Large-scale Atomic-Molecular Parallel Simulator (LAMMPS) [114]. Depending on the problem under consideration, EAM or A-atom EAM potentials were used to compute the total potential energy of the metallic atomistic system. In addition, the visualization and post-processing of the resulting atomic configurations are performed using the Open Visualization Tool (OVITO) [155]. In particular, the Common Neighbor Analysis (CNA) functionality of OVITO is utilized to identify the dislocations in crystal structures.

2.1.1 Embedded atom method

The embedded-atom method (EAM) potential is the most widely used type of interatomic potential in MS simulations to describe BCC metals and alloys. In an EAM representation of a given material, the total energy is computed as follows. Consider an alloy with N_T distinct atom types and a total number of N atoms, with average concentration c_X of each alloying element X , with $\sum_{X=1}^{N_T} c_X = 1$. A configuration of this alloy consists of a set of atomic sites $i \in 1, \dots, N$ occupied by individual atoms. Let s_i^X denote site occupation variable, where $s_i^X = 1$ if a type- X atom sits in i site and 0 otherwise. Within the Embedded Atom Method (EAM) [11],

the total energy of a given configuration is

$$E(\{s_i^X\}) = \sum_i^N \sum_X^{N_T} s_i^X F^X(\rho_i) + \frac{1}{2} \sum_{i,j \neq i}^N \sum_{X,Y}^{N_T} s_i^X s_j^Y V^{XY}(r_{ij}) \quad (2.1)$$

with

$$\rho_i = \sum_{j \neq i}^N \sum_X^{N_T} s_j^X \rho^X(r_{ij}) \quad (2.2)$$

Here X, Y indicate the different individual atom types and r_{ij} denotes the distance between sites i and j . Moreover, $V^{XY}(r_{ij})$ is the pairwise interaction between atoms X and Y , $F^X(\rho_i)$ is the embedding energy for atom X at site i , ρ_i is the total electron density at site i , and $\rho^X(r_{ij})$ is the contribution of an X -atom at site j to ρ_i . It is worth mentioning that all $V_{XY}(r_{ij})$ and $\rho^X(r_{ij})$ are radially symmetric. Therefore, the EAM represents a reasonable approximation for materials without preferred angles, such as FCC and BCC metals.

Given that the functional form representing the EAM potential has a limited number of adjustable parameters, the fitting process involves heuristic decisions as to which properties are most desirable. Consequently, each EAM potential may be suitable for specific types of problems and may lead to unphysical results for other problems. For instance for an EAM potential which has been developed by fitting the parameters to such material properties as lattice constant, elastic constants, and stacking fault energies, it may not be suited for studying the mechanisms involved in the dislocation motion. The EAM potentials are even more problematic when applied to simulations concerning plasticity in BCC materials, where the motion is controlled by screw dislocations. For instance, most of the widely-used EAM potentials for BCC metals and/or alloys produce unphysical screw core structures despite good predictions for other material and defect properties. The problematic features of the EAM potentials for BCC metals with a special focus on the screw dislocation core structure properties will be discussed in Section 2.4.

2.1.2 Average-atom approximation of random alloys

As explained above, the core idea in the A-atom method is to replace the true atom types with a single fictitious "average" atom type (A-atom) which, to a good approximation, yields the same average energy. The A-atom medium can be modeled by a corresponding A-atom EAM potential which was derived by Smith et al. [149] and Vervenne et al. [173]. The corresponding "average alloy" is shown to possess all of the important average properties of the true random alloy: lattice constant, elastic constants, and stable/unstable stacking fault energies. It should be noted that the A-atom method, in contrast to true random alloy, is free from fluctuations. As such, the A-atom cannot predict properties that are controlled by solute fluctuations, e.g. the Peierls stress.

Averaging Eq. (2.1) over occupation variables s_i^X , and under the assumption that the occupa-

tions in sites i and j are uncorrelated in the random alloy, i.e., $\langle s_i^X s_j^Y \rangle = \langle s_i^X \rangle \langle s_j^Y \rangle$, Varvenne et al. [173] obtained the preliminary result for the average potential energy of the system

$$\langle E \rangle = \sum_i^N \sum_X^{N_T} c_X \langle F_X(\rho_i) \rangle + \frac{1}{2} \sum_{i \neq j}^N \sum_{X,Y}^{N_T} c_X c_Y V^{XY}(r_{ij}), \quad (2.3)$$

where $\langle s_i^X \rangle = c_X$. Eq. (2.3) is simplified further by performing a Taylor expansion of the embedding energy around the average electron density $\langle \rho_i \rangle$, $\langle F^X(\rho_i) \rangle = \langle F^X(\langle \rho_i \rangle) \rangle + \mathcal{O}(\rho_i - \langle \rho_i \rangle)^2$, in which the first order term vanishes since $\langle (\rho_i - \langle \rho_i \rangle) \rangle = 0$. Neglecting the second and higher order terms, which is the only approximation, leads to the following expression for the average energy

$$\langle E \rangle = \sum_i^N F^A(\langle \rho_i \rangle) + \frac{1}{2} \sum_{i,j \neq i}^N V^{AA}(r_{ij}), \quad (2.4)$$

where

$$F^A(\langle \rho_i \rangle) = \sum_X^{N_T} c_X F_X(\langle \rho_i \rangle), \quad V^{AA}(r_{ij}) = \sum_{X,Y}^{N_T} c_X c_Y V^{XY}(r_{ij}), \quad \langle \rho_i \rangle = \sum_{j \neq i}^N \sum_X^{N_T} c_X \rho_X(r_{ij}), \quad (2.5)$$

where A denotes an average-atom having embedding function, F^A and self-pair-interaction, V_{ij}^{AA} . The A -atom interatomic potential of Eq. (2.4) has exactly the EAM form for the potential energy of an elemental atom, Eq. (2.1) and the A -atom EAM potential functions are the concentration-weighted averages of the corresponding pure element functions. Varvenne et al. [173] showed that the A -atom accurately predicts average properties of true random alloys at zero temperature such as the lattice parameter, the elastic constants, and the stacking fault energy. Furthermore, it facilitates the calculation of solute-defect interaction energies, which would be cumbersome using a direct approach based on true random alloys. Recently, Nöhring and Curtin [107] verified the A -atom approach for finite temperature calculations.

The A -atom EAM potential can further be used in combination with the individual alloying elements X in simulations. This is particularly useful when computing the solute/dislocation interaction energies. The average properties of a substitutional "solute" atom of type X_0 in the A -atom host matrix, where X_0 is any of the constituent alloying elements can be computed by A -atom potentials. These properties require computing the average energy change when a solute X_0 is added to the random alloy. Suppose for a random configuration described by occupation variables, s_i^X the atom at site k is replaced by a type X_0 -atom, then it can be shown that the average energy change for such a replacement becomes [173]:

$$\langle \Delta E \rangle = \left[F^{X_0}(\langle \rho_k \rangle) + \sum_{i \neq k} V_{ki}^{X_0 A} \right] - \left[F^A(\langle \rho_k \rangle) + \sum_{i \neq k} V_{ki}^{AA} \right], \quad \text{with } V_{ki}^{X_0 A} = \sum_Y c_Y V_{ki}^{X_0 Y}, \quad (2.6)$$

where $V_{ki}^{X_0 A}$ is the pairwise interaction between X_0 and A -atoms. Eq. (2.6) is identical to the result obtained by introducing an atom X_0 into site k of the A -atom material. Figure 2.2

illustrates the use of *A*-atom EAM potentials in computing the interaction energy of a Nb solute at various sites around the core of screw and edge dislocations in an average NbTaV alloy. The map interaction energy change due to the movement of the screw dislocation by a and edge dislocation by w is also shown in this figure. As will be seen in the forthcoming Chapters, the key parameter entering the strengthening theories is the change in interaction energy as the dislocation moves by specific distances, here a and w for screw and edge dislocations, respectively.

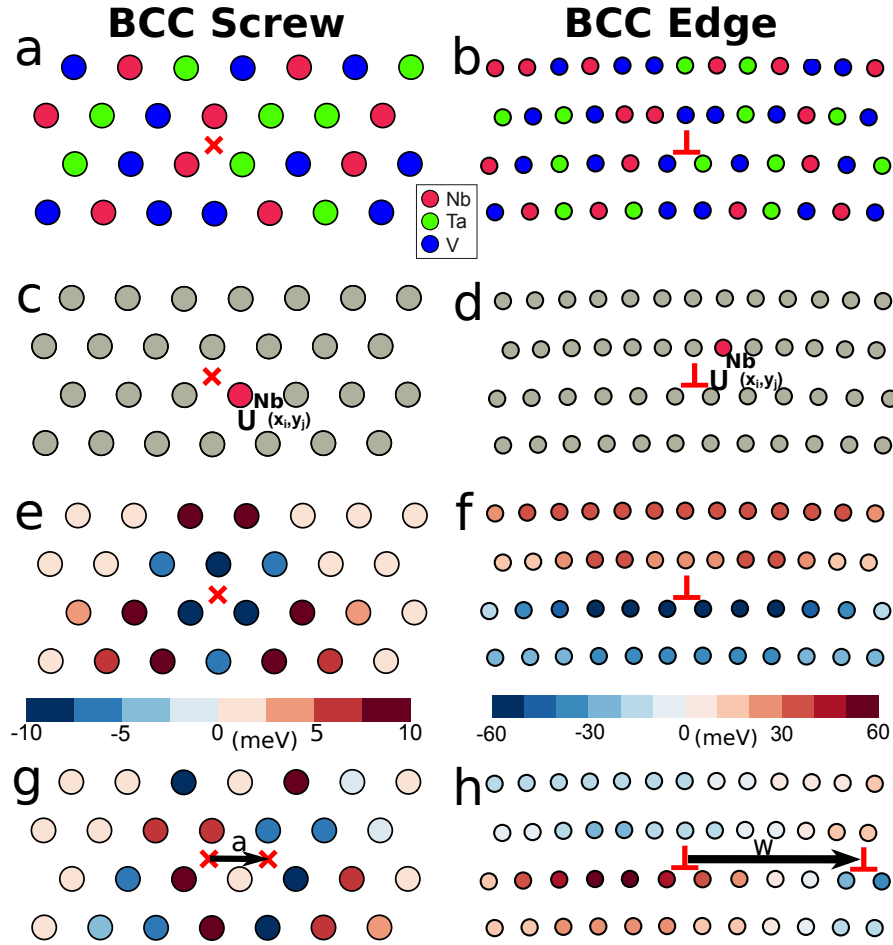


Figure 2.2 – **Average-alloy method for solute-dislocation interaction energy.** (a,b) A screw and an edge dislocation in a model NbTaV random BCC alloy. (c,d) The screw and edge dislocations in the corresponding average-alloy effective mediums. The *A*-atom at site (x_i, y_j) is replaced by a Nb solute to compute the interaction energy $U^{\text{Nb}}(x_i, y_j)$. (e,f) The map of solute/dislocation interaction energy at various sites around the dislocation core. (g,h) The corresponding interaction energy change as the screw and edge dislocation move by a and w , respectively.

2.2 Transition state theory

This section provides a brief overview of the transition state theory utilized to compute the rate of transition between two metastable states. Interested readers should refer to Refs. [79, 116, 134, 135] for more details on the transition state theory, with an emphasis on thermally activated dislocation mechanisms.

As it was alluded to above, the process of transformation of the system from one valley (metastable state) to the next one occurs through a path, termed the minimum energy path (MEP). MEP is the lowest energy trajectory connecting the two valleys through a saddle point in between. The saddle point is the state with the maximum potential energy on the MEP corresponding to the transition state. The rate (events/second) of transformation is then controlled by the activation energy (energy barrier) defined as the energy difference between the transition state and the initial metastable state.

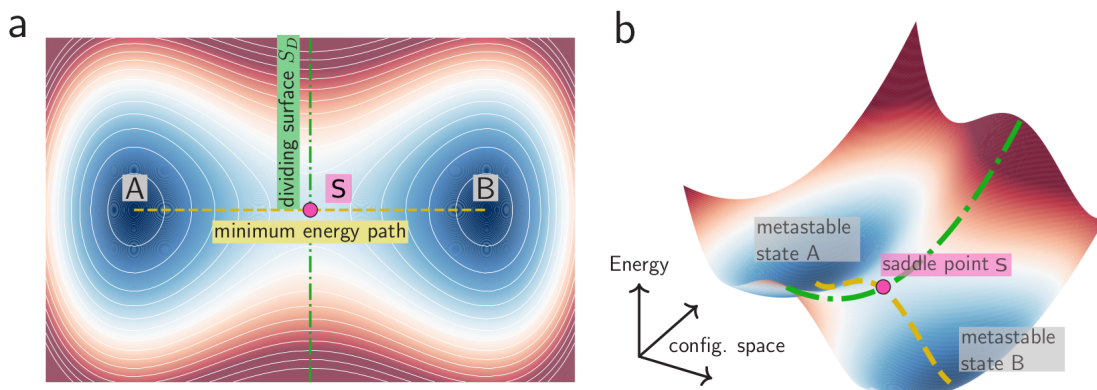


Figure 2.3 – **Schematic of a thermally activated process from an initial metastable state A to final metastable state B in a potential energy surface through the transition state S.** (a) The metastable states and transition state are shown in a two-dimensional potential energy surface. The dividing surface S_D divides the potential surface into two regions corresponding to states A and B. The yellow dashed line is the minimum energy path connecting the two metastable states with a transition state located on the dividing surface. (b) A three-dimensional representation of the potential energy surface. From Ref. [1].

Consider an N -atom system undergoing a transition from state A to state B , in a $3N$ -configuration space, passing through the transition state S , with the help of thermal fluctuations, as shown in Figure 2.3. Moreover, assume a (hyper)surface S_D which passes through the transition state P , lies perpendicular to the contour of potential energy and divides the PES into two regions of the basins corresponding to A and B . Transition state theory (TST) [178, 40] uses equilibrium statistical mechanics to determine the rate of transition between A and B . For an NVT distribution of microstates, under the TST, the rate of transition from state A to state B

happening at temperature T is expressed as [178]

$$v_{A \rightarrow B}^{\text{TST}} = \sqrt{\frac{k_B T}{2\pi m}} \frac{\int_{S_D} e^{-U(\mathbf{R})/k_B T} dS}{\int_A e^{-U(\mathbf{R})/k_B T} d\mathbf{R}} \quad (2.7)$$

Here k_B is the Boltzmann constant, m is the atomic mass, and $U(\mathbf{R})$ is the potential energy of the system in configuration \mathbf{R} . In order to avoid the cumbersome evaluations of the integrals in above equation, a more tractable, simplified expression for the transition rate is obtained based on the harmonic transition state theory (HTST) as

$$v_{A \rightarrow B}^{\text{HTST}} = \frac{\prod_{i=1}^{3N} v_i^A}{\prod_{i=1}^{3N-1} v_i^P} \exp\left(-\frac{\Delta E}{kT}\right) \quad (2.8)$$

where v_i^A and v_i^P are the normal frequency modes arised near states A and P , respectively, and $\Delta E = U(\mathbf{R}_P) - U(\mathbf{R}_A)$ is the energy barrier of the transition. The computation of all the N normal modes, however, becomes intractable as the system size N becomes large.

A further simplification is then followed by condensing the prefactor in Eq. 2.8 to a trial frequency ν_0 , reducing the transition rate to the simple form of the Arrhenius equation [6, 82]

$$v_{A \rightarrow B} = \nu_0 \exp\left(-\frac{\Delta E}{kT}\right) \quad (2.9)$$

Frequently, for thermally activated transitions in crystalline materials ν_0 is taken to be the Debey frequency which is in the order of 10^{13} s^{-1} [126, 174]. The Arrhenius equation above has been sucessfully applied to investigate various thermally activated dislocation mechanisms in materials with HCP [191, 190, 3, 2], FCC [38, 39, 182], and BCC [126, 94, 93] crystalline structures. The main goal of this thesis is to find the relevant activation energies for various thermally activated processes associated with screw dislocation motion in BCC alloys. Upon substitution of such activation energies into the Arrhenius equation, Eq. (2.9), the rate of transition for corresponding thermally activated processes can then be computed at specific temperatures.

2.3 Nudged Elastic Band method

From Eq. (2.9), it can be clearly seen that the quantity which plays the crucial role in determining the transition rate of a thermally activated process is the energy barrier ΔE . Therefore, calculating this energy barrier is of tremendous interest which, however, is not a trivial task. We typically have access to the initial and final metastable states involved in the transition and are curious about the MEP that connects them. The MEP is a trajectory connecting two metastable states (energy minima) in a transition and the highest energy point along the MEP is called the saddle point. The MEP thus allows us to identify the transition state, i.e. saddle point, and, consequently, the energy barrier associated with it. In light of the above, we need to find the MEP between two known metastable states on either side of an energy

barrier. Several computational approaches have been proposed for finding the MEP, such as the nudged elastic band (NEB) method [63, 64, 104, 92], doubly nudged elastic band method [168], and the string [184] and simplified string [185] methods.

The Nudged Elastic Band (NEB) and string methods are two widely-used computational techniques for computing the MEP between known initial and final states. In this thesis, we use the NEB method as implemented in the *replica* package in LAMMPS to find the MEP, and hence the energy barrier, for the mechanisms involved in the dislocation motion in random BCC alloys. Broadly, our dislocation problems of interest can be classified into two categories; (a) the screw dislocation in random dilute alloys and (b) edge dislocation in random HEAs. The details on constructing the initial and final configurations for the NEB simulations are presented in Appendix A.3.

Here we briefly present the basics of NEB simulations following the work of Jonsson et al. [75]. In an NEB simulation, by a linear interpolation between initial and final configurations, the MEP is first discretized into a chain of intermediate states, termed replicas or images and designated by Q . Let the MEP is discretized into $M + 2$ replicas which are denoted by positions $\mathbf{R}_0, \mathbf{R}_1, \dots, \mathbf{R}_{M+1}$ in the configurational space. Consequently, \mathbf{R}^0 and \mathbf{R}^{M+1} denote, respectively, the first and last replicas which correspond to the initial (metastable state A) and final (metastable B) states. The remaining M intermediate replicas, as initialized by some interpolation scheme, are connected to other replicas by inter-replica spring forces. In a NEB simulation, the end replicas are kept fixed, while the intermediate replicas are allowed to evolve towards the MEP under two combined forces. An attractive force due to underlying potential energy tries to attract the replica towards the nearest metastable state and can be expressed as

$$\mathbf{F}_i^{\text{pot}} = -\nabla U(\mathbf{R}_i) \quad (2.10)$$

and an inter-replica spring force which seeks to maintain equal separation between replicas and is given by

$$\mathbf{F}_i^S = k^S (\mathbf{R}^{i+1} - \mathbf{R}^i) - k^S (\mathbf{R}^i - \mathbf{R}^{i-1}) \quad (2.11)$$

where k^S is the spring constant. The sum of the two forces above, give the force acting on each intermediate replica as,

$$\mathbf{F}_i = \mathbf{F}_i^{\text{pot}} + \mathbf{F}_i^S, \quad 1 \leq i \leq M \quad (2.12)$$

However, the above representation of the force may not effectively lead to the MEP due to high sensitivity of the chain of replicas on the spring constant k . The NEB method alleviates this by using certain components of each force contribution and, instead of Eq. (2.12), writes the force acting on replica i as

$$\mathbf{F}_i^{\text{NEB}} = \mathbf{F}_i^\perp + \mathbf{F}_i^{S\parallel}, \quad 1 \leq i \leq M \quad (2.13)$$

where \mathbf{F}_i^\perp and $\mathbf{F}_i^{\text{S}\parallel}$ are, respectively, the components of the potential force perpendicular to the path tangent and components of the spring force parallel to the local path tangent on i^{th} image, as schematically shown in Figure 2.4, which are expressed as

$$\begin{aligned}\mathbf{F}_i^\perp &= \mathbf{F}_i^{\text{pot}} - (\mathbf{F}_i^{\text{pot}} \cdot \hat{\tau}_i) \hat{\tau}_i, \\ \mathbf{F}_i^{\text{S}\parallel} &= (\mathbf{F}_i^{\text{S}} \cdot \hat{\tau}_i) \hat{\tau}_i\end{aligned}\quad (2.14)$$

where

$$\hat{\tau}_i = \frac{\mathbf{R}_{i+1} - \mathbf{R}_{i-1}}{|\mathbf{R}_{i+1} - \mathbf{R}_{i-1}|}, \quad 1 \leq i \leq M \quad (2.15)$$

Finally, by using a force-based minimization algorithm, the replicas are minimized towards the MEP of the transition until the convergence criteria is achieved. Only, a brief introduction of the NEB method was presented here. For a more detailed and elaborate explanation of the NEB method, the reader is referred to Refs. [63, 64, 104, 92].

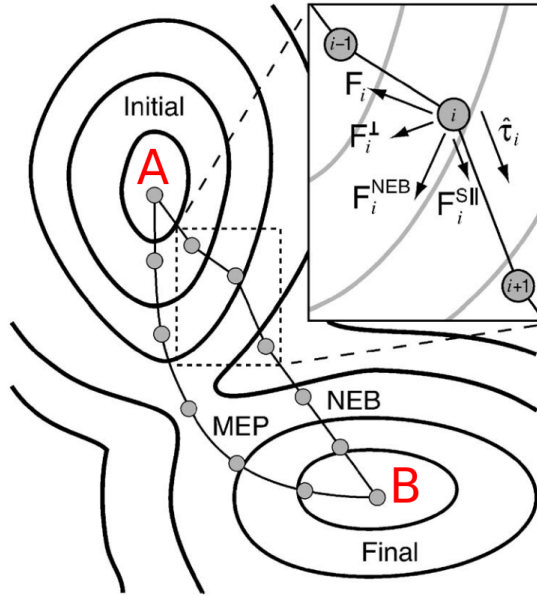


Figure 2.4 – **Schematic of force components involved in NEB calculation for the MEP between initial (A) and final (B) metastable states in a two dimensional potential energy surface.** The i^{th} image has tangent $\hat{\tau}_i$ and the NEB force on it $\mathbf{F}_i^{\text{NEB}}$ contains two components, $\mathbf{F}_i^{\text{S}\parallel}$ and \mathbf{F}_i^\perp , which are, respectively, the component of the potential force perpendicular to $\hat{\tau}_i$ and the spring force parallel to $\hat{\tau}_i$. From Ref. [146]

2.4 Atomistic simulations of screw dislocations

Atomistic simulations have emerged as a powerful and insightful tool, providing insight about dislocation behavior in crystalline materials. As it was mentioned before, due to the very

large sizes required, the study of dislocation motion via DFT calculations is not possible. Instead, interatomic EAM potentials have played an important role in exploring the dislocation behavior in BCC materials at the atomic level. Although, there has been numerous potentials developed for BCC pure elements, such as Fe and W, the interatomic potentials for BCC alloys are still quite limited. Moreover, most of the existing EAM potentials do not provide a good representation of screw dislocation properties in BCC metals when compared to DFT calculations. These properties include the correct core structure and Peierls potential shape. If the potentials are meant to be used to simulate the screw dislocation motion in BCC metals, they should first be validated in order to ensure they do not lead to unphysical behaviors. As such, this section aims to give a brief introduction on the dislocation properties and also examine the widely used EAM potentials in the literature for BCC metals. An interatomic potential satisfying the key features will be introduced which will be used in our atomistic simulations of screw dislocation mobility.

2.4.1 Screw dislocation core structure

The screw dislocation mobility is highly influenced by the core structure of screw dislocation in BCC metals and alloys. Therefore, it is imperative to gain a thorough understanding of the various types of core structures and their effect on the mobility of screw dislocations. In BCC crystals, the most common Burgers vector is $\mathbf{b} = a/2\langle 111 \rangle$ where a is the cubic lattice parameter. When visualizing screw dislocations, the BCC crystals are commonly considered as a collection of atomic rows along $\langle 111 \rangle$ direction as depicted in Figure 2.5.

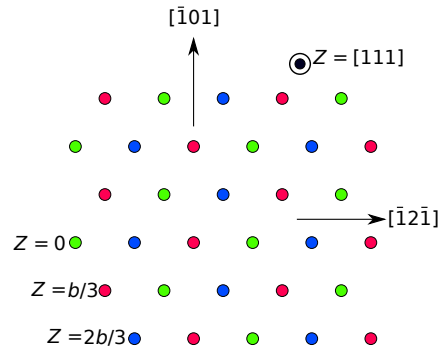


Figure 2.5 – **Pristine BCC crystal structure viewed as a collection of atomic rows along $[111]$ direction.** Circles represent atomic positions. Colors identify atomic positions in the pristine bcc crystal, for one periodic unit cell (length b) along the dislocation line direction Z , where green atoms are taken as reference ($Z = 0$), red atoms are in position $b/3$ and blue in position $2b/3$. The spacing between neighboring atoms in each row is $b = a\sqrt{3}/2$.

We now consider the case where a screw dislocation is inserted in the material. The screw dislocation core is centered in between three $\langle 111 \rangle$ neighboring atomic rows. The screw dislocations have been studied in different pure and alloyed metals using various atomistic approaches such as EAM potentials [35, 21, 96, 121, 192, 52, 117], bond-order potentials [102, 101], density functional theory (DFT) [72, 188, 189, 45, 167, 130, 175, 85, 176, 194, 10, 25]

and Gaussian approximation potential (GAP) [95]. By performing atomistic simulations, two different core configurations can be obtained, 'easy' and 'hard'. In an easy core configuration, the three atomic rows in the vicinity of the dislocation core exhibit a reversed helicity compared to the undeformed crystal, whereas in the hard core state the three rows are constrained to be at the same height. All the atomistic simulations confirm that the easy core is the most stable state, since it has much lower energy than the hard core configuration. In our study, we will only consider stable easy core configurations.

Depending on the material and the interatomic potential used, the easy core of the BCC screw dislocation can adopt two configurations, termed compact (symmetrical) and non-compact (asymmetrical) cores. DFT simulations predict that the easy core structure will be compact (symmetric) in pure metals [72, 188, 189, 45, 32, 26]. However, the majority of existing EAM potentials predict a non-compact core structure in elemental metals. In order to identify the type of easy core structure from atomistic simulations, differential displacement maps (DDM) can be utilized [34, 179, 35]. DDMs also enable us to determine at which position a dislocation is located. Figure 2.6 shows the DDMs for two compositions of TiZrNb complex alloy as atomistically modeled by the average-alloy method using the EAM potentials developed by Zhou et al. [203, 88]. The particular configurations shown for $\text{Ti}_{0.3}\text{Zr}_{0.3}\text{Nb}_{0.4}$ and $\text{Ti}_{0.3}\text{Zr}_{0.5}\text{Nb}_{0.2}$ alloys correspond to compact and non-compact core structures, respectively.

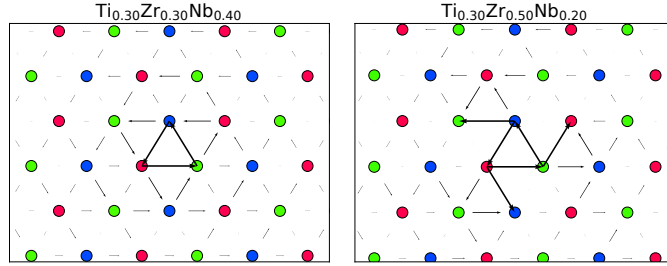


Figure 2.6 – **Differential displacement maps (DDMs) at the dislocation core for two compositions of TiZrNb ternary alloys.** The arrows are normalized by $b/3$ with a length $b/3$ scaled to connect neighboring atoms. Arrows represent the displacement of atoms along $[111]$ direction in the relaxed dislocated BCC structure, computed with respect to the pristine BCC atomic positions.

2.4.2 Peierls potential

Another important aspect of screw dislocation glide is the Peierls potential which shows how the energy changes between two neighboring easy core positions. The Peierls potential is the minimum energy path due to the rigid motion of the screw dislocation without kink nucleation. Such a minimum energy path can be obtained by performing nudged-elastic-band (NEB) simulations between two adjacent minimum energy configurations (Peierls valleys). The Peierls potential has been extensively studied in pure BCC metals by various atomistic approaches, such as EAM potentials [97], and DFT [31, 187, 176]. Fig. 2.7 shows the Peierls potential for five BCC transition metals as obtained by DFT simulations [31]. Note that the

DFT calculations reveal a single-hump shape in the Peierls potential for the selected BCC metals, including Fe and W.

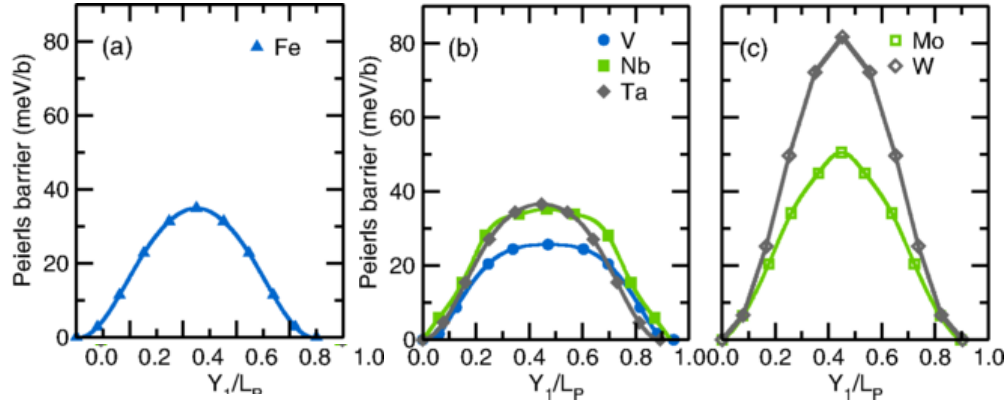


Figure 2.7 – **Peierls potential for different BCC metals computed by DFT.** Minimum energy path per unit b for BCC (a) Fe, (b) V, Nb, Ta, and (c) Mo, W. Adapted from [31].

In contrast to the DFT calculations, most of the existing EAM potentials exhibit a double-humped (camle-humped) shape in Peierls potential with two saddle-points configurations and an intermediate metastable configuration, including the widely used EAM potential developed by Mendelev et al. [97]. An example of such double-humped Peierls potential is shown in Fig. 2.8(a) for screw dislocation in α -Fe obtained using various EAM potential. The EAM potentials which show double-humped shape in their Peierls potential, are not consistent with the ab-initio simulations and thus fail to provide a good representation of the screw dislocation motion. The main issue with the EAM potentials showing double-humped Peierls potential is that they lead to the so-called split core structure during glide or with kink formation [55] which is not physical.

There has been some effort put into the development of EAM potentials for BCC metals that do not display the unphysical properties associated with screw dislocations as described above. The EAM potential developed by Provile et al. [117] is one of the potentials that correctly predicts all the key features for the screw dislocation in pure Fe, relative to DFT [73]. In particular, the Provile Fe potential predicts the compact (non-degenerate) core structure, single hump Peierls potential (see Figure 2.8(b)) and glide on 110 glide plane, all of which are consistent with DFT simulations. Gaussian approximation potential is another type of empirical potentials which have been shown to re-produce the key features of screw dislocation in Fe [95] and W [159] BCC metals. However, aside from the very high computational cost of GAP, to our knowledge, these potentials have only been developed for Fe and W pure BCC metals, and not alloys.

Since the main objective of this thesis is to study the mechanisms involved in the dislocation motion in the presense of solutes, it is essential to have a reliable interatomic potential for alloys. Recently, an EAM potential was developed by Shinzato et al. [147] for Fe-Si. The Fe-Fe interactions are based on the Provile Fe potential developed which, as discussed above, has

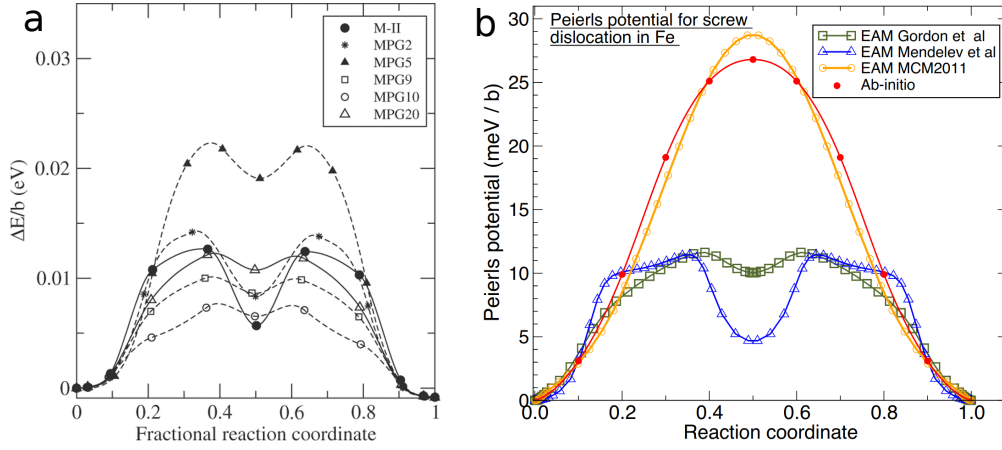


Figure 2.8 – Peierls potential for screw dislocation in pure Fe computed by EAM potentials and DFT Minimum energy path per unit b computed by (a) various EAM potentials; M-II developed in [97], all the rest developed in [56] and (b) EAM potentials; Gordon et al [56], Mendelev et al [97], and MCM2011 [117] and DFT [175]. Adapted from [56] and [117]

all the underlying DFT-based features of screw dislocation in pure Fe. The Fe-Si EAM potential will thus be used for our atomistic simulations of screw dislocation motion in random BCC alloys.

3 Solute/Screw Dislocation Interaction Energy Parameter

This chapter is extracted from the following publication

Ghafarollahi, A., Maresca, E., and Curtin, W. A. (2019). Solute/screw dislocation interaction energy parameter for strengthening in bcc dilute to high entropy alloys. *Modelling and Simulation in Materials Science and Engineering*, 27(8), 085011.

The plastic deformation in BCC metals and dilute alloys, as discussed in Section 1.2, is well-established to be mainly controlled by the motion of screw dislocations via thermally-activated double-kink nucleation and kink migration mechanisms [127, 136, 33]. In pure BCC metals, the rate-limiting step is the nucleation of a double-kink pair along an initial long straight screw dislocation. The migration of the kinks to advance the entire screw dislocation by one Peierls valley is then a relatively fast process. In dilute solid solution alloys, the solute interactions with the screw dislocation can affect both the kink-pair nucleation and kink migration [158]. Due to these interactions, the energy barriers for double-kink nucleation and for kink migration are changed, and this can lead to softening or hardening depending on the alloy and the solute concentration. These features are generally contained within the classical screw strengthening model of Suzuki [158] and subsequent models [167, 68]. However, these models make approximations about the nature of the solute-screw interaction energies, about the statistical aspects relevant in a random solid solution, and are only applicable to dilute binary alloys. With the emergence of BCC High Entropy Alloys that can show interesting and impressive mechanical properties, existing theories must be adapted, or new theories formulated, to handle such multicomponent non-dilute solid solution alloys.

The most important fundamental feature in solute strengthening theories of BCC alloys is the interaction energy of a $a/2[111]$ screw dislocation with an individual solute atom. In existing theories, only the interaction energy of solutes within the first three [167] or six [158] atomic rows of atoms (one or two sets of three atomic rows, each set of three identical by symmetry) immediately surrounding the center of the compact screw core are deemed relevant. This approximation emerged from Suzuki's estimation of the interaction energy

Chapter 3. Solute/Screw Dislocation Interaction Energy Parameter

using a rudimentary model, as shown in Fig. 3.1, where the solute-dislocation interaction energy was computed to be high and nearly equal for the inner 6 atomic rows. All interactions further from the core were neglected. The solute-dislocation interaction energies enter the strengthening theories through the *change* in energy as the screw dislocation moves by one Peierls barrier through the field of random solutes. The change in energy for a solute at each possible position, as computed by Suzuki, is shown in Figure 3.1(b). In this special case, the changes in energy are dominated by the six atomic rows immediately around the core, reinforcing Suzuki's concept that only these atomic sites are important.

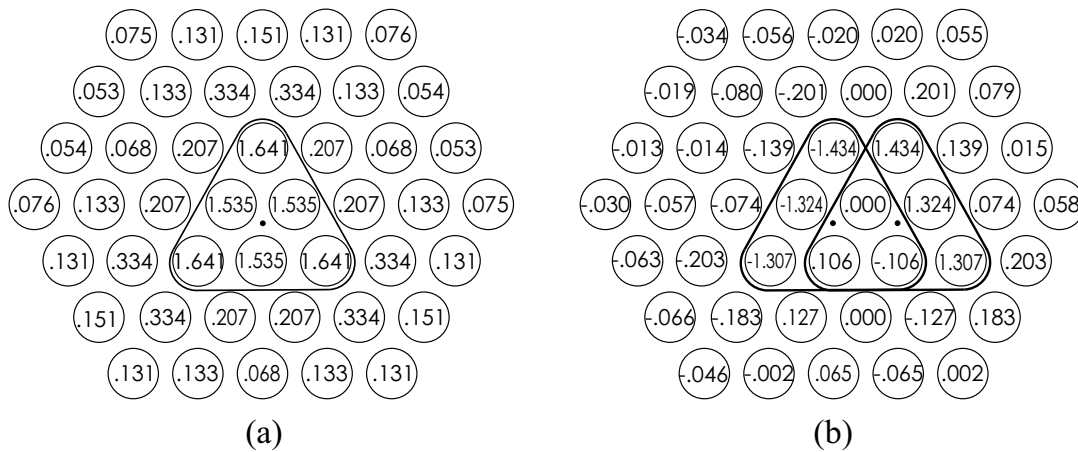


Figure 3.1 – **Suzuki's estimation of the solute/screw interaction energy** (a) Projected atomic positions of a screw dislocation core, viewed parallel to the dislocation line direction. Values at each atomic site indicate the interaction energy of the screw dislocation with a solute atom at that site as estimated by Suzuki, in arbitrary units. (b) Change in solute/dislocation interaction energy at each atomic site after movement of the core by one Peierls valley distance.

In contrast, examination of recent first-principles calculations of solute-screw interaction energies shows a more subtle field of interaction energies that extends beyond the six atom rows considered by Suzuki. Figure 3.2a shows the example of a Ti solute in W [70]. Here, the interaction energies of the two sets of three atomic rows - those considered by Suzuki - are not equal. Furthermore, there are significant additional interactions for solutes located at further distances from the core, with the highest single value being at a fifth-neighbor distance. The corresponding change in energy after screw glide by one Peierls valley is shown in Figure 3.2b. Clearly, there is a wide spectrum of energy changes associated with any individual atomic row, and non-negligible energies extend out well beyond the six atomic rows envisioned by Suzuki. Similar results are found for other solutes in W, for other solutes in other BCC metals, and in atomistic simulations using interatomic potentials. Figure 3.2c,d shows the case of Nb in NbTaTiV computed using EAM interatomic potentials (see below). The features in Figure 3.2 are common, and so the historical assumptions are not generally valid.

Given the interaction energy map of the type shown in Figure 3.2(a,c) and the associated energy change map shown in Figure 3.2(b,d), a number of fundamental issues arise. The

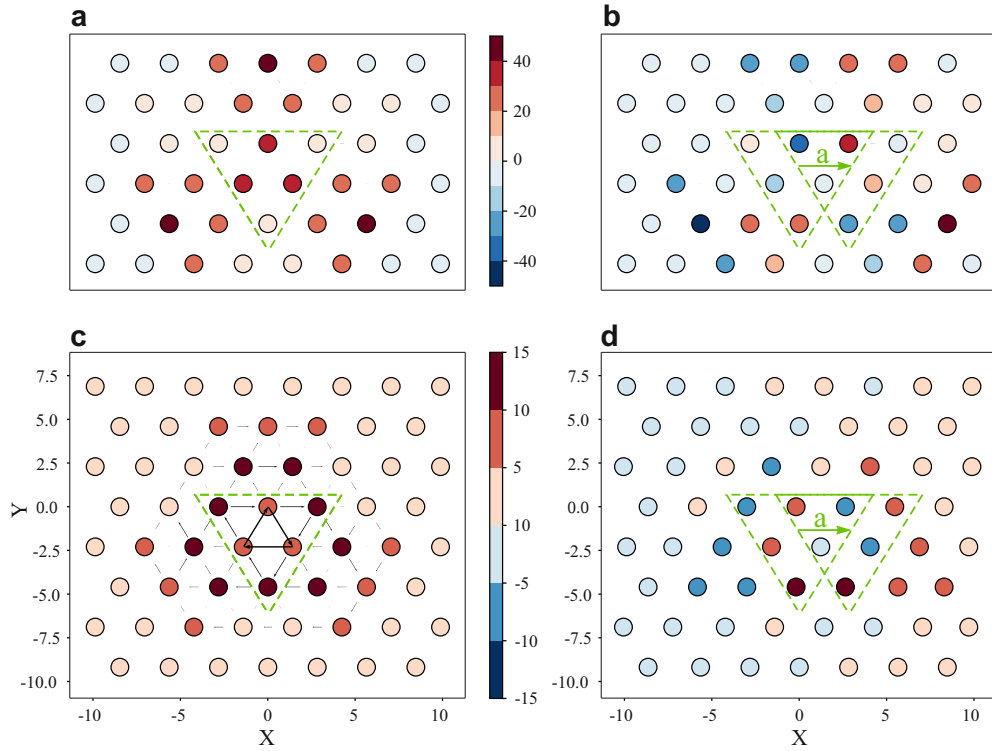


Figure 3.2 – Solute/screw dislocation interaction energy map. (a) Solute-dislocation interaction energy versus solute position around the screw dislocation core for a Ti solute in a W matrix, as computed by Density Functional Theory [70]. Green dashed line indicates the 6 atoms closest to the core that are considered in Suzuki model. (b) Interaction energy difference as the core moves by one Peierls valley distance a (green arrow). (c) Solute-dislocation interaction energy versus solute position around the screw dislocation core for a Nb solute in the average atom NbTaVTi matrix. Arrows correspond to the differential displacements (DD), showing that the core is compact and symmetric. Green dashed line indicates the 6 atoms closest to the core which are considered in Suzuki model. (d) Interaction energy difference as the core moves by one Peierls valley distance a (green arrow).

first issue is the identification of the correct solute/dislocation interaction energy parameter that should enter any theory for screw strengthening in alloys. The second issue is then what range of solute interactions are necessary to accurately compute this solute/dislocation energy parameter. The third issue is how to compute such a parameter in a complex multicomponent random alloy. The fourth issue is whether there is any simplified approximation that might enable sufficiently accurate estimation of the parameter. The final, and most important, issue is how the correct solute/dislocation interaction energy parameter should enter into any theory for solute strengthening. This last issue is not addressed here and is the subject of subsequent Chapters. The first four issues are the subject of this Chapter, and establish a basis for a theory for strengthening in BCC solid solutions including HEAs as is the main objective of this thesis.

Rao et al. [119, 120] have recently examined an interesting concept related to the fourth

issue above. Specifically, they have shown that there exists a good correlation between the solute-screw interaction energy in the first three atomic rows at the dislocation core and the interaction energy between the solute and the $[111]/6$ unstable stacking fault (USF). This correlation was made only for the central core rows. Although not carried out, the implication was that this single interaction energy could then be used in the Suzuki model assuming the energies of the six central atomic rows are equal to the solute/USF interaction energy. The correlation was established in several model High Entropy Alloys. Here, we further assess the correlation of the solute/USF energy with the new solute/dislocation interaction energy parameter.

3.1 Solute/Screw Interaction Energy Parameter

The solute/screw dislocation energy parameter in an alloy of arbitrary composition is obtained following the previous analysis for the same quantity in fcc materials [172]. The general concept is independent of crystal structure and/or dislocation type.

We consider a BCC HEA consisting of N types of alloying elements with concentration c_n of the n^{th} element ($\sum_{n=1}^N c_n = 1$). There is no correlation between the types of solutes on different distinct BCC lattice sites (i.e. the alloy is a random alloy). So, the probability that any specific lattice site is occupied by a type- n solute is exactly c_n . For the true random alloy at a given composition, we define a corresponding effective homogeneous alloy that has all the average properties of the true random alloy (e.g. lattice constant a_0 , elastic constants, C_{ij} , unstable stacking fault energy Γ_{USF} , etc.) but does not have the randomness. Each elemental alloy component can then be considered as a solute embedded in the effective alloy matrix. We can then conceptually create a straight screw dislocation in the effective matrix. The interaction energy of a type- n solute at position (x_i, y_j) relative to the screw dislocation positioned at the origin and aligned along z is denoted as U_{ij}^n . A schematic of this conceptual approach is shown in Figure 3.3. The quantity U_{ij}^n is shown in Figure 3.2(a,c) for many solute positions ij around the core in two different systems. As the dislocation glides by one Peierls valley distance a , a solute at position (x_i, y_j) now resides at a position $(x_i - a, y_j)$ relative to the new position of the dislocation core. Therefore, the energy change is $\Delta U_{ij}^n = U_{i-1,j}^n - U_{ij}^n$, as shown in Figure 3.2(b,d).

Strengthening of the dislocation by solutes is related to the changes in energy as a dislocation segment glides through the random alloy and experiences fluctuating environments of the surrounding solutes. These fluctuating energies are independent of how the dislocation actually moves, such as by double-kink nucleation and kink glide. So, we consider a straight screw dislocation segment of length ζ aligned along z -direction and centered at $(x = y = 0)$. The interaction energy of a solute of type n located at position (x_i, y_j, z_k) relative to the center of dislocation is denoted as U_{ijk}^n . Neglecting direct solute-solute interactions and due to the periodicity along z , this quantity is actually independent of z and is equal to U_{ij}^n for all atomic sites z_k associated with the in-plane position (x_i, y_j) . The analysis can be extended to include

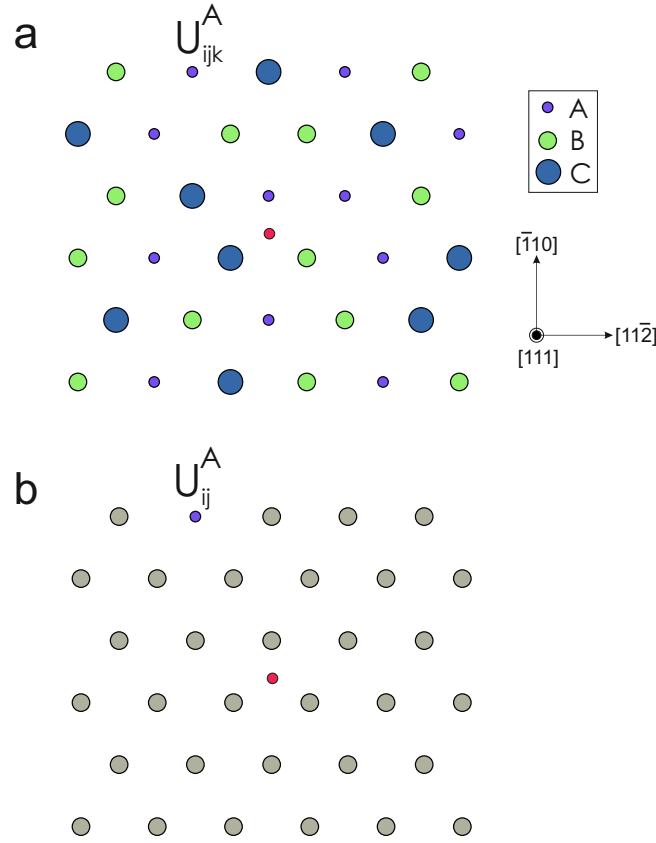


Figure 3.3 – **Average alloy method for solute-screw dislocation interactions.** (a) True random 3-component alloy containing a screw dislocation. The A solute at position (x_i, y_j, z_k) relative to the dislocation centered at the origin, has interaction energy U_{ijk}^A , (b) Average-atom material of the same alloy, with an embedded A solute at projected position (x_i, y_j) , with the same average interaction energy $U_{ij}^A = U_{ijk}^A$.

a distribution of local environments along z [172] but this feature is not discussed here, for simplicity. When the dislocation segment glides by a , the change in dislocation position relative to all of the fixed solutes leads to a potential energy change of

$$\Delta U_{tot}(\zeta, a) = \sum_{i,j,k} \sum_n s_{ijk}^n \left[U_{i-1,j,k}^n - U_{ijk}^n \right], \quad (3.1)$$

where the site occupation variable $s_{ijk}^n = 1$ if a type- n solute is at position (x_i, y_j, z_k) and 0 otherwise.

The mean energy change is zero. A (configurational) force acting on the dislocation due to the solute-dislocation interactions can only arise due to local spatial fluctuations in the solute concentrations. Such fluctuations create a statistical distribution of potential energy changes for the dislocation segment as it moves through the alloy. The magnitude of the typical energy

change is then characterized by the standard deviation of the potential energy change,

$$\sigma_{\Delta U_{\text{tot}}} = \left[\langle \Delta U_{\text{tot}}^2(\zeta, a) \rangle - \langle \Delta U_{\text{tot}}(\zeta, a) \rangle^2 \right]^{\frac{1}{2}} \quad (3.2)$$

where brackets denote averaging over random occupation variables s_{ijk}^n . With ζ/b sites along z for all (x_i, y_j) , the averaging process leads to

$$\sigma_{\Delta U_{\text{tot}}} = \left(\frac{\zeta}{b} \right)^{\frac{1}{2}} \Delta \tilde{E}_p(a), \quad (3.3)$$

where

$$\Delta \tilde{E}_p(a) = \left(\sum_{i,j} \sum_n c_n \Delta U_{ij}^n(a)^2 \right)^{\frac{1}{2}}, \quad (3.4)$$

where $\Delta U_{ij}^n(a) = U_{i-1,j}^n - U_{ij}^n$. Independent of the segment length ζ , and independent of the details of the dislocation motion, this analysis identifies the quantity $\Delta \tilde{E}_p(a)$ as the relevant scale for variations in the dislocation energy as a screw dislocation moves by one Peierls valley. The summations over i and j in Eq. (6.1) extend to infinity, in principle, and there are no limitations on the number of solute types or their concentrations. Eq. (6.1) is thus the fundamental energy parameter related to screw dislocation strengthening in random alloys. Its application in a new strengthening theory for BCC alloys is pursued elsewhere. Here we focus on evaluating $\Delta \tilde{E}_p(a)$ across a range of alloys.

3.2 Molecular Static Simulations

Here we describe the simulation details employed to compute the solute/screw dislocation interactions energies and the solute/ $\frac{1}{6}[111]$ unstable stacking fault interaction energy. The methods are standard, but details are provided for completeness.

All Molecular Statics simulations are performed using the Large-scale Atomic-Molecular Massively Parallel Simulator (LAMMPS) [114]. The alloy interatomic interactions are all described using the EAM potentials developed by Zhou et al. [203, 88] for the elemental family Nb-Ta-Ti-V-Zr. For each specific random alloy composition, it is possible to create the effective homogeneous matrix material of the alloy using the “average alloy” formulation of Varvenne et al. [173]. The resulting “average-atom” EAM potential for the alloy has, to high accuracy, all of the average properties of the true random alloy, but not the actual random atoms. Furthermore, an individual elemental solute of the alloy can be introduced into the average-atom material to measure the interaction energy of the solute with any defect created in the effective matrix/average-atom material, as shown in Fig. 3.3b and as described next.

To simulate the screw dislocation structure and the solute/screw interactions, we use a rectan-

gular simulation cell oriented with $[1\bar{1}2]$ along the glide direction X , $[110]$ along the glide plane normal direction Y , and $[\bar{1}11]$ along the line direction Z . The dimensions of the simulation cell are $L_1 \sim 300\text{\AA}$, $L_2 \sim 300\text{\AA}$, and $L_3 \sim 34\text{\AA}$ corresponding to 175,000 atoms. The perfect BCC lattice is populated with the corresponding average atoms. A screw dislocation of Burgers vector $a/2[111]$ with line direction along Z is then introduced by displacing the atomic positions according to the anisotropic elastic Volterra solution, and subsequent relaxation. During relaxation of atomic positions, periodic boundary condition is imposed along Z direction, while holding those atoms within two times the cutoff radius ($2r_c$) from the outer boundaries fixed at the initial Volterra displacement. The total energy E^{disl} of this relaxed system is computed.

It is well-established that the screw dislocation core structures predicted by various EAM potentials for the elemental BCC metals can have unphysical features. In particular, many potentials predict a so-called “polarized” core or 3-fold-symmetric core, whereas DFT studies nearly uniformly show an “unpolarized” or 6-fold-symmetric core. We thus carefully identify the core structure for each average-atom screw core obtained using the Zhou et al. potentials. We focus our study on those cores for which the core is 6-fold symmetric, but separately show results for cases that have polarized cores.

The type- n solute-screw dislocation interaction energy U_{ij}^n is measured at each symmetry-unique atomic site (x_i, y_j) around the dislocation core as follows, with all symmetry-equivalent sites having the same interaction energy. First a separate computation of the type- n solute solution energy $E^{\text{sol-bulk}}$ in a periodic bulk BCC crystal is performed. This is the difference between the energy of a bulk crystal with one solute and the same bulk crystal with no solute. Next, in the system with the screw dislocation, the average atom at the atomic site (x_i, y_j) is replaced by a type- n solute. The simulation cell is then relaxed to the minimum energy structure, while still holding the outer boundaries fixed at the initial Volterra displacements. The total energy of the relaxed system with the solute $E_{n,ij}^{\text{sol-disl}}$ is then computed. The interaction energy between the solute and the screw dislocation is then computed as

$$U_{ij}^n = \left(E_{n,ij}^{\text{sol-disl}} - E^{\text{disl}} \right) - \left(E^{\text{sol-bulk}} \right) \quad (3.5)$$

The neglect of the strain energy created by introducing the misfitting solute while holding the outer boundaries fixed can be estimated as misfit volume change, and associated misfit strain energy, is $E = \frac{1}{2} K \frac{\Delta V^2}{V}$ where V is the sample volume, ΔV the misfit volume of the solute, and K is the alloy bulk modulus. For all alloys studied here, this energy is at most 4×10^{-6} eV, and hence negligible. Direct tests also confirm that the dislocation length of $L_3 \sim 34\text{\AA}$ is sufficient to prevent any solute-solute image effects.

The solute-unstable stacking fault interaction energy is computed as follows. We use a simulation cell with the $[1\bar{1}2]$ direction along X ($\sim 60\text{\AA}$), $[110]$ direction along Y ($\sim 200\text{\AA}$), and $[\bar{1}11]$ direction along Z ($\sim 60\text{\AA}$) containing approximately 40000 atoms. The simulation cell is periodic in the X and Z directions, and has free boundaries in the Y direction. This cell is relaxed, giving rise to surface relaxations on the Y surfaces that do not affect the interaction

energy calculation. The upper half of the cell is then displaced by the $[111]/6$ unstable stacking fault vector relative to the bottom half of the cell. The simulation box is then relaxed only in the Y direction to form the relaxed stacking fault. The energy E^{usf} of this relaxed system is computed. A type- n solute is then introduced at an atomic position adjacent to the fault plane, the system is fully relaxed, and the energy $E_n^{\text{sol-usf}}$ is computed. The solute/USF interaction energy is then computed as

$$E_n^{\text{usf}} = \left(E_n^{\text{sol-usf}} - E^{\text{usf}} \right) - \left(E^{\text{sol-bulk}} \right) \quad (3.6)$$

The concentration-averaged solute/screw interaction energy, $\sum_n c_n U_{ij}^n$ for all ij and solute/USF interaction energy, $\sum_n c_n E_n^{\text{usf}}$ must both be zero, by construction. Deviations from zero can arise because the average-atom potential for the alloy is not exact or due to errors in the simulation methodology. We find only very small deviations from zero in all alloys studied in this Chapter, reinforcing the accuracy of the computational methods described here.

3.3 Results

We study multicomponent alloys across a wide range of compositions for the succession of Ti-Zr-Nb, Nb-Ta-V-Ti, and Nb-Ta-V-Ti-Zr alloys. Obtained using the Zhou et al. potentials, the computed energies are not expected to be accurate for the real alloys but are used to examine features of the key quantity $\Delta\tilde{E}_p(a)$.

3.3.1 Full results and convergence

The summations over i and j in Eq. 6.1 extend to infinity. However, $\Delta\tilde{E}_p(a)$ converges nicely because the energy differences $U_{ij} - U_{i-1,j}$ decrease rapidly beyond some distance away from the core. Here we study the convergence of $\Delta\tilde{E}_p(a)$ as a function of the inclusion of successive shells of atomic sites. The 1st, 2nd, and 3rd, shells contain 3, 6, and 12 atomic sites and correspond to the inclusion of 1st, 2nd, and 3rd nearest-neighbors, respectively, as depicted in Fig. 3.4. The 4th shell contains 27 atomic sites including the 4th, 5th, and 6th nearest-neighbors. The fully converged value is obtained considering 320 atomic sites around the core (not shown). The total interaction energy parameter corresponding to the n^{th} shell uses the atomistic interaction energies for all atoms within the n^{th} shell while setting all interaction energies outside the n^{th} shell equal to zero.

Figs. (3.5)a, (3.5)b, and (3.5)c show the interaction energy parameter $\Delta\tilde{E}_p(a)$ for the different shells of neighbors versus the composition of various BCC Ti-Zr-Nb, Nb-Ta-V-Ti, and Nb-Ta-V-Ti-Zr alloys having unpolarized cores, respectively. Inclusion out to the 4th shell of atoms (6th neighbors) is required to achieve good agreement with the fully-converged results. Consideration of the 1st shell only yields results that deviate from the converged result by approximately 10% across all alloys, which is surprisingly good. For 1st, deviations for Ti-

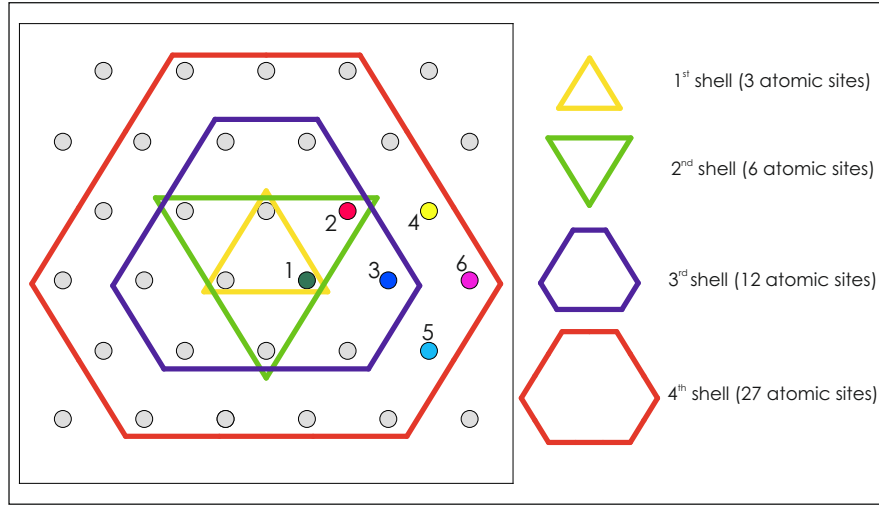


Figure 3.4 – **Successive shells of atomic sites around the compact dislocation core.** Definition of 1st, 2nd, 3rd, and 4th successive shells of atomic sites around the compact dislocation core used to study convergence of the solute/screw interaction energy parameter. Colored atoms and numbers show the first six near-neighbor atoms.

Zr-Nb are both positive and negative, while values for both Nb-Ta-V-Ti and Nb-Ta-V-Ti-Zr are typically underestimated. Consideration of the 2nd shell, however, yields a significant overestimate of the interaction energy parameter. Addition of the 3rd shell reduces that error, with the convergence achieved by including the 4th shell. We keep in mind that other interatomic potentials or first-principles methods may require more neighbor shells to achieve convergence although, to our knowledge, there is no evidence of this in any published results to date.

3.3.2 Suzuki approximation

The Suzuki approximation considers the first two shells and assumes the interaction energies in the two shells to be equal. Rao et al. used the interaction energy in the first shell within the Suzuki model. The interaction energy parameter for this model then reduces to

$$\Delta \tilde{E}_p(a) = \sqrt{6} \left[\sum_n c_n (U_{\text{first}}^n)^2 \right]^{\frac{1}{2}}, \quad (3.7)$$

where U_{first}^n is the solute/screw dislocation interaction energy at the first nearest-neighbors around the center line of the dislocation core. Figs. 3.5 (a), (b), and (c) show that this approximation is quite poor, significantly overestimating the interaction parameter and tending to be close to the results obtained using the 2nd shell interaction energy parameter (which are the worst among all shells).

The Suzuki theory of strengthening scales, at moderate temperatures, with the square of the

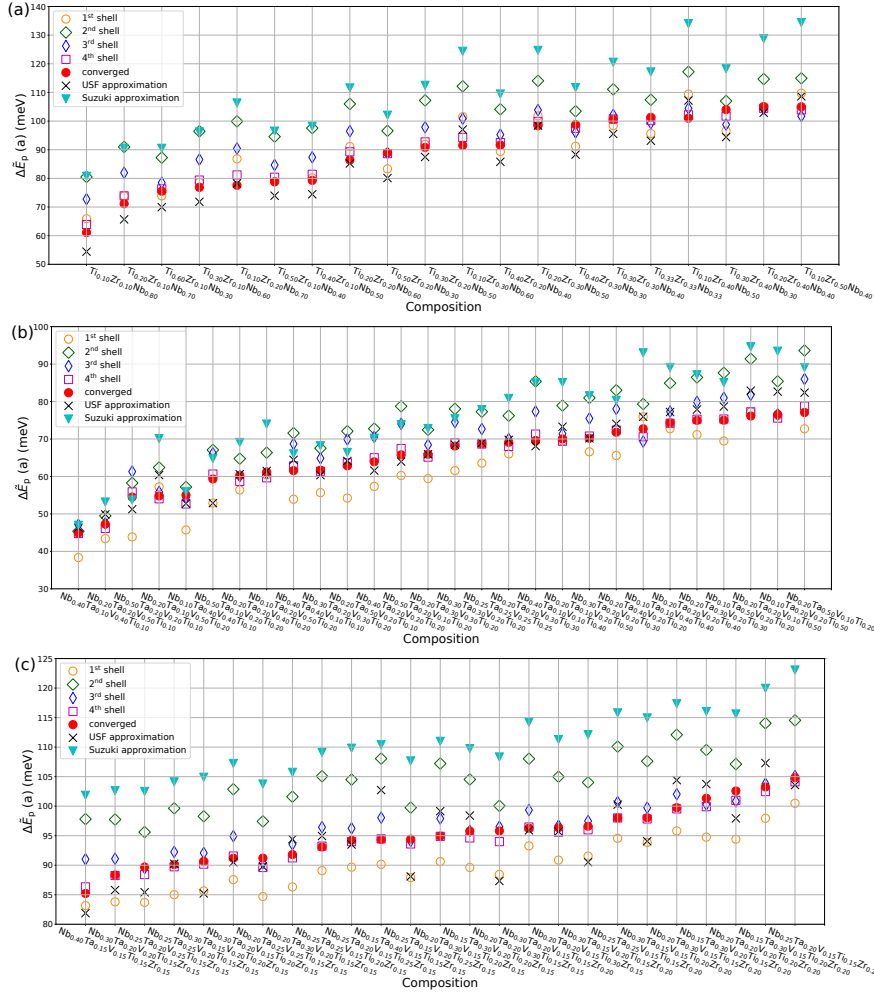


Figure 3.5 – **Interaction energy parameter $\Delta\tilde{E}_p(a)$ versus alloy composition.** Interaction energy parameter $\Delta\tilde{E}_p(a)$ versus alloy composition obtained by full atomistic solute-screw dislocation interaction energies for various shells of atoms, by the USF approximation, and by the Suzuki approximation. (a) Ti-Zr-Nb ternary; (b) Nb-Ta-V-Ti quaternary; (c) Nb-Ta-V-Ti-Zr quinary alloys, only compositions with compact (unpolarized) core structure are shown.

interaction parameter. Therefore, the overestimate of the interaction parameter leads to a significant overestimate of the strength. A similar scaling emerges, from an entirely different analysis, in the new theory of Maresca and Curtin [94], and so use of the Suzuki-type parameter in such a theory would again be expected to greatly overestimate the strengthening.

3.3.3 Correlation with solute/USF interaction energy

We first examine the correlation proposed by Rao et al. between the solute-screw interaction energy in the first three atomic rows at the dislocation core and the interaction energy between the solute and the $[111]/6$ USF. The absolute differences between these interaction energies for

each solute type for a wide range of compositions for Ti-Zr-Nb, Nb-Ta-V-Ti, and Nb-Ta-V-Ti-Zr alloys is shown in Figures 3.6(a), (b), and (c), respectively. The differences are not negligible for some solutes in most alloys, with one or more solutes often showing a difference of 0.1 eV or more. Some of the larger differences occur for solutes at lower concentrations in the alloy, however, which thus reduces the effects of the error on the overall estimate of the solute/screw interaction energy parameter.

It is the full converged solute/screw interaction energy parameter that is relevant for solute strengthening. Thus, we assess if there is any correlation between this parameter and an estimate based on the solute/USF interaction energy. To make such a correlation, we estimate the solute/screw interaction energy parameter by setting $U_{\text{first}}^n = E_n^{\text{usf}}$ and setting all other interaction energies to zero. This is equivalent to using the 1st shell model with the solute/USF energy in place of the solute/screw energy. The estimated interaction energy parameter is then

$$\Delta\tilde{E}_p(a) = \sqrt{4} \left[\sum_n c_n \left(E_n^{\text{usf}} \right)^2 \right]^{\frac{1}{2}}. \quad (3.8)$$

This estimated value is shown in Fig. 3.5 denoted as "USF approximation". The USF approximation describes the converged interaction energy parameter fairly well across all alloy families, with absolute relative differences across all alloys of less than 10%. Results for the Ti-Nb-Zr ternaries are comparable to those using U_{first}^n directly, with some cases being better and others worse, but results for the 4- and 5-component alloys tend to be better.

3.3.4 Polarized cores

The EAM potentials sometimes lead to polarized cores, as also noted by Rao et al. Here, we examine the Ti-Zr-Nb alloys that exhibit the polarized core structure. The solute/screw interaction energies are shown in Figure 3.7. For such cores, the results are significantly different from those for unpolarized cores. The interaction energies using the first and second shells and the USF approximation all greatly underestimate the total converged interaction energy parameter. Then, fortuitously, the Suzuki approximation is a better estimate of the total interaction energy parameter. Convergence is still achieved by considering the 4th shell. In general, we recommend that atomistic studies entirely avoid alloy cases where the cores are polarized.

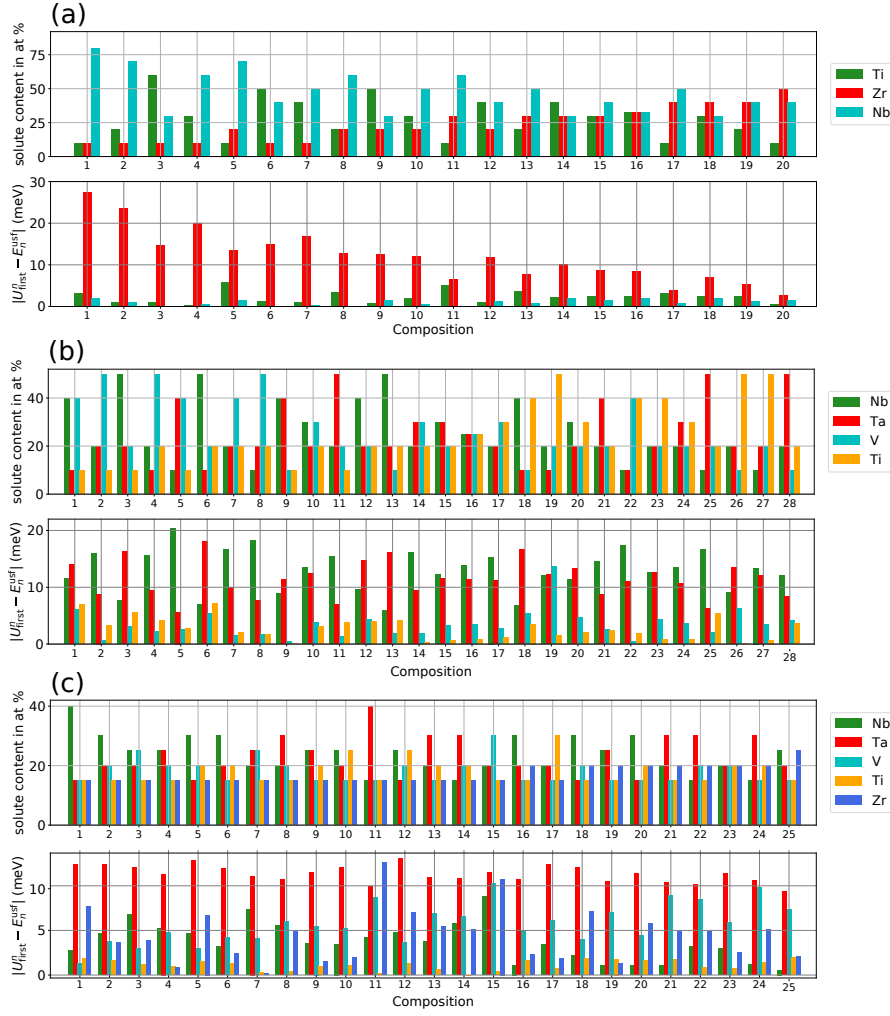


Figure 3.6 – **Examination of correlation of solute/screw interaction energies with solute/USF interaction energy.** Absolute differences between the solute-screw interaction energy in the first three atomic rows at the dislocation core, U_{first}^n and the interaction energy between the solute and the $[111]/6$ USF, E_n^{usf} for each solute type and for a wide range of compositions in (a) Ti-Zr-Nb ternary, (b) Nb-Ta-V-Ti quaternary, and (c) Nb-Ta-V-Ti-Zr quinary alloys having compact (unpolarized) core structures.

3.4 Discussion and Summary

We have defined the proper solute/screw interaction energy parameter relevant for strengthening of screw dislocations in random BCC alloys with any number of components and concentrations. In contrast to the assumptions made by the previous researchers, the solute/screw interaction energy is not confined to any finite range and the effect of all solutes, out to infinite distance in principle, are considered. Using EAM potentials as a model system, we find that an accurate interaction energy parameter requires consideration of solutes out to

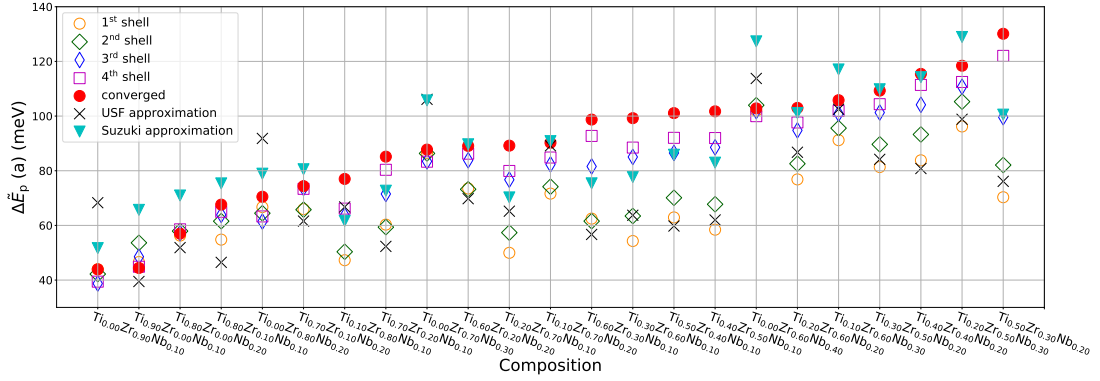


Figure 3.7 – **Interaction energy parameter $\Delta\tilde{E}_p(a)$ for BCC Ti-Zr-Nb ternary alloys.** Solute/screw interaction energy parameter $\Delta\tilde{E}_p(a)$ versus alloy composition for BCC Ti-Zr-Nb ternary alloys having a polarized (3-fold) core structure, as obtained by direct solute-screw dislocation interaction energies, USF approximation, and the Suzuki approximation.

6th neighbors (4 shells). This range is also consistent with literature first-principles studies in dilute alloys.

We have also found that a “USF approximation” is reasonably accurate. This is unexpected since the converged interaction energy parameter involves many sites around the screw core. Nonetheless, the correlation is extremely valuable. It suggests that alloy design can proceed by computing the solute/USF interaction energies to make an estimate of the true interaction energy parameter. First-principles computation of the USF energy alone is challenging because such studies must be performed in the true random alloy; there is currently no equivalent of the average-alloy potential in the first-principles framework. First-principles studies thus require sufficiently large SF surfaces in the true random alloy. The solute/USF interaction energy for a type- n solute can be computed by a substitution procedure where solutes of types $n' \neq n$ along the stacking fault are replaced by the n -type solute and the energy difference computed. A concentration-weighted averaging over many such substitutions for all solutes $n' \neq n$ then provides the average solute/USF interaction energy for the type n solute. Such a procedure was described and used for validating the average-alloy method [173], and is not limited to EAM potentials. In contrast, computing the direct solute/screw interaction parameter using first-principles methods in a complex alloy is not only computationally more challenging but physically difficult. In the random alloy, the relaxed dislocation structure has already found the minimum-energy configuration in the presence of the particular random realization of solutes. A substitution procedure such as that suggested above for the solute/USF problem thus has significant additional uncertainties that may make such a study unreliable.

Rao et al. suggested $E_n^{\text{usf}} \approx U_{\text{first}}^n$ but then also used $U_{\text{second}}^n = U_{\text{first}}^n$ and considered only the first two shells. Our results show that such a model gives an interaction energy parameter that is $\sqrt{6/4}$ larger than the present “USF approximation”. Since the latter is close to the fully-converged results, and the Suzuki model strength scales as the square of this parameter,

the Rao et al. model is expected to yield strength predictions that are 1.5 times larger than the same model using the fully-converged (and presumably more accurate) interaction energy parameter. This is a significant difference for the purposes of accurate predictions. Nonetheless, Rao et al. showed reasonable agreement between predictions and experimental strengths estimated from hardness data on a number of BCC HEAs. However, in those comparisons, Rao et al. used the upper limit of the measured hardness [Rao], and recent compression test data on some of the single-phase alloys shows their strengths to be rather lower than deduced from hardness measurements [27]. Thus, correcting the interaction energy by a factor of 2/3 may re-establish some reasonable agreement between the analysis of Rao and the experiments. Rao et al. also used their Suzuki-type model to make predictions for alloys in which the interatomic potential has a polarized core. However, since the real material presumably does not have a polarized core and since Rao et al. only use the first shell (first neighbor) interaction, the errors created by the polarized core may have been partially cancelled.

The use of EAM potentials to obtain realistic values for this interaction energy parameter remains uncertain, especially for complex multicomponent alloys. However, the general methodology employed here remains valid. We would recommend that EAM models be used solely to test new theoretical concepts and only on alloys that do not have polarized cores. EAM potentials generally have the additional problem of showing a metastable split-core configuration that influences analysis of dislocation glide problems. Thus, first-principles calculations ([167, 68, 119, 70]) in combination with theoretical models seem preferable. However, as noted above, first-principles computations of the necessary quantities in a true random alloy remains very challenging.

In summary, future modeling of screw dislocations in BCC alloys - whether dilute or concentrated - should use the interaction energy parameter derived here. Computations of that energy parameter should consider solutes out to 6th neighbors, although an estimated parameter can be obtained using solute/USF energies in a manner analogous to that suggested by Rao et al. Accurate determination of this interaction energy parameter is challenging, but it remains essential to have the proper theoretical framework that is expected to govern the behavior of real materials.

Strengthening mechanisms in dilute BCC alloys

Part II

4 Double-kink nucleation in dilute BCC alloys

This chapter is extracted from the following publication

Ghafarollahi, Alireza, and William A. Curtin. "Theory of double-kink nucleation in dilute BCC alloys." *Acta Materialia* 196 (2020): 635-650.

In BCC metals and dilute substitutional alloys, plastic deformation is controlled by double-kink nucleation and migration processes. In pure BCC metals, the double-kink nucleation is the rate-limiting process because kink migration has a negligible barrier. In dilute solid solution BCC alloys, the solutes modify the barriers for both double-kink nucleation and kink migration. The controlling process is that with the largest barrier; this requires a statistical determination of the relevant barriers as a function of the applied stress and concentration. In general, the double-kink nucleation barrier is reduced because nucleation occurs in that region where the solute fluctuations in the random alloy will most-favor formation of the double kink. Kink migration must then overcome the largest barriers for migration along the remaining line length. With increasing solute concentration, the conventional understanding is that the nucleation barrier is steadily reduced and the kink migration barrier steadily increased such that there can be a cross-over from control by nucleation to control by migration. This can lead to a transition from softening (reduced flow stress, relative to the pure metal, with increasing concentration) to hardening (increasing flow stress with increasing concentration). Such behavior has been predicted via models [167] and observed in recent Monte Carlo simulations in both Fe-Si [147] and W-Re [202], although results depend on details of the models and simulation methods.

The softening by solutes in the dilute limit was recognized long ago [183, 113, 158]. Considering the attractive force of impurity atoms on a dislocation line, Weertman [183] showed that the impurity atoms could reduce the Peierls energy in their immediate neighborhood, leading to a reduction in the required stress. Softening can be achieved, however, with either attractive or repulsive solutes (see Figure 4.1). For repulsive solutes, an initial straight dislocation is simply pushed away from the solute, and the double-kink nucleation barrier is reduced.

There is substantial evidence of softening due to small additions of many solutes in many BCC elements at low temperatures [113, 153]. Suzuki [158] developed a statistical model for solute effects on double-kink nucleation and kink-migration processes. He envisioned a single solute/dislocation interaction energy E_0 and considered that somewhere along the dislocation line there could be m solutes within the double-kink nucleation length. Suzuki then postulated that the decrease in double-kink nucleation energy would be $-m|E_0|/2$ where the absolute value accounts for the fact that both attractive and repulsive solutes could reduce the barrier and where the factor of $1/2$ was postulated as the reduction in barrier following simple chemical kinetics models. The value of m was then computed as the largest value along a dislocation line length L . The Suzuki model thus contains the key features of the problem, but with crucial assumptions about the solute/dislocation interaction energies and their effects on the nucleation barrier that limit quantitative predictions. That is, the single parameter E_0 , the statistical factor m , and the factor of $1/2$, are all ad-hoc approximations that are not accurate in realistic systems.

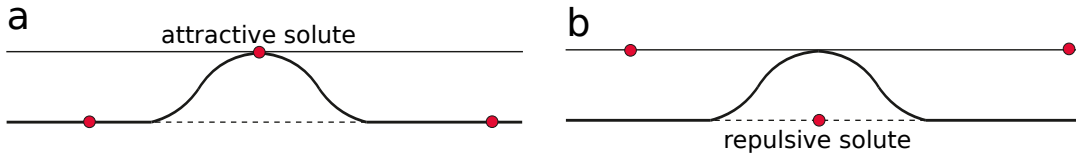


Figure 4.1 – **Schematic of double-kink nucleation in the presence of a single solute.** (a) An attractive and (b) a repulsive solute pulling and pushing the initial dislocation line away, respectively, towards the next Peierls valley. In both cases, the double-kink nucleation barrier is reduced.

In spite of the above early studies, the recent literature [167, 68] makes a different set of assumptions. Retaining only a single solute/dislocation interaction energy E_0 , these works postulate that the rate of double-kink nucleation along a long line is changed by the factor $c e^{-E_0/kT}$ where c is the solute concentration. This model thus effectively considers only individual solutes (the very dilute limit) with no statistical effects and, moreover, predicts that repulsive solutes ($E_0 > 0$) decrease the double-kink nucleation rate (leading to increased yield stress). Solutes with positive and negative interaction energy are thus predicted to be fundamentally different [68] (hardening vs. softening). This is in conflict with experiments at the yield point. For instance, as shown later below, data of Stephens [153] shows softening at low temperature and low solute concentrations for both W-Ta and W-Re alloys even though first-principles DFT predicts the interaction energy of Ta to be positive and that of Re to be negative [68] (see figures 4.2(a) and (c)). Other comparisons with experiments were made using hardness data [167], corresponding to plastic strains of ~ 7 -10% while the data in Ref. [153] shows that behavior at yield and at a few percent plastic strain can lead to conflicting conclusions regarding softening versus hardening.

Prior analyses [167, 5] also included an additional direct change to the Peierls stress in an alloy. This contribution can be viewed as the Peierls stress of the effective homogeneous representation of the alloy. Such a representation is important at non-dilute concentrations

where the identities of solute and matrix become less clear [131]. In the dilute limit, the explicit dominant effects of the individual solute additions are clear and provide perturbations to the double-kink nucleation barrier of the underlying matrix material. These effects change the apparent Peierls stress, as discussed below, with no additional considerations.

Here, we re-consider double-kink nucleation in the presence of low concentrations (a few percent or below) of solutes. We present and validate a general analytical statistical model for the effects of solutes on the double-kink nucleation barrier as a function of concentration and applied stress. This model is a significant improvement over the simplified model of Suzuki, and reveals the limitations of other models. It should be noted that all screw-dislocation-based theories to date including the present model assume that the screw dislocation core is the well-defined compact symmetric core. This is true for dilute alloys [68, Romaner, 67, 170] of interest here, but first-principles studies by Rao et al. [119], Romaner et al. [131], and Li et al. [86] show that screw cores may not always remain symmetric and compact in some non-dilute alloys.

In applications of the model, we obtain reasonable agreement with experiments at low concentrations where double-kink nucleation is expected to dominate. With increasing concentration, we then show a cross-over from softening, controlled by the present theory, to hardening, controlled by the recent non-dilute theory of Maresca and Curtin [94]. The Maresca-Curtin theory argues that the low-energy state of a screw dislocation is intrinsically kinked over a characteristic length scale, making double-kink nucleation irrelevant. The cross-over from softening to hardening is then mainly related to whether the spacing of the intrinsic kinks is smaller than the typical dislocation length between dislocation junctions. If not, then the dilute theory (softening) applies. If so, then the non-dilute theory (hardening) applies. The strength in the non-dilute domain of the Maresca-Curtin theory is still controlled by some combination of kink-migration, cross-kink formation/pinning of screws, and, at very low temperatures, a Peierls-like motion. These features are similar to, although different in detail than, those postulated by Suzuki [158]. So, both new [94] and old [158] theories, while different, show that double-kink nucleation does not control strengthening at higher concentrations. The present theory and that of Maresca et al. thus bridge across the full composition range of BCC alloys from very dilute up to multicomponent non-dilute High Entropy Alloys.

4.1 Solute effects on the double-kink nucleation barrier

4.1.1 Basic quantities

We consider a binary dilute alloy in which there is only one type of solute at concentration c and the other component has a high concentration and serves as the "matrix". The model is easily generalized to multiple components. The solute concentration c is low (below a few percent) but above a "very dilute limit" defined later by a critical concentration c^* .

Underpinning double-kink nucleation in the alloy is the stress-dependent double-kink nu-

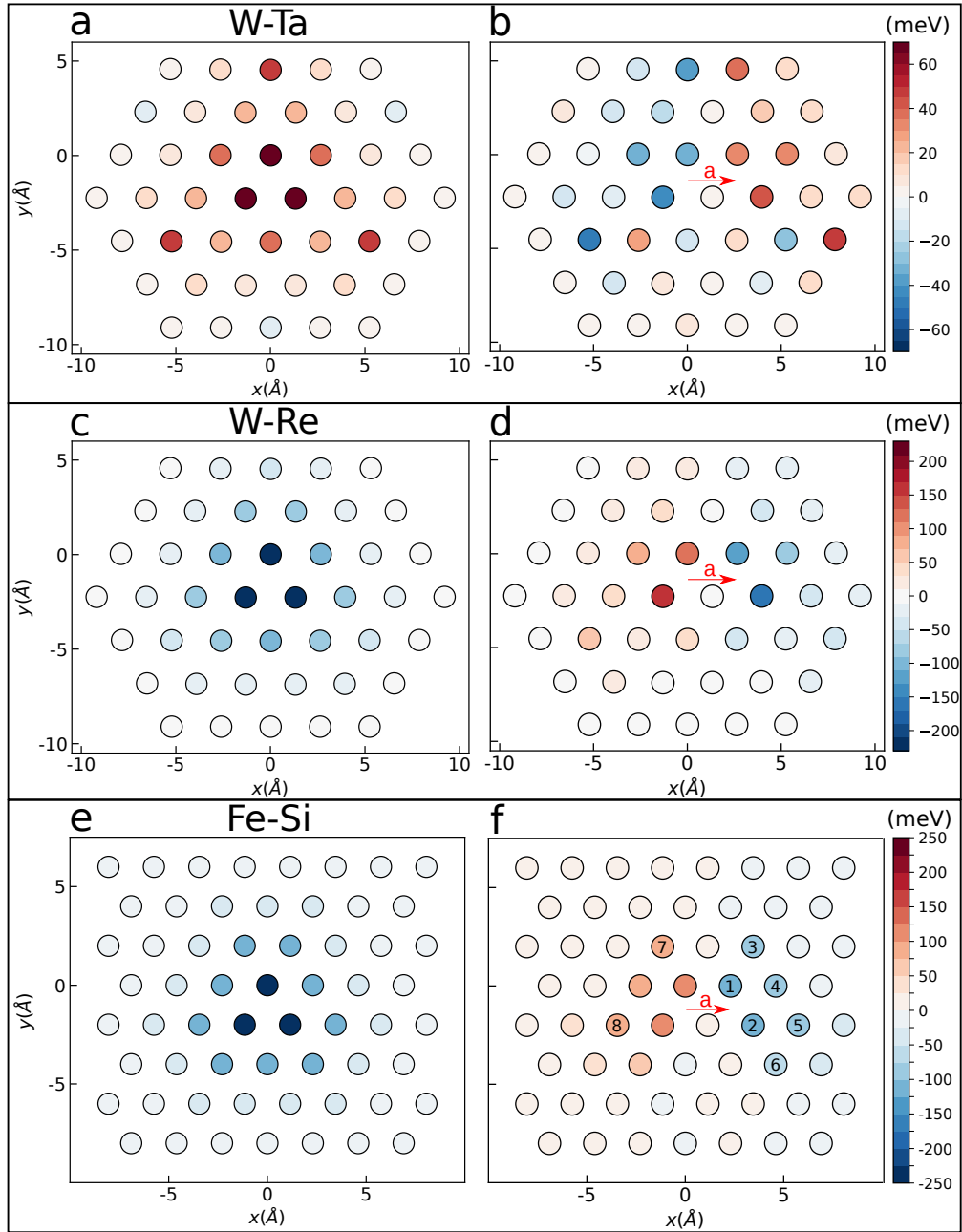


Figure 4.2 – **Solute/screw dislocation interaction energy map.** Solute/screw dislocation interaction energy versus solute position for **a** Ta [68, 69] and **c** Re [68, 69] in single crystal BCC W as calculated by DFT and **e** Si in Fe as computed using the EAM potential of [147]. Interaction energy difference as the screw dislocation core moves by one Peierls valley distance a (red arrow) for **b** Ta and **d** Re solutes in W and **f** Si in Fe. Sites marked with 1-8 in **f** are substituted with Si atoms for subsequent NEB calculations, and are referred to in Figs. 4.5 and 4.6.

cleation barrier and transition state in the pure matrix. Fig. 4.3 shows the transition state configurations for pure Fe at various applied stresses, as obtained using a reasonable EAM

potential for Fe [117] (see [95] for a study using a machine-learning potential and [31] for configurations obtained using a line tension model). At zero stress, the transition state is symmetric, has two fully-developed kinks, and spans 1/2 the simulation cell size. With increasing applied stress, the initial position of the dislocation moves away from the zero-stress Peierls valley to position $x_{\text{eq}}(\tau)$. More importantly, the critical double-kink configuration becomes progressively smaller: the kinks are closer together and the kink is not fully-developed. Only at low stresses does the kink extend into the next Peierls energy minimum at distance $a = 0.943b$ from the original minimum.

The dislocation shape $x_{\text{disl}}(z, \tau)$ of the double-kink transition state versus applied stress can be expressed generally as

$$x_{\text{disl}}(z, \tau)/a = g(z, \tau) + g_{\text{eq}}(\tau) \quad (4.1)$$

where $g_{\text{eq}}(\tau) = x_{\text{eq}}(\tau)/a$ is the dimensionless initial straight screw position at stress τ and $g(z, \tau)$ is the dimensionless kink shape, or deviation from the initial straight dislocation, as a function of τ . At low stresses (e.g. 100 MPa in Figure 4.3), the nucleation occurs over a length l_{dk} approximately equal to that of the two kink widths. Across a range of systems, this length is $l_{dk} \approx 20b - 25b$. The geometry of the transition-state double-kink structure versus stress serves as one main input for our analysis of solute effects on nucleation.

Associated with each stress and transition state is the nucleation enthalpy barrier $\Delta H^0(\tau)$ of the pure matrix. The functional form of $\Delta H^0(\tau)$ is not directly relevant for most of our analysis below, but is needed for predictions. This barrier can be obtained by simulations, models, or fitting. The latter often takes the form of a Kocks law [79] $\Delta H^0(\tau) = \Delta H^0(0) [1 - (\tau/\tau_p)^p]^q$ where $0 \leq p \leq 1$ and $1 \leq q \leq 2$ are fitting parameters and $\Delta H^0(0)$ and τ_p are the zero-stress enthalpy barrier and Peierls stress, respectively.

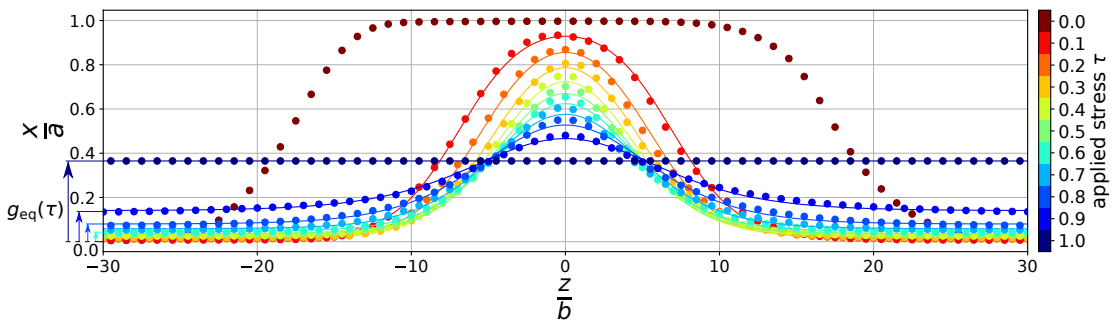


Figure 4.3 – **Stress-dependent transition state configurations in pure Fe.** Transition state configurations $x_{\text{disl}}(z, \tau)/a$ versus normalized applied shear stress τ/τ_p with $\tau_p = 1\text{GPa}$ determined using pure Fe EAM potential [117]. The points are the direct outcome of the disregistry method [177]. The solid lines are the fits to the functional form for $g(z, \tau)$ given by Eq. (4.19) with parameters shown in Table 4.1. On the lower left, the equilibrium position $g_{\text{eq}}(\tau)$ of the initial straight dislocation is indicated by the arrows for several applied stresses.

The second major quantity of importance is the interaction energy between a type- n solute at position (x_i, y_j, z_k) and a straight screw dislocation positioned in the Peierls valley minimum at the origin and aligned along the z axis. This interaction energy is denoted as U_{ijk}^n . Fig. 4.2(e) shows U_{ijk}^n for many solute positions ij around the core within the periodic length b along the line direction z for Si solutes in Fe as computed using a model Fe-Si alloy described by EAM potentials [147]. The solute/dislocation interaction energies for Ta and Re solutes in single crystal BCC W as computed by Density Functional Theory (DFT) [68, 69] are shown in Figs. 4.2(a) and (c); quantitatively similar results are reported in other works [Romaner]. With this projection, the interaction energy is independent of the z coordinate. For the model Fe-Si and W-Re systems all solute/dislocation interactions are negative (attractive) while the interactions for Ta in W are all positive (repulsive). The interaction energies are not localized to the first or second neighbors around the core, as commonly assumed in theories that use these computed energies to predict strengths [158, 167, 68].

Dislocation motion is determined by the *changes* in solute/dislocation energy as a dislocation glides. Fig. 4.2(f) shows the change in energy of a Si solute in Fe upon glide of the screw dislocation by one Peierls valley distance, a . Figs. 4.2(b) and (d) show the corresponding DFT energy changes for Ta and Re solutes in W matrix, respectively. Non-negligible changes in energy can exist for solutes located at initial positions up to sixth neighbors from the center line of the core. As discussed extensively in Chapter 3, and important in the present work, it is necessary to consider solutes out to such distant neighbors to capture the relevant energy changes accurately. These interaction energies and changes upon glide are the fundamental quantities driving double-kink nucleation in a dilute alloy.

4.1.2 Solute/double-kink interaction energy

Direct computation of the solute/double-kink interaction energies for all possible solute positions around the (transition state) double-kink structure is not possible. Computation of an interaction energy requires full relaxation of the system containing the solute and dislocation but the double-kink structure is a constrained state and is not a low-energy relaxed equilibrium structure. Here, we thus make a model assumption and then validate that assumption via direct simulations in Section 4.3.2.

We assume that the solute/double-kink interaction energy at each stress and for a single solute at position (x_i, y_j, z_k) is

$$E_{\text{dk}}(x_i, y_j, z_k, \tau) = \frac{x_{\text{disl}}(z_k, \tau)}{a} \Delta U_{ij}(a) + U(x_i, y_j), \quad (4.2)$$

where $\Delta U_{ij}(a) = U(x_i - a, y_j) - U(x_i, y_j)$ is the solute/screw dislocation energy change as the dislocation moves by one Peierls valley distance a (Figures 4.2b,d,f). That is, the solute/double-kink interaction energy of a solute in plane z is equal to the full energy change upon glide by a scaled by the distance x of the kink in the same z plane. This approximation is reasonable because the kink width is fairly large, so that the character of the kink is near screw. Therefore,

a solute experiences a surrounding region that is very nearly a straight screw dislocation at position $x_{\text{disl}}(z_k, \tau)$. This approximation also satisfies the limiting cases where the dislocation is in the initial and final Peierls valleys, i.e. $x_{\text{disl}}(z_k, \tau) \rightarrow 0$ and $x_{\text{disl}}(z_k, \tau) \rightarrow a$.

In the presence of any specific arrangement of solutes, the change in nucleation barrier is the sum of the changes, whether positive or negative, contributed by each individual solute. In the dilute limit, we can safely neglect any effects of multi-solute interactions because the average solute-solute separation is large ($\approx b/c^{1/3}$); each solute thus has an effect independent of any other solutes. A specific random arrangement of solutes is represented by a set of occupation variables s_{ijk} where $s_{ijk} = 1$ if a solute is at position (x_i, y_j, z_k) and $= 0$ otherwise. Overall all sites $N \gg 1$ in the alloy, $1/N \sum_{i,j,k} s_{ijk} = c$. The double-kink nucleation barrier is then the energy difference between all solutes interacting with the transition state structure $g(z, \tau) + g_{\text{eq}}(\tau)$ and with the initial straight dislocation at $g_{\text{eq}}(\tau)$, and so involves only the non-straight portion $g(z, \tau) = x_{\text{disl}}(z_k, \tau)/a$ of the transition state shape. Using Eq. (4.2) for the single solute/double-kink interaction energy, the solute contribution to the nucleation barrier is computed by summing the contributions of all the solutes in the specific realization of the random alloy as

$$\Delta H^{\text{sol}}(\tau) = \sum_{i,j,k} s_{ijk} g(z_k, \tau) \Delta U_{ij}(a) \quad (4.3)$$

4.1.3 Model for solute softening in dilute alloys

For a dislocation segment of length l_{dk} , the mean energy change over all possible fluctuations in the positions of the solutes is zero. This is shown by averaging Eq. (4.3) over all realizations s_{ijk} . However, the local fluctuations in the spatial arrangement of solutes give rise to a statistical distribution of energy changes of the nucleated dislocation segment. The standard deviation of this energy change is

$$\sigma_{\Delta H^{\text{sol}}} = \left[\langle \Delta H^{\text{sol}}(l_{dk}, x_{\text{disl}})^2 \rangle - \langle \Delta H^{\text{sol}}(l_{dk}, x_{\text{disl}}) \rangle^2 \right]^{1/2}, \quad (4.4)$$

where brackets denote averaging over the random occupation variables s_{ijk} . Carrying out the averaging and algebra leads to (A.1)

$$\sigma_{\Delta H^{\text{sol}}} = \Delta \tilde{E}_p(a) G(\tau), \quad (4.5)$$

where

$$G(\tau) = \left(\sum_{k=-N_s}^{N_s} g(kb, \tau)^2 \right)^{1/2}, \quad (4.6)$$

is a geometrical shape factor and $N_s = l_{dk}/(2b)$ is the total number of atomic sites along the dislocation line z within one kink length $l_{dk}/2$. The standard deviation of the statistical

distribution of nucleation barriers at length l_{dk} thus scales with the quantity

$$\Delta \tilde{E}_p(a) = \left(\sum_{ij} c \Delta U_{ij}(a)^2 \right)^{\frac{1}{2}} ; \quad (4.7)$$

this is precisely the solute/screw dislocation interaction energy parameter that enters in the theory for yield strength of a BCC alloy [94, 51], but reduced to the dilute binary alloy limit. This feature will later enable a bridging between dilute and non-dilute alloys. The shape of the double-kink transition state enters only as an overall stress-dependent numerical factor $G(\tau)$.

Considering one nucleation length l_{dk} , the random fluctuations in solutes leads to a Gaussian probability distribution of the solute contributions to the double-kink nucleation enthalpy ΔH^{sol} as

$$P[\Delta H^{\text{sol}}] = \frac{1}{\sqrt{2\pi}\sigma_{\Delta H^{\text{sol}}}} \exp \left[-\frac{1}{2} \left(\frac{\Delta H^{\text{sol}}}{\sigma_{\Delta H^{\text{sol}}}} \right)^2 \right]. \quad (4.8)$$

The above result is for a dislocation of length l_{dk} only. A longer dislocation line of length L can be considered approximately as a set of $N = L/l_{dk}$ statistically-independent segments of length l_{dk} , and double-kink nucleation could initiate at any one of these segments. Each segment has a distinct local solute configuration and hence has a local double-kink nucleation barrier that is sampled randomly from the above statistical distribution. The total rate of double-kink nucleation due to nucleation at all sites is the sum of the rates of all N segments, which can be written as (see A.2)

$$R = \nu_0 N \exp \left(-\frac{\Delta H^0(\tau)}{k T} \right) \exp \left(\frac{\sigma_{\Delta H^{\text{sol}}}(c, \tau)}{\sqrt{2} k T} \right)^2 \frac{1}{2} \operatorname{erfc} \left(\frac{\Delta \tilde{H}^{\text{sol}}(N, c, \tau)}{\sqrt{2} \sigma_{\Delta H^{\text{sol}}}(c, \tau)} + \frac{\sigma_{\Delta H^{\text{sol}}}(c, \tau)}{\sqrt{2} k T} \right), \quad (4.9)$$

where $\Delta \tilde{H}^{\text{sol}}$ is the the largest reduction in activation energy among all the N segments (the "weakest-link", see below), k is Boltzmann's constant, ν_0 is an appropriate attempt frequency, and erfc is the complementary error function. In the absence of solutes, or for very weak solute/screw interactions, the nucleation rate is $R = \nu_0 N \exp \left(-\frac{\Delta H^0(\tau)}{k T} \right)$ which is the rate for a dislocation length in the pure matrix.

The temperature- and stress-dependent plastic shear strain rate $\dot{\epsilon}$ at applied stress τ then follows from Orowan's law as $\dot{\epsilon} \approx \rho b a R$, where ρ is the mobile dislocation density and R is the nucleation rate. Using this relationship, the yield stress as a function of temperature and strain rate can be determined, as described in more detail in the context of the applications presented in Section 5.4.

At sufficiently low temperatures, the rate of double-kink nucleation is controlled by that one segment having the greatest reduction of the kink-pair nucleation barrier; i.e. nucleation is an extreme-value (weak-link) problem. For a dislocation of length $N l_{dk}$, the *mean* of the lowest

activation energy is

$$\Delta \bar{H}^{\text{sol}} = \frac{\int_{-\infty}^{\infty} \dots \int_{-\infty}^{X_3} \int_{-\infty}^{X_2} X_1 \prod_{n=1}^N P(X_n) dX_n}{\int_{-\infty}^{\infty} \dots \int_{-\infty}^{X_3} \int_{-\infty}^{X_2} \prod_{n=1}^N P(X_n) dX_n}, \quad (4.10)$$

The standard deviation of activation energies around this mean lowest value is

$$\bar{\sigma}_{\Delta H^{\text{sol}}}^2 = \frac{\int_{-\infty}^{\infty} \dots \int_{-\infty}^{X_3} \int_{-\infty}^{X_2} (X_1 - \Delta \bar{H}^{\text{sol}})^2 \prod_{n=1}^N P(X_n) dX_n}{\int_{-\infty}^{\infty} \dots \int_{-\infty}^{X_3} \int_{-\infty}^{X_2} \prod_{n=1}^N P(X_n) dX_n}, \quad (4.11)$$

For long lengths L , corresponding to large N and relevant for real physical systems, the above distributions are asymptotically approximated by the extreme-value Gumbel distribution having the cumulative probability

$$C_N(\Delta H^{\text{sol}}) \approx 1 - e^{-e^{\frac{\Delta H^{\text{sol}} - \sigma_{\Delta H^{\text{sol}}} b_N}{\sigma_{\Delta H^{\text{sol}}} a_N}}}, \quad (4.12)$$

where the Gumbel scale a_N and location b_N parameters are

$$\begin{aligned} a_N &= \frac{1}{\sqrt{2 \log(N)}}, \\ b_N &= \frac{\log(\log(N)) + \log(4\pi)}{\sqrt{8 \log(N)}} - \sqrt{2 \log(N)}, \end{aligned} \quad (4.13)$$

respectively. In terms of $\sigma_{\Delta H^{\text{sol}}}$, the mean and standard deviation at length Nl_{dk} are

$$\begin{aligned} \Delta \bar{H}^{\text{sol}}(c, N, \tau) &= \sigma_{\Delta H^{\text{sol}}}(c, \tau) (b_N - \gamma a_N), \\ \bar{\sigma}_{\Delta H^{\text{sol}}}(c, N, \tau) &= \sigma_{\Delta H^{\text{sol}}}(c, \tau) \frac{\pi}{\sqrt{6}} a_N, \end{aligned} \quad (4.14)$$

where $\gamma \approx 0.5772$. Numerical tests show these asymptotic results to be quite accurate for $N > 15$ while exact results from Eqs. (4.10) and (4.11) can be computed for $N < 15$. One feature of the weak-link analysis is that the mean contribution of solutes increases with increasing N but the standard deviation decreases. Also, the temperature T_0 below which the weak-link dominates can be determined (see A.2) and the double-kink nucleation rate can be expressed as

$$R = \nu_0 \exp \left(- \frac{\Delta H^0(\tau) + \Delta \bar{H}^{\text{sol}}(c, N, \tau)}{k T} \right), \quad (4.15)$$

The weak-link limit provides an easy-to-use analytic form.

Eqs. (4.5), (4.6), and (4.8) together with Eq. (4.10) (for $N < 15$), and Eqs. (4.13) and (4.14) (for $N > 15$) constitute our analytic statistical model for the reduction in double-kink nucleation barrier due to solutes in the dilute limit. The only inputs to the theory are the matrix transition

state shape versus stress, the solute/dislocation interaction energies, and the dislocation line length Nl_{dk} .

Lastly, the solute/double-kink interaction energies are modeled using the transition state configurations of the pure matrix at the relevant applied stress. However, a careful treatment is required at zero stress since the transition state in the pure metal is strictly equal to 1/2 the total simulated dislocation length. As shown below, even in the very dilute limit where the transition is affected only by one isolated solute, the transition state at zero stress is always localized around the position of a single favorable solute. The transition state structure is never that found in the pure material (spanning 1/2 the cell size). Therefore, here we use the transition state configuration at the lowest non-zero stress where the kinks are well-formed but only separated enough such that the leading part of the transition state is very nearly in the final-state Peierls valley. For our model system, this corresponds to the configuration at 0.1 GPa in Figure 4.3. In all subsequent analyses, the transition state configuration at zero stress $x_{\text{disl}}(z_k, 0)$ refers to this configuration. This assumption enters the model only through the structure-dependent factor $G(0)$; any other approximation to the zero-stress transition state structure would simply correspond to a (small) change in the value of $G(0)$. We validate our zero-stress transition state structure via direct simulations for specific solute configurations in a model Fe-Si alloy in Section 4.3.2.

4.2 Solute effects in the very dilute limit

The previous analysis is valid for concentrations above a critical value in which multiple solutes are present across the double-kink nucleation length l_{dk} so that a statistical analysis is appropriate. In the very dilute limit, however, at most only a single solute will exist around the dislocation over length l_{dk} and its affect on the double-kink nucleation requires special treatment as discussed here.

Far from the screw dislocation core, the solute/dislocation interaction energy differences are vanishingly small and so do not affect the double-kink nucleation barrier. There are thus only some finite number of distinct atomic sites that contribute to the double-kink nucleation energy difference. We denote the number of atomic sites with appreciable negative interaction energy differences per unit b of line length as N_T . Due to symmetry, there are then also N_T sites with positive appreciable energy difference. A critical concentration is then defined as $c^* = b/(2N_T l_{dk})$, at which there exists, on average, only one solute among all the $2N_T$ -type sites over the entire double-kink nucleation length l_{dk} . For concentrations above this critical concentration, multiple solutes are found within the double-kink nucleation length and the analysis of the previous section quickly becomes relevant. When $c < c^*$, there will be only one solute or no solute within each double-kink nucleation length. The concentration c^* is thus the boundary between the very dilute limit and the dilute limit cases (see Fig. 4.4).

In the very dilute limit, the change in interaction energy of a solute initially at the i -th distinct site ($i = 1, \dots, N_T$) due to motion of the straight screw dislocation from the initial to the final is

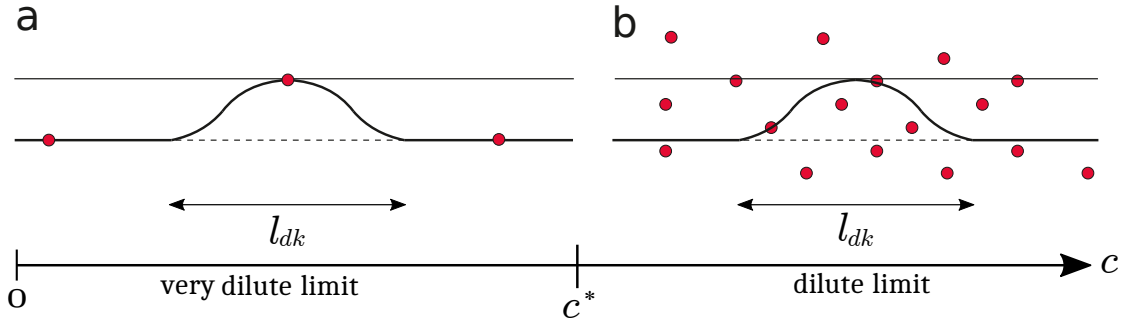


Figure 4.4 – **Schematic of the very dilute and dilute solute regimes around a double-kink nucleation.** Schematic of the solute (red dots) distribution surrounding a double-kink nucleation structure with length l_{dk} for (a) very dilute ($c < c^*$) and (b) dilute limit ($c > c^*$) cases. When $c < c^*$ there will be at most one solute within the length l_{dk} . Whereas, multiple solutes may be found within double kink nucleation length when $c > c^*$.

now labeled simply as ΔU_i . A dislocation of length L with $N = L/l_{dk}$ double-kink nucleation segments will have a fraction c/c^* of segments containing one solute randomly distributed among the $2N_T$ possibilities while the remaining fraction $(1 - c/c^*)$ of segments are solute-free. The latter fraction have a double-kink activation barrier ΔH^0 equal to that of the pure matrix. Nucleation will be preferred in segments containing solutes having favorable interaction energies, and nucleation will be centered on the solute position. Therefore, the barrier change due to a single favorable solute at site i is

$$\Delta H_i^{\text{sol}}(\tau) = \Delta U_i g(0, \tau). \quad (4.16)$$

The nucleation rate is slower in segments containing solutes with unfavorable interaction energies. As an approximation, we treat these segments as having zero solutes, which slightly overestimates the nucleation rate in these segments. The total double-kink nucleation rate R_{dk} is then the sum of the rates over all segments, with or without solutes,

$$\begin{aligned} R_{dk} = & \sum_{k=1}^{(1-\frac{c}{c^*})N} \underbrace{v_0 \exp\left(-\frac{\Delta H_0(\tau)}{kT}\right)}_{\text{pure matrix}} + \sum_{k=1}^{(\frac{c}{c^*}N)/2} \underbrace{v_0 \exp\left(-\frac{\Delta H_0(\tau)}{kT}\right)}_{\text{segments containing one unfavorable solute}} \\ & + \sum_{k=1}^{(\frac{c}{c^*}N)/2} \sum_{i \in N_T} \underbrace{v_0 s_i \exp\left(-\frac{\Delta H_0(\tau) + \Delta H_i^{\text{sol}}(\tau)}{kT}\right)}_{\text{segments containing one favorable solute}}, \end{aligned} \quad (4.17)$$

where the summation over i extends over all N_T favorable sites and $s_i = 1$ for site i containing a favorable solute and $s_i = 0$ for all other sites. Noting that $\langle s_i \rangle = 1/N_T$ the above equation can

be reduced to

$$R_{dk} = N\nu_0 \exp\left(-\frac{\Delta H_0(\tau)}{kT}\right) \left[1 + c \frac{l_{dk}}{b} \sum_{i \in N_T} \left(\exp\left(-\frac{\Delta H_i^{\text{sol}}(\tau)}{kT}\right) - 1 \right) \right] \quad (4.18)$$

Recall that N_T is the number of sites with appreciable negative interaction energy changes. The above relation shows that the inclusion of more-distant sites, i.e. those having comparatively low interaction energy changes compared to those within the N_T sites, will not influence the double-kink nucleation rate since $\exp(-\Delta U_i g(0, \tau)/kT) - 1 \approx 0$ for such sites. Thus, the choice of the N_T sites mainly affects the definition of the critical concentration c^* rather than the actual rate of nucleation in this domain.

The transition from the very dilute to the dilute limit is not fully developed. Neither result is quite correct at concentrations $c \sim c^*$: there will often be more than one solute with l_{dk} but not quite enough such that the asymptotic random Gaussian statistics is applicable. However, the critical concentration c^* may be below commonly-studied solute concentrations of dilute BCC binary alloys (1 at.%). Therefore, a lack of precision in the definition of c^* and the behavior in the vicinity of c^* is not a major issue.

4.3 Validation against atomistic simulations using a model Fe-Si alloy

We now compare predictions of our analytical model for double-kink nucleation enthalpy barrier against direct atomistic simulations using a model Fe-Si alloy. The only input parameters to the model are the solute/screw-dislocation interaction energies $U(x_i, y_j)$ at all distinct solute positions ij around the screw core, the length L of the dislocation, and the stress-dependent enthalpy barrier and transition state dislocation configurations of the pure matrix material. There are no fitting parameters.

We use a model Fe-Si alloy system as represented by a recent EAM potential [147]. The Fe-Fe interactions are based on the Fe EAM potential developed by Provile et al. [117], which has all the key aspects for Fe screw dislocations such as the non-degenerate compact core structure, the single-hump Peierls potential, and {110} slip-plane. We further set the Si-Si interaction energies to those of Si-Fe, which eliminates direct solute-solute interactions. Since we are interested in dilute alloys and since the theory does not include solute-solute interactions, this treatment of solute-solute interactions is convenient and very useful. We note clearly that this Fe-Si potential is not an accurate representation of real Fe or real Fe-Si. However, it is a well-defined model system with no pathological behaviors that often plague atomistic modeling of BCC screw dislocations. Thus, this model Fe-Si system is well-suited to validate our general analytic model in detail.

The solute/screw dislocation interaction energy parameter $\Delta \tilde{E}_p(a)$ is computed using the individual solute/dislocation interaction energies shown in Figure 4.2b. The individual energies

4.3. Validation against atomistic simulations using a model Fe-Si alloy

were computed as discussed carefully in Section 3.2. The resulting solute/dislocation interaction energy parameter for this model Fe-Si alloy is then computed as $\Delta\tilde{E}_p(a) = 344\sqrt{c}\text{ meV}$.

To compute the transition path from the initial to the final state, we use the nudged elastic band (NEB) method as implemented in LAMMPS. Details of the NEB simulation can be found in A.3. NEB calculations on the pure Fe matrix at various stresses up to the Peierls stress $\tau_p \approx 1000$ were performed. The transition state configurations, determined using the disregistry method [177], are shown in Figure 4.3. These configurations were fit to a functional form for $g(z, \tau)$ as

$$g(z, \tau) = \frac{1}{2} \left(\tanh \left[\frac{z/b + \zeta(\tau)}{\alpha(\tau)} \right] - \tanh \left[\frac{z/b - \zeta(\tau)}{\alpha(\tau)} \right] \right), \quad (4.19)$$

where $\zeta(\tau)$ and $\alpha(\tau)$ are two fitting parameters shown in Table 4.1. The kink-pair nucleation length was estimated as $l_{\text{dk}} = 20b$, consistent with the result of [147]. The initial positions $g_{\text{eq}}(\tau)$ and the geometrical shape factor $G(\tau)$ are shown in Table 4.1. The maximum energy along each energy path is the double-kink nucleation energy barrier $\Delta H^0(\tau)$ for pure Fe as described by this potential, which was fit to the empirical form $\Delta H^0(\tau) = (0.62\text{ eV})(1 - (\tau/1000\text{ MPa})^{0.62})^{1.02}$ for later use.

Table 4.1 – Parameters describing the transition state configurations for double-kink nucleation of pure Fe at various normalized applied stresses, τ/τ_p . The geometrical factor, $G(\tau/\tau_p)$ is obtained by Eq. (4.6) with $g(z, \tau)$ given by Eq. (4.19) and $N_s = 10$.

τ/τ_p	$\alpha(\tau/\tau_p)$	$\zeta(\tau/\tau_p)$	$g_{\text{eq}}(\tau/\tau_p)$	$G(\tau/\tau_p)$
0.0	4.347	6.987	0.00	3.07
0.1	4.347	6.987	0.00	3.07
0.2	4.381	5.367	0.01	2.55
0.3	4.444	4.487	0.02	2.20
0.4	4.571	3.918	0.03	1.94
0.5	4.792	3.584	0.04	1.77
0.6	5.184	3.419	0.05	1.64
0.7	5.755	3.311	0.06	1.52
0.8	6.725	3.241	0.08	1.39
0.9	7.886	2.666	0.14	1.06
1	-	0	0.365	0

To study the (weak-link) scaling of the nucleation barrier with total dislocation length, NEB simulations are performed for lengths $40b$, $70b$, $100b$, and $200b$. The shortest length of $40b$ is the shortest length at which the double-kink nucleation barrier in pure Fe becomes essentially length-independent, i.e. at which there is very limited interaction between the two kinks formed during kink-pair nucleation. Specifically, the pure Fe enthalpy barrier at $40b$ is 572 meV, only 28 meV smaller than the value 600 meV at $200b$. NEB calculations are then performed to find the double-kink nucleation barrier in random Fe-Si dilute alloys for a range of stresses and solute concentrations of 1, 2, and 4%. At zero stress 200 different realizations of random Si are considered at each concentration while 120 cases are studied at non-zero stresses.

4.3.1 Very dilute limit: the single solute

NEB calculations of the double-kink nucleation process in the model Fe-Si alloy containing a single Si atom at 6 different atomic sites (numbered in Fig. 4.2f) were performed. The interaction energy changes upon glide range from -113 meV to -69 meV for these 6 sites. Fig. 4.5 shows the enthalpy barriers for double-kink nucleation barrier versus the applied stress τ for each solute position. Similar studies were performed by [147], which served as the only input into their subsequent Monte Carlo studies at all concentrations. All of these favorable sites reduce the pure double-kink nucleation barrier, with a decreasing effect with increasing applied stress. Also shown is the prediction for one particular case, site #4 with interaction energy change -89 meV. For each solute, the trends follow the model predictions (not shown except for site #4) in general, but the precise results do not agree exactly. The nucleation path adjusts very subtly to the precise solute position, affecting the energy barrier slightly, and this cannot be captured in the model. Across all these cases, the differences between NEB and model are roughly ± 20 meV, which is comparable to the differences among the 6 solute interaction energies. This result sets a level of agreement that can be expected for subsequent results.

4.3.2 Validation of solute/double-kink interaction energies

In our model, the collective interaction energies of the solutes with the double-kink transition state (Eq. (4.3)) were modeled using the transition state configuration of the pure matrix at the relevant applied stress (Fig. 4.3) and an approximation for the solute/transition state interaction energies (Eq. (4.2)). Here, we test the model by comparing the predicted and NEB-computed *changes* in nucleation barrier $\Delta H^{\text{sol}}(0)$ due to *specific* arrangements of solutes at zero stress.

Si solute configurations were created by placing multiple Si solutes at selected atomic sites around the dislocation core. The configurations were selected so as to sample various local energy environments (combinations of solute positions, including favorable and unfavorable sites, at different distances). The configurations used are shown schematically in see Figure 4.6(a), with solutes labeled by the atomic row (1-8 as indicated in Figure 2e) and with an additional overbar notation for multiple solutes spaced along the same row. The spacings of solutes along the same row are indicated by either w or d , as shown in the figure. For each specific set of solute positions, we calculated the double-kink nucleation barrier change at zero stress using Eq. (4.3) and the transition state shape parameter $G(0) = 3.07$ shown in Table 4.1. Direct NEB calculations were performed on the exact same solute configurations at zero applied stress.

The atomistic and predicted results for the change in nucleation barrier are shown in Fig. 4.6(b). The trends in the simulation are well-predicted by the analytic model with no adjustable parameters. The generally good agreement between the predicted and simulated energy changes for most of the cases (deviating by only 20-30 meV except for one extreme case

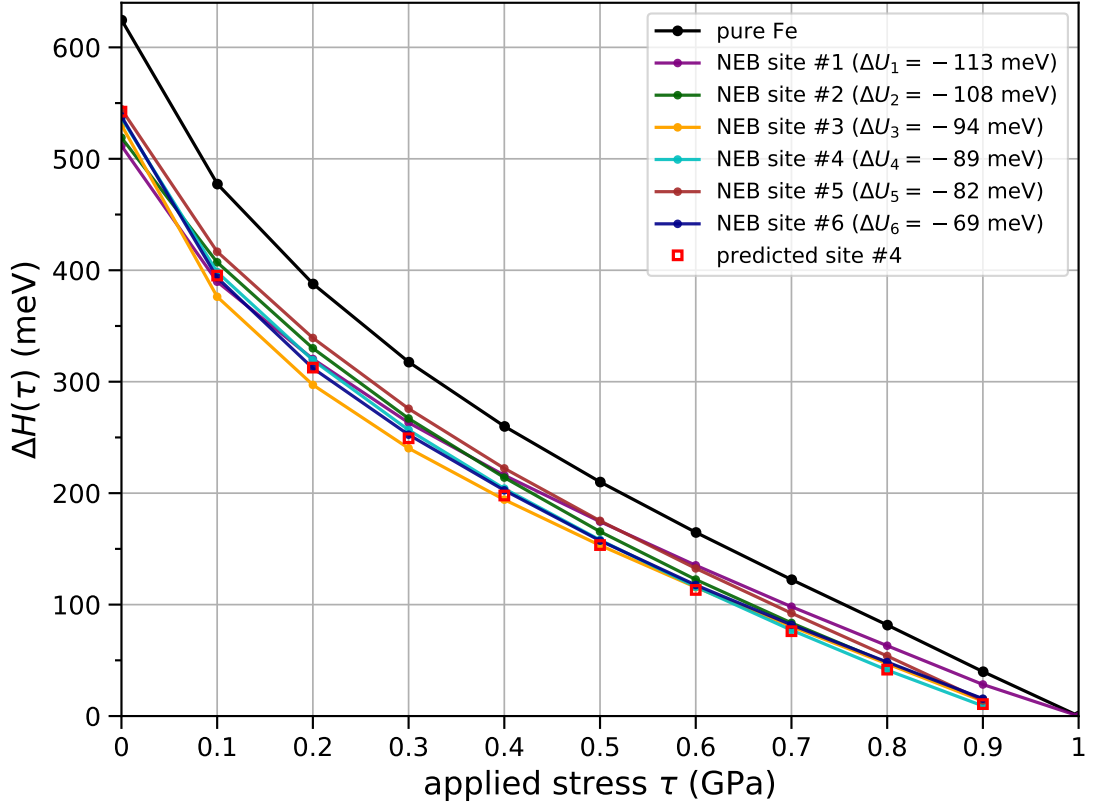


Figure 4.5 – **Single-solute effect on the double-kink nucleation barrier.** The double-kink nucleation enthalpy barriers, $\Delta H(\tau)$ versus the applied stresses τ for various single Si positions in Fe matrix. The solute/screw interaction energy change associated with each site, ΔU_i is also shown.

discussed below) shows that the use of the zero stress transition state structure to describe the collective effect of multiple solute/double-kink interaction energies is quite accurate. The maximum deviation in Fig. 4.6(b) is for the case $1 + \bar{1} + 5 + \bar{5}$, $d = 3b$. However, this configuration consists of solutes in four energetically-favorable positions, two of which are in the most favorable positions, and no other solutes. This is thus an extreme case - all the solutes are strongly attracting the double-kink - that is very unlikely to occur in the dilute alloys. Evidently, it distorts the transition state shape away from the assumed shape sufficiently to reduce the effect of the solutes. Overall, however, while the precise double-kink transition state structure in the NEB varies with each distinct solute configuration, with solutes pulling/pushing the dislocation line away from the pure Fe shape, our model remains quite good, and so is a quantitative parameter-free analytical model.

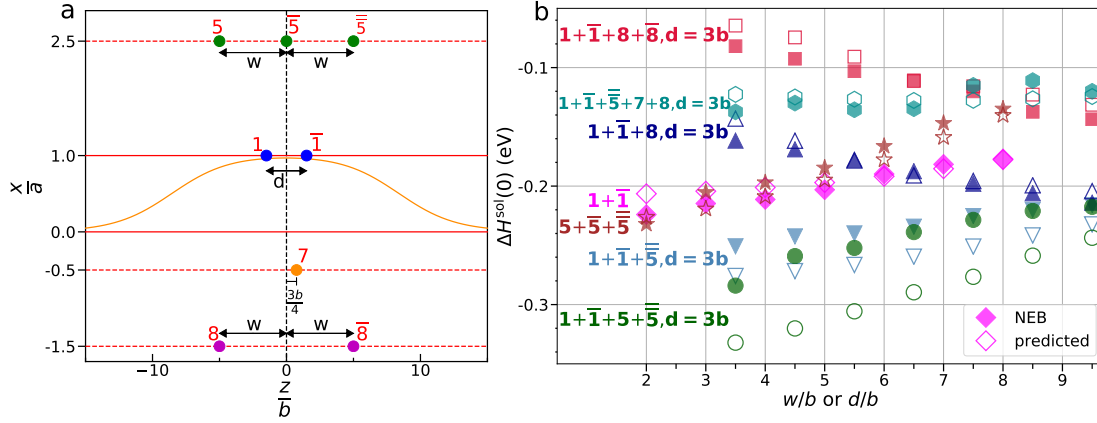


Figure 4.6 – **Validation of the model for solute/double-kink interaction energies.** (a) Definition of solute positions relative to a double-kink nucleation shape (orange solid line). Same color and number is used for solutes in a same atomic row position (x_i, y_j) consistent with sites marked in Fig. 4.2f. (b) The zero stress double-kink nucleation enthalpy barrier changes $\Delta H^{\text{sol}}(0)$ due to different solute combinations. The numbers indicate the numbered solutes in (a); e.g. $1 + \bar{1} + 8, d = 3b$ denotes solutes at sites #1 and # $\bar{1}$ at fixed distance $d = 3b$ plus a solute at site #8 at various w distances.

4.3.3 Double-kink nucleation in model dilute Fe-Si random alloys

Finally, we compare our predictions of the double-kink nucleation barrier for the model binary random Fe-Si dilute alloys to direct NEB simulations for a range of solute concentrations and dislocation lengths and under zero and non-zero stresses. The NEB selects the lowest barrier in any particular realization, and so our predictions use the weakest-link limit (Eq. 4.10) appropriate for the NEB simulations.

zero stress

Figures 4.7(a)-(d) show the mean, statistical distribution, and standard deviation of the NEB double-kink nucleation barrier ΔH as a function of solute concentration for dislocation lengths $L = 40b, 70b, 100b$, and $200b$, respectively, at zero stress. The corresponding predictions of the theory for the mean and standard deviation, with no adjustable parameters, are also shown. As predicted, the changes in nucleation energy barrier are statistically-distributed in random dilute alloys and are a function of both solute concentration and dislocation length.

At the shortest length of $40b$, there is essentially no weak-link scaling effect. The distribution of barriers is centered on the single-solute result, not the zero-solute result, because the nucleation will typically occur around the single most-favorable solute. The standard deviation, which is representative of the statistical variations from sample to sample, increases as the concentration increases. The theory predicts both the mean and standard deviation in good agreement with the simulations, with no adjustable parameters. The results at $40b$ represent

the "unit" statistical process, with weak-link length effects entering for longer lengths.

For the longer lengths $70b - 200b$, the mean barrier decreases because the system can find the weakest among several possible nucleation environments along the dislocation line, as predicted by the theory. The standard deviation also narrows slowly, as predicted. All the trends predicted by the theory agree quantitatively with the simulations. At length $200b$, essentially none of the simulations at 1, 2 or 4% has a barrier that exceeds that of pure Fe. The system always finds some favorable solute fluctuations that reduce the double-kink nucleation barrier, i.e. "softening" the alloy, even at this rather small dislocation length. Note that these results are for double-kink nucleation only; kink migration is not investigated even though it may become the rate-controlling factor at the higher concentrations.

Non-zero stress

The predictive model is further verified by comparing to NEB simulations under applied stresses in the range 100-900 MPa. Simulations were performed for a single dislocation length of $70b$ and concentration of 2%. Figure 4.8 shows the mean enthalpy barrier as simulated and as predicted, along with the enthalpy barrier for pure Fe. The statistical distribution of barriers as simulated is shown as a histogram and is important because nucleation in realistic systems will occur along lengths much larger than $70b$.

Very good agreement is found between the predicted and NEB results. The barrier reduces as the stress increases, but the difference between pure Fe and the alloy decreases with increasing stress. At a stress of 70% of the Peierls stress, the spectrum of barriers extends to zero (and below). That is, for some cases, the initial dislocation position is unstable (zero barrier) against gliding forward into the lower-energy state in the next adjacent Peierls valley. These cases are not shown and the predictions for the mean barrier at the higher stresses must use a lower limit of $-\Delta H^0(\tau)$ in the integrals in Eq. (4.10). More importantly, for longer lengths, the mean barrier at any stress will decrease even further, with the standard deviation decreasing only slowly, enabling zero-energy barriers to occur with increasing frequency.

The results in Figure 4.8 fully validate our analytic model for double-kink nucleation in random alloys as a function of both concentration and stress. For any length dislocation beyond more than a few segments, and at all stresses below the Peierls stress, the presence of solutes reduces the double-kink nucleation barrier, i.e. solutes always soften double-kink nucleation. This validation is performed on a model Fe-Si alloy where all material parameters are known, but now enables application of the analytic model to be applied to realistic alloys using input material parameters relevant for the real alloys.

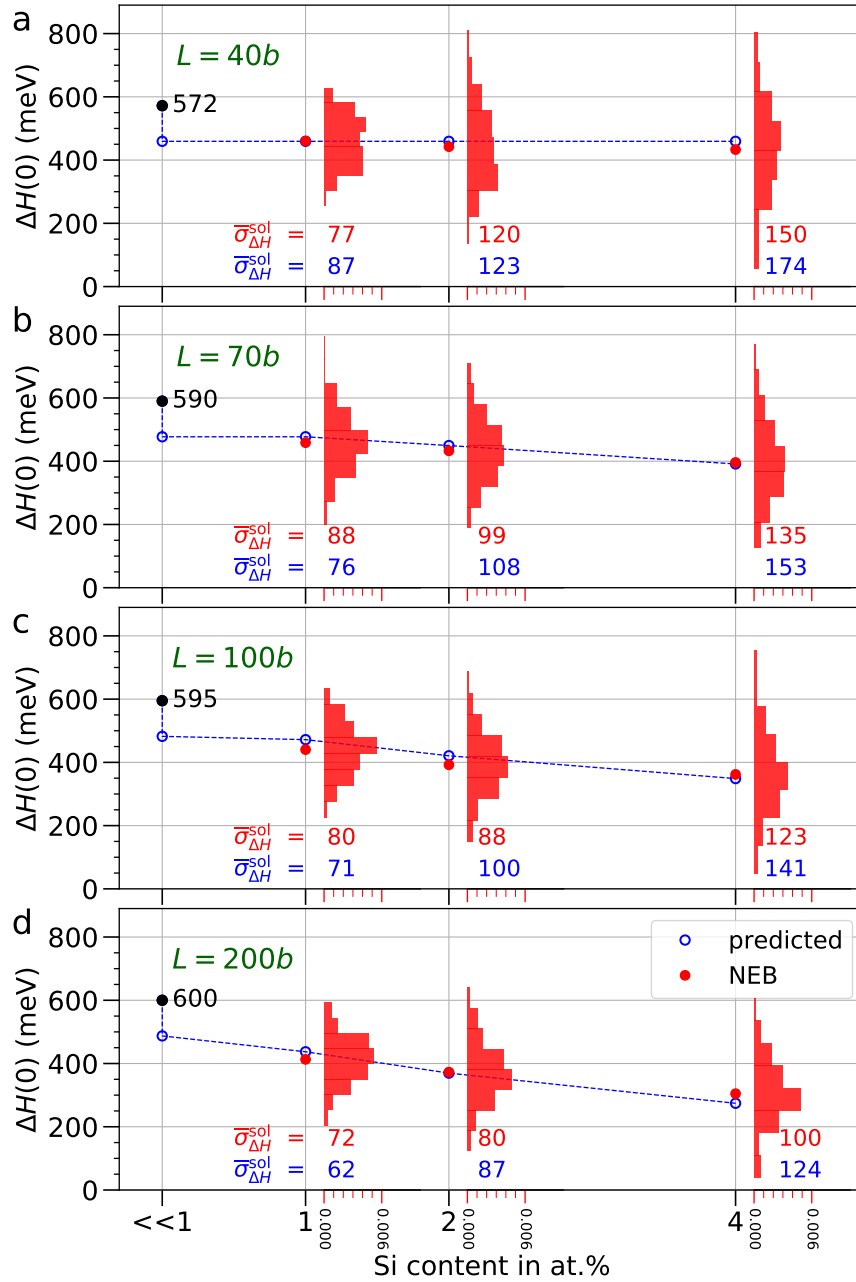


Figure 4.7 – NEB and predicted results of zero-stress double-kink nucleation barrier. Zero stress double-kink nucleation barrier $\Delta H(0)$ versus solute concentration c for dislocations with length L (a) $40b$, (b) $70b$, (c) $100b$, and (d) $200b$. The histograms show the distribution of double-kink nucleation barriers obtained by NEB calculations. The black numbers are the enthalpy barriers for double-kink nucleation in no solute pure Fe. The red and blue numbers are the standard deviations of the distributions of double-kink nucleation barrier obtained by NEB simulations and theory, respectively.

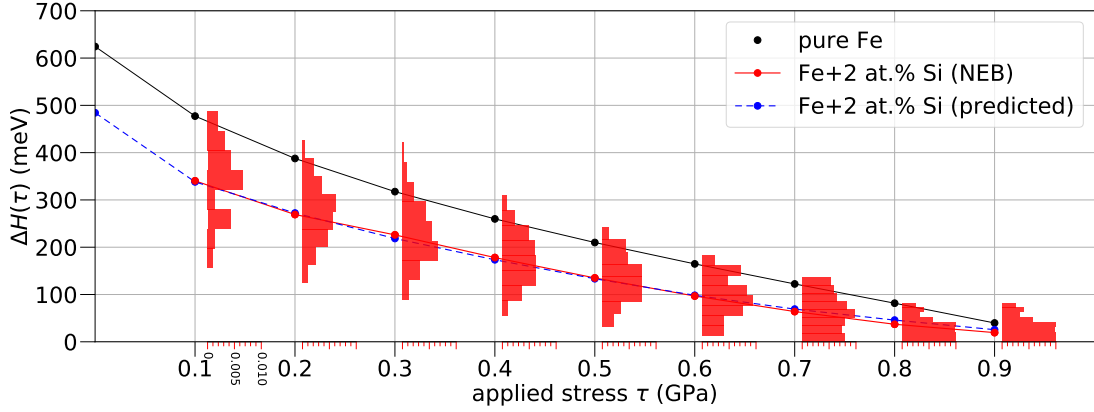


Figure 4.8 – NEB and predicted results of double-kink nucleation barrier versus applied stress. The double-kink nucleation barrier $\Delta H(\tau)$ versus applied stress τ for dislocations with length $L = 70b$ in Fe-2at%Si dilute alloys. The histograms are the distribution of double-kink nucleation barriers obtained by NEB atomistic calculations.

4.4 Applications and implications

The agreement between theory and simulation shown in the previous section on a model random dilute Fe-Si alloy validates all of the major features of the theory, and demonstrates the quantitative accuracy of the approximations that render the theory analytic. The theory can thus be applied with confidence to any bcc alloy system in the dilute limit. Challenges in applying the theory lie in obtaining accurate input data and also accurate experimental results. Nonetheless, below we achieve some insights in making comparisons to experiments at a level of detail well beyond previous literature.

We first address how the theory can be used to estimate the yield strength of a dilute alloy. The material parameters in the theory are reiterated: (i) the double-kink nucleation barrier and transition state configurations of the pure matrix; (ii) the double-kink nucleation length and total dislocation length; and (iii) the solute/screw dislocation interaction energies. The interaction energies can in principle be computed using first-principles (e.g. Figures 4.2(a) and (c)), although this is computationally challenging and still not necessarily precise for the real material. The double-kink nucleation length can be estimated reasonably by various means [95, 31]. The stress-dependent double-kink nucleation barrier for the pure matrix is derived from experiments of the flow stress versus temperature as explained below.

Obtaining $\Delta H^0(\tau)$ from experiments requires accounting for the number of nucleation sites N along each dislocation segment of length $L = 1/\sqrt{\rho}$ between dislocation junctions. When deformed at a constant strain rate $\dot{\epsilon}$, the thermally-activated Arrhenius model plus the Orowan model leads to a strain rate $\dot{\epsilon} = N\rho b a v_0 \exp(-\Delta H^0(\tau)/kT)$ where $N \sim 1/(l_{dk}\sqrt{\rho})$ is the number of possible nucleation sites along dislocations in between dislocation junctions. A reference strain rate $\dot{\epsilon}_0$ often replaces the combination $\rho b a v_0$. The enthalpy barrier at stress τ is then

obtained as

$$\Delta H^0(\tau) = \Delta H_{\text{exp}}^0(\tau) + k T \log(N). \quad (4.20)$$

where $\Delta H_{\text{exp}}^0(\tau) = k T \log(\dot{\epsilon}_0/\dot{\epsilon})$ is the experimental enthalpy barrier obtained from the experimental flow stress versus temperature experimental data.

With the above details, softening by solutes is then determined as shown schematically in Fig. 5.9. Starting with the experimental enthalpy barrier versus stress, the correction is made for N , and then the contribution of the solutes is added, where the figure shows the case where the low-temperature weak-link result is applicable. An experiment carried out at a particular $\Delta H^{\text{exp}} = k T \log(\dot{\epsilon}_0/\dot{\epsilon})$ determined by the specified temperature and strain-rate will then measure the strengths indicated in Fig. 5.9.

While the weak-link analysis can only be applied for low temperatures $T < T_0$, the total nucleation rate due to all nucleation sites, Eq. (4.9), can be applied for the whole temperature range of interest. In this case, considering Eq. (4.20) along with Orowan's law, Eq. (4.9) is solved numerically to determine the yield stress at a given strain rate and temperature. In the following, the full rate theory has been used to predict the yield stress of real dilute Fe-Si, W-Re, and W-Ta alloys.

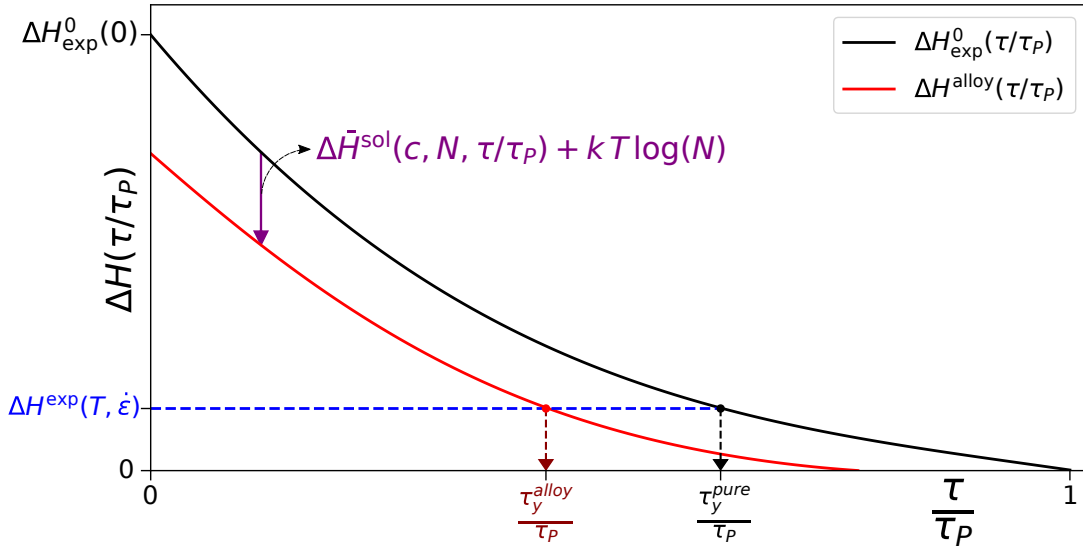


Figure 4.9 – **Generic prediction of solute softening by double-kink nucleation starting from double-kink nucleation in the pure metal.** The experimental barrier versus stress must first be corrected for the number of nucleation segments N , and then the additional effect of softening is added to obtain the total activation enthalpy. At a given experimentally-imposed activation enthalpy determined by the temperature and strain rate, the alloy has a lower yield stress than the pure metal. The example here uses the weak-link limit for illustration.

4.4.1 Application to Fe-Si alloys

We now use the theory to make specific predictions for real dilute Fe-Si (0.52 at%, 1.3 at%, 3.2 at%, and 5 at%) alloys over a wide temperature range and compare to the experimental data of [78] performed at a strain rate of $1.7 \times 10^{-4} \text{ s}^{-1}$. We use a reference strain rate of 10^4 s^{-1} and take a dislocation density of $\rho = 10^{12} \text{ m}^{-2}$ ($L \sim 1 \mu\text{m}$; $N \sim 170$) based on the TEM measurements of Takeuchi [162].

The same Fe-Si alloys at 5 at% and higher were previously studied by [94] using the non-dilute theory. There is significant strengthening at this concentration, indicating that the non-dilute theory is appropriate. Good agreement in strength versus temperature at these higher concentrations was obtained using a solute/dislocation interaction energy parameter $\Delta \bar{E}_p = 178\sqrt{c} \text{ meV}$, and so we use this value here. The transition state configurations for pure Fe are taken from a study using a machine-learning interatomic potential trained on a very large DFT dataset [95] with double-kink nucleation length $l_{dk} = 12b$. Both the interaction energy parameter and the double-kink transition state structures differ from those of the model Fe-Si EAM potential precisely because that potential is not quantitative for real Fe-Si.

Our predictions are shown in Fig. 4.10. For 0.52at%Si at low T, the experiments show a very small hardening while the theory predicts a very small amount of softening. At higher $T > 200\text{K}$, the prediction and experiment are similar, and deviations from pure Fe are quite small. There is a small hump in the data around 150K, widely discussed but unexplained to date [80, 13, 19]. For the 1.3at%Si alloy, there is again a very small strengthening seen at low T and minimal effects at higher T. The predictions show a small softening at low T and then little net effect at higher T. For 3.2at%Si, at low T there is slight softening and then a small but distinct strengthening at higher $T > 100\text{K}$. The theory shows a stronger softening that remains roughly constant relative to pure Fe over the entire temperature range. At 3.2at%Si, the double-kink nucleation theory deviates significantly from experiments throughout the entire temperature regime, suggesting another mechanism controlling deformation (see below). Further significant deviations are obtained at an even higher concentration of 5at%Si, where the alloy is significantly strengthened but the double-kink nucleation theory predicts a large softening, relative to pure Fe, again indicative of another controlling mechanism (see below). The observed strengthening at low T for 0.52at%Si and 1.3at%Si is small and not explained by the present model. However, we show below another set of data at 1.0at%Si that shows distinct softening relative to pure Fe. Thus, the theory is qualitatively consistent with experiments at low concentrations in showing little effect of the solutes while the experiments themselves are in some conflict.

The failure of the present double-kink nucleation theory in comparison to the experiments at 3.2at%Si and higher concentrations is attributed to a transition from nucleation controlled softening at lower concentrations to some strengthening mechanisms at the higher concentrations. The traditional view is a transition to strengthening controlled by kink migration [158, 167, 147, 202]. Here we apply the non-dilute yield strength model of Maresca et al. [94]

that has successfully captured strengths in a number of bcc alloys. In this theory, an initially-straight screw dislocation in a random alloy lowers its energy by spontaneously forming a multiply-kinked structure at zero stress. The strength is then controlled by a combination of kink glide and cross-kink (also called jog or dipole) pinning, with a Peierls-like mechanism replacing kink glide at very low T . Crucially, there is no role of thermally-activated nucleation of double-kinks in this model, and so it is applicable only in the non-dilute regime.

The transition between dilute (double-kink nucleation controlled softening) and non-dilute (kink glide and cross-kink controlled strengthening) is then mainly dictated by the spacing of the spontaneous kinks. If this length is smaller than the distance between forest junctions L , then the Maresca et al. model should apply and the alloy is in the non-dilute regime. If the kink spacing is predicted to be larger than L , then the spontaneous kinked structure cannot actually form, and thermally-activated double-kink nucleation is necessary; such alloys are in the dilute regime where the present theory should apply. Maresca et al. predict the spontaneous energy-minimizing kink-spacing to be $2.5\zeta_c$ where $\zeta_c = (1.083E_k/\Delta\tilde{E}_p)^2 b$ is a critical length scale that depends only on the ratio between the kink formation energy ($E_k = 0.5\Delta H^0(0)$) and the solute/dislocation energy quantity $\Delta\tilde{E}_p$. The length scale $2.5\zeta_c$ that determines the boundary between dilute and non-dilute domains thus depends on precisely the two major material quantities that enter into the present double-kink nucleation theory ($\Delta H^0(0), \Delta\tilde{E}_p$), enabling direct comparisons of the two theories with no additional material parameters.

The legend in Figure 4.10 shows the predictions of Maresca et al. for the length scale $2.5\zeta_c$ at each Si concentration. At both 0.52at%Si and 1.3at%Si, the length scale $2.5\zeta_c$ is larger than or comparable to L . According to our criterion, these alloys are thus expected to be in the “dilute” regime where double-kink nucleation controls the strengthening. This conclusion is supported by the reasonable agreement of the strength predictions using the double-kink nucleation theory and the poor agreement of the strength predictions (too low) of the Maresca et al. theory as shown in Figure 4.10. In contrast, at 3.2at%Si, the length scale $2.5\zeta_c$ is definitely smaller than L and, correspondingly, the strength predictions of Maresca et al. are in fairly good agreement with experiments, aside from a small over-prediction at low $T < 75K$. At this concentration, the double-kink nucleation prediction is too low at all temperatures. The experiments at 5at%Si with $2.5\zeta_c \ll L$ are then, as expected, captured well by the Maresca et al. model while the double-kink nucleation model predictions are poor. This analysis supports a transition from the dilute softening regime to the non-dilute strengthening regime between 1.3at% and 3.2at%.

The transition here is based on temperature-independent length scales. The experiments at 3.2at%Si suggest that there can be both softening at low T and strengthening at higher T . The trends in strength versus temperature of the two different models also suggest that at concentrations in between 1.3at% and 3.2at%, there could be changes in the strongest mechanism vs. temperature. Such details are well beyond the scope of the present models.

Our predictions for Fe-Si can be further compared to experiments of Chen et al. [23] who

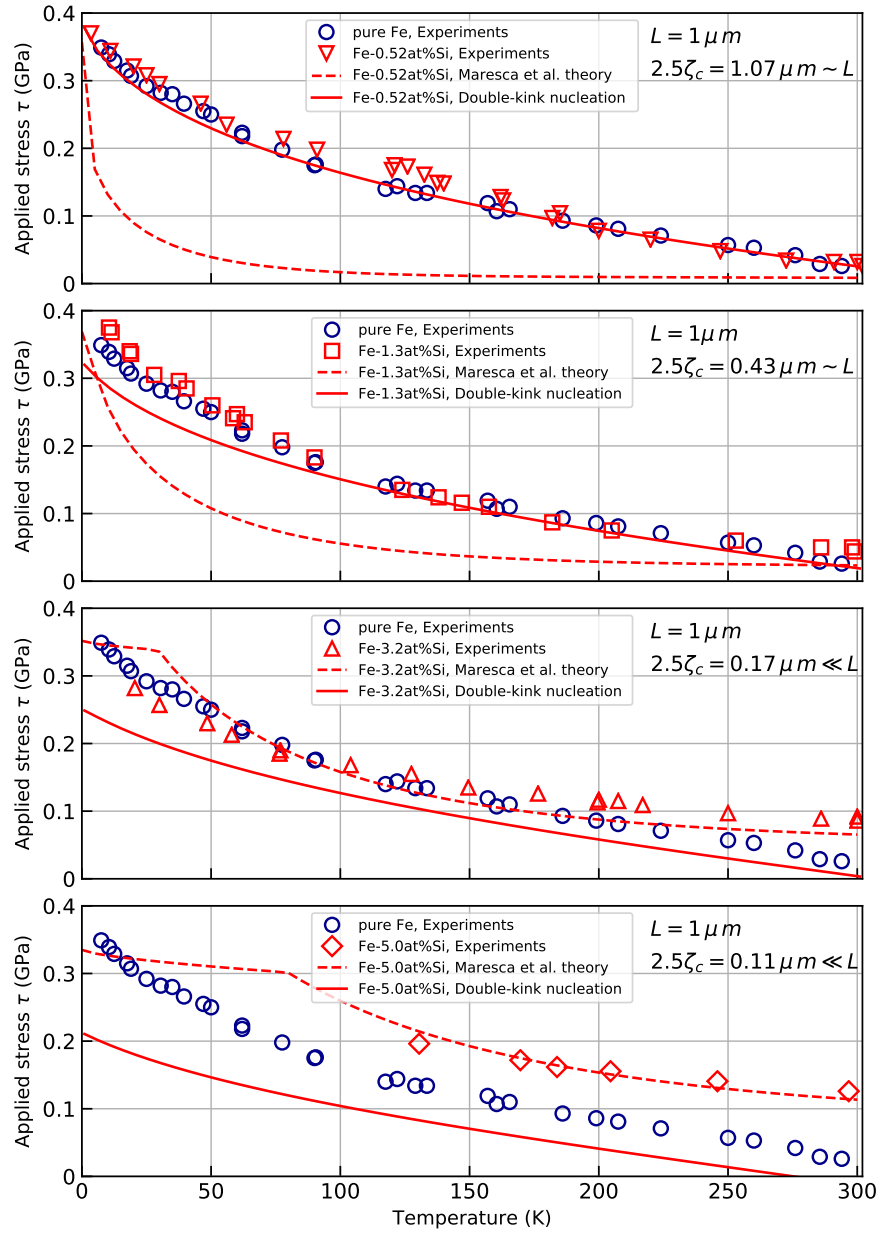


Figure 4.10 – Theory predictions for dilute $\text{Fe}_{1-x}\text{Si}_x$ alloys.

reported the yield stress of dilute Fe-1at%Si and Fe-4at%Si polycrystals. Chen et al. converted the uniaxial polycrystalline yield stresses to critical resolved shear stresses (CRSS) by using the Taylor factor ~ 2.75 for bcc pencil glide. The CRSS for pure Fe was then approximately 20% higher than that of Ref. [78], indicating the possibility that the data of Ref. [78] on pure Fe is low (for unknown reasons) which then brings into question the apparent strengthening at 0.52at%Si relative to the pure Fe data of Kitajima et al. More importantly, Chen et al. report distinct softening in Fe-1at%Si relative to pure Fe, in contrast to the results of Ref. [78] at 1.3at%Si. These comparisons demonstrate uncertainty in the pure and dilute Fe-Si data, which

then leads to uncertainty in assessing softening versus strengthening.

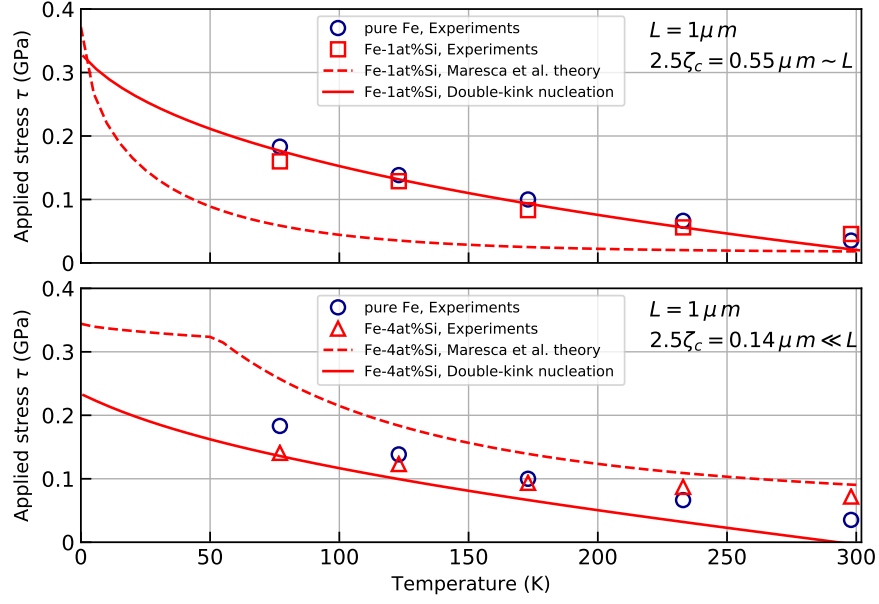
To apply our analysis to the data of Chen et al., we must first shift the results of Chen et al. because our analysis was based on the pure Fe of Ref. [78]. To do so, we simply rescale all the data of Chen et al. by a single factor of 0.8 to best-match the pure Fe experimental data of Kitajima et al. We then make predictions for Fe-1at%Si as shown in Fig. 4.11. For 1at%Si and at very low temperature $T = 77\text{K}$, both experiments and theory show slight softening. The experiments then show a slight strengthening at $T=300\text{K}$. The length scale $2.5\zeta_c$ and the strengthening predicted by Maresca et al. are also shown in Figure 4.11. At 1at%Si, the predicted strengthening is well below the experiments and the length scale $2.5\zeta_c$ is comparable to L . These results indicate that this alloy is in the 'dilute' regime where double-kink nucleation controls the screw dislocation motion. This is consistent with our conclusions based on the data of Kitajima et al.

Similar predictions for Fe-4at%Si are shown in Fig. 4.11. At $T = 77\text{K}$, the experiments show a notable softening followed by a transition to strengthening above 200K. The length scale $2.5\zeta_c$ of Maresca et al. indicates this alloy should be in the non-dilute regime. In addition, the non-dilute theory captures the strengthening reasonably well at the higher temperatures. The double-kink nucleation theory is in good agreement with the experiments at low T , which is surprising since we would expect this alloy to be in the non-dilute regime.

In spite of uncertainties in the experimental data, our analysis of the classic Fe-Si alloy provides a solid conceptual understanding of the nature of the transition in strengthening with increasing concentration. At low concentrations, there is generally softening by double-kink nucleation. At high concentrations, double-kinks are pre-existing and strength is controlled by kink migration and cross-kink formation. The transition is formulated in terms of length scales only, however. So, at concentrations in the transition range between 1.3 and 4 at%Si, strengthening may be a complex and temperature-dependent interplay between the two mechanisms. Such an interplay could be revealed by detailed kinetic Monte Carlo studies on long dislocation lengths that account carefully for the origins of kinks (pre-existing versus nucleating) and using the full statistical analyses for solute/screw interactions developed here. Existing kMC methods have already shown a transition generically, but have made simplifying assumptions about the solute/screw interactions, the kink formation, and the initial structure of the dislocation [157, 147, 202], that can perhaps be revisited.

4.4.2 Application to W-Ta and W-Re alloys

We now examine the yield stress for W-Re and W-Ta alloys at 0 (pure W), 1, and 3 at%, and temperatures $T = 150\text{K}$, $T = 300\text{K}$, and $T = 590\text{K}$. Experimental data was reported by Stephens[153] at a strain rate of $5.5 \times 10^{-4}\text{s}^{-1}$. We use the pure W data to estimate the pure W enthalpy barrier versus stress assuming the reference strain rate $\dot{\epsilon}_0 = 10^4\text{s}^{-1}$ and fitting a Kocks law as $\Delta H_{\text{exp}}^0(\tau) = \Delta H_{\text{exp}}^0(0) \left(1 - \left(\frac{\tau}{\tau_P} \right)^{0.49} \right)^{1.69}$ with $\Delta H_{\text{exp}}^0(0) = 1.4\text{eV}$ and $\tau_P = 1.1\text{GPa}$.

Figure 4.11 – Theory predictions for dilute $\text{Fe}_{1-x}\text{Si}_x$ alloys.

We use the transition state configurations obtained by GAP for pure Fe, since estimates for W are similar [31]. We use the solute/dislocation interaction energies obtained by DFT (Fig. 4.2) from which we compute the solute/dislocation interaction energy parameters as $\Delta\tilde{E}_p = 345\sqrt{c}$ meV for W-Re and $\Delta\tilde{E}_p = 137\sqrt{c}$ meV for W-Ta. We again use a mobile dislocation density of $\rho = 10^{12} \text{ m}^{-2}$ corresponding to $L = 1 \mu m$ and $N \sim 150$ segments along the length L when considering the transition to the non-dilute limit. We note clearly that, given the limited data to fit H_{exp}^0 and the uncertainty of other parameters, our predictions below are mainly qualitative and illustrative.

Predictions of the strength using the double-kink nucleation theory for the W-Re alloys are shown in Fig. 4.12 (a). The predicted softening for W-1at%Re is in reasonable agreement with the experiments at all three temperatures. For W-3at%Re, the predicted softening increases, as expected, while the experiments at 150K and 500K show a slight strengthening relative to 1at%Re and the experiments at 300K exhibit continued softening. This suggests a mechanism transition between 1at%Re and 3at%Re. We thus evaluate the length scale $2.5\zeta_c$ of the Maresca model to assess a possible transition at 3at%Re. Using the kink energy $E_k = 0.905 \text{ eV}$ from the DFT-based GAP potential for W [160], we predicted $2.5\zeta_c = 0.55 \mu m$ for W-1at%Re. This is comparable to the (approximate) dislocation length L , indicating that W-1at%Re is in the dilute regime. In contrast, we predict $2.5\zeta_c = 0.18 \mu m$ at 3at%Re, which is rather smaller than the (approximate) dislocation length L , suggesting that 3at%Re is in the non-dilute regime. The underpredictions of strength by the double-kink nucleation model at 3at%Re are thus qualitatively understood as being due to a transition to the non-dilute limit. The Maresca et al. model does not predict a temperature-dependence of $2.5\zeta_c$ and so the observed softening at $T=300\text{K}$ in W-3at%Re requires a full application of the Maresca et al. model before further

conclusions can be made.

Both trends and uncertainties in the experiments on W-Re are revealed by examining the data of Raffo [118] on very clean polycrystals at 0, 1, and 2at% at temperatures of 77K, 298K, and 589K. Data at 77K (not shown) shows a steady softening, although very small at 1at%; there is no comparable data by Stephens. At $T=298\text{K}$, as shown in Figure 12a scaled by the Taylor factor 2.71, Raffo shows a small strengthening at 1at%Re followed by softening at 2at% (but still stronger than pure W). At $T=589\text{K}$, as shown in Figure 12a, there is softening at 1at% and strengthening at 2at%. If the single data point for pure W at $T=298\text{K}$ were higher, the Raffo data would be qualitatively similar to the data of Stephens, and generally consistent with our analysis. Raffo also showed data at 7at% indicating continued softening at 77K but continued strengthening at 298K and 589K, the latter two results consistent with our analysis.

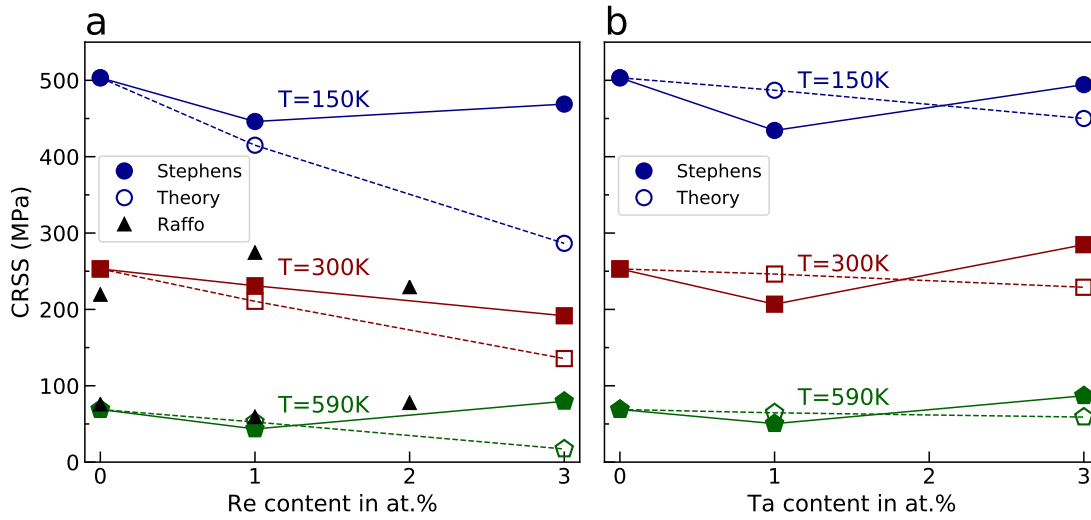


Figure 4.12 – **Theory predictions for W-Re and W-Ta alloys.** Critical resolved shear stress (CRSS) versus solute concentration at various temperatures as indicated for (a) W-Re (filled symbols: data from Stephens [153]; open symbols: present theory; black triangles: data from Raffo [118]); (b) W-Ta (filled symbols: data from Stephens [153]; open symbols: present theory) dilute alloys.

Predictions of the strength using the double-kink nucleation theory for the W-Ta alloys are shown in Fig. 4.12 (b). The experiments on W-Ta show a softening at 1at%Ta for all three temperatures studied. The double-kink nucleation theory predicts only a very slight softening for the 1at%Ta alloys, and so agrees only qualitatively with the experiments. The experiments at 3at%Ta show a slight strengthening at all three temperatures. The double-kink nucleation theory predicts continued softening, suggesting a transition in mechanism between 1 and 3at%Ta. However, the non-dilute theory of Maresca et al. predicts a length scale of $2.5\zeta_c = 1.1\mu\text{m}$ at 3at%Ta that remains comparable to the (assumed) L and so does not quite indicate a transition at this composition. A transition would be expected only at slightly higher Ta content.

Overall, softening at 1at% is predicted and observed for both Re and Ta solutes, supporting the general concept that softening arises for all solutes. A transition to hardening at 3at% is captured by our analysis for Re but not for Ta. These findings remain tentative on both theoretical and experimental sides. The material parameters needed for the theory are estimated to the best of current ability but remain uncertain. In addition, it is not expected that there is a distinct transition from softening to hardening at some very specific concentration but rather a delicate and possibly temperature-dependent interplay of mechanisms. Identifying a precise transition is also not of practical importance - what is important is that the operative physical mechanisms be identified and quantified so that alloy design can proceed on the basis of these mechanisms. Even with these significant caveats, the two theories together (present theory and Maresca et al. theory) remain broadly consistent with the experiments and so provide the desired framework for alloy design.

We conclude with some remarks about previous modeling and simulation on the W-Re and W-Ta alloys. The model of [68] was applied to W-Re and compared to hardness data at $T=298\text{K}$. Hardness and yield strength are not directly related, unfortunately, because hardness depends on the work hardening rate as well as the yield strength. This is clearly seen in the differences in flow stress versus solute type as a function of plastic strain in the uniaxial data of Stephens. Conclusions about relative softening and hardening based on experiments at a few percent plastic strain are thus inconsistent with the actual data at the onset of yielding. Hu et al. nonetheless converted the hardness data of Stephens and Witke at 298K [154] to a CRSS, leading to a CRSS for pure W of $\sim 350\text{ MPa}$ significantly higher than the $\sim 250\text{ MPa}$ reported by Stephens in direct uniaxial single crystal experiments. Hence, quantitatively, the predictions of Hu et al. do not agree with the uniaxial data of either Stephens or Raffo. The trends in converted hardness data do, however, suggest softening up to 5at%Re at $T=298\text{K}$ while the uniaxial data of both Stephens and Raffo also indicate softening up to at least 2-3at%Re at $T=298\text{K}$. The uniaxial data, however, shows hardening at 3at%Re at both 150K and 590K, suggesting an underlying transition around 3at%Re that might not be predicted by the Hu et al. model. Zhao et al. [202] compared results from Monte Carlo studies to the data of Stephens at 2% plastic strain rather than to the data reported at yield. Zhao et al. also calibrated the pure W parameters to DFT results that are well-established to greatly overestimate the yield strength, and so the quantitative results of Zhao et al. are far higher than the experiments at both yield and 2% plastic strain. Examining trends only, Zhao et al. predict slight softening relative to pure W up to 5at%Re at 150K, in conflict with the experimental hardening at 3at%Re. They also predict essentially no softening at $T=300\text{K}$ up to 1.5at%Re and very slight strengthening up to 5at%Re, in conflict with the distinct softening observed experimentally up to 3at%Re. At $T=590\text{K}$, Zhao et al. show a trend in good agreement with experiments. Overall, the results of Zhao et al. are quantitatively far from experiments and the trends are inconsistent with experiments. Finally, as noted in the Introduction, the model of Hu et al. was also applied to W-Ta and can only predict strengthening, inconsistent with the softening data of Stephens.

4.4.3 Implications for spontaneous kinking in the non-dilute regime

In the non-dilute screw strengthening theory of Maresca et al., the initial straight dislocation in the random alloy at zero stress is spontaneously kinked at a characteristic length of $2.5\zeta_c$. Envisioning that the system is somehow prepared with initially-straight dislocations, the present analysis can assess what barriers must be overcome to achieve the spontaneously-kinked length. This was not addressed in Maresca et al., where it was assumed that there is sufficient time to overcome such barriers in any real systems. Here, we can use the present analysis to examine the typical reduction in double kink nucleation barrier due to solutes over the characteristic length of ζ_c . The reduction in barrier then corresponds to a reduction in the average time required for the dislocation to attain the fully-kinked configuration envisioned by Maresca et al.

The relevant solute/screw interaction energy is a generalization of the dilute limit of Eq. (4.7) in which all elements of the alloy are considered to be solutes within an effective or average alloy matrix (see Maresca et al. and Chapter 3 for details). The interaction parameter is then $\Delta\tilde{E}_p = \left(\sum_{i,j} \sum_n c_n \Delta U_{ij}^{n2}\right)^{1/2}$ where the ΔU_{ij}^n is the energy change for a solute of type- n at initial position ij relative to a screw dislocation in the effective or average alloy material. This interaction parameter has been estimated for various HEAs in Maresca et al. and has been examined for a wide range of alloys described by interatomic potentials in Chapter 3. Below, we use the values previously reported by Maresca et al. as shown in Table 4.2.

For simplicity, we assume a single double-kink nucleation length $l_{dk} = 20b$ for all of these non-dilute complex alloys. Based on the number of possible nucleation segments over each characteristic length $N = \zeta_c / l_{dk}$, the energy reduction at zero stress due to the solutes can be then estimated from Eqs. (4.10) and (4.11) as $\left|\Delta\tilde{H}^{\text{sol}}(\sigma_{\Delta H^{\text{sol}}}, N)\right| + \bar{\sigma}_{\Delta H^{\text{sol}}}(\sigma_{\Delta H^{\text{sol}}}, N)$, where the standard deviation of the solute energy changes $\bar{\sigma}_{\Delta H^{\text{sol}}}$ has been also taken into account and $\sigma_{\Delta H^{\text{sol}}} = G(0)\Delta\tilde{E}_p$ is the zero stress standard deviation. For each of the non-dilute complex alloys considered, the energy reduction $\left|\Delta\tilde{H}^{\text{sol}}\right| + \bar{\sigma}_{\Delta H^{\text{sol}}}$ normalized with respect to $\sigma_{\Delta H^{\text{sol}}}$ has been computed as shown in Table 4.2. The time required for the dislocation to kink is the inverse of the nucleation rate $t = 1/R$, where R is given by Eq. (4.15). We consider room temperature $T = 300\text{ K}$, an attempt frequency $\nu_0 = 10^{12}\text{ s}^{-1}$, and a zero-stress geometrical factor $G(0) = 2.8$.

Fig. (4.13) shows the double-kink nucleation enthalpy barriers and the time required to move a kink over the length ζ_c at room temperature for various alloys. There is a considerable reduction in the zero stress double-kink nucleation barrier at room temperature for all the non-dilute complex alloys. This leads to a huge reduction in time required for the kink to overcome the nucleation barrier. For instance, the NbMoTaW high-entropy alloy has the largest estimated double-kink nucleation barrier among all these alloys and the solute fluctuations reduce the barrier by $\sim 0.4\text{ eV}$, which decreases the nucleation time from years to less than 2 hours (note however that Maresca et al. contend that the strength of this alloy is controlled by edge dislocations [93]). The maximum nucleation time across all alloys is 7 hours for the

Table 4.2 – The kink formation energy E_k , solute/dislocation interaction energy parameter $\Delta\tilde{E}_p$, characteristic length ζ_c , and the typical energy reduction due to solute fluctuations ($|\Delta\tilde{H}^{\text{sol}}| + \bar{\sigma}_{\Delta H^{\text{sol}}}$) at characteristic length $\zeta_c = N l d_k$, for various non-dilute complex alloys.

Alloy	E_k (eV)	$\Delta\tilde{E}_p$ (meV)	ζ_c/b	$(\Delta\tilde{H}^{\text{sol}} + \bar{\sigma}_{\Delta H^{\text{sol}}})/\sigma_{\Delta H^{\text{sol}}}$
Nb ₉₅ Mo ₅	0.634	48.8	198	2.13
Nb ₇₅ Mo ₂₅	0.611	84.7	61	1.59
Fe _{91.7} Si _{8.3}	0.493	51.4	108	1.83
NbMoTaW	0.6695	86.2	71	1.66
VNbMoTaW	0.6214	90.6	55	1.59

dilute alloy Nb₉₅Mo₅.

The present analysis thus shows that attaining the low-energy kinked screw structure envisioned by Maresca et al. is facilitated by the reduction of the double-kink nucleation barrier in a complex alloy over the crucial length scale ζ_c . However, at very low temperatures, the time to overcome these barriers remains very large and this may inhibit the transition to the non-dilute low-energy configuration in the Maresca et al. model. This might explain some differences between experiments and the non-dilute theory at T=77K and T=150K at higher solute concentrations where the non-dilute theory is expected to be applicable.

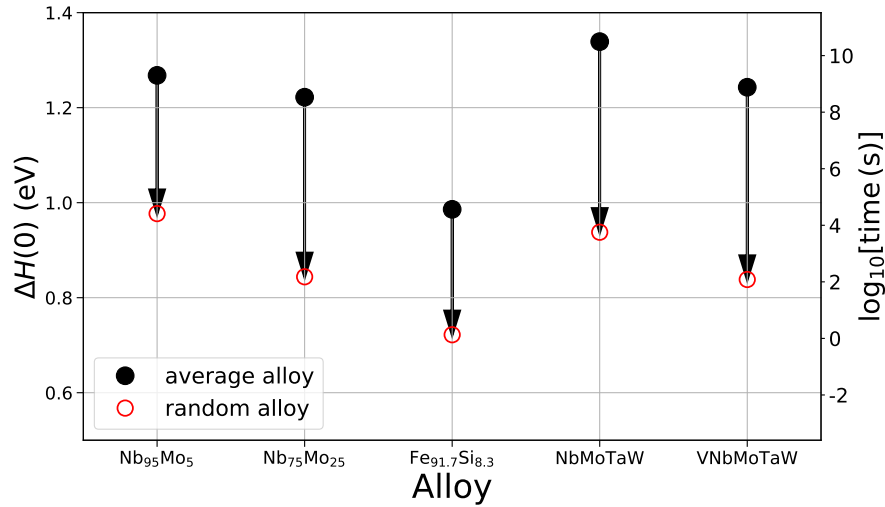


Figure 4.13 – Double-kink nucleation enthalpy barrier and the time required to move a kink over the length ζ_c at room temperature for various non-dilute complex alloys.

5 Kink migration in dilute BCC alloys

This chapter is extracted from the following publication

Ghafarollahi, Alireza, and W. A. Curtin. "Theory of kink migration in dilute BCC alloys." *Acta Materialia* (2021): 117078.

The temperature-dependent plasticity of BCC metals and dilute substitutional alloys is controlled by the motion of $1/2\langle 111 \rangle\{110\}$ screw dislocations between local energy minima (Peierls valleys at spacing a) by a two-step thermally-activated process [113, 158, 20, 5]. The first step is nucleation of a pair of kinks somewhere along an initial long straight screw dislocation. The second step is the migration of these kinks along the screw dislocation of length L , where $L = 1/\sqrt{\rho}$ is estimated as the distance between dislocation junctions/jogs at dislocation density ρ . These steps lead to a plastic displacement of a for each dislocation segment. The macroscopic plastic strain rate due to the motion of all N dislocations is then consistent with Orowan's law $\dot{\epsilon} = Nab/L^2\bar{t} = \rho ba/\bar{t}$ where \bar{t} is the average time for the two-step process [158, 5, 167, 68]. Nucleation and migration processes each have stress-dependent activation energies $\Delta H(\tau)$ and the rate-controlling process is the one with the higher activation energy and longer time $\bar{t} \sim \exp(\Delta H(\tau)/kT)$.

In pure BCC metals, flow is controlled by the double-kink nucleation process because kink migration has a negligible barrier. In dilute random alloys, the added solutes affect the activation energies for both nucleation and migration processes [132, 111]. Generally, solutes reduce the nucleation barrier, as understood theoretically [113, 158, 183] and observed experimentally [113, 153], because nucleation always occurs in a region along the dislocation line where the local solute fluctuations in the random alloy most-favor double-kink formation. In contrast, solutes increase the kink migration barrier because the kinks must overcome the largest barrier(s) created by the extreme solute statistical fluctuations along the remaining line. Since stress provides a driving force for overcoming barriers and since longer lengths will have larger extreme fluctuations somewhere along the length, it becomes critical to accurately determine the stress- and length-dependent barriers $\Delta H_{dk}(\tau, L)$ and $\Delta H_{km}(\tau, L)$ for nucleation

and migration, respectively, in a random alloy.

Note that any model that embodies the above two effects of the solutes in some manner will predict a transition from nucleation to migration control of strength. Predicting a transition is thus not sufficient validation of a model. Furthermore, models that involve adjustable parameters allow for the transition to be tuned to match data, and so again are not sufficient validation. Historical models for nucleation and migration do not fully handle the energetic and statistical aspects of the problem [158, 167, 68]. These models simplify the solute/screw dislocation interactions to a single value E and then use approximate statistics to estimate the effects of solute fluctuations. The Suzuki model predicts a reduced barrier for nucleation but the model of Trinkle and Woodward does not (see [51] for more discussion). For kink migration, Suzuki [158] considered the statistical number of accumulated solute atoms $m(z)$ around the screw core that have been passed during the movement of the kink a distance z along the dislocation line with barrier $\Delta H_{km} = m(z)E - \tau zab$ where b is the Burgers vector and $a = 0.943b$. The kink width w was then introduced by averaging the barrier over $z \pm w/2$. Trinkle and Woodward [167, 68] approximated the barrier as $\Delta H_{km} = m|E|$ with fixed $m = 25\sqrt{c}$, or other related forms, as an estimate of the largest cluster, with no accounting for kink width. Kinetic Monte Carlo methods have also been used recently to model both double-kink and kink-migration in dilute alloys [67, 202, 147]. The formulations ensure that a transition is obtained but treatment of the kink structure, solute/screw interactions, and/or solute effects on the nucleation barrier remain approximate.

We note that after the transition from double-kink nucleation to kink migration control has occurred, additional phenomena are possible. In particular, when the kink migration barriers are high (low stress, high temperature), it is possible that more than one double-kink can nucleate along the same dislocation segment. If this nucleation occurs on one of the other crystallographically-equivalent slip systems, the eventual intersection of two kinks on different planes gives rise to cross-kinks. Cross-kinks form strong pinning points that are only broken by formation of vacancy or self-interstitial point defects, and so contribute to strengthening. This phenomenon tends to arise in the non-dilute regime, and is incorporated into various theories [158, 94] and can occur in KMC simulations [17, 16, 100, 204]. This topic is beyond the scope of the present study.

Here, we develop a rigorous statistical model for the effect of solutes on the kink migration barrier as a function of concentration and applied stress. Interactions of all solutes at all distances from the straight and kinked screw are considered, as in our previous model of double-kink nucleation. The model for the kink migration barriers is validated against direct atomistic nudged elastic band (NEB) calculations and related stochastic simulations on a model Fe-Si alloy. We then show that the kink migration process under stress is essentially the random walk-type "Wiener process with drift", which yields analytic results for the barrier in terms of all relevant material properties. The resulting model for the kink migration barrier as a function of stress, solute concentration, and dislocation length is fully compatible with our previous analytic solution for the double-kink nucleation barriers, enabling natural predictions

of the transition from nucleation to kink control of strength as function of temperature and strain rate in any dilute alloy. Application to real dilute Fe-Si with independent inputs show that kink migration becomes controlling around 3% Si. Application to real dilute W-Re up to 7%Re using DFT calculations of the W-Re screw interaction energies and other independent inputs also show good agreement for the transition from nucleation softening to migration strengthening at $T=300\text{K}$ and above.

5.1 Solute effects on the kink migration barrier

5.1.1 Solute/kink interaction energy

We consider a dilute binary alloy with "solute" atoms at concentration $c \ll 1$ and "matrix" atoms at concentration $1 - c$. The model is easily generalized to multiple components and non-dilute concentrations. For a dislocation at the origin $x = y = 0$ lying along the z direction, a solute at lattice site (x_i, y_j) has an interaction energy $U(x_i, y_j)$ with the dislocation, independent of the z coordinate due to translational invariance. When the dislocation glides by a along the glide direction x , the energy of the same solute has an interaction energy $U(x_i - a, y_j)$, and the change in interaction energy is then denoted as $\Delta U_{ij}(a) = U(x_i - a, y_j) - U(x_i, y_j)$.

After double-link nucleation, the two kinks propagate away from each other through the random field of solutes. The two kinks are assumed to be independent, neglecting their very small elastic interactions. We thus focus on a single kink. The kink is the structure that shifts the screw dislocation from the initial to the final Peierls valley. The shape of the kinked dislocation with the kink centered at z_c and gliding in the positive z -direction is commonly described by a hyperbolic tangent function [157, 74]. We thus describe the kinked dislocation as

$$x(z - z_c; w) = \frac{a}{2} \left(1 - \tanh \left[\frac{2(z - z_c)/b}{w/b} \right] \right) \quad (5.1)$$

where w denotes the kink width defined as distance between the intersections with the adjacent Peierls valleys of a tangent line at the kink inflection (see Figure 5.1a). Estimates and models show that $w \sim 10 - 20b$ is typical, so that the kink character is very nearly screw (character angle at most $\tan^{-1}(2a/w) \approx 5^\circ$).

We must compute the total energy change $\Delta E(z_c)$ of the system (dislocation plus solutes) as a function of the center position z_c of the kink as it glides across the segment length ($0 < z_c < L$). Here, we assume a model for the solute/kink interaction energies and validate that assumption via direct simulations in Section 5.2.2. The solute/dislocation interaction energy should vary smoothly from $U(x_i, y_j)$ to $U(x_i - a, y_j)$ as the kink glides past the solute, and this total change is independent of the kink shape. Thus, although the theory is developed by carefully considering the solute/kink interactions, the final results emerge to be weakly dependent on the actual kink width and shape (see Eq. (5.10)). Since the kink shape is very

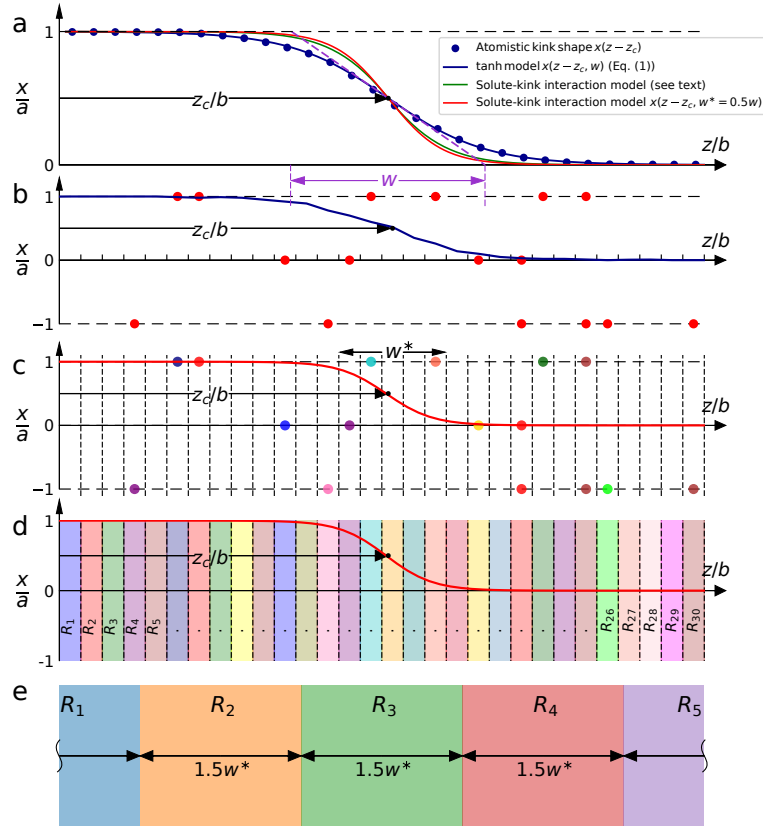


Figure 5.1 – (a) **Schematic of the models for the kink shape and solute/kink interaction energy.** The atomistic kink shape in the pure metal is described by a hyperbolic tangent function Eq. (6.12) with kink width w defined by the geometric construction shown. The solute/kink interaction energy (Eq. (5.2)) is related to the square of the distance of the kink to the nearest Peierls valley, which is nearly identical to a tanh function with effective kink width $w^* = w/2$ as shown. (b,c,d,e) **Schematic of models developed here for determining the energy landscape of single kink migration across a random field of solutes.** (b) Fully-atomistic NEB simulation with a possibly-varying kink shape and all solutes interacting with all portions of the dislocation line; (c) Discrete Rigid-Kink Model (DRKM) with solute/kink interactions governed by the effective kink shape (effective width $w^* = 0.5w$) and interactions of each solute at z_k scale with the relative distance $z_k - z_c$; (d) Stochastic Rigid-Kink Model (SRKM) where the total solute/dislocation interactions at z_k are replaced by a single stochastic value $R_i \Delta \tilde{E}_p$ chosen from the statistical distribution of the solute/dislocation interaction energies where R_i is a random number chosen from a Gaussian probability distribution of mean zero and unit standard deviation; (e) Wiener Process Model (WPM) where the dislocation is divided into $L/1.5w^*$ statistically uncorrelated segments each of which is assigned an energy $R_i \Delta E_p (1.5w^*/b)^{1/2}$ where R_i is a random number chosen from a Gaussian probability distribution of mean zero and unit standard deviation randomly selected from a normal distribution with zero mean and standard deviation. This model does not involve the kink shape, only the decorrelation length $1.5w^*$ of the solute/kink interaction.

nearly screw-like at either end, i.e. at $|z - z_c| \rightarrow \pm w/2$, the solute interaction energies in these regions are very nearly those of the straight screw. Here, we assume that the interaction energy between a solute at (x_i, y_j, z_k) and a kinked dislocation with kink centered at z_c is proportional to the normalized square of the kink position relative to the nearest Peierls valley in the same z_k plane as the solute. This effective kink shape is shown schematically in Fig. 5.1(a); it is essentially identical to the original kink shape but with an effective kink width $w^* = 0.5w_k$. Therefore, the solute/kinked-dislocation interaction energy is approximated as

$$U(x_i, y_j, z_k, z_c) = \frac{x(z_k - z_c; w^*)}{a} \Delta U_{ij}(a) + U_{ij}. \quad (5.2)$$

In this approximation, the kink is assumed rigid, i.e. not affected by the solutes, which is also implicit in prior screw strengthening theories [158, 167]. Nevertheless, using the NEB method as described later, we have examined variations in the kink shape as it glides through a random atomistic in Fe-4 at.%Si model alloy that has significant solute/dislocation interactions. Among hundreds of specific random solute environments, we find very little, if any, change in kink shape and width.

5.1.2 Energy landscape models for kink glide

Here, we present a sequence of models for determining the energy landscape experienced by a kink gliding through a random field of solutes. A schematic illustration of these models is shown in Fig. 5.1.

Using Eq. (5.2) for the single solute/kink interaction energy, the total interaction energy of the solutes with a kink centered at z_c is simply the sum of the interaction energies contributed by each individual solute in the specific configuration of solutes in the random alloy,

$$U(z_c) = \sum_{i,j,k} s_{ijk} U(x_i, y_j, z_k, z_c; w^*) \quad (5.3)$$

where the site occupation variable $s_{ijk} = 1$ if a solute is at position (x_i, y_j, z_k) and 0 otherwise. The energy landscape that determines the overall kink migration corresponds to the total solute/dislocation energy change as a function of the migration distance starting from an initial position $z_c = z_0$ to the current z_c , which can now be written as

$$\Delta E(z_c) = \sum_{i,j,k} s_{ijk} \frac{x(z_k - z_c; w^*) - x(z_k - z_0; w^*)}{a} \Delta U_{ij}(a) \quad (5.4)$$

We call this model for the energy landscape of the migrating kink the Discrete Rigid-Kink Model (DRKM); a schematic is shown in Figure 5.1c. The DRKM differs from the true atomistic problem only by the assumed solute/kink interaction model and rigid kink shape.

The DRKM energy landscape is for one specific configuration of random solutes. A further simplification is required to ultimately achieve an analytic model. We first note that the

statistical average of the solute/kinked dislocation interaction energy change is zero, $\langle \Delta E(z) \rangle = 0$, where the average is taken over the stochastic variable s_{ijk} . Thus, only the statistical fluctuations lead to energy variations with position, as discussed in [51]. The relevant statistical quantity is the standard deviation in the interaction energy change per Burgers vector of line length. For a straight segment of dislocation, the standard deviation can be computed as [51, 49]

$$\Delta \tilde{E}_p = \left(\sum_{ij} c \Delta U_{ij}(a)^2 \right)^{\frac{1}{2}} \quad (5.5)$$

Then, within our solute/kinked-dislocation interaction energy model, each individual section of material of width b perpendicular to the dislocation line has some random set of solute positions that dictate the contribution to the total energy at that position z . The fluctuations in this energy over all possible solute configurations are proportional to $\Delta \tilde{E}_p$ and to the dislocation position $x(z - z_c; w)$. The energy of each section of width b with the kink at position z_c is thus $R \Delta \tilde{E}_p x(z - z_c; w^*) / a$ where R is a random number selected from a Gaussian probability distribution having zero mean and standard deviation of unity. For a dislocation segment of length $L = N b$ the energy landscape can then be written as

$$\Delta E(z_c) = \Delta \tilde{E}_p \sum_{k=1}^{N=L/b} x(z_k - z_c; w^*) R_k \quad (5.6)$$

We call this model the Stochastic Rigid Kink Model (SRKM), schematically shown in Figure 5.1d. This model involves no direct discrete solutes, only the relevant stochastic energy quantity $\Delta \tilde{E}_p$, the kink shape, and a set of random numbers along the line that capture the exact statistical fluctuations due to random solutes, within our approximation for the solute/kinked-dislocation interaction energy.

The above models are representations of the entire energy landscape over a length L in a specific random alloy as a function of the solute/dislocation interaction energies, the kink shape, and the length L . An applied stress is added subsequently as discussed below. From these models, we extract the largest global barrier for kink glide, i.e. the difference between the highest energy and the lowest energy along the entire path in the direction of the kink glide. It is this (stress-dependent) barrier that will control the kink migration over length L .

5.2 Validation using an atomistic model Fe-Si alloy

We now compare predictions of our analytical model for the solute/kink interaction energy and the stress assisted kink migration enthalpy barrier against direct atomistic simulations using a model Fe-Si alloy. The only input parameters to the model are the solute/screw-dislocation interaction energies $U(x_i, y_j)$ at all distinct solute positions ij around the screw core, the length L of the dislocation, and the single kink shape in the pure matrix material.

5.2.1 Simulation Details

We use a model Fe-Si alloy system as represented by an EAM potential [147]. The Fe-Fe interactions [117] have all the underlying DFT-based features for Fe screw dislocations such as the compact core structure, the single-hump Peierls potential, and $\{110\}$ slip-plane. Since we are interested in dilute alloys, we further set Si-Si interactions to those of Si-Fe, eliminating direct solute-solute interactions. Therefore, although not being an accurate representation of real Fe or real Fe-Si, this potential is a well-defined model system that can be used with confidence to validate our analytical model; it was also used previously to study solute effects on double-kink nucleation [49]. The kink shape in pure Fe is determined using the registry method [177] and fit to the functional form given by Eq. (6.12) leading to $w = 10b$. The critical solute/dislocation energy change ΔU_{ij} as a function of solute position for this potential is shown in Figure 5.2. The key statistical quantity entering the analytic theories is then calculated as $\Delta \tilde{E}_p = 344 \text{ meV} \sqrt{c}$ at Si solute concentration c . We study both $c = 0.01$ and $c = 0.04$, for which $\Delta \tilde{E}_p = 34.4 \text{ meV}$ and $\Delta \tilde{E}_p = 68.8 \text{ meV}$. All quantities entering the model are well-defined and computed independently of the model.

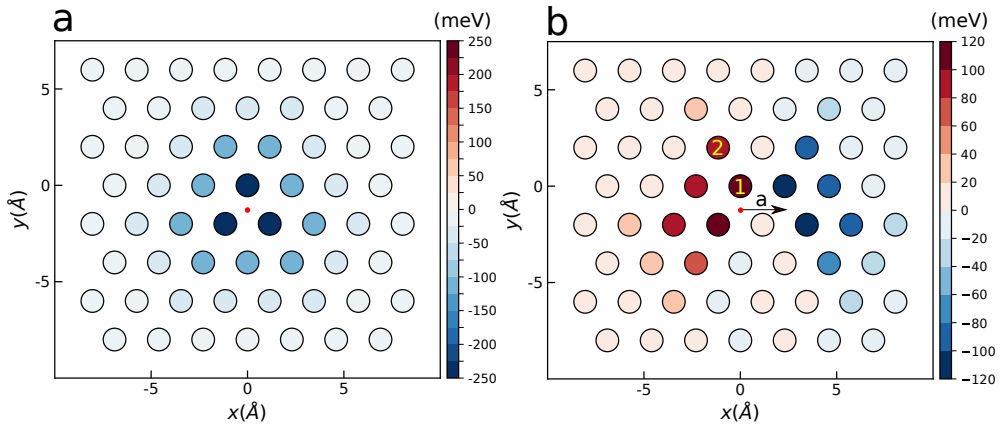


Figure 5.2 – **Solute/screw interaction energy and energy change for single Si solute in Fe matrix.** (a) Solute/screw interaction energy U_{ij} versus solute position for single Si solute in Fe matrix computed using the EAM potential of [147]. (b) Interaction energy difference $\Delta U_{ij}(a)$, as the screw dislocation core moves by one Peierls valley distance a (black arrow). Sites marked with 1 and 2 are substituted with Si atoms for subsequent NEB calculations, and are referred to in Fig. 5.3.

The minimum energy path during kink migration from an initial position to a final position is computed using the nudged elastic band (NEB) method as implemented in LAMMPS. Since kinks must come in pairs, the simulation of motion of a single kink requires special details. We start with pure Fe and create a cell having total dislocation line length longer than the simulated kink glide length $L = 120b$ subsequently studied in the alloy. A single solute is placed in the most energetically favorable location for aiding double-kink nucleation and a second solute placed at $\sim w$ away to inhibit glide of one of the two nucleated kinks. An NEB simulation is then performed during which the double-kink nucleates at the favorable solute

and only one kink glides across the remaining length of the simulation cell. A large number of replicas are used so that increments of kink motion between each replica are nearly one b distance. These replicas are then used as the initial path for NEB through a random solute field. More details of the NEB simulation can be found in A.3.

5.2.2 Validation of solute/kink interaction energies

Here we validate the solute/kink interaction model shown in Figure 5.1a where the interaction involves the effective kink width $w^* = w/2$. This is achieved by comparing predicted and NEB-computed changes in energy as the kink moves past specific selected arrangements of solutes.

The specific Si solute configurations studied here are shown schematically in Fig. 5.3(a). For each specific set of solute positions, we calculated the energy landscape of the system as function of kink position z_c using Eq. (5.4). Direct NEB calculations of the total system energy change are then performed on the exact same solute configurations. Figs. 5.3(b-i) show the atomistic NEB and predicted energy landscapes of the selected solute configurations. The agreement is very good in all cases, with deviations of less than ~ 10 meV across all cases. Subsequent similar studies discussed below in fully-random Fe-Si will further confirm, at a statistical level, the agreement between the model and NEB.

5.2.3 Validation of Kink Migration Models

Here, we validate the Discrete Rigid-Kink Model and Stochastic Rigid-Kink models by comparison against direct fully-atomistic NEB simulations of a single kink migrating across a random field of solutes at zero stress.

In order to perform the NEB simulations of kink migration in random solute field, using the NEB simulation setup generated as discussed in 5.2.1, a random solute field of the Fe-Si alloy is created by randomly distributing Si atoms at concentration c over a central section of length $L = 120b$ in the simulation cell away from the original double-kink nucleation site. This length is approximately $24w^*$, which is sufficient for validating our models. NEB is then executed to obtain the energy change $\Delta E(z_c)$ as a function of the kink position z_c . We create 200 different realizations of random Si at concentrations 1% and 4% to assess the average barrier and variations around the average with good accuracy. For each individual random distribution of solutes, we have a precise corresponding DRKM simulation.

Example energy landscapes as computed from the NEB and from the DRKM on exactly the same solute configuration are shown in Figs. 5.4b-e. By definition, the zero of energy corresponds to the energy at the initial kink position when it is first fully within the solute region. The net energy change over the length L can be positive or negative, depending on the overall fluctuations of the particular solute configuration. The DRKM captures the overall full NEB landscape very well in magnitude and length scales of major energy variations. Recall that

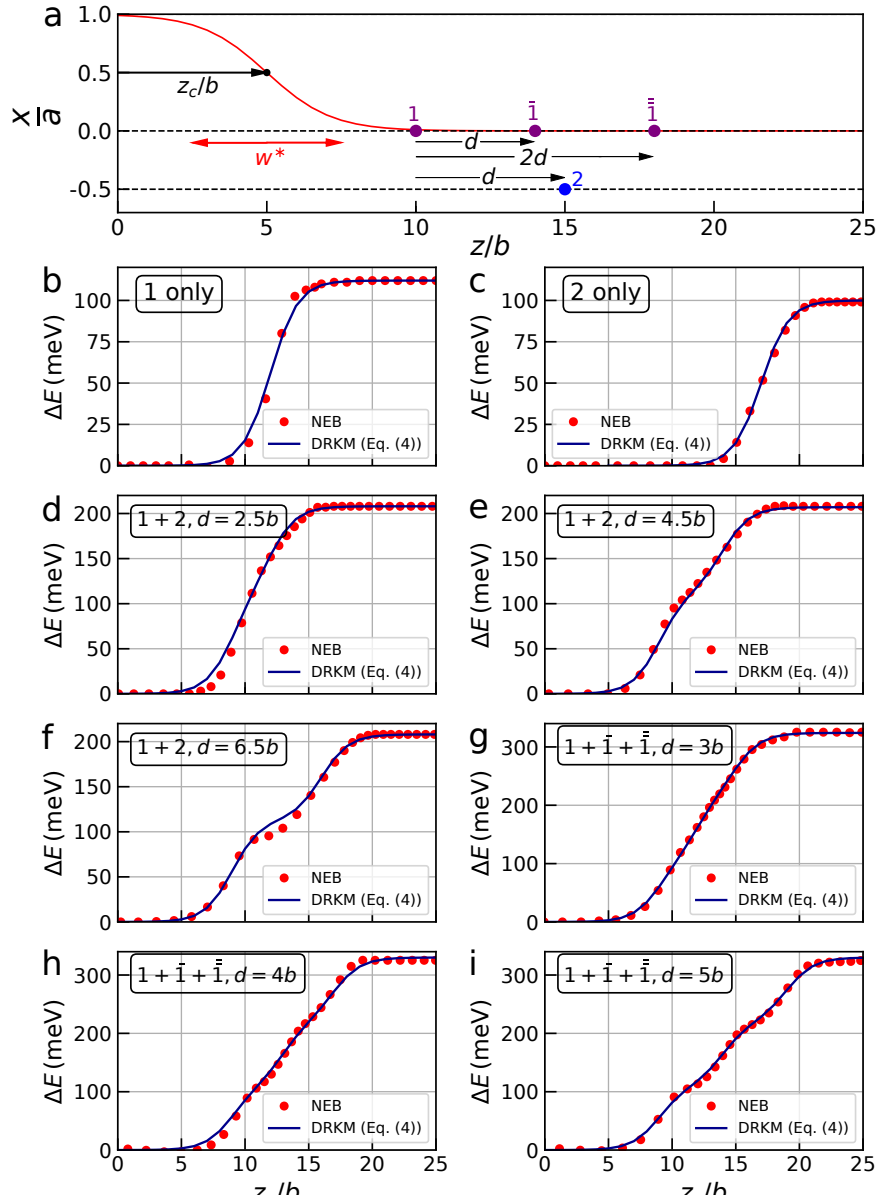


Figure 5.3 – **Validation of the model for solute/kink interaction energies.** (a) Schematic of solute positions that are bypassed by a single kink, with similar colors and numbers for solutes in the same atomic row position (x_i, y_j) and corresponding to sites marked in Fig. 5.2b with $\Delta U_1 = 112$ meV and $\Delta U_2 = 95$ meV. (b)-(i) NEB and predicted kink migration energy versus kink position z_c/b for each special solute arrangement as indicated; e.g. 1 + 2, $d = 6.5b$ in (f) denotes solutes at sites #1 and #2 at fixed distance $d = 6.5b$.

the DRKM has no adjustable parameters. As expected, the NEB landscape shows additional energy variations on scales smaller than $w^* = 5b$ because the atomistic kink may adapt subtly to the precise solute configurations and because the model for the solute/kink interactions is not exact. Nonetheless, the differences between the NEB and the DRKM are typically below

0.05 eV and 0.1 eV for $c = 1\%$ and $c = 4\%$, respectively, which are small compared to the overall variations of 0.4 eV and 1.0 eV.

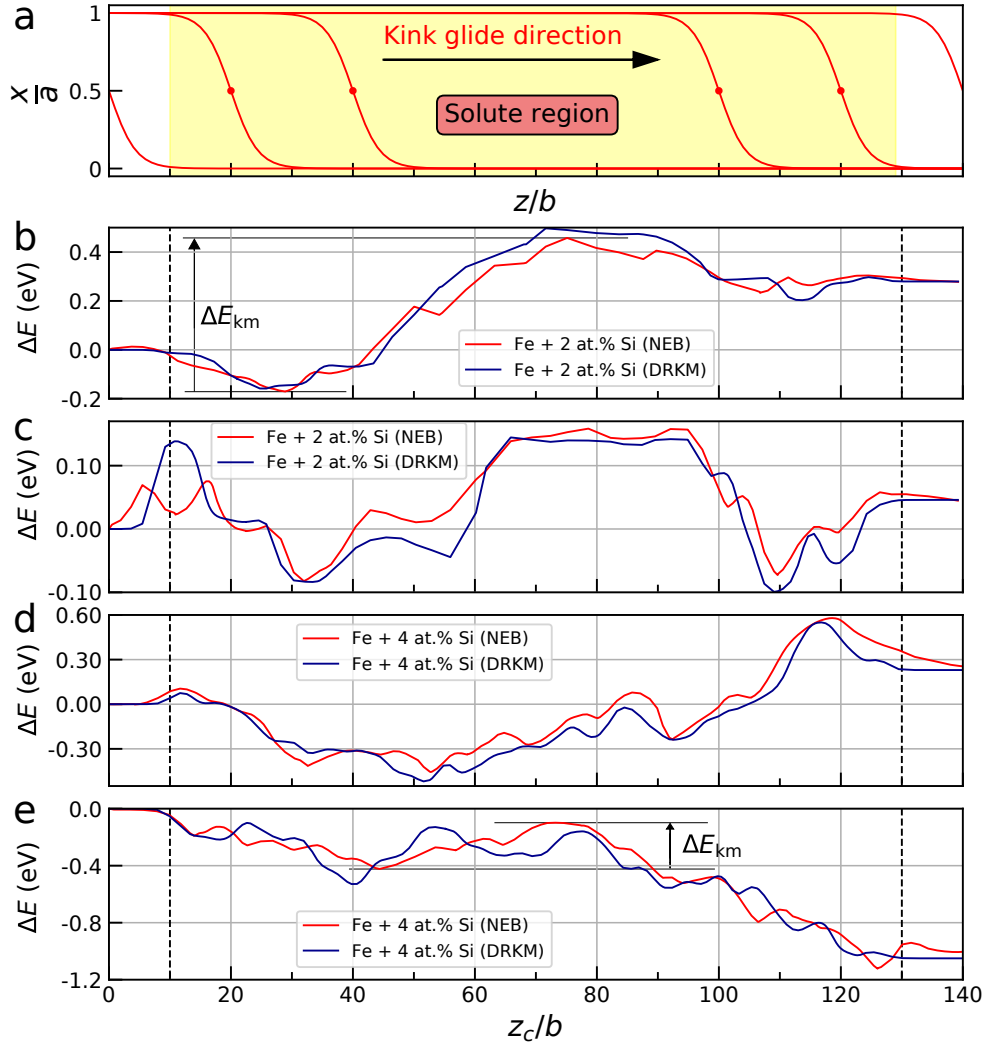


Figure 5.4 – NEB and predicted results for energy landscape of a single kink motion in random field of solutes. (a) Schematic of a single kink migrating from left to right through a field of solutes randomly distributed within the yellow-shaded region of length $L = 120b$. (b,c,d,e) Energy landscape as a function of the center position z_c of the kink as computed from direct atomistic NEB and from the Discrete Rigid Kink Model on exactly the same solute configuration, for two typical samples of Fe-1%Si and two typical samples of Fe-4%Si alloys. The largest barrier encountered by the kink for two of the NEB landscapes is indicated as ΔE_{km} for illustration.

The most important quantity controlling the rate of the kink motion is the largest typical energy barrier encountered by the kink over a glide distance z . We have thus extracted the maximum barrier over the length $L = 120b$ from our NEB, DRKM, and SRKM simulations. Figure 5.5 shows the average barrier energy and the distribution of barriers over 200 simulations for the

NEB and DRKM and over ten thousand simulations for the SRKM at $c=1\%$ and 4% , and also the average values from the SRKM over a wider range of Si concentrations c . Results are also shown for the Wiener process model (WPM) discussed later. The DRKM captures the average barrier very accurately. The average maximum barrier for the SRKM is slightly higher at both concentrations. The statistical distributions of barriers around the mean all have the same overall shape and magnitude, and the standard deviations are nearly identical. The mean of the SRKM deviates from the NEB and DRKM by less than $\Delta\tilde{E}_p$, which is itself a factor of ~ 6 smaller than the standard deviations of all models. These results quantitatively validate the DRKM and SRKM.

The good agreement between the NEB and the SRKM demonstrates that the dominant energy barriers are controlled by the well-defined solute/dislocation interaction energy parameter. Details of specific solute distributions and deviations of the kink shape from an idealized model are not important in determining the operative distribution of barriers. This is not surprising because the kink is primarily affecting the transition of solute positions relative to the (shifting) dislocation line, and the energy difference at any z once the kink has fully passed by z is captured exactly in the model. This agreement has two important consequences: (i) it justifies the application of the computationally-inexpensive SRKM to examine barriers over length scales L that are much larger than can be studied using direct atomistic NEB or the DRKM and (ii) it points toward the development of an analytic stochastic model.

5.3 Kink migration under stress

The analyses in the previous section were performed at zero stress. The competition between nucleation and migration is intrinsically stress-dependent, with the applied stress doing work on the system as the double-kinks nucleate and then as the kinks migrate. Here we extend the models and analysis to incorporate the driving force due to an applied shear stress. Specifically, an applied shear stress τ on the glide plane does work (starting from $z_c = 0$) of $-\tau b a z_c$ and hence the energy landscape becomes $\Delta E(z_c, \tau) = \Delta E(z_c, \tau = 0) - \tau b a z_c$. This model assumes a rigid kink, but fluctuations in the area swept due to atomistic changes in kink shape at a fixed mean kink position z_c are negligible.

In the landscape $\Delta E(z_c, \tau)$ with increasing applied stress, the maximum energy barrier ΔE_{km} and the activation distance z^* between the points of minimum and maximum energies that determine the barrier are both reduced. For each individual energy landscape $\Delta E(z_c, \tau = 0)$ computed from the NEB, DRKM, and SRKM, the stress-dependent kink migration barrier $\Delta E_{\text{km}}(\tau)$ is computed as a function of τ . Fig. 5.6(a) shows the average $\Delta H_{\text{km}}(\tau)$ over 200 independent simulations for the NEB and DRKM and over twenty thousand simulations for the SRKM at length $L = 120b$ for $c = 1\%$ and $c = 4\%$. Fig. 5.6(b) shows the activation distance z^* versus stress, varying smoothly from $\sim L/2$ at $\tau = 0$ to 0 at the stress where $\Delta H_{\text{km}} = 0$. The overall agreement is very good. The slightly higher barrier for the SRKM at $\tau = 0$ seen previously is again evident, but the absolute difference then decreases with increasing stress.

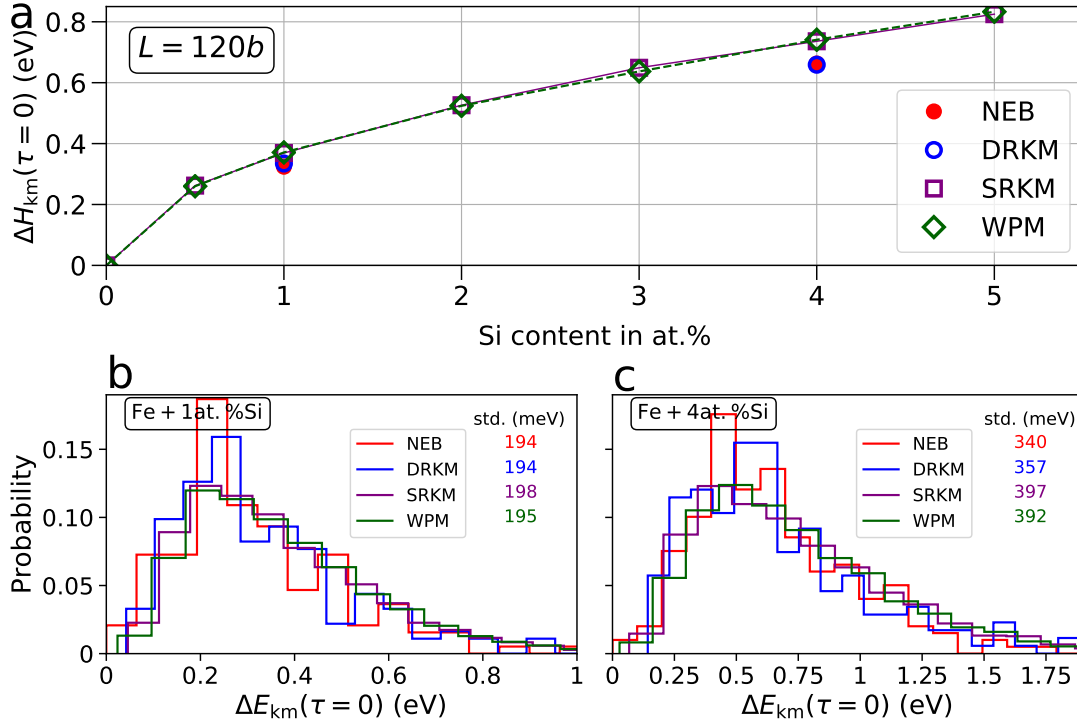


Figure 5.5 – **Comparison of the results of the kink migration barrier as obtained by NEB and developed models.** (a) Average kink migration barrier ΔH_{km} versus Si solute concentration at zero stress as obtained from NEB, the Discrete Random Kink Model (DRKM), the Stochastic Random Kink Model (SRKM), and the Wiener Process Model (WPM). The distributions of kink migration barriers ΔE_{km} associated with each models for 200 Fe-1at.%Si and 200 Fe-4at.%Si realizations are also shown, with the standard deviations indicated.

5.3.1 Kink migration under stress: a Wiener Process

The fluctuating energy landscape of a single kink migrating through a random field of solutes over a distance z has several key features: (i) the mean energy change over all possible fluctuations in the solute positions is zero, (ii) the standard deviation of the energy changes due to the fluctuations in the spatial arrangement of solutes scales with \sqrt{z} , and (iii) the incremental energy change during kink migration over a distance $z_{c2} - z_{c1} \approx 1.5w^*$ is a stochastic variable. The decorrelation distance of $1.5w^*$ is obtained by examining the correlation function between two kinks separated by $z_{c2} - z_{c1}$, which decreases rapidly from ~ 0.21 at w^* toward zero (~ 0.02) at $1.5w^*$. These features also appear in the random-walk "Wiener process" [36] and so the known solution of the Wiener process can be adapted to address kink migration.

The Wiener process is a continuous-time random walk in which the increments (in our case the energy changes as the kink migrates) are independent. Here, the kink energies become essentially independent after motion by the decorrelation distance $1.5w^*$. In the presence of an applied stress, the kink migration is then similar to the "Wiener process with drift" where

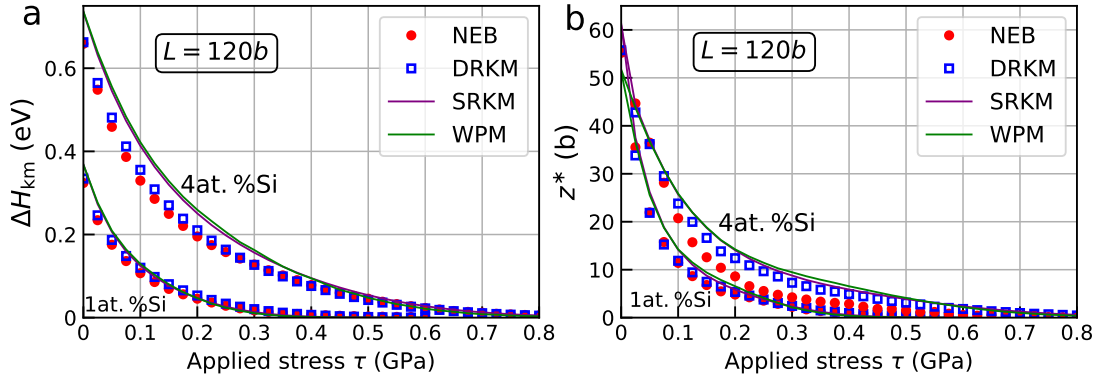


Figure 5.6 – Comparison of the results of the kink migration barriers and activation distances at different applied stress as obtained by NEB and developed models. (a) Average kink-migration barrier ΔH_{km} and (b) average activation distance z^* versus applied stress τ in model Fe-1at%Si and Fe-4at%Si alloys as obtained from NEB, the Discrete Random Kink Model, the Stochastic Random Kink Model, and the Wiener Process Model.

there is a constant-magnitude bias introduced in each step of the random walk. The Wiener process does not appear to capture all the statistical fluctuations of the real energy landscape on the scale of b but it is verified below to capture the all-important mean energy barrier as a function of τ and L . From here on, we will use a normalized kink width $\bar{w} = 1.5w^*/b$ to reduce the notation.

To validate the Wiener process as applied to the kink migration problem, we first execute stochastic simulations at the increment scale of \bar{w} as follows and as shown schematically in Figure 5.1e. A dislocation of length L is first divided into $N = L/(b\bar{w})$ sections, each of which is assigned an energy $\Delta\tilde{E}_p \bar{w}^{1/2} \times R_i$ where R_i is a random number selected from a normal distribution with mean zero and standard deviation of unity. A bias energy of $(-ab^2\bar{w})\tau k$ is then added to the k -th segment centered on $z_c/b = k\bar{w}$. The discrete kink-migration energy landscape sampled at discrete $b\bar{w}$ intervals can then be written as

$$\Delta E(k\bar{w}) = \Delta\tilde{E}_p \bar{w}^{1/2} \sum_{i=1}^k R_i - (ab^2\tau\bar{w})k, \quad k = 1, 2, \dots, L/(b\bar{w}) \quad (5.7)$$

This model is called the Wiener Process Model (WPM).

At zero stress ($\tau = 0$), we compare the mean and standard deviations of the barrier distributions predicted by the WPM against the SRKM for $L = 120b$ ($N = 16$), as shown in Fig. 5.5. The agreement is essentially perfect. The mean energy barrier versus applied stress as predicted by the WPM is shown in Fig. 5.6, and again excellent agreement with the SRKM is obtained. To further validate the WPM, we considered longer migration lengths $L/b = 200, 400, 800$ and a range of relevant concentration and stress levels. The comparison between the WPM and the SRKM is shown in Figure 5.7, and again the agreement is excellent. *Hence, the physical problem of kink migration in a random solute environment and under stress is quantitatively*

captured by the random walk Wiener process with drift.

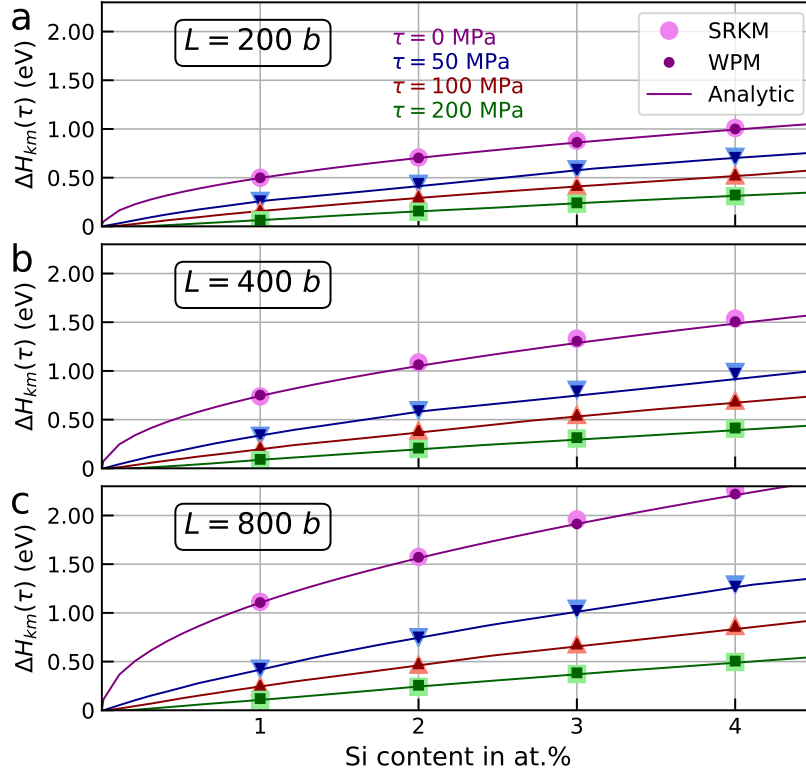


Figure 5.7 – **Model predictions for single kink migration barrier for long migration distances.** Single-kink migration barrier ΔH_{km} versus Si concentration as predicted by the SRKM, WPM, and analytic result, Eq. (5.10), at various applied stresses τ as indicated for migration distances L of (a) $200b$, (b) $400b$, and (c) $800b$ in the model Fe-Si alloys.

We now make the final step to an analytic model, eliminating entirely the need for any stochastic simulations. The analytic model will then enable direct applications of the model to any system under any experimental conditions (temperature, strain rate, stress, dislocation density) in terms only of the underlying material parameter $\Delta \tilde{E}_p$, $w^* = w/2$, and L . Specifically, Magdon et al. [90] showed that the mean maximum minus minimum of the continuous Wiener process could be written as $-\frac{2\sigma^2}{\mu} Q_p\left(\frac{\mu^2 N}{2\sigma^2}\right)$ where $Q_p(x)$ is a tabulated function and σ and $\mu \leq 0$ are the standard deviation and the drift bias of the process and N denotes the total number of uncorrelated steps. Applied to the kink migration problem, $\sigma = \Delta E_p \bar{w}^{1/2}$, $\mu = -ab^2 \bar{w} \tau$, and $N = L/(b\bar{w})$. When these relationships are substituted into the result of

Magdon et al., we obtain

$$\begin{aligned}\Delta H_{\text{km}} &= \frac{2\Delta\tilde{E}_p^2}{ab^2\tau} Q_p \left(\frac{a^2 b^4 \tau^2 L/b}{2\Delta\tilde{E}_p^2} \right) \\ &= 2\Delta\tilde{E}_p \frac{\tau_c}{\tau} Q_p \left(\frac{\tau^2}{\tau_c^2} \frac{L}{2b} \right); \quad \tau_c = \frac{\Delta\tilde{E}_p}{ab^2},\end{aligned}\tag{5.8}$$

where the characteristic stress τ_c is the stress required to overcome a single typical kink energy difference $\Delta\tilde{E}_p$ over unit glide distance b . Interestingly, the kink width \bar{w} no longer appears in the barrier, and the barrier scales directly with the fundamental energy $\Delta\tilde{E}_p$. This result demonstrates why the WPM and SRKM are essentially identical at lengths $L/b \gg 1$.

The kink migration is discrete, and the discrete-time Wiener process involves an additional correction term that is a function of σ and the discrete interval length (here \bar{w}) [128]. The Wiener process also does not nominally apply when the activation distance is $z^*/b < \bar{w}$. We can thus derive a correction factor by imposing the requirement that the energy barrier at the minimum WPM distance $L/b = \bar{w}$ is zero at the stress $\tau = \frac{\Delta\tilde{E}_p \sqrt{\bar{w}}}{ab^2 \bar{w}}$ that is needed to overcome the average single-step barrier in the WPM. This leads to a correction factor $-2Q_p(\frac{1}{2})\Delta\tilde{E}_p \sqrt{\bar{w}}$. The coefficient $-2Q_p(\frac{1}{2}) = -0.926$, however, does not yield sufficiently agreement with the simulations and so we fit the numerical prefactor as -1.24 to best-match the WPM simulations, obtaining

$$\Delta H_{\text{km}} = \Delta\tilde{E}_p \left[2 \frac{\tau_c}{\tau} Q_p \left(\frac{\tau^2}{\tau_c^2} \frac{L}{2b} \right) - 1.24 \bar{w}^{\frac{1}{2}} \right]\tag{5.9}$$

The function $Q_p(x)$ with $x \equiv \frac{\tau}{\tau_c} \sqrt{\frac{L}{2b}}$ remain tabulated only. However, we can accurately ($\sim 2\%$) approximate $Q_p(x^2)x^{-1} = 1.63(x + 1.91)^{-1} + 0.025$ over the full range of x relevant in applications. Hence, a fully-analytic result for the kink migration barrier is then, after a bit of algebra, obtained as

$$\Delta H_{\text{km}} = \Delta\tilde{E}_p \left[3.26 \left(\frac{\tau}{\tau_c} + \frac{2.7}{\sqrt{L/b}} \right)^{-1} + 0.035\sqrt{L/b} - 1.07\sqrt{w/b} \right]\tag{5.10}$$

where we have also reverted to using the true kink width w . The results of the analytical solution, Eq. (5.10) for relatively short dislocation segments of $L/b = 200, 400$, and 800 versus the Si concentration at various applied stresses are shown in Fig. 5.7. Excellent agreement is obtained with the previous stochastic simulations which demonstrates the accuracy of this fully analytical solution. Introducing the correction factor introduces a very small error in the activation volume $V_{\text{act}} = z^* ab$, as discussed in A.4.

Before comparing the analytic model to more simulations with longer dislocation lengths, we discuss the final step of connecting the kink migration model to the double-kink nucle-

ation/kink migration problem of physical interest. In the real physical problem, two kinks are nucleated and migrate away from each other. The implicit assumption in essentially all models of the overall plasticity process is that the next double-kink nucleation and kink migration event should only occur after the previous process is complete. Retaining this assumption, each of the two kinks experiences a similar statistical process but the migration distances L_{right} and L_{left} are different because the double-kink nucleation may occur anywhere along the total length $L = L_{\text{right}} + L_{\text{left}}$ with equal probability. Since the migration barrier increases with L , the kink with the longer migration path will typically encounter the largest barrier, and hence be the slowest process. The larger of the two sections is then randomly distributed in the range $(L/2, L)$ with an average of $3L/4$.

We thus adapt the SRKM to account for the double-kink nucleation process. For a dislocation of length L with stochastic energies assigned for each section of width b , we use the solute/double-kink interaction energy developed in [51] to find the most favorable nucleation site along the entire line. The left and right kinks are nucleated at this location and the kinks migrate through their remaining landscapes of lengths L_{right} and L_{left} , respectively. The energy landscape for each kink is computed (Eq. 5.6) from which the stress-dependent kink migration barrier $\Delta E_{km}(\tau)$ is computed. We perform twenty thousand realizations for three dislocation lengths $L/b = 500, 1000, 2000$. For each realization, we determine the right and left migration distances L_{right} and L_{left} and the two associated migration barriers. The relevant barrier is the one corresponding to the longer of the lengths L_{right} and L_{left} . Although there are cases where the largest barrier is found along the shorter path, their effects on the mean migration barrier are negligible (a few %). We thus apply the WPM at the mean $3L/4$ of the longest segment, leading to $N = L/w$. The results of the SRKM and WPM models are shown in Fig. 5.8, and excellent agreement is obtained. Finally, Fig. 5.8 also shows the analytical result for the mean migration barrier, Eq. (5.10). The agreement is again excellent, demonstrating the accuracy of the fully analytical solution in this regime.

5.4 Applications

The analytic theory of kink-migration has been extensively verified against simulations. This enables us to apply the theory with confidence to real BCC alloy systems in the dilute limit. Here we combine the kink migration theory with our recent double-kink nucleation theory to examine the transition from solute softening to solute strengthening in several dilute binary alloys. The challenges in comparing predictions to experimental data mostly lie in obtaining accurate input data, especially the solute/screw interaction energies, and accurate experimental results.

Experiments measure yield strength versus temperature and/or strain rate. Results here for the activation barrier are thus related to experiments via a standard thermally-activated Arrhenius model and Orowan's law. The total rate of dislocation motion in terms of the rates r_{dk} for

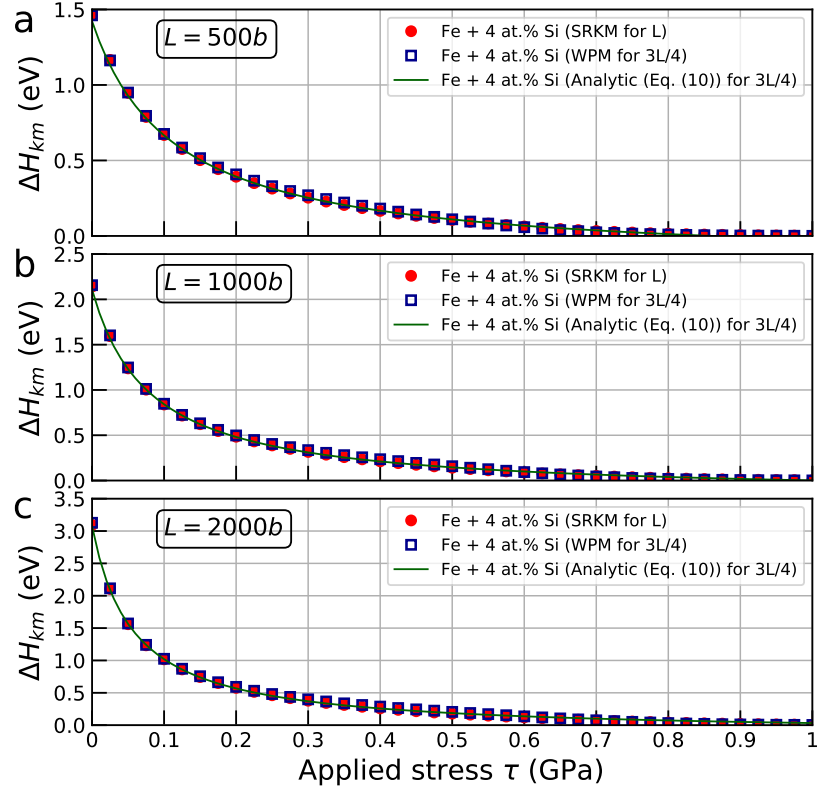


Figure 5.8 – **Model predictions for single kink migration barrier for very long migration distances.** Migration barrier ΔH_{km} as computed by the SRKM, WPM, and fully-analytic theory versus applied stress τ for dislocations with length L (a) $500b$, (b) $1000b$, and (c) $2000b$ in Fe-4at.%Si model alloy.

double-kink nucleation and r_{km} for kink migration is

$$r = \left(\frac{1}{r_{dk}} + \frac{1}{r_{km}} \right)^{-1}. \quad (5.11)$$

Under almost all conditions, either r_{dk} or r_{km} dominates the rate and thus the total rate is expressed as

$$r = v_0 \exp\left(-\frac{\Delta H(\tau)}{kT}\right), \quad (5.12)$$

where the rate-controlling $\Delta H(\tau)$ is the larger of the double-kink nucleation and migration barriers and v_0 is an appropriate attempt frequency [171]. As noted in the introduction, the temperature- and stress- plastic shear strain rate $\dot{\epsilon}$ at applied stress τ follows from Orowan's law as $\dot{\epsilon} \approx \rho \bar{v}$ and hence

$$\dot{\epsilon} = \dot{\epsilon}_0 \exp\left(-\frac{\Delta H(\tau)}{kT}\right), \quad (5.13)$$

Chapter 5. Kink migration in dilute BCC alloys

where $\dot{\epsilon}_0 = \rho b a v_0$ is the reference strain rate. Experiments impose a temperature and strain rate, and hence an experimental enthalpy barrier $\Delta H^{\text{exp}} = k T \log(\dot{\epsilon}_0/\dot{\epsilon})$.

Inverting Eq. (5.10) gives the yield stress required to achieve the imposed experimental enthalpy barrier as

$$\tau(\dot{\epsilon}, T) = \tau_c \left[3.26 \left(\frac{\Delta H^{\text{exp}}}{\Delta \tilde{E}_p} - 0.035\sqrt{L/b} + 1.07\sqrt{w/b} \right)^{-1} - 2.7\sqrt{b/L} \right] \quad (5.14)$$

Eq. (5.14) constitutes our analytical model for the migration-controlled strength as a function of temperature and strain rate. The only inputs to the theory are the solute/dislocation interaction energies that determine $\Delta \tilde{E}_p$, the dislocation line length, and kink width. The reference strain rate appears in a logarithm and thus has modest quantitative effects. Moreover, in real physical problems where the dislocation length is very large, $L \sim 2 \times 10^3 b$, the kink width has rather small effects on final strength predictions.

Double-kink nucleation occurs at one of the most favorable local region of solute fluctuations for the process. At low temperatures when the most-favorable region dominates, the barrier can be written as

$$\Delta H_{\text{dk}}(\tau) = \Delta H^0(\tau) + \Delta \tilde{H}^{\text{sol}}(c, N, \tau). \quad (5.15)$$

Here, $\Delta H^0(\tau)$ is the nucleation enthalpy barrier of the pure matrix which often takes the form of a Kocks law [79] $\Delta H^0(\tau) = \Delta H^0(0)[1 - (\tau/\tau_p^0)^p]^q$ where p and q are fitting parameters and $\Delta H^0(0)$ and τ_p^0 are the zero-stress enthalpy barrier and pure Peierls stress, respectively. The solute contribution $\Delta \tilde{H}^{\text{sol}}(c, N, \tau)$ is the mean largest reduction in activation energy among all the $N = L/2w$ segments, and is [51]

$$\Delta \tilde{H}^{\text{sol}} = \Delta \tilde{E}_p G(\tau) \frac{\log(4\pi \log N) - 4\log N - 1.1544}{\sqrt{8\log N}}, \quad (5.16)$$

where $G(\tau)$ describes the stress-dependent double-kink transition state shape in the pure BCC metal under stress. At higher temperatures, additional regions could contribute to enhance the rate. We will use the full solution, as given in [51], in results shown below using the equations in [51]. Of importance here is that all of the effects of solutes on the nucleation barrier depend on exactly the same material parameters as derived here for the migration barrier ($\Delta \tilde{E}_p$, w , dislocation length L).

With theory for both the migration barrier $\Delta H_{\text{km}}(\tau, L)$ and the nucleation barrier $\Delta H_{\text{dk}}(\tau, L)$, the stress and temperature regimes of the controlling plasticity mechanism can be found. A schematic result of the two barriers versus stress, using parameters for real W-Re (see below), is shown in Figs. 5.9(a),(b), and (c) for W-1%Re, W-3%Re, and W-10%Re, respectively. With increasing solute concentration and at any specified stress, the barrier for nucleation is

decreasing and the barrier for migration is increasing. Experimental conditions of temperature and strain rate determine the accessible barrier as ΔH^{exp} and the highest-strength mechanism controls the strength under those conditions. The experimental barrier at $T=300\text{K}$ and $\dot{\epsilon} = 5.5 \times 10^{-4}/\text{s}$ is shown in the Figs. 5.9. At 1%Re, yield is controlled by double-kink nucleation and is lower than pure W (solute softening). At 3% Re kink migration controls the strength but the double-kink nucleation strength is only slightly lower; the alloy is still softer than pure W. At 10% Re, the kink migration continues to control the strength, with the double kink nucleation stress now being much lower. This demonstrates the transition in mechanism. Furthermore, at 10% Re, the alloy is stronger than pure W, demonstrating solute strengthening. At a higher temperature, ΔH^{exp} is higher and both the mechanism transition and onset of strengthening relative to pure W occur at a lower concentration. For example, but not shown, at $T=650\text{K}$ ($\Delta H^{\text{exp}} = 936\text{meV}$), the strength of W-3% Re is migration controlled and slightly larger than that of pure W.

5.4.1 Fe-Si alloys

Experimental yield stresses for Fe-Si (0.52 at%, 1.3 at%, 3.2 at%, and 5 at%) alloys versus temperature at a strain rate of $1.7 \times 10^{-4}\text{s}^{-1}$ were reported by [78]. Other data by [23] at 1 and 4 at%, shown previously [49], is slightly lower than the data used here, and so the experimental results are not definitive. For predictions, we use a reference strain rate of 10^4s^{-1} , a dislocation density of $\rho = 10^{12}\text{m}^{-2}$ [162] and kink width $w = 12b$ [51] obtained by GAP for pure Fe [95]. The solute/dislocation interaction energy parameter $\Delta \tilde{E}_p = 178\sqrt{c}\text{meV}$ was obtained previously by Maresca et al. [94] as the value needed to fit data at 5at% using their non-dilute theory, with good agreement of that model at all higher concentrations. The interaction energy parameter differs from that of the model Fe-Si EAM potential because the EAM potential is not quantitative for real Fe-Si.

Fig. 5.10 shows the strength vs. temperature as measured and as predicted by various mechanisms. The data for pure Fe is shown for reference. The predictions are made for the kink migration model presented here, the double-kink nucleation model (Eqs. (9),(14),(20) [51]), and also the non-dilute model of Maresca et al. applied at these lower concentrations. The strength-controlling mechanism is the mechanism with the highest strength at a given concentration and temperature. At the low concentrations of 0.52 at.%, double-kink nucleation is the controlling mechanism, with both kink migration strength and the non-dilute theory being much lower than experiments; the theory predicts almost no solute effects while experiments appear to show a slight strengthening (but see Ref. [49]). At 1.3 at.%, double-kink nucleation continues to control strength over nearly the entire temperature range. However, both kink migration and the non-dilute theory are close to the nucleation strength near $T=300\text{K}$. At 3.2 at.%, a transition in mechanism is predicted. The kink migration strength is higher than the double-kink nucleation strength over the entire temperature range. The experiments show a clear strengthening at higher T , consistent with predictions but slightly higher. At this concentration, in spite of different contributions to the total strengthening, the non-dilute

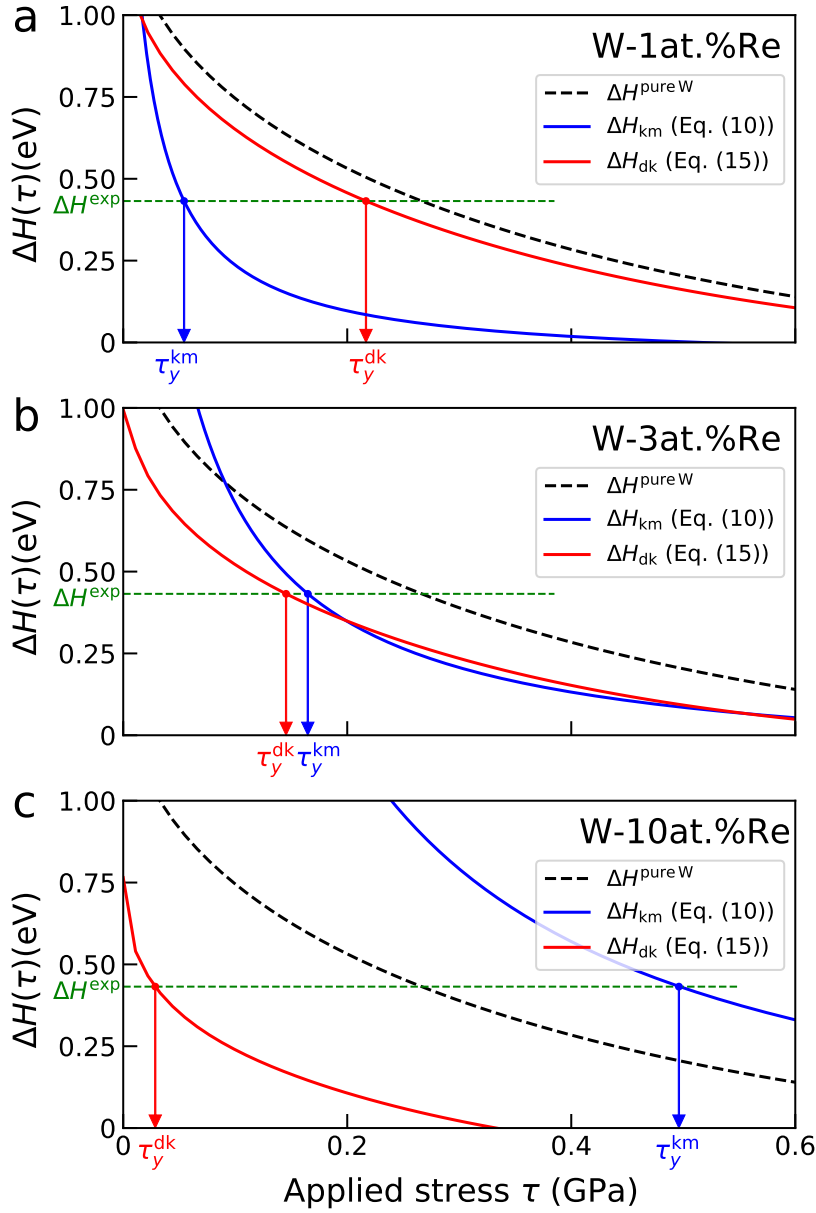


Figure 5.9 – Prediction of double-kink and kink migration barriers for W-Re alloys. Predicted barriers for double-kink nucleation ΔH_{dk} (red) and kink-migration ΔH_{km} (blue) versus applied stress τ , using parameters for W-Re at (a) W-1%Re, (b) W-3%Re, and (c) W-10%Re alloys. For illustration, an experimentally imposed $\Delta H^{\text{exp}} = 0.43$ eV corresponding to $T=300\text{K}$ and $\dot{\epsilon} = 5.5 \times 10^{-4}/\text{s}$ is shown and the strength of each mechanism is indicated. The higher strength sets the alloy yield stress. A transition from double-kink nucleation to kink migration control of the strength is observed with increasing Re concentration. The barriers and strength for pure W are also shown, illustrating regimes of alloy softening and hardening relative to pure W.

strength is predicted to be nearly identical to the kink migration strength, with differences

only at very low T . The nucleation-to-kink-migration and dilute-to-non-dilute transitions thus occur at essentially the same concentration. Then, at the higher concentration of 5.0 at.%, the alloy strength is significantly higher than that of pure Fe, the kink migration strength is also much higher but below the experiments, and the non-dilute theory captures the experiments with $\Delta\tilde{E}_p$ having been fit to this data.

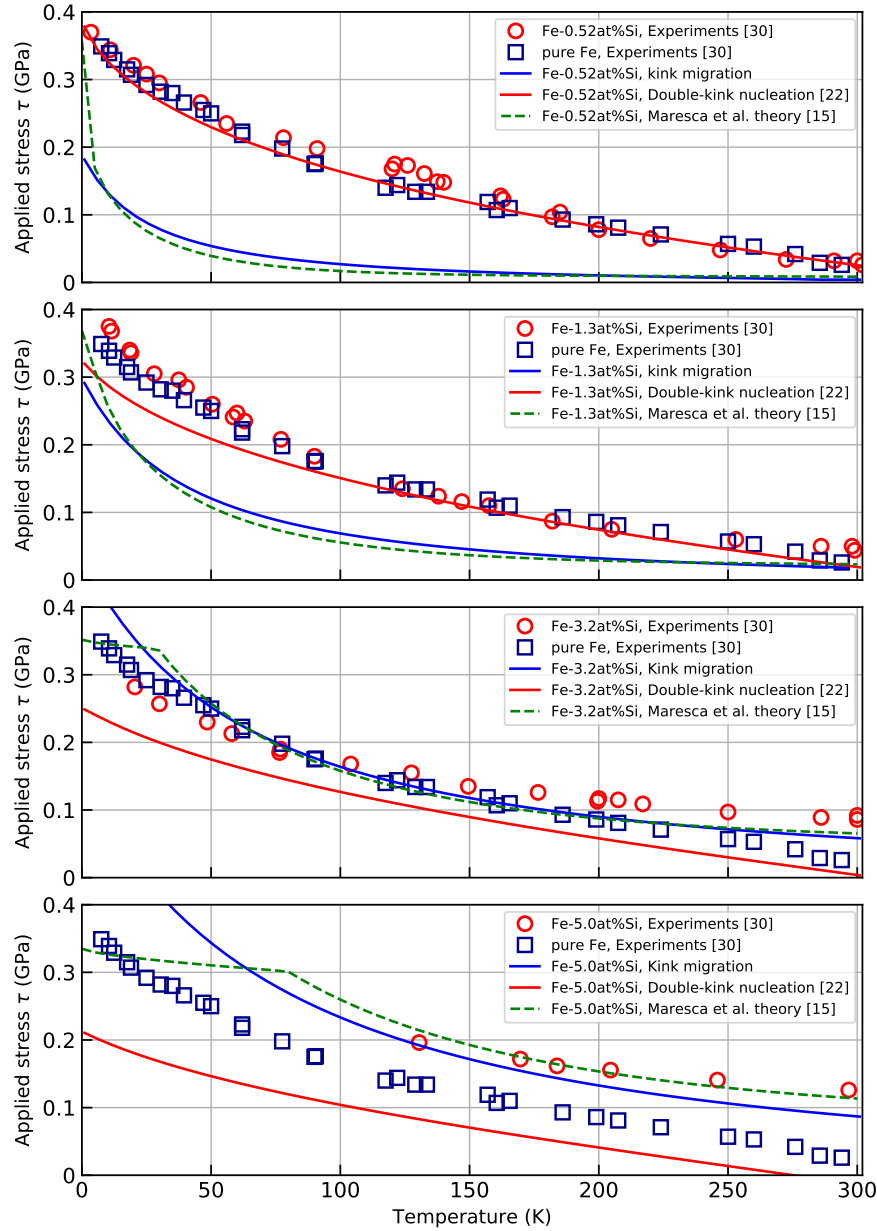


Figure 5.10 – **Theory predictions for dilute $\text{Fe}_{1-x}\text{Si}_x$ alloys.** Yield strength versus temperature, as predicted for the double-kink nucleation model, kink migration model, and non-dilute model, $\text{Fe}_{1-x}\text{Si}_x$ alloys at the concentrations shown.

As discussed previously, other literature data on Fe-Si shows very small softening at 1%Si

and slightly less strengthening at 4at%, both being more consistent with theory. With such uncertainties in the experiments, we consider the parameter-free predictions here to capture the major trends versus temperature and concentration quite well. We also conclude, however, that there is only a very narrow concentration around 3at% where the kink migration mechanism may control strength but where the non-dilute mechanisms give nearly identical results. Thus, while increasing Si in Fe-Si shows very weak (if any) softening followed by hardening, the traditional transition from nucleation to migration is quickly superseded by the non-dilute theory/mechanisms.

5.4.2 W-Re alloys

We now turn to the W-Re system and examine the yield stress of this alloy over a wide concentration range and temperatures $T=150\text{K}$, $T=300\text{K}$, $T=590\text{K}$, and $T=700\text{K}$. Experimental data are reported by [153] and [118] which were performed at nearly identical strain rates of $5.5 \times 10^{-4}\text{s}^{-1}$ and $8.3 \times 10^{-4}\text{s}^{-1}$. We again take $\rho = 10^{12}\text{m}^{-2}$ ($L = 1\mu\text{m}$), as a typical value for well-annealed metals, and $\dot{\epsilon}_0 = 10^4\text{s}^{-1}$. The kink width in pure W is taken as $12b$ [51]. The data on pure W reported by [153] is used to fit the Kocks model parameters $\Delta H_0 = 1.4\text{ eV}$, $\tau_p^0 = 1.1\text{ GPa}$, $p = 0.49$, $q = 1.69$. Note that this fit does not have high accuracy due to the limited data but that it only appears in the double-kink migration model and does not affect kink migration predictions. The solute/dislocation interaction energies were computed previously by first-principles DFT [Romaner] from which the solute/dislocation interaction energy is obtained as $\Delta \tilde{E}_p = 345\sqrt{c}\text{ meV}$. Strength is again predicted as the larger of the nucleation and migration strengths. There are no adjustable parameters.

Predictions of the strength versus Re concentration for several temperatures are shown in Fig. 5.11 along with the experimental data. The experiments are not definitive: the two datasets at $T=300\text{K}$ show some differences at low concentrations. Nonetheless, the data generally show a transition from softening to hardening with increasing Re at temperatures up to 590K and no softening at 700K . The theory predicts the transition from softening to hardening at all temperatures, but with very little softening at 700K . The concentration at the transition is predicted to decrease with increasing temperature, as observed for 300K , 590K , and 700K . The experiments at 150K suggest a transition below 3%, with strengthening; this is a significant quantitative deviation between experiment and theory that remains unexplained. However, the experiments and theory at $T=300\text{K}$ suggest a transition around 3%, and there is no mechanistic theory that would predict that the transition concentration increases with increasing temperature, so the experiments at $T=150\text{K}$ and 3% Re are inconsistent with any model. The 7at.%Re alloy is predicted to be in the strengthening regime at all the temperatures studied (300 , 590 , 700K) and there is very good quantitative agreement with available experiments.

Predictions of the non-dilute theory of Maresca et al. [94] at 7at.%Re are also shown in Fig. 5.11, and also agree very well with experiments and the kink migration strength. Thus, as for Fe-Si around 3%Si, there is also a concentration domain in W-Re (7% Re) where dilute and

non-dilute theories give very similar results, indicating a smooth transition.

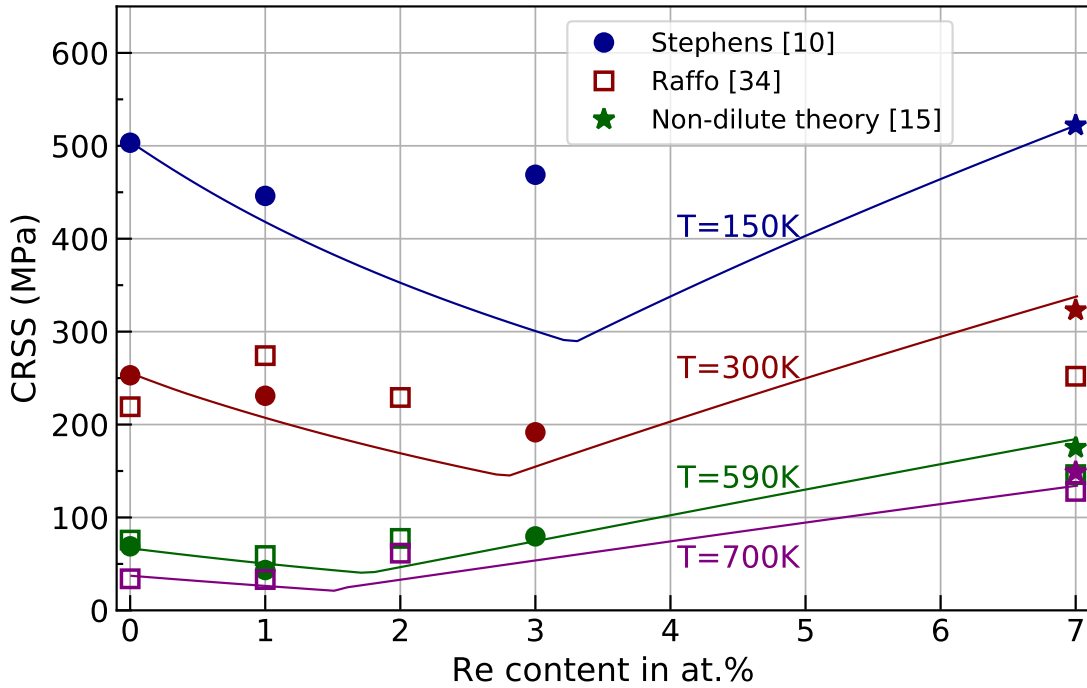


Figure 5.11 – **Theory predictions for W-Re alloys.** Critical resolved shear stress (CRSS) versus solute concentration at various temperatures (blue: $T=150\text{K}$; red: $T=300\text{K}$; green: $T=590\text{K}$; purple: $T=700\text{K}$) for dilute W-Re alloys. Experiments (filled symbols: data from Stephens [153]; open symbols: data from Raffo [118]); present theory (solid lines); non-dilute theory at 7%Re [94] (bold ★ symbols)

Overall, the predictions for W-Re are in good quantitative and qualitative agreement with the totality of available experiments. Note that no material parameters (beyond those for pure W) were fitted to achieve this level of agreement. The parameters were chosen based on independent considerations. Hence, we consider the predictions of the essentially parameter-free fully-derived statistical models for double-kink nucleation [51] and kink migration (this work) to be quite good.

5.5 Discussion

We have developed an analytical theory for the stress-dependent kink migration barrier in random dilute BCC alloys. We have shown that the kink migration process under stress is essentially the random walk-type "Wiener process with drift". The material parameters in the theory are only (i) the solute/screw dislocation interaction energies leading to a single relevant energy quantity $\Delta\tilde{E}_p$, (ii) the total dislocation length L , and (iii) emerging to a play a minor role, the kink-width w in the pure metal. The theory has been extensively validated on a model Fe-Si alloy via NEB calculations and direct stochastic simulations. Combined

with a recent double-kink nucleation theory that involves the same material quantities, we have thus established a fully-analytic model for strengthening of screw dislocations over the full temperature range in the dilute regime concentration. A transition from double-kink nucleation and softening to kink-migration and strengthening is predicted with increasing temperature and/or concentration. We also find a smooth transition from the dilute theory to a recent non-dilute theory in application to both Fe-Si and W-Re alloys.

Our derived theory rationalizes some results from the Suzuki model. At high temperatures, corresponding to low stresses, the second and third terms in the bracket of Eq. (5.10) can be neglected. Also, in real alloys the dislocation segments length are typically large and so $\frac{\tau}{\tau_c} \gg 2.7\sqrt{\frac{b}{L}}$. Then, setting the barrier equal to the experimental $\Delta H = kT \log(\dot{\epsilon}_0/\dot{\epsilon})$, the strength versus temperature can be estimated as

$$\tau \simeq \alpha' \frac{\Delta \tilde{E}_p^2}{kTb^3}, \quad (5.17)$$

where α' is nearly constant. The yield strength thus decreases as $\approx 1/T$ and increases linearly with solute concentration since $\Delta \tilde{E}_p^2 \propto c$. This rationalizes Suzuki's high-T estimate [158]

$$\tau \simeq \alpha \frac{E^2 c}{kTb^3}, \quad (5.18)$$

The agreement in scalings with T and c arises because Suzuki's counting of the fluctuations in total solutes passed as the kink glides over long distances is captured correctly. However, E and α differ from $\Delta \tilde{E}_p$ and α' , leading to both qualitative and quantitative differences.

Existing kMC methods have also made simplifying assumptions about the solute/screw interactions and the kink structure. For instance, [147] show schematics of a sharp kink (pure edge) so that kink glide corresponds to very few solutes entering the advancing screw segments. In a real kink, extending over $10 - 20b$, the change in energy due to solutes entering and leaving the kink is more gradual (spread over $\sim 1/2$ the kink width). Our SRKM and WPM analysis demonstrate that the effect of the kink width is fairly small, especially at higher temperatures. The kink width is, however, critical for double-kink nucleation. Thus, kMC approaches to tackling the overall problem of nucleation and migration should include details such as accurate interactions and accurate representation of the kinks and double-kink nucleation process.

The motion of screw dislocations in BCC High Entropy Alloys has emerged as an important and challenging issue for theory. One contribution to the strengthening is due to kink migration barriers. Recent work has shown that screw motion in complex alloys depends on a generalized form of $\Delta \tilde{E}_p$ [171, 94, 93] as

$$\Delta \tilde{E}_p = \left(\sum_{i,j} \sum_n c_n \Delta U_{ij}^n(a)^2 \right)^{\frac{1}{2}}, \quad (5.19)$$

where all atom types n are considered solutes, c_n is the concentration of atom type n , and ΔU_{ij}^n

is the change in interaction energy of a type- n solute at position (x_i, y_j) with the dislocation of the average alloy (see [173, 94]) as the dislocation glides by a . The results here do not directly apply to screw controlled HEAs because HEAs adapt to the local energy landscape by forming kinks spontaneously along their length. The dislocation segments are in low-energy environments rather than random environments, and this must be accounted for in assessing kink glide. These aspects will be discussed in future work. We further note that the strengthening in HEAs may be controlled by edge dislocations rather than screw dislocations [93], making the kink migration process irrelevant.

The present theory applies within the standard approximation that solute interactions are weak enough for (i) screw motion to occur one Peierls valley at a time and (ii) the screw core structure is not altered by the solutes. The present analysis can be adapted to address the first assumption, but that is well beyond the scope of the present work. The second approximation has been found suitable for most substitutional solutes but not for interstitial solutes such as C, N, and O [89, 122, 59]. Interstitial interactions in the core can also be very large such that even the annihilation of two kinks converging at the site of the interstitial is not sufficient to overcome the interstitial interaction energy. Thus, multiple kinks are required. These issues are beyond the scope of the present work, but the concepts here can be generalized to address some aspects of interstitial strengthening.

In summary, our nucleation and migration models provide a complete, accurate, and nearly analytical statistical theory of strengthening in dilute substitutional BCC alloys. The set of material properties is small, and the same properties enter both double-kink nucleation and kink migration theories. While obtaining these properties remains challenging, we believe the theory here cements the long-sought quantitative understanding of strengthening in dilute BCC alloys.

Strengthening mechanisms in high-entropy BCC alloys

Part III

6 Screw-controlled strength of BCC non-dilute and High-Entropy alloys

This chapter is extracted from the following publication

Ghafarollahi, Alireza, and William A. Curtin. "Screw-controlled strength of BCC non-dilute and High-Entropy alloys." *Acta Materialia* (2022): 117617.

Owing to their impressive mechanical properties including high yield strength at room temperature, high ultimate strength, high ductility, high fracture toughness, or superior mechanical performance at high temperatures, HEAs have recently attracted considerable attention from the mechanics and materials science communities [142, 198, 169, 99, 47, 46]. Unlike conventional alloys, HEAs are composed of many (4, 5, or more) elements all at non-dilute concentrations [193]. The immense composition space opens the possibility for discovery of many more new alloys with even better performance in one or more properties. Any such discovery can be greatly facilitated by theoretical understanding that provides guidance for identifying the most promising alloy families and compositions.

The mechanisms of strengthening in BCC HEAs differ significantly from their dilute counterparts. Dilute alloy strength is controlled by the nucleation of double kinks and then kink migration along long straight screw dislocations. In non-dilute alloys, Suzuki [158] postulated that kink formation is easy while Maresca et al. [94] showed that screw dislocations become spontaneously kinked at zero load and zero temperature so as to lower their total energy due to solute/screw-dislocation interactions. The kinked structure forms because the dislocation finds local regions of favorable random concentration fluctuations that lower the dislocation energy in spite of the energy cost of the kinks. Kinks along a single dislocation can also form on different glide planes. When these kinks intersect during kink migration, high-strength cross-kinks are formed that must be overcome. The screw-controlled strength of the alloy is thus controlled mainly by the processes of kink migration and cross-kink formation and pinning. At low temperatures, a Peierls-like motion that can supplant kink migration. Each of these processes have their own length and energy scales, and thus have different consequences on the overall temperature- and strain-rate-dependent strength of the alloy. In some BCC

HEAs, Maresca et al. also showed that edge dislocations can be significantly strengthened [93, 81, 83] making edge motion competitive or exceeding screw strengthening. Here, we focus on the screw dislocation motion.

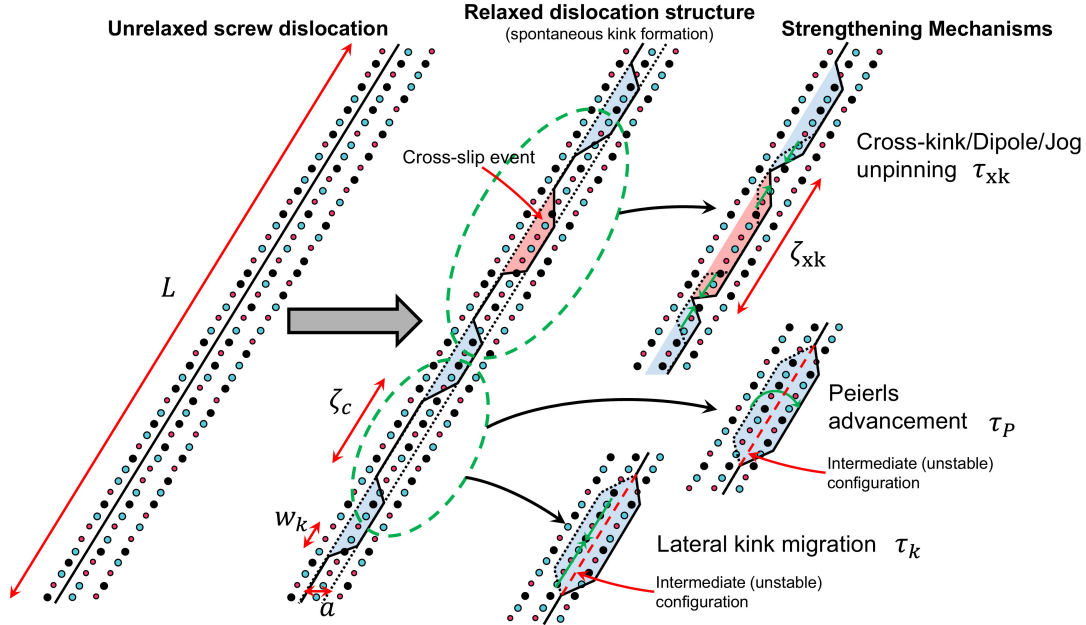


Figure 6.1 – **Structure and motion of a screw dislocation in a non-dilute random solute environment.** An initially straight dislocation of length L in a random solute environment becomes spontaneously kinked which are spaced by a characteristic length ζ_c . Three mechanisms contribute to the screw dislocation strengthening; (I) Peierls-like mechanism (II) kink glide mechanism, and (III) cross-kink formation and unpinning (adapted from [94]).

The analysis of kink glide barriers in [94] was developed based on an incorrect focus on the local interactions of a screw kink with its surrounding solute environment. First, the solute/kink interaction energy therein is not consistent with the recent atomistically-verified model developed in [48]. Fortunately this error still results in some of the correct scalings in the problem. Second, migration of the kink was considered using only the solute/kink energy of the kink at its current position, whereas a proper analysis must consider the total accumulated energy change during kink glide. The kink migration energies were then obtained only through stochastic simulations that were fitted to an ad-hoc analytic form. The resulting theory of Maresca et al. enabled, with the use of limited fitting, quite good agreement with a number of experiments on well-studied non-dilute binary alloys. In spite of any success, these two theoretical issues, once recognized, require attention and rectification.

The purpose of this Chapter is to re-examine the kink migration barriers by generalizing our

new accurate and atomistically-validated analysis of kink migration in dilute alloys. While deriving a new model for the kink migration process in non-dilute alloys, we will then retain many key aspects of the Maresca et al. model, especially those related to the length scales for spontaneous kinking, cross-kink formation, cross-kink failure, and the Peierls motion, for the overall strengthening. We do not see a need to re-evaluate these other features of the Maresca et al. model, although future studies might demonstrate aspects that should be re-assessed. Kink migration is then shown to be essentially described by the random walk-type "Wiener process with drift", enabling analytic results for kink migration. Application of the revised model shows, surprisingly but fortunately, exceptionally good agreement with the model of Maresca et al. under most circumstances. The new analytic formulation provides, however, a solid theoretical footing for future applications and should replace the Maresca et al. model as the benchmark model for screw motion in multicomponent BCC alloys.

In section 6.1 of this Chapter, we review the entire Maresca et al. screw strengthening theory and discuss the shortcomings of their kink migration model in detail. A statistical model for the kink migration barrier versus the applied stress is presented in section 6.2, resolving issues of the previous model. Section 6.3 presents applications of the theory and comparison with experiments on Fe-Si, Nb-Mo, and Nb-W alloys. In the last Section 6.5 of this Chapter, we compare the precise kink migration model to the previous models of Maresca et al. and Suzuki, which has been adapted to HEAs by Rao et al. [120, 123], demonstrating the qualitative and quantitative issues in those earlier formulations.

6.1 Maresca-Curtin model for screw strengthening in non-dilute alloys

Here we provide a brief overview of the previous screw strengthening theory for non-dilute to high-entropy alloys [94] with a focus on the problematic kink migration. Again, we do not re-evaluate most aspects of this model because, beyond the kink migration model, the other aspects appear robust. We consider a random alloy containing N solute types each at concentration c_n ($n = 1, 2, \dots, N$). For a given true random alloy, there is a conceptual homogenized reference alloy that has all the macroscopic properties of the alloy but is composed of a single "average" atom. In particular, the reference "average" alloy has the same lattice constant, elastic constants, stacking fault energies, average screw kink formation energy, and other relevant properties, and is only lacking the effects due to the atomic scale randomness. The individual true elemental atoms are then considered as solutes residing within this average alloy matrix. Starting from the average alloy containing a screw dislocation and introducing the solutes, there is an interaction energy between a solute and the dislocation. Let U_{ij}^n denote the interaction energy of a type- n solute located at position (x_i, y_j) with a screw dislocation at the origin $x = y = 0$ aligned along z . When the straight dislocation glides by one Peierls valley distance a , the change in interaction energy between the solute and dislocation is $\Delta U_{ij}^n = U_{i-1,j}^n - U_{ij}^n$. In a random alloy, solutes exist at every site in the alloy and there is a collective solute/screw interaction energy. On average over all possible random solute arrangements, this energy is

zero. The motion of the screw dislocation thus depends on the fluctuations in solute/screw interaction energy as the dislocation glides by a distance a . Thus, as derived earlier [51, 94], the relevant scale for variations in the dislocation energy is the solute/screw interaction energy parameter

$$\Delta \tilde{E}_p = \left(\sum_{i,j} \sum_n c_n \Delta U_{ij}^n (a)^2 \right)^{\frac{1}{2}} \quad (6.1)$$

In the presence of all of the random solutes, an initially straight screw dislocation does not remain straight (Fig. 6.1). Rather, due to the solute energy fluctuations that scale as $\Delta \tilde{E}_p$, the dislocation will be attracted and repelled by favorable and unfavorable fluctuations, respectively, along its length. Over a sufficient length, these fluctuations are sufficient to overcome the (high) kink formation energy E_k . As derived in Ref. [94], the initially straight dislocation will thus lower its total energy by spontaneously forming a kinked structure with characteristic length ζ_c

$$\zeta_c = \left(1.083 \frac{E_k}{\Delta \tilde{E}_p} \right)^2 b \quad (6.2)$$

Although ζ_c is the characteristic length in the screw strengthening theory, statistical aspects show that adjacent segments of length ζ_c should often be at the same position, so that the average spacing between kinks is $2.5\zeta_c$. The formation of kink pairs can occur on different glide planes. Adjacent kinks on different planes would form cross-kinks, which is energetically very costly. Thus, kinking on different planes is less frequent, and analysis shows that the average spacing of the cross-kinks is $7.5\zeta_c$. Starting from the kinked structure, the screw dislocation motion is governed by three strengthening mechanisms, each characterized by distinct energy and length scale.

In a Peierls-like mechanism, the entire segment of length $2.5\zeta_c$ advances forward from its initial low-energy position across the adjacent higher-energy position (Fig. 6.1). This mechanism is only active at very low temperatures/high stresses where the dislocation is poised near the Peierls barrier. The energy barrier consists of the intrinsic Peierls barrier ΔV_p of the average alloy barrier plus the barrier due to solutes minus the energy gain by annihilation of two kinks. The stress associated with the Peierls mechanism is

$$\tau_P(\dot{\epsilon}, T) = \tau_{P0} \left[1 - \left(\frac{\Delta H(\dot{\epsilon}, T)}{\Delta E_{b,P}} \right)^{\frac{2}{3}} \right] \quad (6.3)$$

where

$$\Delta H(\dot{\epsilon}, T) = kT \log \left(\frac{\dot{\epsilon}_0}{\dot{\epsilon}} \right) \quad (6.4)$$

is the experimental enthalpy barrier; T and $\dot{\epsilon}$ are the imposed temperature and strain rate,

respectively, and $\dot{\epsilon}_0$ is the reference strain rate. Moreover

$$\tau_{P,0} = \frac{\pi \Delta V_p}{ab} + \frac{0.44 E_k}{ab \zeta_c} \left[1 - \frac{5 \Delta V_p \zeta_c}{20 \Delta V_p \zeta_c + 0.7 E_k} \right], \quad (6.5)$$

$$\Delta E_{b,P} = \frac{(10 \Delta V_p \zeta_c + 0.7 E_k)^3}{(20 \Delta V_p \zeta_c + 0.7 E_k)^2}, \quad (6.6)$$

Dislocation glide and plastic flow also requires breaking of the cross-kinks (see Fig. 6.1). The failure of a cross-kink occurs by the creation of either vacancies or self-interstitials. The energy barriers are thus the vacancy and self-interstitial formation energies. Vacancy formation energies are lower, and so the length scale for failure of these cross-kinks is $7.5 \zeta_c$. The remaining self-interstitial cross-kink spacing is $15 \zeta_c$. The strengths for cross-kink failure of these two processes are considered by Maresca-Curtin to be thermally-activated and thus modeled as

$$\tau_{xk}(\dot{\epsilon}, T) = \tau_{xk,0} \left[1 - \left(\frac{\Delta H}{E_{v/i}} \right)^{\frac{2}{3}} \right] \quad (6.7)$$

where

$$\tau_{xk,0} = \frac{\pi E_{v/i}}{ab \zeta_{v/i}}, \quad (\zeta_v = 7.5 \zeta_c, \zeta_i = 15 \zeta_c) \quad (6.8)$$

Cross-kink strengthening at a specified temperature and strain rate is determined as the larger of the two strengths. Since defects must be formed, the cross-kink strength may actually be athermal, with temperature entering through the vacancy and self-interstitial free energies, but this requires further study.

Finally, lateral glide of the kinks across the straight segments of average length $2.5 \zeta_c$ presents another strengthening mechanism that competes with the Peierls mechanism as schematically shown in Fig. 6.1. Insightfully, Maresca and Curtin recognized that, because the initial screw segments of the spontaneously-kink dislocation are lying in local energy minima, lateral kink migration always faces a net energy barrier of magnitude $2.7 E_k$ across the length $z = 2.5 \zeta_c$; i.e. the net energy lowering due to the spontaneous kinking must always be overcome during kink glide. In addition, there are additional stochastic variations in the kink migration energy as a function of the position of the gliding kink. Maresca and Curtin assumed that (i) these stochastic variations are independent of the overall $2.7 E_k$ energy barrier and (ii) that the stochastic variations were only due to the variations of the *local* kink/solute interactions. That is, as the kink of width w glides through a random solute field, the energy of relevance is the local interaction energy of the kink with the solutes within w . Maresca et al. simulated these energy fluctuations by (i) dividing a long dislocation into slices of width b , (ii) assigning a solute/dislocation interaction energy chosen randomly from a distribution with zero mean and standard deviation $\Delta \tilde{E}_p$, (iii) computing the local solute/screw energy at position z as the sum of the solute/screw energies within $z - w/2$ and $z + w/2$. They then considered an activation distance z^* and computed, from the stochastic simulations, the typical minimum-to-maximum energy

over length z^* . These numerical results were taken to be the kink migration barrier over a length z^* . The barrier $\Delta E_b(z^*)$ was fitted to a convenient but ad-hoc analytic form. This barrier was added to the average energy barrier $2.7E_k z^* / (2.5\zeta_c)$ to obtain a total barrier for motion over z^* . In all, the analysis results in the following fitted analytical form for the energy barrier for kink glide of

$$\Delta H_{km}(\tau) = 1.37\sqrt{w/b}\Delta\tilde{E}_p \begin{cases} \frac{\tau - \tau_b}{\tau_{k,0} - \tau_b} - \log\left(\frac{\tau - \tau_b}{\tau_{k,0} - \tau_b}\right) - 1, & \tau > \tau_b \\ -5.75\frac{\tau - \tau_b}{\tau_{k,0} - \tau_b} \frac{\zeta_c}{w} + \log\left(5.75\frac{\zeta_c}{w} + 1\right), & \tau < \tau_b \end{cases} \quad (6.9)$$

where

$$\tau_{k,0} = \frac{6.3\Delta\tilde{E}_p}{ab^2\sqrt{w/b}} + \tau_b \quad (6.10)$$

$$\tau_b = \frac{1.08E_k}{ab\zeta_c}. \quad (6.11)$$

Here $\tau_{k,0}$ is the zero-temperature flow stress for kink migration process and τ_b is the "back-stress" imposed on the kink due to the global energy change of $2.7E_k$. Table 6.1 summarizes all the notations used in the theory.

Table 6.1 – Symbols defining all relevant quantities in the theory.

Symbol	Meaning
a_0	BCC lattice parameter
a	Peierls valley spacing
b	Burgers vector magnitude
w	kink-width
ζ_c	Characteristic length for solute-induced kink formation
ζ_{xk}	Characteristic length for cross-kink formation
$\Delta\tilde{E}_{b,p}$	Energy barrier for advancing $1.5\zeta_c$ segments
$\Delta\tilde{E}_p$	Solute/screw interaction energy parameter
ΔH	Imposed experimental enthalpy barrier
ΔV_P	Peierls barrier
E_v	Vacancy formation energy
E_i	Self-interstitial formation energy
$\dot{\epsilon}$	Strain rate
$\dot{\epsilon}_0$	Reference strain rate

The broad framework of Maresca and Curtin involving spontaneous kinking to lower the energy, the resulting energy and length scales, and the mechanisms of strengthening, is, we believe, robust. There are no fundamental issues that we can find with the Peierls motion mechanism and cross-kink failure model, although both could certainly be refined further and/or significantly revised if fundamental issues emerge. The kink migration analysis is flawed, however, for the following reasons. First, the overall energy change $2.7E_k$ is embedded

into the overall stochastic process, and the treatment of Maresca and Curtin may not be proper. Second, Maresca and Curtin did not treat the solute/kink interactions using the true kink shape. Third, and by far the most important, the kink migration barrier, under zero or finite stress, is the barrier between a *global* minimum and a *global* global maximum in the total energy of the system over the length $2.5\zeta_c$. The local analysis where the barrier is taken as determined by the deepest *local* minimum and the highest *local* maximum, local minima and maximum being over the scale w is simply not generally correct within the standard framework of thermal activation theory [60].

The predictions of the Maresca-Curtin theory must be recognized as quite good, but that success must thus be understood within the context of a more-robust theory. We note that a similar situation arose for Maresca and Curtin. They discussed the Suzuki model and its extensions to HEAs, which has showed good agreement with some experiments and also capturing some of the behaviors and scalings predicted by the Maresca-Curtin model, but they highlighted some clearly incorrect assumptions and unphysical predictions. The purpose of this Chapter is to derive a new kink migration model for complex alloys that avoids the assumptions in the Maresca-Curtin model and thus rectifies the clear shortcomings of that model, while leading to an analytic result that is easy to apply.

6.2 New theory for kink migration in non-dilute alloys

6.2.1 Energy landscape for kink migration in a random solute environment

We start with the general framework for kink motion in a random alloy that will then be adapted to deal with the spontaneously-kinked situation arising in non-dilute alloys and HEAs. We consider a single kink that is migrating (direction z) across a random solute environment. The kink motion transfers the screw dislocation by one Peierls valley along the glide direction, as shown schematically in Figure 6.2. The atomistic shape of the kinked dislocation can be well described by a hyperbolic tangent function as [157, 74, 48]

$$x(z - z_c; w) = \frac{a}{2} \left(1 - \tanh \left[\frac{2(z - z_c)/b}{w/b} \right] \right) \quad (6.12)$$

where z_c is the center position of the kink and w denoted the kink width. We wish to compute the *total* energy change $\Delta E(z_c)$ of the dislocation/solute system as a function of the center position z_c of the kink as it glides across a length L ($0 < z_c < L$) in a random field of solutes. This requires the interaction energy between a solute and the kink. Following the validated analysis of Ref. [48], the interaction energy between a solute at (x_i, y_j, z_k) with a kink located at z_c is

$$U(x_i, y_j, z_k) = \frac{x(z_k - z_c; w^*)}{a} \Delta U_{ij}(a) + U_{ij} \quad (6.13)$$

where the width $w^* = 0.5w$ is an effective kink width for the interactions (see Fig. 6.2). Final results below will have a very weak dependence on the kink width, however. Kink motion through a random environment is then very well captured by the stochastic rigid-kink model (SRKM) developed in [48]. In the SRKM, a dislocation segment of length $L = Nb$ is divided into N slices of width b . Each slice is then assigned a random energy of magnitude $R\Delta\tilde{E}_p$ where R is a random number selected from a Gaussian probability distribution having zero mean and standard deviation of unity. The energy landscape for the kink can then be written as

$$\Delta E(z_c) = \Delta\tilde{E}_p \sum_{k=1}^{N=L/b} x(z_k - z_c; w^*) R_k \quad (6.14)$$

Note that the fundamental underlying energy scale for kink motion is always $\Delta\tilde{E}_p$. The SKRM model has been validated against full atomistic NEB simulations on dilute alloys but does not itself depend on the dilute limit assumption.

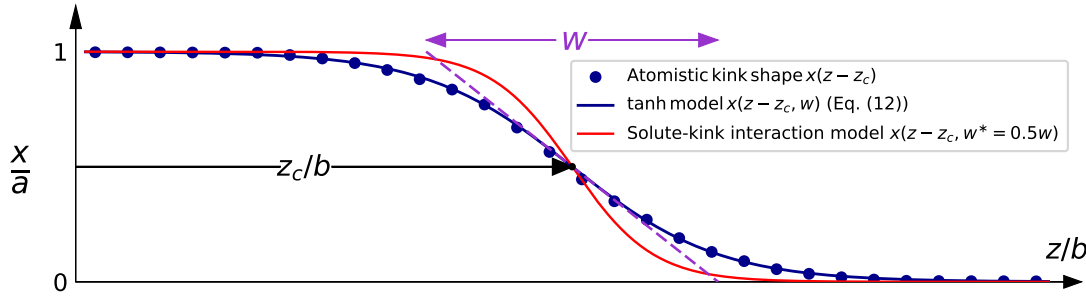


Figure 6.2 – **Schematic of the models for the kink shape and solute/kink interaction energy.** The atomistic kink shape in the pure metal is described by a hyperbolic tangent function Eq. (6.12) with kink width w defined by the geometric construction shown. The solute/kink interaction energy is proportional to a hyperbolic tangent function with effective kink width $w^* = w/2$ (adapted from Ref. [48]).

6.2.2 Kink migration in a non-dilute random alloy

The above discussion pertained to a kink whose initial position is random and gliding over a distance L through a random environment. In non-dilute alloys, the initial dislocation is spontaneously kinked. The straight segments in between kinks are not in a random alloy environment but in a low-energy environment. Motion of the kinks that bound these segments is thus occurring in an environment where the initial dislocation segments of length $L = 2.5\zeta_c$ are lower in energy, on average, by $2.7E_k$; this was derived by Maresca et al. The kink motion in the non-dilute alloy is thus, on average, energetically uphill by $2.7E_k$.

To obtain the proper statistics for kink motion in the spontaneously-kink screw dislocation, we must thus select a *subset* of energy landscapes from among all possible random energy landscapes. Executing the SKRM over a length $L = 2.5\zeta_c$, we obtain a full set of energy landscapes that include paths with net energy changes that are (i) negative, reflecting that the migrated

segments are the low energy segments or (ii) positive, reflecting that the initial segment is in a low energy environment with an energy cost to migrate. Figure 6.3(a) shows the SRKM model executed on 50 random realizations of kink migration along a length $L = 100b$ with kink width $w = 10b$. Some landscapes (blue lines) have a net negative energy change and others (red lines) have a net positive energy change.

In the true spontaneously-kinked dislocation, the relevant energy landscapes are that *subset* of landscapes that have an average uphill energy of $2.7E_k$ over the length L . Sorting the energy landscape from highest to lowest, we can identify the N_r^* realizations having, on average, a net energy change of $+2.7E_k$. For the 50 samples shown in Fig. 6.3a, there are $N_r^* = 9$ samples whose average net energy change is $2.7E_k$, as indicated in Fig. 6.3b. The average energy landscape over all 9 paths is also shown. This selected group of energy landscapes has, by construction, the critical features of the kink migration problem in the non-dilute alloy: (i) the local solute fluctuations based on a proper model for solute/kink interaction energy, (ii) the total accumulated energy change during glide from $0 < z_c < L = 2.5\zeta_c$, and (iii) on average, an energy change of $2.7E_k$. Furthermore, as envisioned by Maresca et al., the average over all paths yields a nearly linear increase in energy change with increasing glide distance, showing that the fluctuations versus glide distance along any individual path, relative to the mean bias, are randomly distributed along the length of the path and so average to zero.

We note here that the simulations above are actually a general analysis of kink glide over some length L in a set of paths with an average bias E_{bias} . The specific choices of $L = 2.5\zeta_c$ and $E_{\text{bias}} = 2.7E_k$ make the study here specific to the Maresca-Curtin model but the subsequent analytic modeling can be adapted to any other choice of L and E_{bias} if other values are shown to be more relevant.

In the Maresca-Curtin model, the relevant quantity for stress-assisted, thermally-activated kink glide is the typical energy barrier, i.e. global minimum to global maximum energy, encountered during the glide over the entire segment of length $2.5\zeta_c$ under an applied shear stress τ . To obtain the energy barrier under stress, we first note that an applied shear stress τ on the glide plane does work (relative to the initial kink position at $z_c = 0$) of $-\tau b a z_c$. Hence the stress-dependent energy landscape is $\Delta E(z_c, \tau) = \Delta E(z_c, \tau = 0) - \tau b a z_c$; the stress has no other effect on the landscape, as demonstrated previously. We have performed SRKM simulations for a spectrum of representative alloys with inputs being the solute/kink interaction energy parameter and the kink formation energy as shown in Table 6.2. A kink width $w = 10b$ is used for all alloys. Fig. 6.4 shows the average kink migration barrier ΔH_{km} versus applied stress obtained from over five thousand simulations for each alloy. These results constitute the kink migration barriers versus stress, for each of these particular alloys. These representative numerical results will be used in the next section to validate an analytical model.

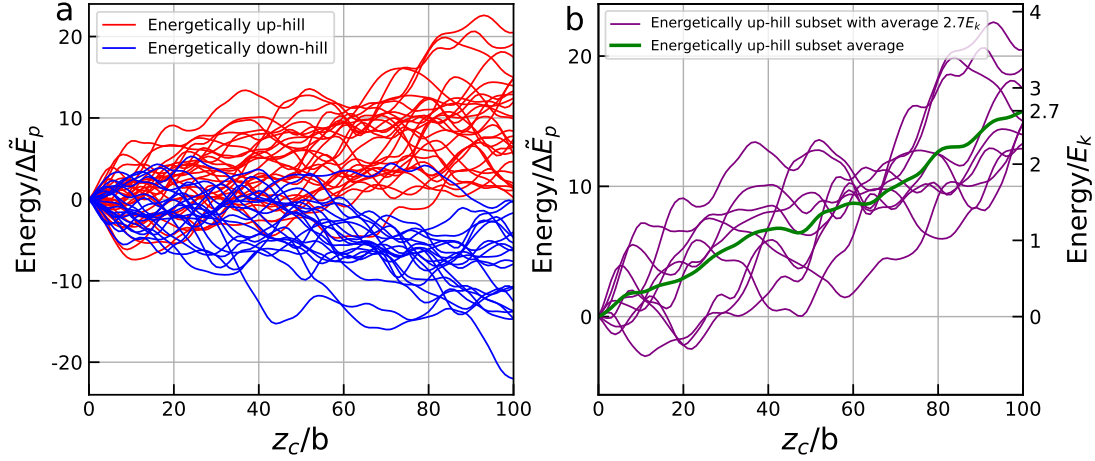


Figure 6.3 – **Energy landscape due to kink migration as computed from stochastic rigid-kink model (SRKM).** **a** Energy landscape as a function of the center position z_c as computed from SRKM for fifty samples of length $L = 100b$. **b** Subset of energy landscapes chosen from those in **a** such that their average (green line) would have a total energy change of $2.7E_k$ at length L .

Table 6.2 – Input parameters to the theory for all alloys studied. Please refer to [94] for more details.

Alloy	a_0 (Å)	$\Delta\tilde{E}_p$ (meV)	E_k (eV)	E_v (eV)	E_{si} (eV)	$\Delta\tilde{V}_p$ (meV.b)
Fe ₉₅ Si ₅	2.864	38.0	0.4932	2.22	5.1	6.6
Fe _{94.2} Si _{5.8}	2.864	40.9	0.4932	2.22	5.1	5.9
Fe ₉₂ Si ₈	2.861	48.1	0.4932	2.22	5.1	3.9
Fe _{91.7} Si _{8.3}	2.861	49.0	0.4932	2.22	5.1	3.7
Nb ₉₅ Mo ₅	3.289	48.8	0.6342	2.989	5.361	20
Nb _{91.5} Mo _{8.5}	3.282	56.2	0.6302	2.987	5.437	20
Nb ₈₁ Mo ₁₉	3.261	74.5	0.6182	2.984	5.664	20
Nb ₇₅ Mo ₂₅	3.250	84.7	0.6112	2.983	5.794	20
Nb ₉₄ W ₆	3.289	54.1	0.6559	3.024	5.511	20.5
Nb ₈₅ W ₁₅	3.275	73.2	0.6798	3.076	5.897	20.5
Ti ₃₃ Nb ₃₃ Zr ₃₃	3.393	71.0	0.255	1.868	3.535	10.7
Ti ₆₆ Nb ₁₇ Zr ₁₇	3.340	56.8	0.257	1.613	3.267	0.9

6.2.3 Analytic model for kink migration

An analytic model for kink migration in the non-dilute alloys can now be developed as follows. Ghafarollahi and Curtin [48] showed that the kink migration process in dilute alloys can be described by a stochastic random walk model also known as a "Wiener process model (WPM)". Here we can adapt that analysis for the non-dilute case. In the WPM, the energy landscape is sampled at discrete $b\bar{w}$ intervals, where $\bar{w} = 1.5 * w/b$ makes the discrete samples essentially statistically independent. The WPM energy landscape can thus be written as (refer to [48] for

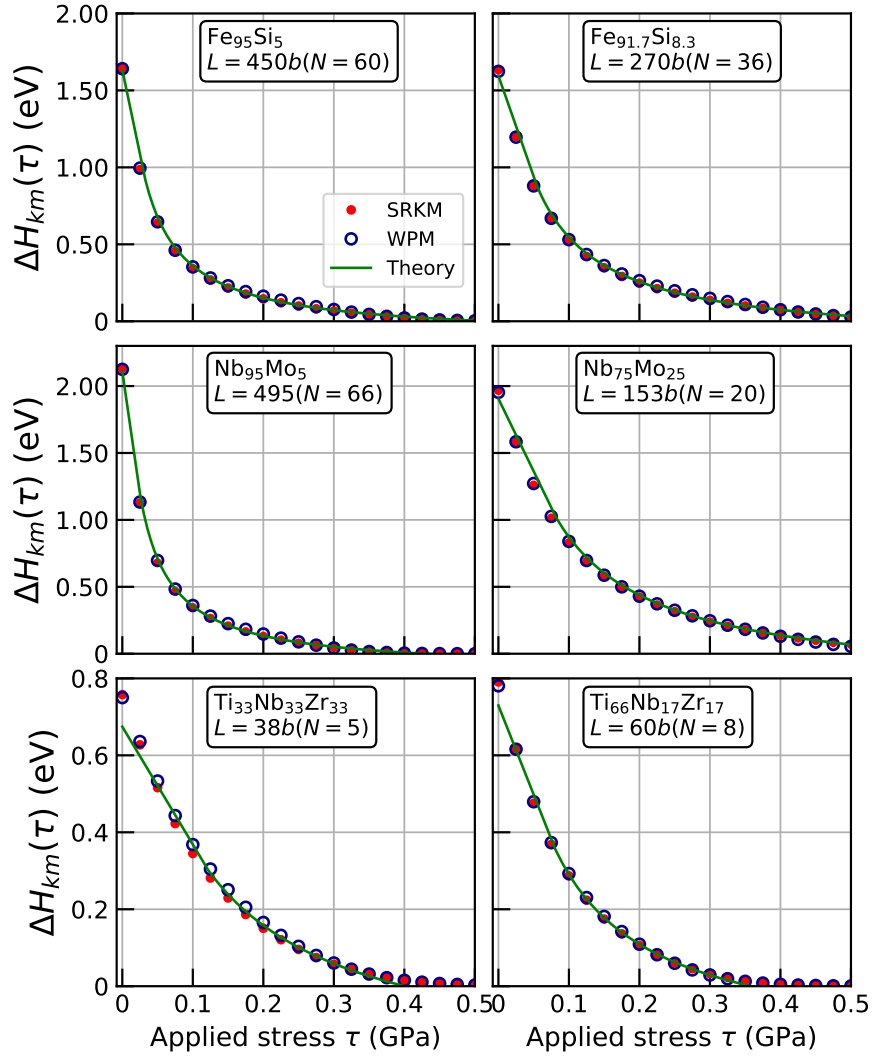


Figure 6.4 – **Kink migration barrier versus applied stress.** Average kink migration barrier ΔH_{km} versus applied stress τ in various model alloys as obtained from the Stochastic Random Kink Model, the Wiener Process Model, and analytical result, Eq. (6.20). The input parameters are tabulated in Table 6.2. The migration distance $L = 2.5\zeta_c$ and the number of statistically-independent segments $N = L/(\bar{w})$ where $\bar{w} = 1.5 * w/b$ is also shown for each alloy.

more details)

$$\Delta E(k\bar{w}) = \Delta \tilde{E}_p \bar{w}^{1/2} \sum_{i=1}^k R_i - (ab^2\tau\bar{w})k, \quad k = 1, 2, \dots, L/(b\bar{w}) \quad (6.15)$$

As in the SRKM, the first adaption of the WPM is to select only those landscapes that have, at zero stress and on average, the net energy change of $E_{bias} = 2.7E_k$. For this subset of landscapes, Fig. 6.4 shows the variation of the mean energy barrier versus applied stress as predicted by the WPM and SRKM for the different alloys. Excellent agreement is found, showing that the

physical problem of kink migration in a non-dilute solute random environment under stress is quantitatively captured by the Wiener process with drift.

A fully analytical model for the kink migration barriers, eliminating entirely the need for any stochastic simulations, is then achieved by using the known solution to the WPM provided by Magdon et al. [90]. Specifically, the mean maximum minus minimum energy of the continuous Wiener process can be written as

$$\begin{aligned} -\frac{2\sigma^2}{\mu}Q_p\left(\frac{\mu^2 N}{2\sigma^2}\right), \quad \mu \leq 0, \\ -\frac{2\sigma^2}{\mu}Q_n\left(\frac{\mu^2 N}{2\sigma^2}\right), \quad \mu \geq 0, \end{aligned} \quad (6.16)$$

where σ and μ are the standard deviation and the drift bias of the process and N is the total number of uncorrelated steps. $Q_p(x)$ and $Q_n(x)$ are tabulated functions that are accurately (3%) approximated as

$$\begin{aligned} Q_p(x^2)x^{-1} &= 1.63(x + 1.91)^{-1} + 0.025 \\ Q_n(x^2)x^{-1} &= 0.878 + 0.542x \end{aligned}$$

over the full range of $x > 0$ relevant in applications to alloys.

In non-dilute alloys, the bias term μ appearing in the above analytical solutions consists of two contributions. The first contribution is due to the applied shear stress and is similar to the dilute case. The second contribution, which does not appear in dilute case, arises because of the global energy change of $E_{\text{bias}} = 2.7E_k$ over the total segment length $L = 2.5\zeta_c$. As shown by the SRKM simulations in Fig. 6.3b, on average, this energy contribution varies linearly with glide distance z from zero to maximum value $E_{\text{bias}} = 2.7E_k$ at $z = L = 2.5\zeta_c$. Therefore, the energy contribution due the global energy change acts like a "backstress" and can be expressed as

$$\tau_b = \frac{E_{\text{bias}}}{abL} = \frac{1.08E_k}{ab\zeta_c}, \quad (6.17)$$

which emerges to be identical to the 'backstress' introduced in Maresca and Curtin model, Eq. (6.11). Applied to the kink migration problem in non-dilute alloys, we can thus write the standard deviation, the bias, and the number of independent segments as

$$\begin{aligned} \sigma &= \Delta\tilde{E}_p\bar{w}^{1/2} \\ \mu &= (\tau_b - \tau)ab^2\bar{w} \\ N &= L/(b\bar{w}). \end{aligned}$$

Substituting these relationships into the result of Magdon et al. Eq. (6.16), after some algebra,

we obtain

$$\Delta H_{km} = 2\Delta\tilde{E}_p \frac{\tau_c}{\tau - \tau_b} \begin{cases} Q_p \left(\frac{(\tau - \tau_b)^2}{\tau_c^2} \frac{L}{2b} \right) & \tau > \tau_b \\ (-1)Q_n \left(\frac{(\tau - \tau_b)^2}{\tau_c^2} \frac{L}{2b} \right) & \tau < \tau_b \end{cases} \quad (6.18)$$

where

$$\tau_c = \frac{\Delta\tilde{E}_p}{ab^2}, \quad (6.19)$$

is introduced as the characteristic stress required to overcome a single typical kink energy difference $\Delta\tilde{E}_p$ over unit kink glide distance b .

The results of Eq. (6.18) are for the continuous Wiener process where the discrete intervals are infinitesimal, i.e., $\bar{w} \rightarrow 0$, so that the interval length \bar{w} does not appear. To properly include the effects of the non-infinitesimal discrete interval length, an additional correction term that depends on σ is required [128]. Following [48], the correction term is $-1.24\Delta\tilde{E}_p \bar{w}^{1/2}$. Hence, a fully-analytic result for the kink migration barrier in non-dilute to HEAs, after a bit of algebra, can be obtained as

$$\begin{aligned} \Delta H_{km}(\tau) &= \Delta\tilde{E}_p \left[3.26 \left(\frac{\tau - \tau_b}{\tau_c} + 1.58 \frac{\Delta\tilde{E}_p}{E_k} \right)^{-1} + 0.06 \frac{E_k}{\Delta\tilde{E}_p} - 1.07\sqrt{w/b} \right], \quad \tau > \tau_b \\ \Delta H_{km}(\tau) &= \Delta\tilde{E}_p \left[2.12 \frac{E_k}{\Delta\tilde{E}_p} + 1.59 \frac{\tau_b - \tau}{\tau_c} \frac{E_k^2}{\Delta\tilde{E}_p^2} - 1.07\sqrt{w/b} \right], \quad \tau < \tau_b \end{aligned} \quad (6.20)$$

where we have reverted to using the true kink width w and written the relevant segment length in terms of material parameters E_k and $\Delta\tilde{E}_p$ (Eq. (6.2)). More general results in terms of L and E_{bias} could be derived similarly. While these analytic results are ungainly, they arise directly from the analytic approximations to Q_p and Q_n and substitution of various derived relationships; there is no fitting involved.

The predictions of our fully analytic solution (Eq. (6.20)) as a function of applied stress for all the alloys examined earlier are shown in Fig. 6.4. Excellent agreement with the direct numerical SKRM is obtained for all cases, validating the analytic adaptation of the WPM to the discrete kink migration problem.

In a rate-dependent theory, we wish to express the stress in terms of the experimentally imposed enthalpy barrier $\Delta H(\dot{\epsilon}, T)$, Eq. (6.4). Inverting Eq. (6.21) we obtain the kink migration

strength $\tau_k(\dot{\epsilon}, T)$ at temperature T and strain rate $\dot{\epsilon}$ as

$$\begin{aligned} \tau_k(\dot{\epsilon}, T) &= \tau_b + \tau_c \left[3.26 \left(\frac{\Delta H}{\Delta \tilde{E}_p} - 0.06 \frac{E_k}{\Delta \tilde{E}_p} + 1.07 \sqrt{w/b} \right)^{-1} - 1.58 \frac{\Delta \tilde{E}_p}{E_k} \right], & \tau_k > \tau_b, \\ \tau_k(\dot{\epsilon}, T) &= \tau_b - \tau_c \left[\frac{\Delta \tilde{E}_p^2}{1.59 E_k^2} \left(\frac{\Delta H}{\Delta \tilde{E}_p} - 2.12 \frac{E_k}{\Delta \tilde{E}_p} + 1.07 \sqrt{w/b} \right) \right], & \tau_k < \tau_b. \end{aligned} \quad (6.21)$$

Eq. (6.21) constitutes our analytical model for the kink migration strength in non-dilute and high-entropy alloys as a function of temperature and strain rate. The only inputs to the theory are the solute/dislocation interaction energies that determine $\Delta \tilde{E}_p$, the kink formation energy E_k , and the width of the kink w , which plays a minor role.

6.3 Applications of the theory

With the extensive validation of the proposed model for the kink migration process in non-dilute to high entropy alloys, we can now confidently apply the kink migration theory to determine the strength of the real BCC systems. For the two other strengthening processes, i.e. the Peierls and cross-kink mechanisms, the models developed in [94] and given by Eqs. (6.3) and (6.7) are used without modification. The alloy yield strength at the imposed experimental enthalpy barrier Eq. (6.4) is

$$\tau(\dot{\epsilon}, T) = \tau_{sk}(\dot{\epsilon}, T) + \min[\tau_k(\dot{\epsilon}, T), \tau_p(\dot{\epsilon}, T)] \quad (6.22)$$

The underlying material parameters for the cross-kink and Peierls mechanisms are vacancy and self-interstitial formation energies $E_{v/i}$ and Peierls barrier ΔV_p , respectively.

We now apply the analytical model to predict the strength versus temperature for real alloys and compare them with existing experiments. Consistent with [94], we take a single values of $\dot{\epsilon}_0 = 10^4 \text{s}^{-1}$ and kink width $w = 10b$ for all alloys. The material parameters for the Peierls mechanism and the cross-kink mechanism are also taken as those used by Maresca et al. We keep in mind that these parameters were estimated but not used to fit any strength data; any refinements to the estimates would change overall predictions, leading to possibly better or worse agreement. The important overall point is that the theory has been fully derived, not fitted to experiments, and the challenges are thus in obtaining the material parameters that enter the theory.

Experimental yield stresses for Fe-Si (5 at%, 5.8 at%, 8 at%, and 8.3 at%) alloys versus temperature were reported by [164, 196, 78, 61]. We use the same input parameters as Maresca and Curtin [94] (Table 6.2) except we use $\Delta \tilde{E}_p = 170 \text{ meV} \sqrt{c}$ fitted to experiments at 5 at% Si rather than the value $178 \text{ meV} \sqrt{c}$ of [94].

Fig. 6.5 shows the predictions for the four compositions over a wide temperature range. As can be seen, for all the compositions our predictions are in fairly good agreement with the

experimental results, especially at higher temperatures. For lower concentrations of 5 at% and 5.8 at% the very low temperature strength is controlled by the Peierls mechanism up to about $T \sim 80\text{K}$ (with underlying cross-kink strengthening). The rest of the temperature range is controlled by the kink glide process and cross-kink mechanism, where the predictions are in good agreement with experiments. The theory also captures the increase in strength upon increasing the concentration to just 5.3at%Si. Increasing the concentration to 8 at%Si and 8.3%Si, the Peierls mechanism becomes the controlling process for a wider temperature range up to about room temperature and the strengths agree well with experiments, with slight under-prediction at low T. The theory also captures the negligible difference between 8at%Si and 8.3%Si up to $T=300\text{K}$. Moreover, the rather significant decrease in experimental strength observed at $T=443\text{K}$ is well-captured by the theory, which is attributed to the transition in strength-control from the Peierls mechanism to kink migration.

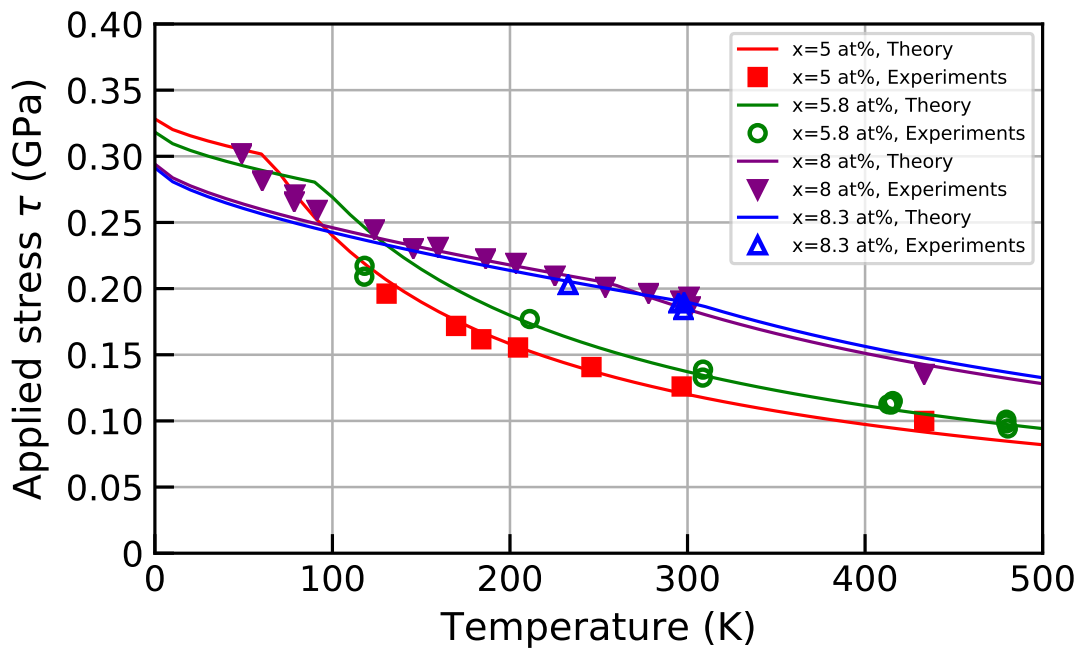


Figure 6.5 – Theory predictions for non-dilute $\text{Fe}_{1-x}\text{Si}_x$ alloys.

Experimental data on stress versus temperature was reported in [152] for Nb-Mo for compositions from 2-25 at%Mo and in [148] for Nb-W at W concentrations from 1-15 at%. Here, we consider the non-dilute regime of concentrations of 5%, 8.5%, 19%, and 25% Mo for Nb-Mo and 6% and 15% W for Nb-W alloys. We use the same material parameters as [94] shown in Table 6.2.

The predictions for the Nb-Mo alloys at different concentrations are shown in Fig. 6.6a along with the experiments. Fairly good agreement is obtained between theory and experiment over all compositions and temperatures. For the low concentrations of 5at% and 8.5at% Mo, the strength is controlled by the kink-glide process (plus the underlying cross-kink mechanism)

over the whole temperature range. With increasing the concentration, the low-temperature strength is revealed to be controlled by the Peierls mechanism. In general, there tends to be some under-prediction at lower T and slight over prediction at higher T. Such differences could be likely be rectified by an increase in the $\Delta\tilde{E}_p$ and decreases in the vacancy and self-interstitial formation energies, but our aim here is not to fit the experiments but rather to demonstrate that theory is reasonably quantitative with accessible estimates of the input parameters. Turning to the Nb-W system, Fig. 6.6b shows the predictions of the theory for 6at%W and 15at%W concentrations over a wide temperature range. The predictions mirror those for Nb-Mo.

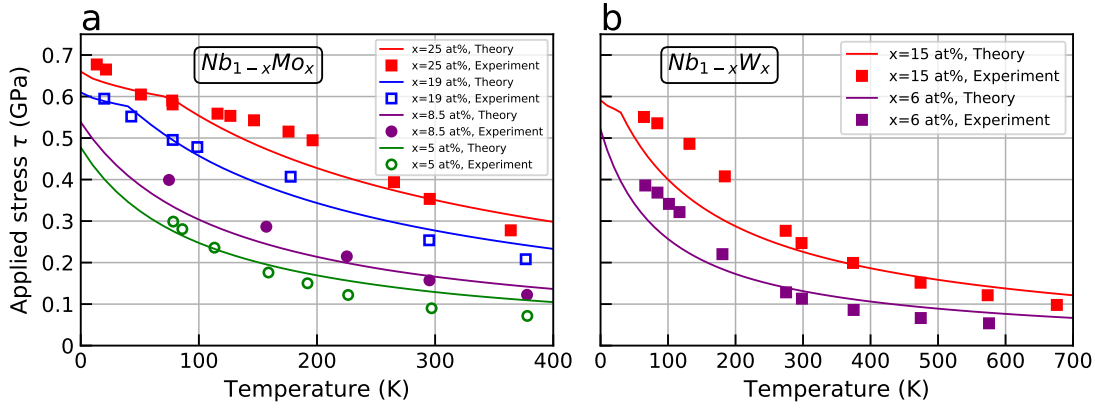


Figure 6.6 – **Theory predictions for Nb-based binary alloys.** **a** $Nb_{1-x}Mo_x$ alloys, data from [152] . **b** $Nb_{1-x}W_x$ alloys, data from [148].

The advantage of considering the alloys above is that experimental data exists for a range of concentrations as well as temperatures. Thus, the trends in the theory predictions can be reasonably verified. In applications to HEAs, available data usually corresponds to a single composition, and the ability to estimate the important material parameters is far more limited. If parameters are fit to the experimental data, then little is learned that can be truly predictive. Applications to HEAs thus await reliable estimates for the material parameters needed in the theory.

6.4 Discussion

The present theory plus the recent theories of double-kink nucleation and kink migration in dilute alloys of Ghafarollahi et al. [49, 48] together provide a coherent framework for strengthening of screw dislocations over the full range of concentrations from dilute (up to a few at.%) to non-dilute alloys including High Entropy Alloys. As explained in [49] the criteria determining the cross-over from dilute to non-dilute domains is how the kink spacing $2.5\zeta_c$ compared with the total dislocation length $L = 1/\sqrt{\rho}$ where ρ is the mobile dislocation density. When the characteristic length $2.5\zeta_c$ is comparable to the total dislocation length L , i.e. $2.5\zeta_c \sim L$ we fall into the dilute limit where the screw dislocation cannot become spontaneously

kinked and so motion is controlled by the double-kink nucleation and migration processes. Conversely, when $2.5\zeta_c \ll L$, the kinked structure is realizable and the current non-dilute theory applies.

The new model derived here for kink migration mechanism has several fundamental differences with that developed by Maresca and Curtin [94]. When applying our model to the real systems, however, agreement with the experimental results is obtained using the same material parameters used in [94]. This surprising agreement is examined more generally in Section 6.5 over a wide general material properties.

The historical model for kink migration by Suzuki is very different from the present model and that of Maresca et al. Yet adaptations of it to HEAs shows reasonable agreement with experiments. In the next Section 6.5, we thus also present the Suzuki model for kink migration and identify some unphysical features in that formulation. But we also show that, in an intermediate range of stresses and length scales, the numerical results for the migration barrier are roughly comparable to those rigorously derived here. This rationalizes some of the successes of the adapted Suzuki model in spite of some fundamental theoretical problems.

In summary, we have derived an accurate model for the migration barriers encountered by screw dislocation kinks as a function of stress in non-dilute alloys of any composition and number of alloying elements. The kink migration model has been integrated into the overall framework for screw dislocation motion in complex alloys developed recently by Maresca et al. Applications to several alloys for which extensive experimental data is available demonstrates the predictive capability of the theory. The open challenge for true predictions now lies in determining the accurate alloy-dependent material parameters that enter the theory. It is entirely expected that these material parameters (mainly the solute/screw interaction energies; kink formation energy; average vacancy and self-interstitial formation energies) should dictate screw motion and they are all physically well-defined. But they are rarely, if ever, directly measurable and very difficult to compute via first principles methods. However, even without detailed values, the theory demonstrates the qualitative and quantitative effects of these parameters on HEA performance. Thus, reasonable estimates and trends can be used now with the theory to guide design of new high-performance HEAs.

6.5 Current vs. existing theories

The existing theories of Suzuki and Maresca and Curtin have shown good agreement with some experiments. However, there are incorrect assumptions made in both theories. Here, we provide some quantitative comparisons between the kink migration theory derived here and these earlier models. We note that the focus is solely on kink migration, which makes only one contribution to the overall alloy strength.

The kink migration model of Maresca and Curtin was stated in Eqs. (6.9) of the main text. It involves the same backstress and same combinations of material parameters as the present

theory. Thus, direct comparisons are easily made. The only quantity that influences the relative difference between the two models is the length L , which is determined by the material ratio $E_k/\Delta\tilde{E}_p$. Figure 6.7 thus shows predictions for the normalized migration barrier versus the normalized stress over a range of lengths L . In general, the barriers in the Maresca model are larger, especially at very low ΔH corresponding to very low T . Since the strength in the low T domain becomes controlled by the Peierls stress, the overprediction of the Maresca-Curtin model in this domain can often be of little practical importance. Moreover, for $L > 150b$ (with $L = 2.5\zeta_c$), the two models agree quite well over most of the range of stresses below the reference stress τ_c . For alloys studied here, the range of $\Delta H/\Delta\tilde{E}_p$ is ~ 1 -3, where the two models agree very well when $L > 150b$. This agreement arises in part because the 'backstress' contribution to strengthening, which dominates at low stresses, is identical in the two theories. The previous agreement of the Maresca-Curtin model with experiments is thus understood, in spite of some incorrect assumptions about kink migration in that model.

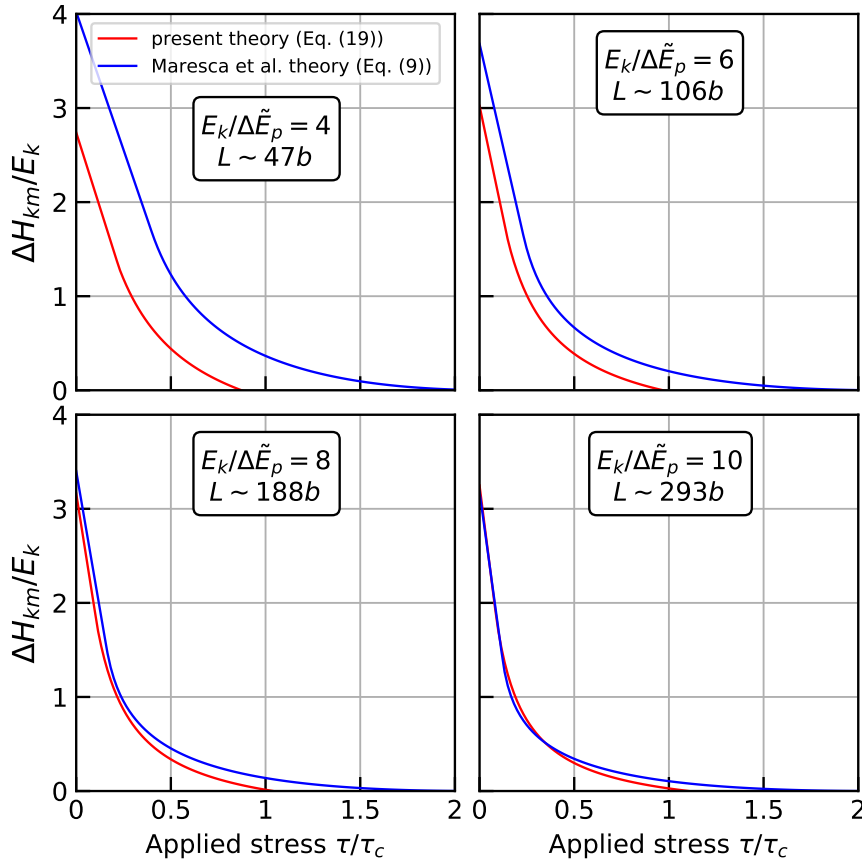


Figure 6.7 – **Comparison of the present theory for the kink migration barrier with the Maresca and Curtin model.** Normalized average kink migration barrier $\Delta H_{km}/E_k$ versus normalized applied stress τ/τ_c for various values of $E_k/\Delta\tilde{E}_p$ as obtained from the present analytical mode, Eq. (6.20) and Maresca and Curtin model, Eq. (6.9).

The Suzuki model for kink migration is substantially different. We will not repeat Suzuki's

analysis here, but only look at the final results for kink migration. Suzuki uses a single solute/dislocation interaction energy labeled E_w . For a screw dislocation of length L in a binary alloy with minor element concentration c , Suzuki obtains an enthalpy barrier as a function of stress as

$$\Delta H_{km} = 3cE_w^2\kappa^2 / (2\tau ab^2) - \tau^3 a^3 b^4 w^2 / (18\kappa^2 E_w^2 c) \quad (6.23)$$

where κ is a concentration- and length-dependent constant given by

$$\frac{1}{\sqrt{2\pi}} \int_{\kappa}^{\infty} \exp\left(-\frac{x^2}{2}\right) dx = \frac{b}{3Lc} \quad (6.24)$$

The dependence of the kink migration barrier on length L thus enters solely through the parameter κ .

Inspection of Eqs. (6.23) and (6.24) immediately reveals two fundamental problems with Suzuki's result. The first problem is that, in any specified finite length L , Suzuki predicts that the migration barrier diverges as τ goes to zero. That is, at zero stress, there is an infinite barrier for migration over any finite length L . This is quite obviously unphysical. The zero-stress barrier must be finite, as also clearly seen in the exact analysis of the problem by Magnon et al. This error translates into a weak dependence of strength versus T at high T that is not correct; i.e. a tendency toward a plateau in strength versus temperature that does not arise in the rigorous kink migration theory derived here. Since the high T behavior of HEAs is crucial for applications, this aspect of the Suzuki model may lead to erroneous predictions in this domain.

The second fundamental problem is that the activation volume, which is the derivative of the enthalpy barrier versus stress $V_{\text{act}} = -\partial\Delta H/\partial\tau$, must be zero at $T = 0$ ($\Delta H = 0$). In the Suzuki model, the activation volume is finite at $2wab/\sqrt{3}$. This value is not negligible, and translates into an incorrect temperature dependence of the kink migration strength versus temperature at low T .

The problems above are revealed in numerical solutions. However, to compare quantitatively to the present model first requires a connection to be made between the Suzuki interaction energy parameter E_w and the correct solute/dislocation interaction energy parameter $\Delta\tilde{E}_p$. This connection has been examined earlier, and for the binary alloy was found to be $\Delta\tilde{E}_p = \sqrt{6c}E_w$ [51]. Thus, the only difference in concentration dependence is in the dependence of κ on c (Eq. (6.24)), which is relatively weak.

The normalized kink migration barrier $\Delta H_{km}/(\sqrt{c}E_w)$ versus the normalized applied stress τ/τ_c , where τ_c is given by Eq. (6.19), is shown in Fig. 6.8 for the Suzuki model and the precise kink migration model developed in this Chapter, for different dislocation lengths L that span the region of lengths emerging from applications of the Suzuki model as adapted to HEAs by Rao et al. [120]. These normalized Suzuki results still depend on concentration while the precise model does not, and so the figure shows a range of concentrations. The Suzuki results

immediately show the fundamental problems - the divergence at low τ and the finite slope at $\Delta H = 0$. However, over a wide intermediate domain of normalized stresses, the magnitude of the Suzuki enthalpy barrier is remarkably comparable to our precise model for a range of relevant L values. The full Suzuki model involves other aspects related to determining the appropriate length L and the cross-kink spacing and total strengthening. But the comparison in 6.8 rationalizes why the Suzuki model and its adaptation to HEAs can give strengths in the range of experiments in spite of differences in the dependence of kink migration barriers with temperature, especially at high and low T. Any application of the Suzuki model must be made with these limitations in mind.

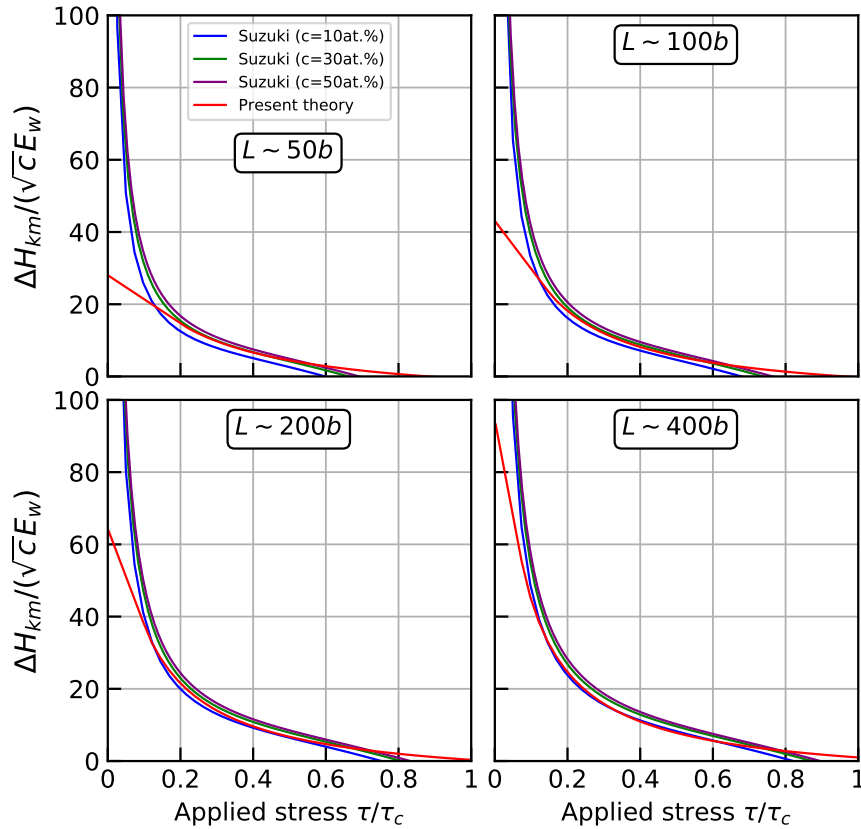


Figure 6.8 – **Comparison of the present theory for the kink migration barrier with the Suzuki model.** Normalized average kink migration barrier $\Delta H_{km}/(\sqrt{c}E_w)$ versus normalized applied stress τ/τ_c for various values of the kink glide distance L as obtained from the present theory and Suzuki theory, Eq. (6.23).

7 Analysis of high energy barriers for edge dislocation motion in BCC high-entropy alloys

This chapter is extracted from the following publication

Kubilay, R.E., Ghafarollahi, A., Maresca, F., and Curtin W.A. High energy barriers for edge dislocation motion in body-centered cubic high entropy alloys. *npj Comput Mater* 7, 112 (2021).

High-entropy alloys (HEAs) are multicomponent alloys with non-dilute concentrations of most or all of the alloying elements. Various HEAs have impressive mechanical properties such as high yield strength at room temperature, high ultimate strength, high ductility, high fracture toughness, or high strength retention at very high temperatures [145, 99, 137, 47, 71, 54]. Of primary interest here is the high strength retention in the refractory BCC HEAs such as MoNbTaW and MoNbTaVW. High strength retention might suggest a solute drag mechanism, but the high strengths starting from low T and the high vacancy formation (see Table 7.2) and migration energies preclude standard solute drag at typical experimental strain rates (estimates can be made using theories such as that found in Ref. [197]). The high strength and strength retention at high T thus requires that the barriers to dislocation glide are substantial. Recent theory [93] has predicted that edge dislocations in these BCC HEAs encounter such high barriers due to the random fluctuations in local environments in the complex alloy. This prediction is unusual because it is commonly assumed that screw dislocations control plastic flow in BCC alloys. However, simulations of edge dislocation motion on model alloys at $T=0\text{K}$ show high strengths comparable to those predicted by the parameter-free theory. Application of the edge dislocation model to real alloys also shows good agreement for the strength versus temperature, including the observed high strength retention at temperatures up to 1600°C . Recent experiments support the key role of edge dislocations in strengthening of some BCC HEAs [83]. The theory makes other predictions that have been validated by atomistic simulations. Here, we report detailed transition-state computations of the atomistic barriers for edge dislocation glide in two model alloys, NbTaV and MoNbTaW, as represented using interatomic potentials that have been shown to be accurate for this problem, and show broad agreement with the theory. We then apply a reduced analytic theory to several further

Chapter 7. Analysis of high energy barriers for edge dislocation motion in BCC high-entropy alloys

HEAs recently reported in the literature. We show that the significant strengthening due to the addition or substitution of Mo into HfNbTaTiZr and of V into MoNbTaW and MoNbTaTiW can be quantitatively captured using the theory for edge dislocations. The loss of strength in the former alloys at 1200°C is correlated with the estimated vacancy formation energy, but no mechanism has yet been identified. Overall, the analytic theory based on large barriers to edge dislocation motion, validated here, provides a path for preliminary alloy selection for high strength and high strength retention at high temperatures.

7.1 Solute strengthening theory

We first briefly review the theory for yield strength for edge dislocations in a random BCC alloy, as presented in [93]. A dislocation in a random alloy minimizes its total energy by becoming wavy over some characteristic length scales ζ_c (wavelength $\sim 5.6 \zeta_c$) and $w_c/2$ (amplitude). The waviness forms because the dislocation exists in a rough potential energy landscape and so finds local regions of favorable random concentration fluctuations that lower the dislocation energy, but at the energetic cost of an increased dislocation line length. In the wavy structure, the dislocation resides in lower energy in segments of length ζ_c and faces barriers created by unfavorable regions at distance w_c along the glide direction. Stress and/or thermal activation are needed to overcome these energy barriers and generate plastic flow by dislocation glide. The detailed derivations in the theory are given in [93] and only the relevant results are stated here.

The theory considers an N -component random alloy composed of atom types $n = 1, \dots, N$ each at concentration c_n . The solute/dislocation interaction energy of a type- n solute at position (x_i, y_j) relative to an edge dislocation aligned along z is denoted as $U_n(x_i, y_j)$. The theory then considers a generic wavy dislocation characterized by unknown length scales ζ and w . The fluctuations in dislocation energy caused by the interactions with the random solutes are characterized by the standard deviation of the energy of a unit Burgers vector b as the dislocation glides a distance w along the x direction,

$$\Delta \tilde{E}_p(w) = \left[\sum_{i,j,n} c_n \left(U_n(x_i - w, y_j) - U_n(x_i, y_j) \right)^2 \right]^{\frac{1}{2}}. \quad (7.1)$$

From this solute/dislocation energy per unit length and the elastic energy cost to create the waviness due to the dislocation line tension Γ , the characteristic wavelength scale $\zeta_c(w)$ as a function of the amplitude w is obtained by minimizing the total energy with respect to ζ . The required stochastic analysis is discussed in [93] with the final result

$$\zeta_c(w) = 1.73 \left(\frac{\Gamma^2 w^4 b}{\Delta \tilde{E}_p^2(w)} \right)^{\frac{1}{3}}. \quad (7.2)$$

Here, the coefficient 1.73 is derived, not fitted, in the analysis [93]. The characteristic amplitude parameter w_c is then computed by minimizing the total energy versus w , which reduces to

the solution of

$$d\Delta\tilde{E}_p(w)/dw = \Delta\tilde{E}_p(w)/2w. \quad (7.3)$$

The characteristic energy barrier facing a segment of length ζ_c that lies in a local favorable energy minimum is then derived to be

$$\Delta E_b = 1.11 \left(\frac{w_c^2 \Gamma \Delta\tilde{E}_p^2(w_c)}{b} \right)^{\frac{1}{3}} \quad (7.4)$$

where again the coefficient 1.11 is derived. At an applied resolved shear stress τ , this characteristic barrier is overcome by a combination of thermal activation and the work $-\tau b \zeta_c x$ done on the length ζ_c segment as it glides a distance x relative to the minimum energy position. For a sinusoidal energy landscape, the stress-dependent energy barrier is well approximated within 1% error over the whole stress regime by

$$\Delta E(\tau) = \Delta E_b \left(1 - \frac{\tau}{\tau_{y0}} \right)^{\frac{3}{2}} \quad (7.5)$$

where τ_{y0} is the zero-temperature flow stress, given as

$$\tau_{y0} = \frac{\pi}{2} \frac{\Delta E_b}{b \zeta_c(w_c) w_c} = 1.01 \left(\frac{\Delta\tilde{E}_p^4(w_c)}{\Gamma b^5 w_c^5} \right)^{\frac{1}{3}}. \quad (7.6)$$

The above results are all analytical, requiring only the solute/dislocation interaction energies, the dislocation line tension, and the Burgers vector. The line tension is taken to be $\Gamma = \frac{1}{12} \mu_{\{110\}\langle 111 \rangle} b^2$ where $\mu_{\{110\}\langle 111 \rangle}$ is the alloy shear modulus for shear on the $\{110\}$ glide plane in the $\langle 111 \rangle$ direction of glide.

In this Chapter, the theory is quantitatively assessed against carefully-executed direct numerical simulations of the barriers encountered by dislocation motion through true random alloys. However, one cannot simply insert a dislocation of arbitrary line length into a simulation cell and follow its motion under stress. The characteristic waviness associated with ζ_c must be captured, which requires the use of a very long line length $L \gg \zeta_c$. This is computationally costly. A second strategy is to use a line length of precisely $L = \zeta_c$. According to the theory, such a segment should remain essentially straight because the line tension prevents the dislocation from becoming wavy on smaller scales. A dislocation segment of length ζ_c is then predicted to encounter an energy landscape along the glide direction that consists of local minima and maxima at an average spacing of w_c and with an average energy difference (barrier) of ΔE_b . We adopt the second strategy below and use the Nudged Elastic Band method to explicitly compute the energy landscape and configurations of a dislocation of length ζ_c in the random alloy (see Methods). This study thus reveals the statistical distribution and average value for both w_c and ΔE_b , from which the distribution of barriers and the strength τ_{y0} can then be determined.

7.2 Material properties

We study two model BCC random alloys, NbTaV and MoNbTaW. In these alloys, we compute the solute/dislocation interaction energy $U_n(x_i, y_j)$ of a type- n solute using the Zhou et al. EAM-type interatomic potentials [203, 88]. The Zhou et al. potentials have been reasonably validated for this problem [93]. More importantly, their accuracy for real alloys is irrelevant for the present study - we will compare simulation and theory on these well-defined model alloys. For the given alloy composition, we first construct the homogenized reference average-atom (A-atom) interatomic potential from the underlying atom-specific potentials [173]. The A-atom potential accurately and automatically encodes, with no fitting, all the average properties (elastic constants, lattice constant, stacking fault energies, etc.) of the true random alloy. Any individual atom type n can be substituted into any position in any configuration of the A-atom material to accurately obtain the energy of the n atom at that position averaged over all possible configurations of atoms in all surrounding positions. The interaction between the n and A atoms thus encodes all the average solute-solute interactions in the alloy. Using this feature of the A-atom potential, an edge dislocation of Burgers vector $a\langle 111 \rangle/2$ is created in the homogeneous A-atom material using standard methods in a large simulation cell. A solute of type n then replaces an A-atom at position (x_i, y_j) near the dislocation, and the energy of the system is measured. The interaction energy $U_n(x_i, y_j)$ is this energy minus the energy of the type n solute in the dislocation-free crystalline A-atom BCC material. Use of the A-atom neglects explicit solute-solute interactions in the alloy but recent theory [103] that includes such solute-solute interactions shows this effect to be small especially in strong alloys. Moreover, explicit results for MoNbTaW using both Zhou EAM potentials and first-principles methods shows that solute-solute interactions have a negligible effect on strength in this alloy [103].

The solute/dislocation interaction energies for two solutes in each of the two alloy studied are shown in Figure 7.1, as examples. The individual energies are not large, typically 0.15 eV or less, and are close to the elasticity estimate $U_n(x_i, y_j) = -p(x_i, y_j)\Delta V_n$ where $p(x_i, y_j)$ is the dislocation pressure field at (x_i, y_j) and ΔV_n is the misfit volume of a type- n solute in the alloy. Although the individual interaction energies are small, the collective random fluctuations of the solutes over the scale (ζ_c, w_c) creates large barriers for the dislocation motion as shown below.

7.3 Computational method

For both model alloys, a rectangular simulation cell oriented with glide direction $X||[\bar{1}11]$, glide plane normal $Y||[101]$ and line direction $Z||[12\bar{1}]$ is first created using the lattice parameter of the corresponding "average atom" alloy. The dimensions of the simulation cell are $(L_x = 1327, L_y = 123)$ Å and $(L_x \sim 190, L_y \sim 90)$ Å for NbTaV and MoNbTaW alloys, respectively. The huge difference between the sample sizes L_x for the two alloys stems from different methodologies used to find the edge dislocation minimum energy positions as discussed later. As explained

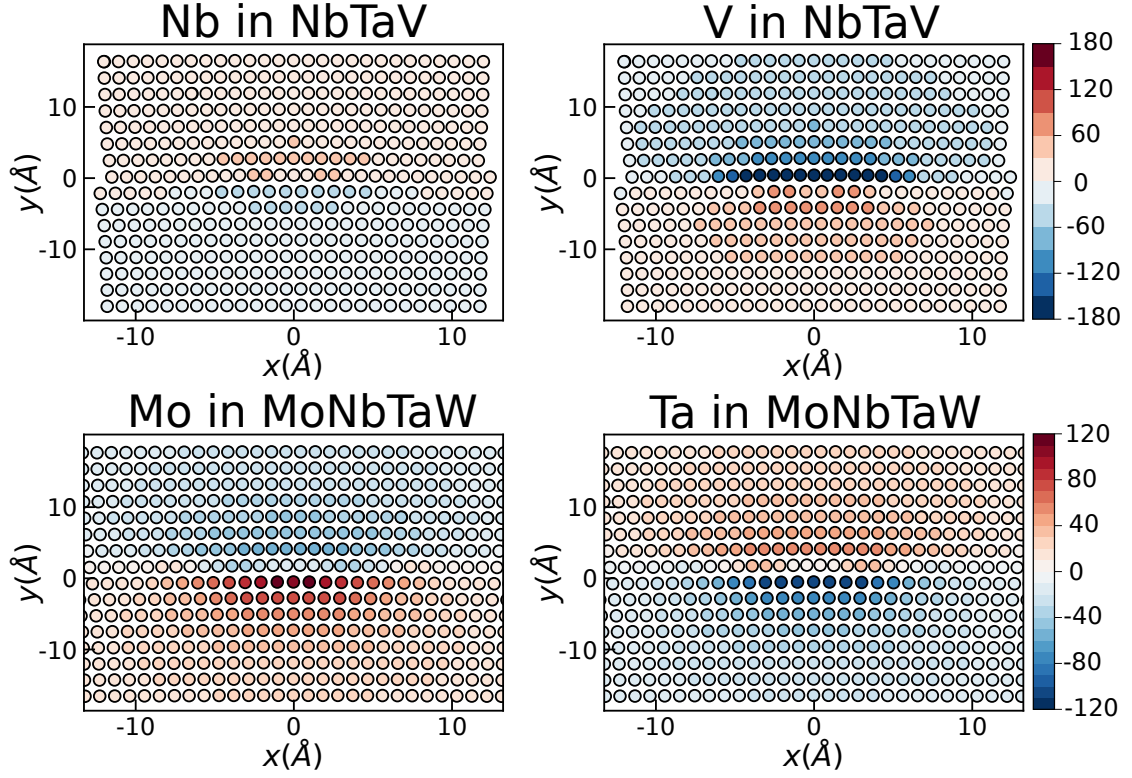


Figure 7.1 – **Solute/edge dislocation interaction energies (in meV)** (a) Nb solutes and (b) V solutes in the average-atom NbTaV alloy. (c) Mo solutes and (d) Ta solutes in the average-atom MoNbTaW alloy.

above, the dislocation line length is fixed at the characteristic length of $L_z = \zeta_c \sim 29\text{\AA}$ for NbTaV and $L_z = \zeta_c \sim 50\text{\AA}$ for MoNbTaW alloys (see Table 7.1). The surfaces normal to the Y-direction are traction-free while those along the X- and Z-directions are periodic.

To insert a single edge dislocation, the simulation cell created above is first populated with the corresponding average atoms. Two adjacent YZ-atomic planes in the lower half of the simulation cell are then removed. The average atom at each lattice site is then randomly replaced with a solute atom of the alloy according to the solute concentration in the alloy. The created simulation cell (with two missing atomic planes in the lower half) enables us to introduce the edge dislocation at any desired position x^* . First, the atomic positions in the lower half of the simulation cell are shifted in the x -direction (keeping the same randomness) such that the gap due to the missing atoms is located at x^* . The empty space in the lower half at location x^* is then eliminated by displacing the atoms on both sides by $u_x = b(2x \pm L_x)/(2x^* \pm L_x)$ where \pm reflects positions to the left and right of x^* . The true random alloy with the dislocation is finally created by relaxing the atomic positions. In order to minimize computation time, the Conjugate Gradient algorithm and then the FIRE algorithm are used in sequence, and the domain is relaxed until convergence is achieved (force tolerance $< 10^{-5}$ eV per atom). All simulations are performed using molecular statics as implemented in LAMMPS

[114].

For the long NbTaV random alloy sample, the minimum energy positions are first found by placing an initial dislocation at every possible location (spacing of one Burgers vector) along the slip plane and then minimizing the energy. During minimization, the dislocation moves from its initial position to the local minimum energy position within the local energy basin [109]. Many close initial positions thus have the same final position. NEB simulations are then performed to find the path and barrier between each pair of adjacent minima, using a sub-domain of $L_x = 200 \text{ \AA}$ centered around the pair of adjacent minima. Two large random realizations were studied, with the minimum energy paths (MEP) obtained using 32 and 50 replicas, respectively, between each pair of initial and final configurations. No significant statistical differences are found between the two realizations, and their results are aggregated. The inter-replica spring constant is set to 1 eV\AA^{-1} (force units) with "ideal-parallel" option in LAMMPS which calculates nudging forces as described in [184] and results in more equally-spaced replicas. Using the same spring constant used for the MoNbTaW NEB computations (see below) results in very similar barriers. Each stage of the NEB calculation (convergence to MEP and barrier climbing) is executed for 10,000 steps and convergence is checked afterwards by observing the MEP progression. These NEB computations were performed for every pair of adjacent minima along the entire length $L_x \sim 1300\text{\AA}$.

For the MoNbTaW alloy, after inserting an edge dislocation in the system and relaxing to the local minimum configuration, a dislocation is again introduced into the same initial simulation cell (same random configuration) at a distance $2w_c$ from the previously-found minimum position. This is the distance around which the adjacent minimum is expected. Full relaxation then enables the dislocation to reach the actual minimum energy position. This procedure establishes the initial and final dislocation positions for an NEB computation of the path and energy barrier between them. This procedure was repeated for over 100 MoNbTaW random realizations of the alloy to generate a statistical distribution of barriers. In no case was another minimum found in between the initial and final positions of any realization. NEB simulations were performed using 100 replicas and inter-replica spring constant is set to $10^{-2} \text{ eV\AA}^{-2}$. Convergence was assumed when the maximum force acting on all of the atoms across all replicas was less than $1 \times 10^{-3} \text{ eV\AA}^{-1}$.

7.4 Results from NEB simulations

From the interaction energies for all solutes in each alloy, the theory predicts the characteristic length scales (ζ_c, w_c), the energy barrier ΔE_b , and the zero-temperature yield stress τ_{y0} as shown in Table 7.1. Direct simulations of long edge dislocations inserted into the random alloy and relaxed at $T=0\text{K}$ were previously performed by Maresca and Curtin [93] and the length scales (ζ_c, w_c) were then derived from examination of the correlation function along the long wavy dislocation. These values are shown in Table 7.1 and agree well with the theoretical values. Here we compare the direct NEB results to the theory predictions.

Table 7.1 – Characteristic length scale and energy barrier, mean(\cdot) \pm standard deviation(\cdot) of the corresponding distributions, as measured by direct NEB simulations and as predicted by theory [93] for two model alloys.

Alloy	Method	ζ_c (Å)	w_c (Å)	ΔE_b (eV)	τ_{y0} (MPa)
NbTaV	Theory [93]	27.6	12.0	1.949	517
	Direct MS [93]	28.7	10.0	–	496
	NEB - this work	–	17.7 \pm 9.1	1.95 \pm 1.23	293
MoNbTaW	Theory [93]	43.6	12.1	2.645	422
	Direct MS [93]	51.8	9.1	–	470
	NEB - this work	–	11.3 \pm 4.5	2.43 \pm 1.33	410

We first present results for the NbTaV random alloy (see Methods). Figure 7.2 shows the entire energy landscape. Many local minima and maxima are found, as expected, indicated by blue and red dots, respectively. From the two random realizations of total length 2500 Å, $N=71$ maxima are found. The average barrier ΔE_b is found to be 1.95 eV, matching the theoretical value very well (see Table 7.1). The relatively large standard deviation for the barriers is expected. The average barrier spacing that corresponds to w_c is $w_c^{\text{NEB}} = L/2N = 17.7$ Å. Several very small barriers (<0.2 eV) that span a few angstrom are disregarded; including these decreases ΔE_b and w_c by 7% and 6.5%, respectively, thus having little effect on τ_{y0} . As seen in Table 7.1, the value of w_c is somewhat larger than both the predicted value and the value deduced from the correlations along an individual relaxed dislocation. We have no explanation for the differences in w_c , which affects the NEB-derived strength (see below), but have performed further convergence checks in the NEB to verify that no significant barriers were missed in the calculations. We do note that the standard deviation of w_c is rather large and encompasses the theoretical value.

The theory predicts that the dislocation line at length $L = \zeta_c$ should remain essentially straight. Fig. 7.3 shows the atomistic configurations of 12 successive minimum-energy dislocations along the glide plane using Common Neighbor Analysis in OVITO for visualization [155, 156]. The cores are spread on the glide plane, as expected (see Fig. 7.1), and variations from a straight dislocation are quite minimal. As noted by Varvenne et al. [172], the theory based on line tension does not apply for fluctuations at the scale of the atomic spacing. So roughness on the atomic scale can exist but is outside the scope of the theory. It was argued in Varvenne et al. that such roughness leads to small energy barriers that are easily overcome at finite temperature, so that strength at finite T is mainly controlled by the larger-scale barrier over glide distance w_c .

The theory also assumes that the dislocation remains essentially straight as it moves through the energy landscape from minimum to maximum and then back to the next local minimum. Figures 7.4(a,c) show typical examples of the dislocation configurations corresponding to different average dislocation position along the minimum energy path between two adjacent

Chapter 7. Analysis of high energy barriers for edge dislocation motion in BCC high-entropy alloys

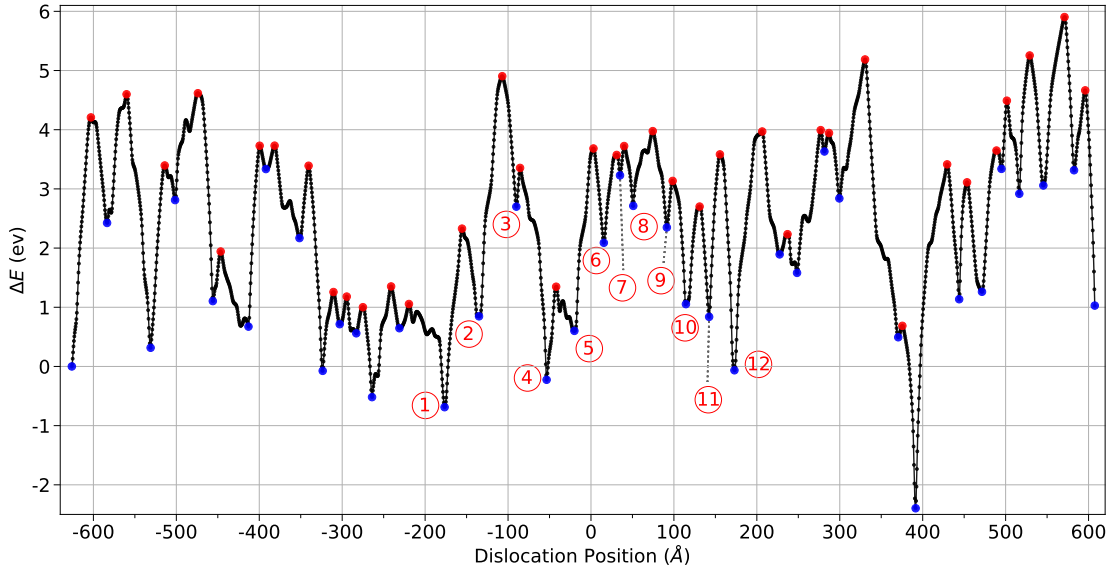


Figure 7.2 – **Energy landscape $E(x)$ versus position x for a dislocation moving through one entire simulation cell for NbTaV.** Minima and maxima are labelled blue and red, respectively. Numbered labels correspond to dislocation configurations shown in Fig. 7.3. Few of the labelled paths are shown in Fig. 7.4 in more detail.

minima, for two different barriers. The dislocation again remains fairly straight as it moves over the distance $2w_c$, in agreement with the theory.

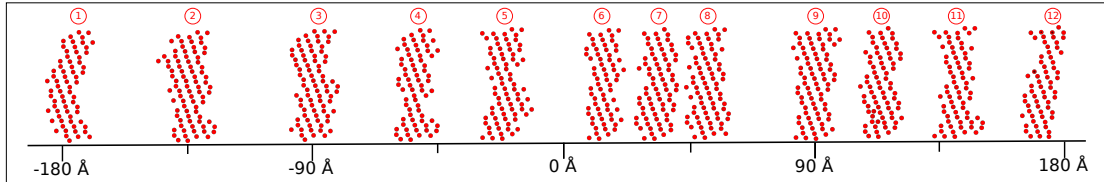


Figure 7.3 – **Dislocations at their minimum energy locations on 360 Å portion of the long NbTaV sample.** The distribution of the distances between the dislocations can also be observed. The dislocations are labelled and can be matched with their energies on Figure 7.2.

Similar results are found for the MoNbTaW alloy. Each individual NEB simulation provides a distance between adjacent minima and the path between them, with an associated energy barrier. Over 100 NEB simulations, the mean of the local minima/maxima spacing w_c and mean of the energy barrier ΔE_b are both shown in Table 7.1. Very good agreement is found between our NEB simulations, the parameter-free theory, and direct atomistic simulations of long wavy dislocations. A typical example of the NEB path and atomistic configurations along the path are shown in Fig. 7.5 for MoNbTaW. As found for NbTaV, the dislocation segment remains quite straight as it moves through the barrier from initial to final configuration (see Fig. 7.5). Similar behavior is found for the other individual configurations.

The above results for both NbTaV and MoNbTaW demonstrate both qualitatively and quan-

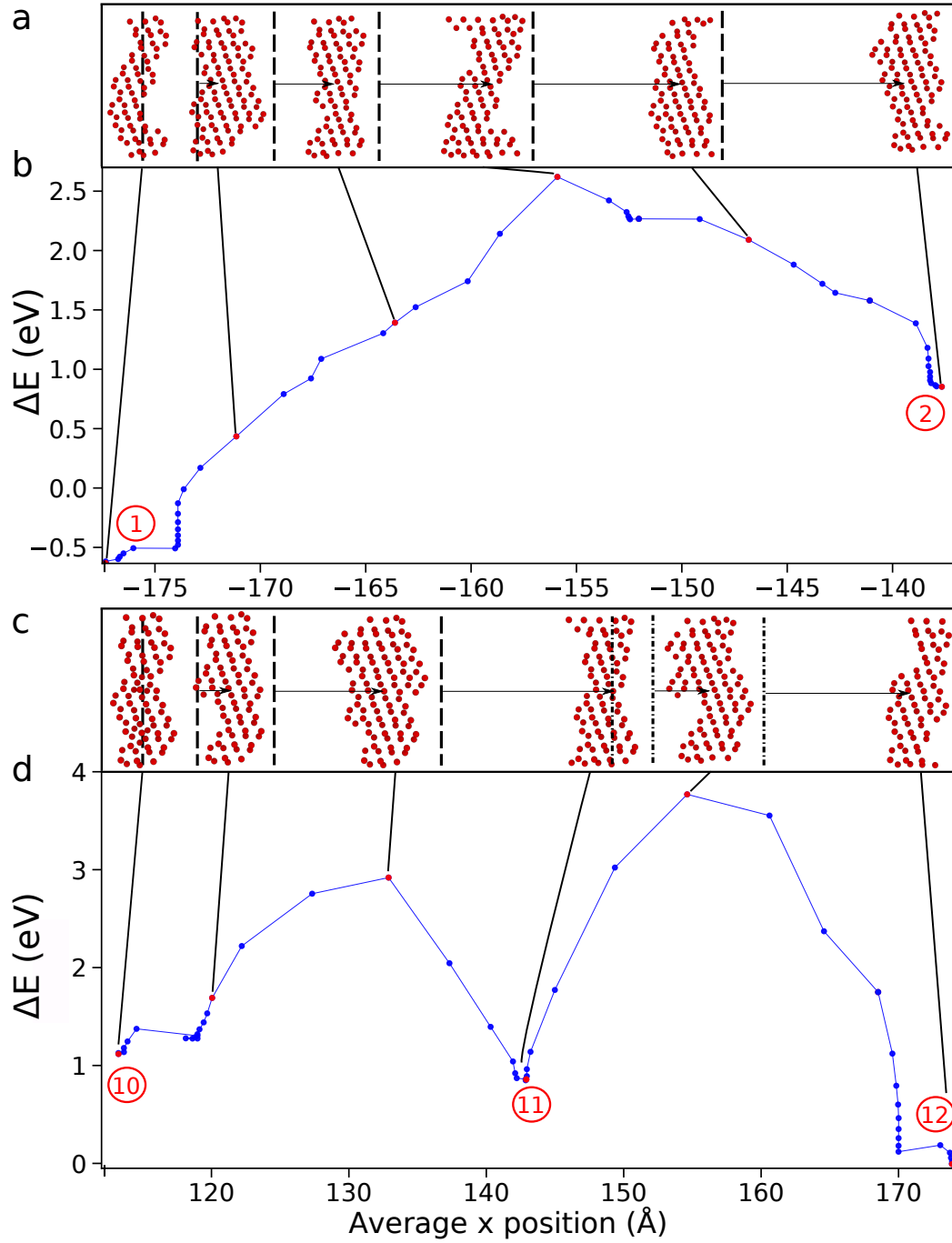


Figure 7.4 – **Energy and shape of an edge dislocation through its minimum energy path in NbTaV.** (a,c) Edge dislocation configurations at several positions along the minimum energy paths, with the dashed lines indicating the original position of the minima to show the glide distance clearly. (b,d) Minimum energy paths (energy versus mean dislocation position) for the dislocations moving from one minimum to the next in one region of the true random alloy. The labels can be matched with those in Figures 7.2 and 7.3.

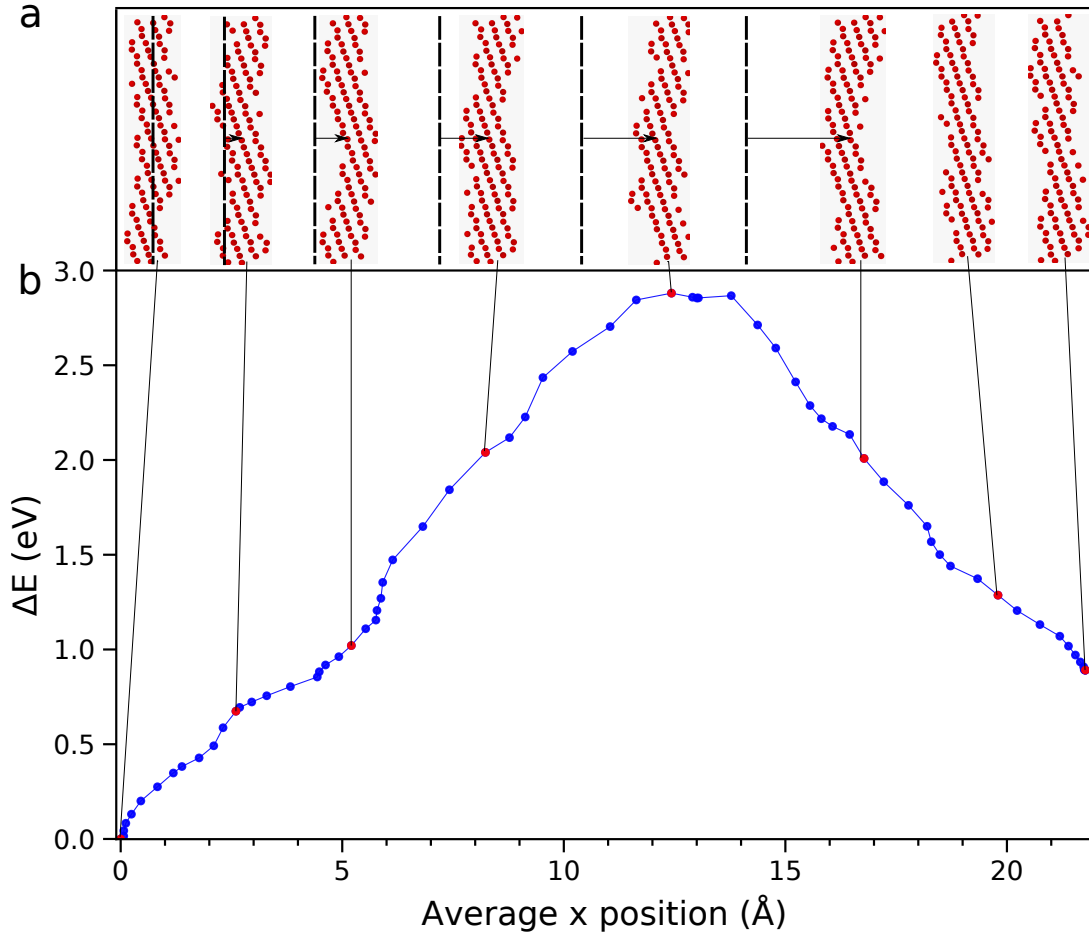


Figure 7.5 – **Energy and shape of an edge dislocation through its minimum energy path in MoNbTaW.** (a) Edge dislocation configuration at several positions along the minimum energy path, with the dashed lines indicating the original position to show the glide distance clearly. (b) Minimum energy path (energy versus mean dislocation position) for the dislocation moving from one minimum to the next in one region of the true random alloy.

titatively the features emerging from predictions of the theory. For a dislocation segment length fixed at the theoretical value of ζ_c , the NEB studies find that (i) the average energy barriers are very large ($\approx 2\text{ eV}$) in very good agreement with the predicted barriers, (ii) the dislocation energy landscape corresponds to minima and maxima separated by a typical spacing w_c that is comparable to the theory, and (iii) the dislocation segments of length ζ_c remain quite straight throughout their entire migration through the rough energy landscape. The essentially 1-dimensional energy landscape postulated and predicted by the theory is thus fully confirmed by the present simulations.

We now turn to the final fundamental aspect of edge dislocation motion: the evolution of the energy barrier under stress and the associated alloy flow stress as a function of temperature and strain rate. It is computationally demanding to perform direct NEB simulations over a

range of stresses for each of the hundreds of barriers studied here and so we take an accurate analytic approach as follows. Starting with the zero-stress energy landscape $E(x)$ as a function of mean dislocation position x (see Figures 7.2, 7.4 and 7.5), the work done by an applied resolved shear stress τ on the glide plane is $-\tau b\zeta_c x$. Even if the dislocation does not remain perfectly straight, the area swept during the motion is still exactly $b\zeta_c x$ when x is the mean dislocation position and the work done remains the same. The total energy landscape at stress τ is then $E^{\text{tot}}(x) = E(x) - \tau b\zeta_c x$. In this new landscape, the individual energy barriers between local minima and adjacent maxima are computed numerically from the NEB landscape $E(x)$. With increasing applied stress, each barrier is reduced steadily, and we can compute the spectrum of barriers $\Delta E_b(\tau)$ at any τ . For each individual barrier, there is a zero-temperature “flow” stress at which the stable local minimum disappears and the barrier becomes zero; this occurs when $dE^{\text{tot}}(x)/dx = 0$ locally. To explicitly validate the analytic approach, we performed direct NEB simulations versus stress for a few typical barriers in MoNbTaW and find that the barrier height versus stress matches the analytical value nearly perfectly in all cases.

Figs. 7.6(a,b) show the cumulative distribution of energy barriers over a range of applied shear stresses for both the NbTaV and MoNbTaV alloys. At zero stress, the barriers span a wide range from near 0 eV to 6 eV. With increasing stress, all barriers are steadily reduced, leading to a leftward shift. Furthermore, an increasing number of barriers are reduced to zero; these are included in the cumulative distribution and so are reflected in the non-zero initial value of the cumulative probability at zero energy.

The theory is developed in terms of a characteristic (mean) barrier and hence mean strength, so that we should compare the theory predictions to the stress at which 50% of the barriers have been reduced to zero. The original formulation of the theory rationalized this choice as follows. A long dislocation moves through a rough (stochastic) potential energy landscape with characteristic length scales ζ_c along the line direction and w_c along the glide direction, and characteristic energy barriers between adjacent minima of ΔE_b . Individual segments of length ζ_c encounter the spectrum of barriers as the entire dislocation moves forward. However, individual segments cannot advance much beyond nor lag much behind the average dislocation position. In advancing beyond, segments are pulled back by the remaining line. In lagging behind, segments are pulled forward by the advanced line. The motion of the long dislocation is thus controlled by neither statistically weaker nor stronger local barriers. This behavior can be observed in direct simulations, but is difficult to quantify. At 50% probability, there are an equal number of advanced and lagging segments, i.e. the dislocation retains the roughness of the relaxed dislocation in the zero stress landscape, and there are no net forces due to segment interactions. Since our goal is to compare to the theory, we use this 50% level here.

The characteristic 50% stress for the zero temperature strength as obtained from Figs. 7.6(a,b) is shown in Table 7.1 for each alloy. The mean strength for NbTaV is 293 MPa. This value only ~60% of the theoretical prediction, a difference that stems solely from the larger typical value

Chapter 7. Analysis of high energy barriers for edge dislocation motion in BCC high-entropy alloys

of w_c found in the NEB simulations while the average energy barrier ΔE_b is very similar to the theory. The w_c deduced from the wavy dislocation scale in NbTaV was, in contrast, slightly smaller than the theory prediction. As discussed earlier, the origins of these differences in w_c are unclear. The NbTaV alloy does show a comparatively large fraction ($\sim 15\%$) of rather low barriers (< 0.4 eV) that are eliminated at very low stress; this may contribute to the reduced average strength. The mean strength for MoNbTaW is 410 MPa, which compares quite well to both the theory prediction of 422 MPa and the direct atomistic simulation of 470 MPa. In this alloy, all three values for w_c are quite comparable, the predicted and NEB energy barriers are also quite close, and there are no very small barriers. Hence all the strengths agree well for MoNbTaW.

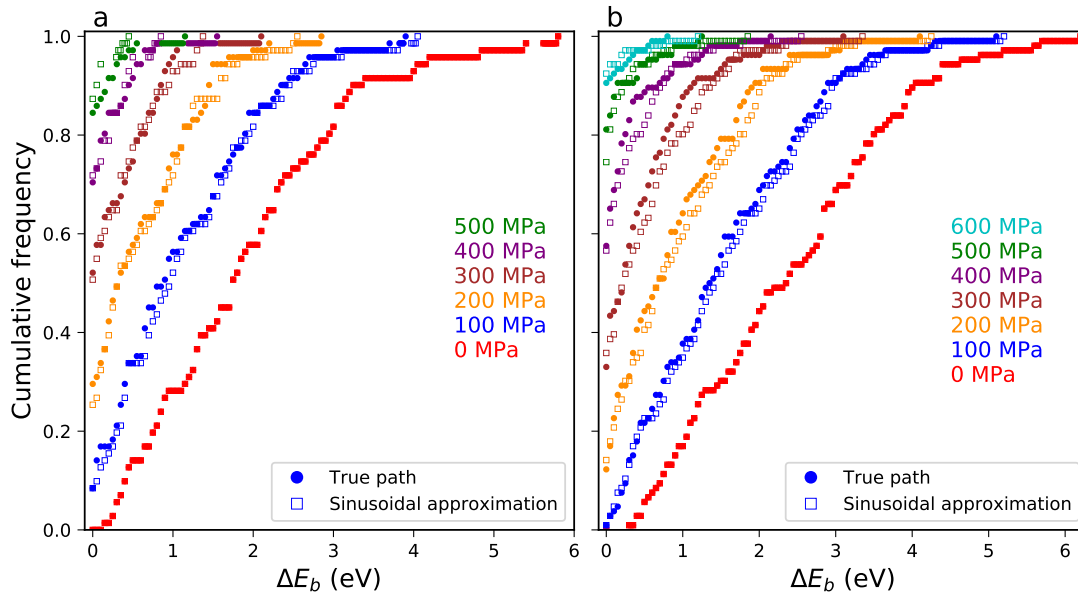


Figure 7.6 – **Cumulative probability distribution of energy barriers versus applied shear stresses.** The barriers are computed using the NEB energy landscape $E(x)$ for (a) NbTaV and (b) MoNbTaW. The same distribution computed using the theoretical sinusoidal model for the local barrier is also shown, and agrees well.

Finally, in solute strengthening theories, the energy landscape is assumed to have a locally sinusoidal shape between the minimum and the maximum, which leads to the stress-dependent energy barrier given by Eq. (7.5). Here, we assess this assumption by extracting the values ΔE_b and w_c from the direct NEB results and use the analytic result of Eq. (7.5) based on a sinusoidal model to predict the energy barriers at finite applied stress. The results are shown in Fig. 7.6, and the distribution agrees very well with the full analysis based on the actual (non-sinusoidal) energy landscapes found in the NEB at all stress levels. The sinusoidal approximation of the energy barrier, and its associated $T=0K$ strength, is thus quite accurate.

7.5 Application to real alloys

Both the analytical theory and direct NEB show that there are very large zero-stress energy barriers of 1.95 eV for NbTaV and 2.45-2.65 eV for MoNbTaW. These values are significant, meaning that high stresses are needed to overcome these barriers, even at high temperatures, and thereby cause plastic flow in the alloys. The strain-rate and temperature-dependent flow stress of an alloy follows from the thermally-activated Arrhenius model that connects the plastic strain-rate $\dot{\epsilon}$ to the energy barrier via $\dot{\epsilon} = \dot{\epsilon}_0 \exp(-\Delta E(\tau))/kT$ where $\dot{\epsilon}_0 = 10^4 \text{ s}^{-1}$ is a reference strain rate (see [171, 93]). Combining this relationship with Eq. (7.5) and inverting gives the finite-temperature, finite strain-rate flow stress $\tau_y(T, \dot{\epsilon})$. This equation holds for low temperatures and/or high stresses ($\tau_y/\tau_{y0} > 0.5$) [93]. At higher temperatures and/or low stresses, the long dislocations ($L \ll \zeta_c$) can explore higher wavelength fluctuations with larger barriers that have a similar scaling [84]. To cover the full range of temperatures, Maresca et al. [93] proposed the approximate form

$$\tau_y(T, \dot{\epsilon}) = \tau_{y0} \exp \left[-\frac{1}{0.55} \left(\frac{kT}{\Delta E_b} \ln \frac{\dot{\epsilon}_0}{\dot{\epsilon}} \right)^{0.91} \right]. \quad (7.7)$$

The uniaxial tensile yield strength in a polycrystalline alloy is then computed as $\sigma_y = M\tau_y$ where $M = 3.067$ is the Taylor factor for an untextured BCC polycrystal deforming by edge dislocation motion. It is clear that the large values of ΔE_b lead to significant strength retention with increasing temperature.

To enable application of the edge theory for alloy design, Varvenne et al. [172] developed a simplified elasticity theory for FCC alloys that was later extended to BCC alloys [83]. The theory uses the elasticity approximation $U_n(x_i, y_j) = -p(x_i, y_j)\Delta V_n$ where ΔV_n is the misfit volume of a type- n atom in the alloy and $p(x, y)$ is the edge dislocation pressure field. Assuming a common dislocation structure (spreading of the BCC edge dislocation) then led to analytic estimates of the T=0K strength and energy barrier as

$$\begin{aligned} \tau_{y0} &= 0.040 \alpha^{-\frac{1}{3}} \bar{\mu} \left(\frac{1 + \bar{\nu}}{1 - \bar{\nu}} \right)^{\frac{4}{3}} \left[\frac{\sum_n c_n \Delta V_n^2}{\bar{b}^6} \right]^{\frac{2}{3}} \\ \Delta E_b &= 2.00 \alpha^{\frac{1}{3}} \bar{\mu} \bar{b}^3 \left(\frac{1 + \bar{\nu}}{1 - \bar{\nu}} \right)^{\frac{2}{3}} \left[\frac{\sum_n c_n \Delta V_n^2}{\bar{b}^6} \right]^{\frac{1}{3}}. \end{aligned} \quad (7.8)$$

Here, $\bar{\mu} = \sqrt{\bar{C}_{44}(\bar{C}_{11} - \bar{C}_{12})/2}$, $\bar{\nu} = \frac{3\bar{B} - 2\bar{\mu}}{2(3\bar{B} + \bar{\mu})}$ are the isotropic elastic constants with Bulk modulus $\bar{B} = (\bar{C}_{11} + 2\bar{C}_{12})/3$, all computed using a simple rule-of-mixtures of the elemental values. \bar{b} is the alloy Burgers vector computed using Vegard's law for the alloy atomic volume, and $\alpha = 1/12$ is a numerical coefficient related to the dislocation line tension. The strength versus temperature and strain rate can then be computed using Eqn. 7.7. The numerical coefficients above were determined by fitting to results of the full theory across a range of alloys in the Mo-Nb-Ta-V-W family, with the fit being most accurate for the high-barrier/high-strength

Chapter 7. Analysis of high energy barriers for edge dislocation motion in BCC high-entropy alloys

alloys. The simplified theory depends only on elastic moduli and atomic misfit volumes, and was implemented for preliminary design across 10^7 different compositions in the Al-Cr-Hf-Mo-Nb-Ta-Ti-W-Zr family [83] to identify promising high-T alloys.

Here, we use the reduced analytic theory to understand the strengths in several alloys recently reported. The first group of alloys consists of the base alloy of HfNbTaTiZr with additions of Mo. Specifically, Mo was substituted for Nb and Ta to create HfTaTiZrMo and HfNbTiZrMo and was also added to the base alloy to create HfNbTaTiZrMo; note that our labelling of the alloys now does not follow conventional alphabetical order of elements but instead appends the new element (Mo) to the end of the elemental list. Table 7.2 shows the atomic volumes and elastic constants used to make predictions via Eqs. 7.8. In this family of alloys, Mo has the smallest atomic volume, leading to the largest misfit volume, and also the largest elastic moduli. Mo substitution or addition to HfNbTaTiZr is thus predicted to give significant strengthening. Figure 7.7a shows the experimental strengths as reported in [137, 76] versus the predicted strengths, at temperatures $T=0^\circ\text{C}$, 1000°C , and 1200°C , and strain rate $\dot{\epsilon} = 10^{-3} \text{ s}^{-1}$. Agreement between theory and experiment is very good at both $T=0^\circ\text{C}$ and 1000°C . Most notably, the theory captures the very significant strengthening achieved due to the addition or substitution of Mo. We discuss the deviation at 1200°C below.

Table 7.2 – Single-element properties used in the reduced edge theory predictions. The list shows the elemental BCC atomic volume, the elastic moduli and the experimental vacancy formation energy E_{vf} .

Element	Volume (\AA^3)	C_{11} (GPa)	C_{12} (GPa)	C_{44} (GPa)	E_{vf} (eV)
Cr	12.321	339.8	58.6	99	2.2 ± 0.2 [106]
Hf	22.528	131	103	45	2.0 (est.) [4]
Mo	15.524	450.02	172.92	125.03	2.9 ± 0.3 [106]
Nb	17.952	252.7	133.2	30.97	2.85 ± 0.25 [106]
Ta	17.985	266.32	158.16	87.36	2.95 ± 0.15 [106]
Ti	17.387	134	110	36	1.55 [4]
V	14.020	232.4	119.36	45.95	2.15 ± 0.05 [106]
W	15.807	532.55	204.95	163.13	3.8 ± 0.3 [106]
Zr	23.02	104	93	38	1.7 [4]

The second group of alloys consists of the base alloys MoNbTaW and MoNbTaTiW to which V is added to create MoNbTaWV and MoNbTaTiWV, respectively, again with the added element V appended to the end of the alloy label. Table 7.2 shows the atomic volumes and elastic constants for these elements, see [83]. V has the smallest misfit volume among all these elements while its elastic constants are roughly comparable to those of Nb, Ta, and Ti; the V-containing alloys should thus be stronger than the base alloys but with less of an effect than Mo in HfNbTaTiZr. Figure 7.7b shows the experimental strengths versus the predicted strengths, again at $T=0^\circ\text{C}$, 1000°C , and 1200°C and strain rate $\dot{\epsilon} = 10^{-3} \text{ s}^{-1}$. While the quantitative agreement is not as good, the theory captures the notable strengthening due to the addition of

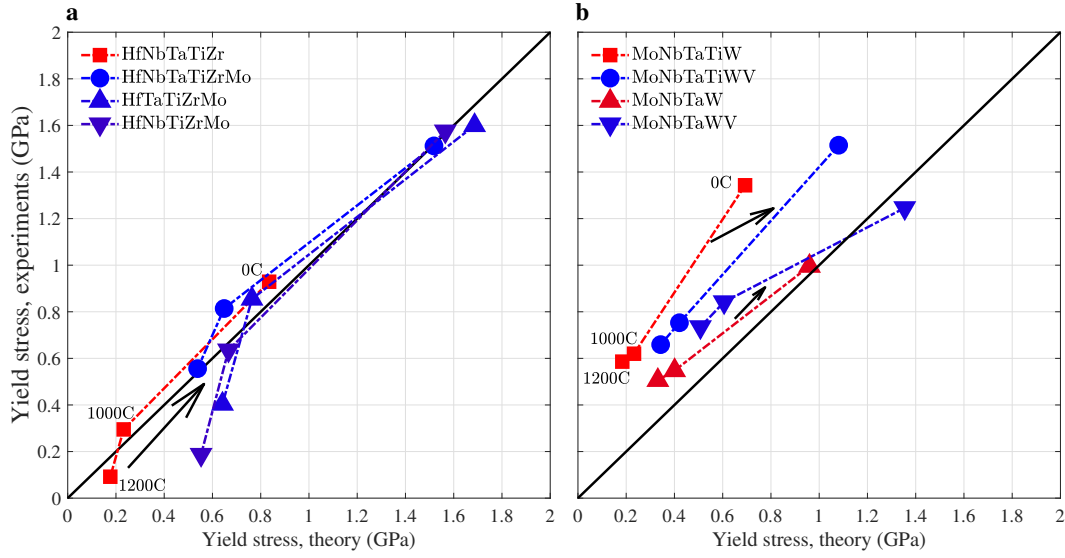


Figure 7.7 – **Yield strength theory predictions vs experiments at 0°C, 1000°C, and 1200°C** Alloys in the (a) HfNbTaTiZr(Mo) family show strengthening due to Mo additions and alloys in the (b) MoNbTaW(Ti)(V) family show strengthening due to V additions.

V in both alloys. We note that the enhanced strength of MoNbTaTiW relative to MoNbTaW, i.e. the role of the Ti addition to MoNbTaW, is not captured by the present theory; one possible origin is O or N contamination, well-established to significantly increase alloy strength.

The Hf-Mo-Nb-Ta-Ti-Zr alloys in Figure 7.7a show a strong loss of strength between 1000°C and 1200°C while the Mo-Nb-Ta-Ti-V-W alloys do not show such a loss of strength and instead continue to agree with the theory trend. High-temperature mechanisms that can defeat edge strengthening are unclear at this time. The random alloy presents edge barriers throughout the material on the scale of w_c and ζ_c and so avoiding these barriers seems difficult. The solute/dislocation interaction energies scale with alloy elastic moduli, but their decreases with temperature are modest for the refractory elements Mo, Nb, Ta, V, and W [41, 42]. We thus postulate that there is some vacancy-related mechanism, such as climb, by which the large edge barriers can be circumvented at sufficiently high temperatures. Such a mechanism would then scale with the vacancy formation energies in these alloys families. In the four Hf-Mo-Nb-Ta-Ti-Zr alloys, the vacancy formation energies estimated by a simple rule-of-mixtures (see Table 7.2) are in the range of 2.2-2.3 eV. In contrast, the estimated vacancy formation energies for the Mo-Nb-Ta-Ti-V-W alloys are higher, in the range of 2.65-3.1 eV. Thus, a mechanism operating at 1200°C in the Hf-Mo-Nb-Ta-Ti-Zr alloys that is related to the vacancy concentration ($c_V = e^{-E_{vf}/kT} \approx 2 \times 10^{-8}$) would require a temperature of 1600°C in the Mo-Nb-Ta-Ti-V-W alloys to achieve the same vacancy concentration. The MoNbTaW and MoNbTaWV alloys do not show a significant drop in strength up until this range of temperature [143]. This analysis can also be related to the alloy melting points. The Hf-Mo-Nb-Ta-Ti-Zr alloy melting points have been estimated to be in the range of 2270-2360K [137] while the

Chapter 7. Analysis of high energy barriers for edge dislocation motion in BCC high-entropy alloys

melting points of the Mo-Nb-Ta-Ti-V-W alloys are much larger, in the range of 2620-3110 K. Hence the latter alloys are expected to retain strength up to higher temperatures [137]. In both families of alloys, the ratio of estimated vacancy formation energy to melting temperature is similar, $E_{\text{vf}}/k_b T_m \approx 11.5 \pm 0.5$, so that we cannot distinguish between vacancy-related mechanisms and any other high-T mechanisms that might operate.

It remains possible that the strength loss at high T arises because the strength is controlled by screw dislocations. Screw dominance has been observed in some BCC HEAs [28], and is the accepted situation for dilute BCC alloys. Theoretically Maresca et al. [94, 93] have shown that some BCC non-dilute alloys and HEAs are controlled by screw dislocations and others by edge dislocations. The high temperature strength of screw dislocations is controlled by cross-kinks that can be defeated by thermal vacancies [94, 119]. Hence, loss of screw strength would also be correlated with E_{vf} and/or T_m . While this mechanism is clear, it is difficult to determine reliable alloy parameters for application of the screw theory. It is thus not possible to determine whether the quantitative strength increase upon addition of Mo to HfNbTaTiZr could be attributed to strengthening of screw dislocations. In contrast, the strength at 0°C and 1000°C, and the role of Mo, are well-captured by the *parameter-free* edge theory. The edge theory should thus be a lower bound for strength and, being analytic, serves as a very useful theory for alloy design/selection. The mechanism(s) of strength loss at high T remain to be resolved; this is a critical open question for BCC HEAs.

In summary, the recent theory of strengthening of edge dislocations in BCC high entropy alloys has been quantitatively supported by detailed atomistic NEB simulations of the complex energy landscape for edge dislocations in two random alloys, NbTaV and MoNbTaW. The analysis reveals the high energy barriers encountered by edge dislocations, and the magnitude and spacing of these barriers is in good agreement with the analytic predictions of the theory. The simulations here further show that the dislocations remain quite straight over the characteristic scale ζ_c , as predicted by the theory. The stresses required for dislocation motion are also comparable to those observed in limited direct simulations. The present work thus supports the theory for critical features of strengthening in two different refractory BCC HEAs. A reduced version of the theory has then been applied to two families of alloys. The theory rationalizes the observed significant increases in strength caused by addition of solutes with large misfit volumes that is a hallmark of the edge theory. The high temperature mechanisms of strength loss remain unknown but appear correlated with vacancy formation energy and/or melting temperature. The reduced analytic theory (Eq. (7.8)) provides a validated mechanistic path for selection of BCC HEA compositions for high strength that can be reaffirmed by application of the full theory for the most promising compositions. The strength theory can also be combined with other performance metrics to identify new compositions that are strong at high temperatures, ductile, single-phase, and/or oxidation-resistant, fulfilling the multi-performance requirements of many applications.

8 Model of Dynamic Strain Aging in BCC High-Entropy Alloys

This chapter is extracted from the following publication

Ghafarollahi, Alireza, and William A. Curtin. "The strength plateau at intermediate temperatures in BCC High-Entropy Alloys: a Dynamic Strain Aging mechanism." *Under preparation*

High Entropy Alloys, i.e. multicomponent non-dilute near-random crystalline metals [98, 99, 57, 46], are showing remarkable mechanical properties such as yield strength [198, 144, 83], ductility [87], fracture toughness [54, 53, 193], and resistance to hydrogen embrittlement [201, 200, 108, 206]. With millions of possible compositions within just one crystal structure, there is a significant effort to understand the detailed underlying deformation mechanisms as a function of the alloy crystal structure, composition, temperature, and thermodynamics, so as to aid the discovery of new alloys that can satisfy many different performance requirements.

The BCC refractory HEAs composed of the family of Cr-Mo-W-V-Nb-Ta-Ti-Zr-Hf-Al are of particular interest due to their high-temperature strength retention [142, 145, 140, 139, 141, 138], exceeding the capabilities of current superalloys, although improvements in low-temperature ductility are needed [145, 91]. For instance, the two well-studied MoNbTaW and MoNbTaVW alloys retain strengths of 400 and 480 MPa at 1600C [145]. Very recent theoretical and experimental studies have proposed that yield strength in these and other BCC HEAs is controlled by edge dislocation [93, 83]. The theory predicts that edge dislocations face very high energy barriers to motion, leading to high strengths and high strength retention at elevated temperatures and attaining good agreement with various experiments. Screw dislocations are also significantly strengthened [94, 50], and may dominate the deformation as in dilute BCC alloys [49, 48]. Screw strengthening includes strengthening due to the formation of jog/cross-kink defects that fail by formation of energetically-costly vacancy and self-interstitial defects, and this can also convey high temperature strength [94].

Existing theories predict that both edge and screw strengths are controlled by thermal acti-

vation, leading to a temperature- and strain-rate-dependent yield strength. While strength generally decreases with increasing temperature, as expected, many of the HEAs show a distinct plateau in strength versus temperature at intermediate temperatures, as seen in Figure 8.1 for a selection of alloys. At higher temperatures, the strength then decreases again, either rapidly or gradually. A true plateau in yield strength corresponds to an alloy with zero strain rate sensitivity (SRS), and it is difficult theoretically to identify mechanisms that have zero SRS. Very low SRS can be achieved for processes that have a very high energy barrier, such as forest hardening, i.e. the breaking of dislocation junctions, and precipitate hardening, i.e. shearing or looping of precipitates in the alloy. Neither of these mechanisms controls the initial yield strength in precipitate-free, well-annealed HEAs, however. The formation of screw cross-kinks may be athermal, but current models result in temperature-dependent cross-kink strengthening and screw strengthening may not control strength in all of the alloys where the plateau is observed. Thus, the origins of the intermediate-temperature strength plateau remain unknown. Understanding the mechanism(s) of this plateau would identify what features of the alloy control this regime of deformation, enabling possible tuning of strength in this domain that could also be important for manufacturing. In addition, understanding of this phenomenon would either cement our knowledge of the deformation mechanisms in BCC HEAs or necessitate the development of new mechanism(s) that might then be controlled or exploited.

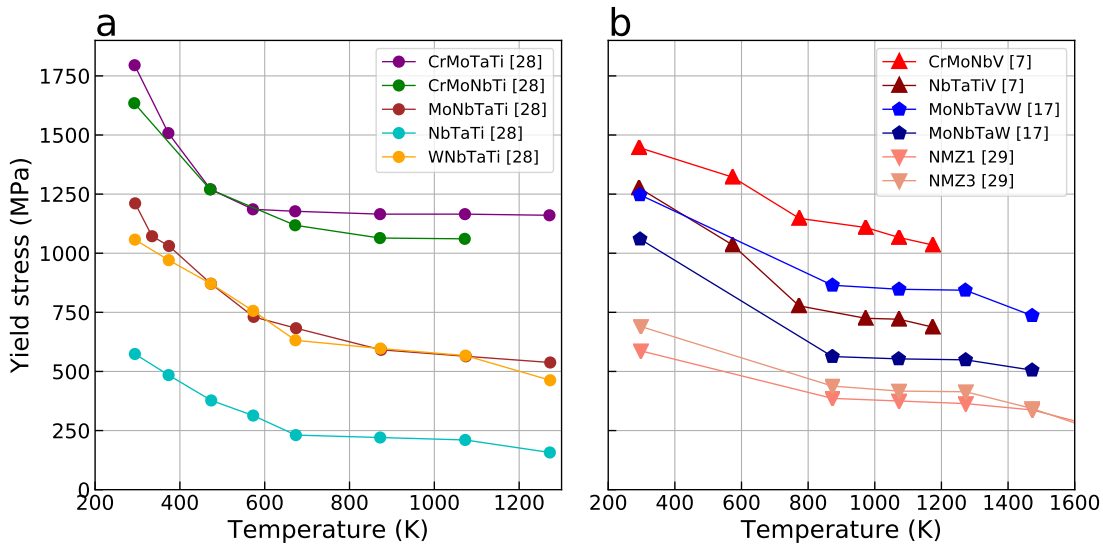


Figure 8.1 – Experimental data of yield stress versus temperature for various BCC HEAs. The experimental data for BCC metals in (a) exhibit a plateau in strength over the temperature range of $\approx 700 < T < \approx 1200$, while those in (b) show a plateau for $\approx 900\text{K} < T < \approx 1300\text{K}$.

Here, we examine one possible mechanism for the intermediate-T strength plateau: the dynamic strain aging (DSA) process of solute diffusion immediately across the core of an edge dislocation. This mechanism, developed to explain DSA in dilute FCC alloys such as Al-Mg 5xxx alloys [30], can lead to a temperature domain of zero SRS followed by a subsequent resumption

of thermally-activated softening at higher temperatures [150, 151], as discussed below. This behavior aligns qualitatively with the observed behavior in BCC HEAs. We thus adopt the cross-core diffusion concept, generalize it to the non-dilute HEA case, and use atomistic simulations to demonstrate the temperature-dependent strengthening that results. An analytic model captures the major dependencies in terms of underlying material properties, and can thus be applied to other alloys. Quantitative agreement with experiments on MoNbTaW is achieved if there is a fairly high non-equilibrium vacancy concentration or accelerated vacancy diffusion in the dislocation core. This should drive further studies of realistic vacancy energetics and kinetics in these complex alloys.

The remainder of this paper is organized as follows. In the next Section, we introduce the cross-core diffusion mechanism and the energetic driving forces for it at the atomic scale. A model for the cross-core energy barrier is then presented and validated by the atomistic simulations. Section 8.1.5 discusses the kinetic model for cross-core diffusion to predict the time-dependence of the cross-core diffusion energy barrier. The energetic and kinetic models are then used in Section 8.2 to predict the strength of the model MoNbTaW HEA. Section 8.3 discusses aspects of the work here and summarizes our results.

8.1 Cross-core diffusion: mechanism and energetics

8.1.1 Solute strengthening

A dislocation in an alloy interacts with solutes, and the interaction energy of a type- n solute at position \mathbf{x} relative to the center of the dislocation is $U_{int}^n(\mathbf{x})$. Figure 8.2 shows the solute/edge dislocation interaction energies at many positions around an edge dislocation in a model MoNbTaW HEA as described using the Zhou et al. interatomic potentials [203], which have been shown to be suitable for reasonable quantitative modeling of BCC edge dislocations in these alloys. Details of the computational methods can be found in A.6. Due to local solute fluctuations in a random alloy, the dislocation becomes wavy. It is pinned in local low-energy regions over a characteristic segment length ζ_c , with adjacent local high-energy regions at a characteristic distance w_c along the glide plane [172, 93]. Under an applied stress, the motion of the dislocation is controlled by thermal activation of these segments out of their local energy minima and over the adjacent energy maxima. This determines the temperature- and strain-rate-dependent flow stress in a random alloy in the absence of any solute diffusion processes.

An edge dislocation generates an elastic pressure field. In an alloy, each atomic species can be viewed as a solute in a hypothetical average matrix material, and thus each solute type n has a misfit volume ΔV_n in that average matrix. The interaction energy of a solute with the pressure field $p(x)$ at atomic position x around the edge dislocation in the average matrix is $U_{int}^n(x) = -p(x)\Delta V_n$. This interaction energy dominates the solute strengthening in the random alloy.

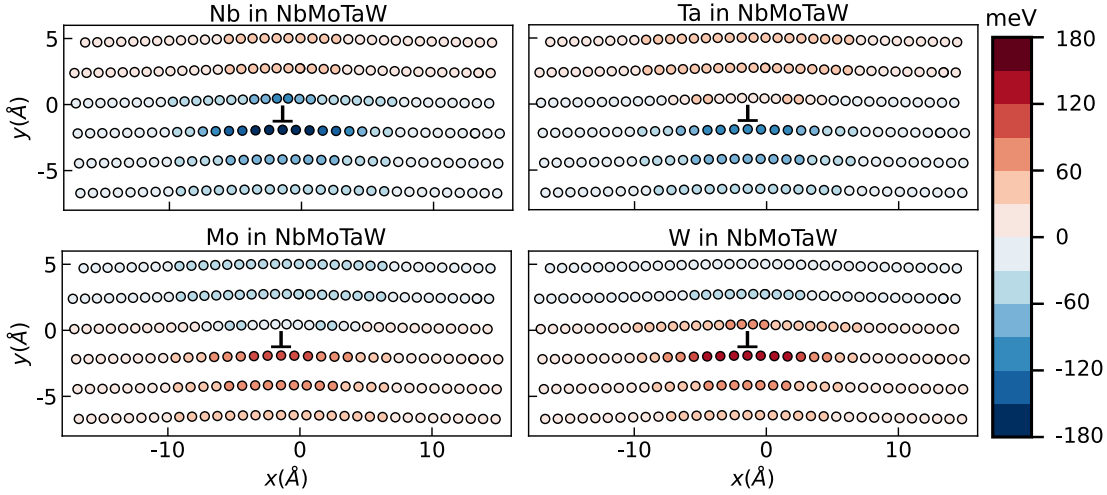


Figure 8.2 – Interaction energy map of Nb, Ta, Mo, and W solutes with the edge dislocation in the average-atom MoNbTaW alloy computed by Zhou et al. EAM-type interatomic potentials [203].

8.1.2 Cross-core diffusion

Solute atoms in the atomic planes immediately above and below the glide plane have different signs of the pressure field, and hence there is an energetic driving force for a solute to move from one side of the glide plane to the other. The pressure field is by far the largest in the core region of the dislocation, and so the energy difference is largest in the core region, leading to the labeling of this phenomenon as "cross-core" diffusion. Cross-core diffusion occurs during the time that the dislocation is pinned in the local minima created by the initial random fluctuations.

Cross-core diffusion of solutes lowers the total energy of the dislocation/solute system at the current position of the dislocation. Glide of the dislocation thus requires an additional applied stress, and so cross-core diffusion leads to strengthening. Since the cross-core diffusion requires solute diffusion, it is a kinetic process. The longer the dislocation resides in its current position, the more solutes can diffuse, and the higher the strengthening. The cross-core diffusion strengthening thus depends on both temperature and strain rate, the latter imposing an average time that dislocations reside in their local solute environments before escaping and moving to new local environments. Cross-core diffusion is thus a mechanism of dynamic strain aging.

Importantly, since there are only a finite number of solutes in the core region, the cross-core process saturates. The driving forces for diffusion of solutes outside of the core are too slow to continue the aging process. In dilute FCC Al alloys [30], it was also found that the vacancy-mediated solute migration barrier in the very core could be substantially lower than that in the bulk [112], leading to greatly accelerated kinetics of solute diffusion across the core and thus further separating the time scales for bulk and cross-core diffusion.

8.1.3 Cross-core energetics

Modeling of cross-core diffusion in an HEA begins with an assessment of the energetic driving forces for solutes just above and below the glide plane and in the core region of the dislocation. As seen in Figure 8.2 for MoNbTaW, solutes Nb and Ta have positive misfit volumes and hence have lower interaction energies on the tension (top) side of the dislocation core. In contrast, Mo and W have negative misfit volumes and so have lower interaction energies on the compressive (bottom) side of the core. The interaction energies are not entirely due to misfit, and for this model alloy there is a "chemical" correction in the core for Nb and W that offsets the pressure field contribution on one side of the core. This leads to positive interaction energies on both planes just above and just below the core.

For the initial pinned dislocation prior to any cross-core diffusion, the solutes (e.g. Nb, Ta, Mo, W) will be found on both sides of the edge core. The diffusion of solutes from unfavorable (high energy) to favorable (low energy) locations across the core results in a lowering the total energy of the system. In the non-dilute alloy, the diffusion of solutes, while vacancy-mediated, eventually occurs in pairs, i.e. on net, solute pairs change positions across the core. Figure 8.3 shows the change in energy for different possible pairs of solute "swaps" upon motion from unfavorable positions to neighboring favorable positions across the core; due to symmetry, only one half of the paths are shown. Here and throughout the rest of the paper, the energy reductions due to swaps in solute pairs from unfavorable to favorable positions are expressed as positive quantities. Due to the similarities between Nb and Ta, and between Mo and W, transitions involving (Nb,Ta) pairs and (Mo,W) pairs have very low energy changes and are not shown. Swaps that are not "cross-core" also have significantly lower energy changes than "cross-core" swaps, and so are also not shown. Fig. 8.3 reveals that the swaps in solute pairs from unfavorable to favorable positions give rise to energy reductions of $\overline{\Delta W} \sim +0.2 \pm 0.05\text{eV}$ for all the different pairs over a core interaction region of width $w \approx 3b = 8.5\text{\AA}$. Solute swaps at distances beyond $w \approx 3b = 8.5\text{\AA}$ decrease steadily toward zero.

The number of cross-core swaps increases with time due to diffusion during the time over which the dislocation is pinned in the local minima. We define ρ as the density of diffused solutes per unit area of the dislocation core; the time dependence of ρ is not indicated but will be address later. With the diffusion of solutes occurring predominantly over a core width of w ($w = 8.5\text{\AA}$ in the model alloy) within the pinned segments of length ζ_c , we approximate the dislocation/solute binding energy change as $\rho w \zeta_c \overline{\Delta W}$ within $-w/2 < x < w/2$ and zero for larger $|x|$. The dislocation energy change solely due to the cross core diffusion can thus be expressed as

$$\Delta E^{xc}(\rho) = H(w - x) \rho w \zeta_c \overline{\Delta W} (1 - x/w) \quad (8.1)$$

where $H(\cdot)$ is the Heaviside step function.

To predict the additional strengthening after cross-core diffusion up to density ρ , we now develop and validate a model for the energy $E(x, \rho, \tau)$ of the dislocation/solute segment of

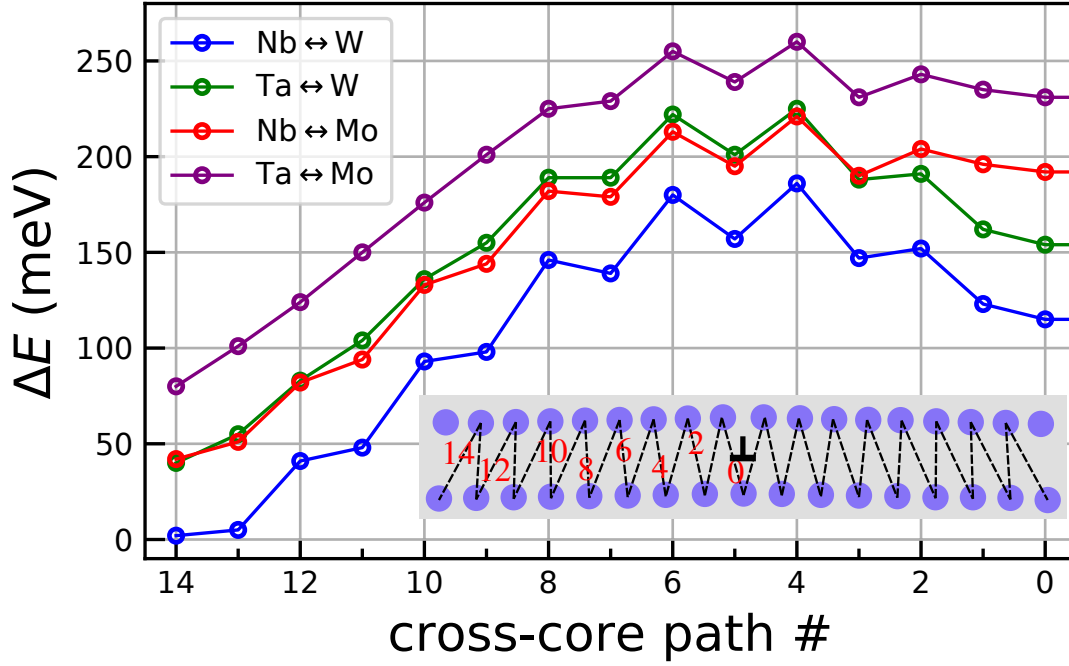


Figure 8.3 – Energy difference for different solute-types swaps versus transition paths across the core as numbered in the inset. Only transitions from higher to lower energy states have been considered in these calculations.

length ζ_c as a function of (i) the dislocation position x relative to its initial position at $x = 0$, (ii) the density of diffused solutes ρ per unit area of the core, and (iii) the applied stress τ . With $E^{(0)}(x)$ the energy landscape in the absence of applied stress and before any solute diffusion, the work done by an applied resolved shear stress over a glide distance x , and the energy change due to the cross core, the total energy is then

$$E(x, \rho, \tau) = E^{(0)}(x) - \tau b \zeta_c x - H(w - x) \rho w \zeta_c \overline{\Delta W} (1 - x/w) \quad (8.2)$$

which, after some algebra, can be re-arranged as

$$E(x, \rho, \tau) = E^{(0)}(x) - (\tau - H(w - x) \Delta \tau) b \zeta_c x - H(w - x) \rho w \zeta_c \overline{\Delta W} \quad (8.3)$$

Here,

$$\Delta \tau(\rho) = \rho \overline{\Delta W} / b \quad (8.4)$$

is the additional strengthening due to cross-core diffusion. The additional strengthening is directly proportional to the cross-core diffusion density and energy change $\overline{\Delta W}$ and independent of ζ_c , w , the original strength, or initial barrier. Eq. (8.3) is the stress- and solute-diffusion-dependent total energy landscape.

The energy barriers between local minima and adjacent maxima can be computed from Eq. 8.3 for each specific alloy realization and local initial energy landscape $E^{(0)}(x)$ of a pinned dislocation segment. The zero-temperature flow stress is the stress at which the stable local minimum disappears and the barrier becomes zero, and occurs when $dE(x, \rho, \tau)/dx = 0$. In the absence of cross-core diffusion, $\Delta E_b^{(0)}(\tau)$ is predicted by the model of Maresca et al. [93] and historical models as

$$\Delta E_b^{(0)}(\tau) = \Delta E_b^{(0)} \left(1 - \frac{\tau}{\tau_{y0}} \right)^{\frac{3}{2}} \quad (8.5)$$

where $\Delta E_b^{(0)}$ is the zero-stress energy barrier and τ_{y0} is the T=0 strength associated with the landscape $E_0(x)$. This result is for high stresses/low temperatures ($\tau > \tau_{y0}/2$) or low temperatures, with a modified result at lower stresses/higher temperatures that is neglected here for analytic simplicity. With cross core, the zero-T strengthening is simply $\tau_{y0} + \Delta\tau$ and the energy barrier ΔE_b as a function of applied stress and cross-core diffusion parameter ρ is then

$$\Delta E_b(\tau, \rho) = \Delta E_b^{(0)} \left(1 - \frac{\tau - \Delta\tau(\rho)}{\tau_{y0}} \right)^{\frac{3}{2}} \quad (8.6)$$

The model of Eq. (8.6) for the barrier versus the degree of cross-core diffusion is validated against atomistic simulations in the next section.

8.1.4 Validation of the cross-core energy barrier model

To assess the theoretical model for the energy landscape and thus the energy barrier due to cross-core diffusion, we execute NEB simulations in the model NbMoTaW alloy. An NEB simulation finds the minimum energy path (MEP) between two neighboring minimum energy states, and here is executed as a function of the degree of cross-core diffusion ρ . Details of the atomistic simulations to find the two adjacent minimum dislocation configurations can be found in a recent work [81]. The cross-core diffusion of solutes is then incorporated as follows. Starting from the initial minimum energy position in the absence of solute diffusion for a given realization of the random alloy, we randomly pick two neighboring solutes on either side of the dislocation core. We do not consider swaps for (Nb,Ta) or (Mo,W) pairs since these are negligible in this system. We then swap the two chosen atoms, minimize the total energy, and compute the energy difference due to the swapping. The swap is accepted if the energy is reduced and rejected if the energy is increased. As the swapping process continues, the cross-core diffusion density ρ increases, the initial minimum energy state is evolving, and NEB is executed for a sequence of configurations having increasing ρ . The solute swapping process is continued until no further energy reductions can be achieved, i.e. the cross-core diffusion has saturated.

A typical example of the evolution of the minimum energy path for a specific random realization as a function of actual solute-pair switches (density ρ) is shown in Figure 8.4. Here x is

computed as the mean dislocation position by averaging over the x component of the core position as identified by Common Neighbor Analysis. Cross-core diffusion around the initial state reduces the energy at the minimum position $x = 0$ and also during initial glide of the dislocation. Because the energy barrier at distance w_c is typically greater than w , however, the energy at the transition state and beyond is essentially unchanged by the cross-core diffusion. The energy barrier is thus increasing with increasing cross-core diffusion density ρ . The barrier energy changes are very large, with the barrier shown in Figure 8.4 evolving from ~ 1.5 eV to ~ 4 eV as diffusion progresses.

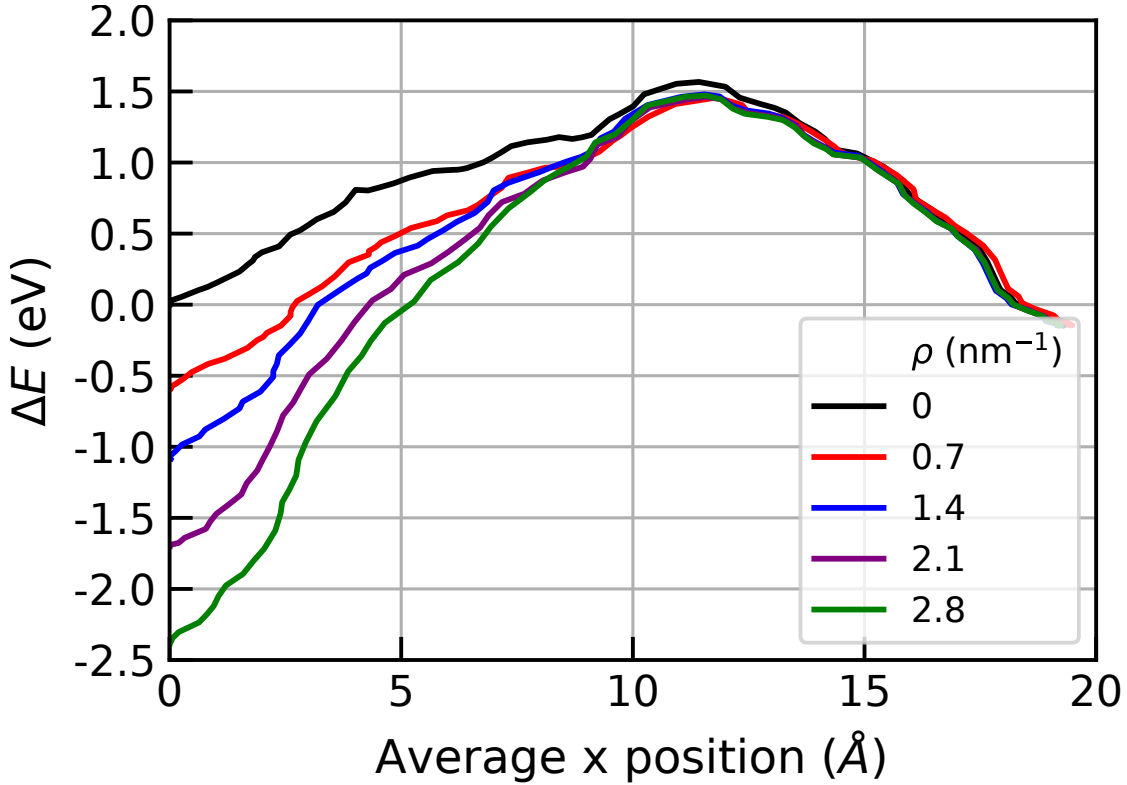


Figure 8.4 – NEB results for a sample MoNbTaW random alloy at different cross-core diffusion states ρ .

The NEB simulations provide the energy landscape $E(x, 0, \rho) = E^{(0)}(x) + \Delta E^{xc}$ in the absence of applied stress for a certain diffusion density ρ . The energy in the presence of the applied stress is then modeled using Eq. (8.2) above. To accurately examine the average barrier versus applied stress, 100 random realizations of the model alloy are studied. For each random realization, the energy barrier (max minus min) as a function of the applied stress τ is computed. Averaging over the 100 random realizations for the same number of accepted solute swaps (same density ρ), we obtain the atomistically-computed average energy barrier as a function of τ and ρ as shown in Fig. 8.5. The results of the analytical model of Eq. (8.6) are also shown and very good agreement is achieved. This analysis validates the analytical theory for the energy barrier versus ρ and τ .

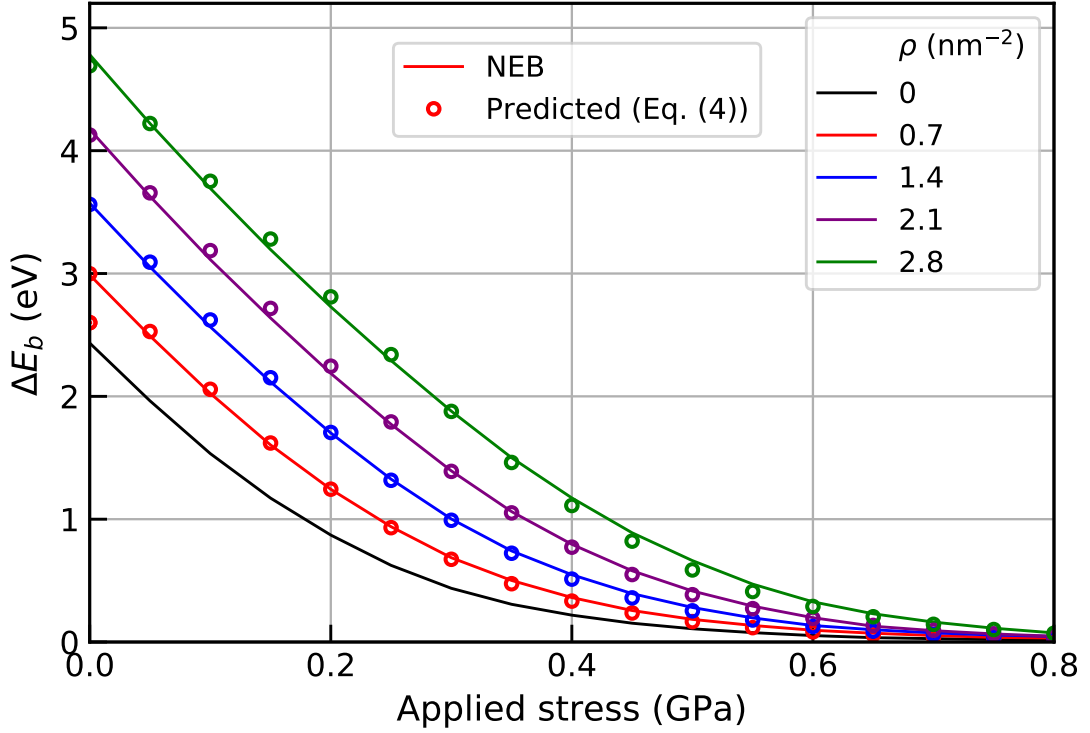


Figure 8.5 – Average energy barrier versus applied stress over 100 realizations of edge dislocation motion in random NbMoTaW alloy between two adjacent local minimum energy states for different number of solute swaps (diffused density ρ) as obtained by direct NEB simulations and predicted by theoretical model, Eq. (8.6) using an average solute-swap energy change of $\overline{\Delta W} = 200$ meV

8.1.5 Kinetic model of cross-core diffusion

Cross-core diffusion is a time-dependent mechanism, occurring while the dislocation is pinned. Thus, $\rho(t)$ is time-dependent, leading to a time-dependent energy barrier and, consequently, dynamic strain aging effects. Here, we model the kinetics of cross-core diffusion to obtain $\rho(t)$ and thus the time-dependent energy barrier for dislocation motion.

Let N_f and N_u denote, respectively, the total number of solutes per unit area of the dislocation core located in favorable (low energy) and unfavorable (high energy) sites in the core region. Moreover, assume that for every solute-pair swap the energy change is the average value $\overline{\Delta W}$. Now, noting that each site has two neighbors on the opposite side of the slip plane, the rate of transition from unfavorable to favorable and from unfavorable to favorable sides can, respectively, be expressed as

$$\Gamma_{u \rightarrow f} = 2\Gamma_c e^{-\beta \overline{\Delta W}/2} \quad (8.7)$$

and

$$\Gamma_{f \rightarrow u} = 2\Gamma_c e^{+\beta \overline{\Delta W}/2} \quad (8.8)$$

where $\beta = 1/kT$ and $\Gamma_c = \nu_0 e^{-\beta \Delta H_c}$ denotes the core transition rate having enthalpy barrier ΔH_c and ν_0 is an attempt frequency. The ratio of the above two rates is $e^{\beta \overline{\Delta W}}$ as required by detailed balance. The evolution of the number of solutes in favorable and unfavorable sites then follows the Master Equations

$$\begin{aligned} \dot{N}_f(t) &= \Gamma_{u \rightarrow f} N_u(t) - \Gamma_{f \rightarrow u} N_f(t) \\ \dot{N}_u(t) &= \Gamma_{f \rightarrow u} N_f(t) - \Gamma_{u \rightarrow f} N_u(t) \end{aligned} \quad (8.9)$$

where the dot denotes the time derivative.

With initial values $N_f = N_u = N_0$, the solution of the above equations is straightforward and the density of diffused solutes per unit area $\rho(t)$ is

$$\rho(t) = (N_f(t) - N_0) / w\zeta_c = \rho_\infty \tanh\left(\frac{\beta \overline{\Delta W}}{2}\right) \left(1 - e^{-\frac{t}{t_d}}\right) \quad (8.10)$$

Here t_d is the characteristic time scale for the diffusion process

$$t_d = \left(4 \cosh\left(\frac{\beta \overline{\Delta W}}{2}\right) \Gamma_c\right)^{-1} \approx \left(2\nu_0 e^{-\beta\left(\Delta H_c - \frac{\overline{\Delta W}}{2}\right)}\right)^{-1} \quad (8.11)$$

and ρ_∞ is the average maximum density of solutes at saturation. In theory, in a random alloy, $\rho_\infty = N_0 / w\zeta_c = 1/2b^2$. For NbMoTaW, this value would be $\rho_\infty = 6.4 \text{ nm}^{-2}$ but the atomistic simulations yield $\rho_\infty \sim 3.5 \text{ nm}^{-2}$; the difference arises, in part, because the initially-pinned solute already has more-favorable solutes than in a random environment.

Using Eqs. (8.1) and (8.10), the time-dependent change in energy barrier of the dislocation segment of length ζ_c due to cross-core solute diffusion is

$$\Delta E_b^{xc}(\rho(t)) = \Delta E_{b\infty}^{xc} \left(1 - e^{-\frac{t}{t_d}}\right) \quad (8.12)$$

where

$$\Delta E_{b\infty}^{xc} = \rho_\infty w\zeta_c \overline{\Delta W} \tanh\left(\frac{\beta \overline{\Delta W}}{2}\right). \quad (8.13)$$

is the maximum change in energy barrier achieved at saturation of the diffusion.

The time-dependent additional strength due to cross-core diffusion is then

$$\Delta \tau(\rho(t)) = \Delta E_b^{xc}(\rho(t)) / bw\zeta_c = \Delta \tau_\infty \left(1 - e^{-\frac{t}{t_d}}\right) \quad (8.14)$$

where

$$\Delta\tau_\infty = \left[\rho_\infty \overline{\Delta W} / b \right] \tanh \left(\frac{\beta \overline{\Delta W}}{2} \right) \quad (8.15)$$

is the maximum additional strengthening due to cross-core diffusion. Eqs. (8.12) and (8.14) constitute our main results for the present study.

8.1.6 Yield strength versus temperature

The previous sections have addressed the evolving barrier of a single dislocation as cross-core diffusion proceeds. We now need to connect this behavior to the dependence of the yield stress versus temperature (T) and strain-rate ($\dot{\epsilon}$). This is achieved using Orowan's Law and thermal-activation theory. However, since the energy barrier is now time-dependent, the analysis is more complex than in the standard situation where the barrier is independent of time. We follow closely the analysis of Soare et al. [150, 151] to obtain the yield stress.

At constant strain rate $\dot{\epsilon}$, Orowan's law dictates that the average waiting time t_w of a dislocation must satisfy

$$\dot{\epsilon} = \Omega / \bar{t}_w \quad (8.16)$$

with $\Omega = \rho_m b \bar{d}$ where ρ_m is the mobile dislocation density and $\bar{d} \sim w_c$ is the average flight distance between dislocation pinning points. Using typical values of $\rho_m = 10^{12} \text{m}^{-2}$ and $w_c \approx 10 \text{\AA}$, $\Omega \approx 10^{-7}$. The yield stress τ is then the stress at which the average waiting time is \bar{t}_w .

The plastic flow involves escape of the dislocations from their (evolving) locally-pinned environments. Starting at the absolute time t_p at which a dislocation last became pinned (i.e. arrive at the current pinning location) and at a stress τ , the instantaneous rate of escape over the time-dependent energy barrier at a later time t is

$$r(\tau, t - t_p) = \nu_0 \exp \left(- \frac{\Delta E_b(\tau, \rho(t - t_p))}{kT} \right). \quad (8.17)$$

where ν_0 is the microscopic attempt frequency for escape over the barrier. The stress- and time-dependent energy barrier with cross-core diffusion (Eq. (8.6)) is

$$\Delta E_b(\tau, t - t_p) = \Delta E_b^{(0)} \left(1 - \frac{\tau - \Delta\tau(\rho(t - t_p))}{\tau_{y0}} \right)^{\frac{3}{2}}. \quad (8.18)$$

The average waiting time \bar{t}_w is then the mean of the escape probability

$$\bar{t}_w = \int_0^\infty \exp \left(- \int_{t_p}^t r(\tau, t' - t_p) dt' \right) dt \quad (8.19)$$

This expression connects the waiting time and stress at temperature T . Orowan's Law is then

used to relate the strain rate and stress at temperature T . Using Eq. (8.5) for the barrier function, Soare et al. [150, 151] derived an accurate analytical form for t_w as a function of ΔE_0 , $\Delta \tau_\infty$, τ , and temperature that is shown in A.7. With the result of Soare et al., the yield stress at $(T, \dot{\epsilon})$ can be computed numerically.

Finally, the tensile yield strength is obtained from the shear stress using the Taylor factor 3.067 for edge glide in BCC polycrystals.

8.2 Dynamic strain aging in MoNbTaW

Here, the energetic and kinetic models developed above are used to predict the strength of the MoNbTaW alloy in the presence of cross-core diffusion. The main input parameters to the theory come from the edge strengthening theory of Maresca and Curtin in the absence of cross-core diffusion. The relevant quantities are the zero-stress energy barrier $\Delta E_0 = 2.65$ eV and zero-temperature strength $\tau_0 = 420$ MPa. The cross-core diffusion parameters are taken from our study on the model MoNbTaW alloy, with average energy change due to solute diffusion $\overline{\Delta W} = 0.2$ eV and maximum cross-core density $\rho_\infty = 3.5 \text{ nm}^{-2}$. The saturation cross-core strengthening is then $\Delta \tau_\infty = 390$ MPa.

For the kinetics, we take the reference core transition rate Γ_c to be equal to that in the bulk. Therefore, the activation enthalpy ΔH_c for the vacancy-assisted transition is $\Delta H_c = \Delta H_{vf} + \Delta H_{vm}$ where ΔH_{vf} and ΔH_{vm} are the vacancy formation and migration enthalpies in the bulk alloy. The appearance of the vacancy formation energy implies an equilibrium vacancy concentration at the specified temperature. To incorporate the possibility of an excess vacancy concentrations, possibly generated by the failure of screw segment cross-kinks occurring at lower stresses, we write the reference transition rate in terms of the vacancy concentration c_v as

$$\Gamma_c = \nu_{0v} c_v e^{-\beta \Delta H_{vm}} \quad (8.20)$$

where $\nu_{0v} = 10^{13}/s$ is taken as the estimated attempt frequency for vacancy diffusion. For the NbMoTaW alloy, we use the concentration-weighted sum of the experimental vacancy migration barriers in the elemental BCC components [37, 106], yielding $\Delta H_{vm} = 1.075$ eV. For reference, the estimated vacancy formation energy taken again as an average of elemental experimental values is $\Delta H_{vf} = 3.125$ eV.

The experiments were conducted at a strain rate of $\dot{\epsilon} = 10^{-3} \text{ s}^{-1}$ [145]. To match prior results of Maresca and Curtin at low temperatures and in the absence of any diffusion, the present model should reduce to

$$\dot{\epsilon} = \dot{\epsilon}_0 \exp \left(-\frac{\Delta E_b^{(0)}(\tau)}{kT} \right). \quad (8.21)$$

where $\dot{\epsilon}_0 = 10^4 \text{s}^{-1}$ is the reference strain rate used by Maresca and Curtin. Matching this result then requires $\Omega = \dot{\epsilon}_0 / \nu_0$. Using $\nu_0 = 10^{11} \text{s}^{-1}$ for the dislocation attempt frequency, we obtain $\Omega = 10^{-7}$ that agrees with an estimate given above. From Eq. (8.16), the average waiting time is then $\bar{t}_w = 10^{-4} \text{s}$.

Figure 8.6 shows the predictions of for the strength versus temperature for MoNbTaW HEA, for various assumed vacancy concentrations along with the experimental results of [145] and the predictions of Maresca and Curtin theory in the absence of cross-core diffusion. Using the equilibrium vacancy concentration, there is no DSA effect at any reasonable temperature because the average vacancy formation energy is very large. If the vacancy concentration is higher than the equilibrium value, a DSA effect is seen at elevated temperatures, with an increasing plateau-like region over intermediate temperatures as the assumed vacancy concentration is increased. Quantitative agreement with experiments requires a vacancy concentration of $c_v = 2 \times 10^{-6}$. At this concentration, a near-plateau in the range 900-1300K is predicted. At higher temperatures the strength then decreases steadily, and follows the same trend as the alloy in the absence of the DSA but with the strength increased by the saturation DSA strength of $\Delta\tau_\infty$ as indicated in the figure. Thus, the DSA model can rationalize the observed experimental plateau.

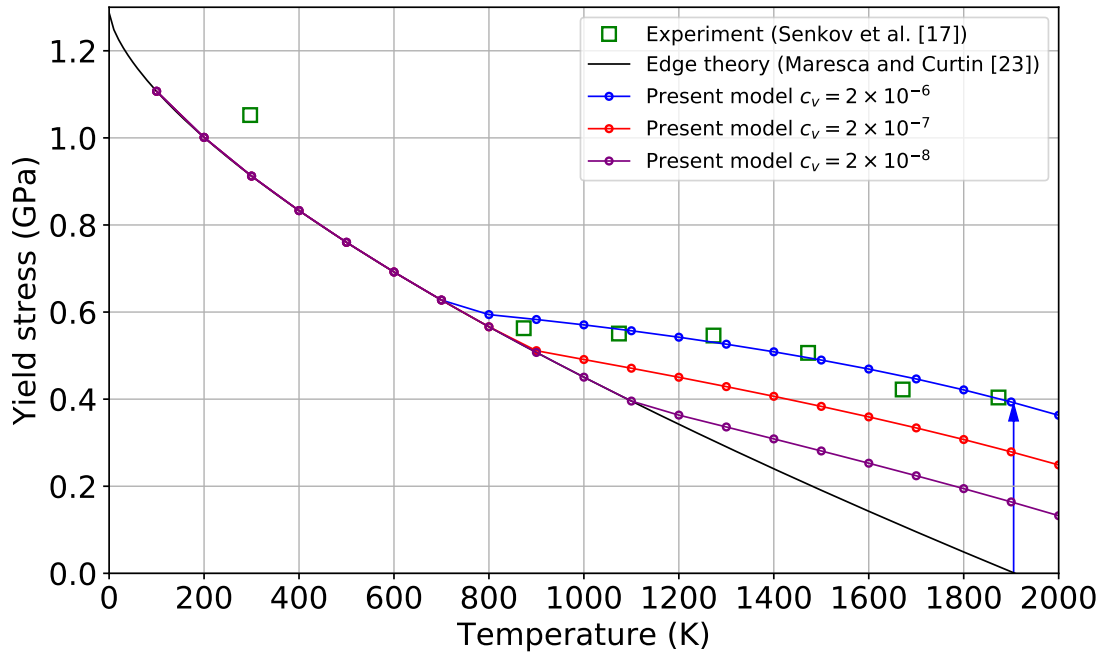


Figure 8.6 – Strength versus temperature for MoNbTaW HEA as obtained by the present theory with different vacancy concentrations together with the experimental data and the results of Maresca and Curtin model.

8.3 Discussion and Conclusions

The cross-core theory can make quantitative contact with experiments for a sufficiently high non-equilibrium vacancy concentration. We also note that specific results depend on the two attempt frequencies ν_{0v} and ν_{0d} in combination with c_v . So, the precise value of c_v needed to match experiments should not be taken as definitive. This c_v value is much larger than the equilibrium values (that vary strongly with temperature). However, such vacancy concentrations can arise during plastic flow in other metals. We mentioned previously that the vacancy concentration could be elevated in BCC alloys due to screw dislocation motion at lower stress levels that occurs by the failure of screw cross-kinks (also called jogs) that require formation of vacancies and self-interstitials [94]. These vacancies could then be available for diffusion until they annihilate with the self-interstitials or elsewhere. Vacancies are also attracted to the core by the driving force $-p(x)\Delta V_v$ and this might enhance the average vacancy concentration in the core on the positive pressure side. The result here could also be achieved if the kinetics of diffusion in the core is accelerated sufficiently by other physical processes. For instance, the vacancy migration energy across the very center of the dislocation core might differ from the bulk, as found in the core of FCC Al. Also, vacancy pipe diffusion along the core of the dislocation could accelerate the cross-core process relative to the present basic analysis. Neither of these phenomena needed to be invoked in describing DSA in FCC Al, however. Furthermore, using the equilibrium vacancy concentration, agreement with experiment cannot be obtained even if the vacancy migration enthalpy is reduced to zero. Hence, a combination of increased vacancy concentration and decreased vacancy migration (in the core) would be necessary.

The cross-core diffusion via dynamic strain aging mechanism was examined as a possible route to provide additional strengthening in BCC HEAs where the strength is controlled by the motion of edge dislocations. The predictive model was shown to provide substantial strengthening through the movement of solute-pairs right at the dislocation core, in agreement with atomistic simulations. The predicted results for the strength of MoNbTaW HEA, however, showed that the range of temperatures at which the diffusion starts to happen are far above the experimental observations, due to their very high values for the vacancy formation energy. Therefore, it was proposed that out-of-equilibrium excessive vacancies need to be present in the system, to have the theoretical results capture the experiments. These excess vacancies could stem from the cross-kink failure, a well known mechanism for screw dislocation motion in BCC HEAs, which requires formation of vacancies.

To make the prediction, we used the concentration-weighted sum over the vacancy formation/migration energies in the elemental BCC components which its accuracy remains uncertain. Moreover, the energies associated with vacancy formation/migration are temperature-dependent and reduce with increasing the temperature. These motivate further studying of energetics and kinetics of vacancy point defect in HEAs.

Although, the theory was merely applied to predict the strength of a model NbMoTaW HEA, it

can be readily extended to other family of BCC alloys which possess a plateau in their plot of strength versus temperature. The main quantity to be computed is the interaction energies at various sites around the edge core which can then be used to calculate the average energy barrier change. In overall, the dynamic strain aging model via cross core diffusion presented in this paper, captures the major features observed in the experiments and sheds light on the origin of the additional strengthening in HEAs causing the plateau in strength, which to our knowledge, has not been established.

9 Conclusion

In this thesis, we investigated in detail the underlying solute strengthening mechanisms in BCC dilute and high-entropy alloys. We developed theoretical models that enable us to predict the yield strength of the alloy as a function of underlying material quantities without any fitting parameter. The developed statistical theoretical models have been extensively validated via atomistic simulations.

The fundamental quantity in solute strengthening theories is the interaction energy between solutes and an individual dislocation which can be obtained by DFT calculations or atomistic simulations using EAM potentials. We first defined the proper solute/screw interaction energy parameter relevant for strengthening of screw dislocations in random bcc alloys with any number of components and concentrations. In contrast to the assumptions made by the previous researchers, the solute/screw interaction energy is not confined to any finite range and the effect of all solutes, out to infinite distance in principle, are considered. Using EAM potentials as a model system, we found that an accurate interaction energy parameter requires consideration of solutes out to sixth neighbors (four shells). This range is also consistent with literature first-principles studies in dilute alloys. This interaction energy parameter plays the essential role in developing our strengthening theories for screw dislocation motion in BCC dilute and high-entropy alloys.

Computing an accurate estimation of the interaction energy parameter in complex alloys is a challenging task. Although, for alloys describable by EAM potential, the convenient average-alloy method can be used as a very clean approach in complex alloys such as HEAs, their accuracy remains uncertain. The use of DFT calculations in computing interaction energies is still limited to binary systems, since there is currently no equivalent of the average-alloy potential in the first-principles framework. Moreover, as discussed in Section 2.4.1, another challenging issue with the existing EAM potentials is the prediction of wrong non-compact core structure. In light of the above, the development of accurate and general-purpose interatomic potentials is a demanding goal, especially for BCC HEAs. State-of-the-art machine learning methods appears to be one of the most likely avenues for developing high accuracy interatomic potentials for complex alloys. A machine learning potential for BCC MoNbTaW refractory HEA

has been developed recently [195] and was employed in molecular dynamic simulations to investigate the mechanisms of the movement of dislocations.

The plastic deformation in dilute BCC alloys occurs by double-kink nucleation and kink migration processes which are influenced by the presence of solutes. We have developed an analytical theory for the stress-dependent double-kink nucleation and kink migration barriers in random dilute BCC alloys. We have shown that the kink migration process under stress is essentially the random walk-type "Wiener process with drift". The material parameters in the theories are only (I) the solute/screw dislocation interaction energies, (II) the transition state configurations of the pure matrix, (III) the double-kink enthalpy barrier versus stress for the pure matrix, (IV) the total dislocation length, and (V) emerging to play a minor role, the kink-width in the pure metal. The theory have been extensively validated on a model Fe-Si alloy via NEB calculations and direct stochastic simulations. The EAM interatomic potential describing the Fe-Fe interactions has all the key features of plastic deformation in BCC alloys. The developed theories provide a fully-analytic model for strengthening of screw dislocations over the full temperature range in the dilute regime concentration. Our theoretical predictions are in quantitative agreement with the experimental results of Fe-Si dilute alloys. However, our theory is incapable of predicting the small hump in the data for 0.52at%Si around 150K. The origin of this hump remains unknown to date and needs additional study and exploration.

The theory of solute strengthening in dilute BCC alloys was developed based on the fact that the interaction energy of solute with the dislocation does not exceed the double-kink nucleation barrier. This limit is valid for many substitutional solutes in most BCC metals but ceases to hold for interstitial solutes where, according to DFT results, possess very large interaction energies. Another issue raised by interstitials is the possibility in changing the screw core from compact to non-compact structures. The above issues call for a deeper study on the effect of interstitial solutes on the energetics of double-kink nucleation and migration processes.

In contrast to dilute alloys, the zero-temperature and zero-stress initial structure of the screw dislocation in non-dilute and HEAs is kinked at a characteristic length of ζ_c . Three mechanisms have shown to involve in the plastic deformation, Peierls-like motion, kink-migration, and cross-kink failure. In this thesis, based on our understanding of kink migration in dilute alloys, we developed a new theory for kink migration process in non-dilute alloys which was validated against stochastic simulations. The double-kink nucleation and migration theories plus the revised version of Maresca et al. theory together provide a coherent framework for strengthening of screw dislocations over the full range of concentrations from extremely dilute ($\ll 1$ at.%), to dilute (up to a few at.%) and non-dilute alloys including High Entropy Alloys.

The transition between dilute and non-dilute regime was understood to be mainly dictated by the spacing of the spontaneous kinks, $2.5\zeta_c$. If this length is predicted to be larger than or comparable to L , then the spontaneous kinked structure cannot actually form, where L is the distance between forest junctions. Such alloys are in the dilute regime where motion is

controlled by double-kink nucleation and migration processes. If the kink spacing is smaller than L we are in the non-dilute regime and the revised non-dilute theory should be applied. The dilute to non-dilute transition is thus not considered to be temperature-dependent because the length scale ζ_c in the Maresca-Curtin model is related to energy minimization that should occur at $T=0K$. However, as discussed in Section 4.4.1, the controlling strengthening mechanism may be a complex and temperature-dependent interplay between the dilute and non-dilute mechanisms. Such an interplay was not considered in this thesis and needs further study.

As it was mentioned above, one of the mechanisms involved in the screw dislocation motion in non-dilute alloys is the breaking of cross-kinks due to kink formation on different glide planes. In Maresca and Curtin theory, this mechanism was assumed to be thermally activated. However, since defects must be formed in this process, the cross-kink strength may actually be athermal, with temperature entering through the vacancy and self-interstitial free energies. Therefore, cross-kink failure mechanism is another intriguing aspect of strengthening in non-dilute alloys which, to our knowledge, has not been carefully studied in the literature, and needs additional examination.

Refractory high entropy alloys show high strength retention at elevated temperatures. Our detailed NEB simulations of the energy landscape for edge dislocations in two random NbTaV and MoNbTaW model alloys, revealed the high energy barriers encountered by edge dislocations. A reduced version of the theory has then been applied to two Hf-Mo-Nb-Ta-Ti-Zr and Mo-Nb-Ta-Ti-V-W families of alloys. The theory rationalizes the observed significant increases in strength caused by the addition of solutes with large misfit volumes that is a hallmark of the edge theory. There is a strong loss of strength observed for the Hf-Mo-Nb-Ta-Ti-Zr family of alloys between 1000 and 1200 °C. High-temperature mechanisms that can defeat edge strengthening are unclear at this time and requires further research. We postulated that there is some vacancy-related mechanism, such as climb, by which the large edge barriers can be circumvented at sufficiently high temperatures. Considering the dislocation climb in random BCC HEAs is thus a point of interest for future research study.

While strength generally decreases with increasing temperature, as expected, many of the refractory HEAs show a distinct plateau in strength versus temperature at intermediate temperatures. At higher temperatures, the strength then decreases again, either rapidly or gradually. In this thesis, we examined one possible mechanism for the intermediate-T strength plateau: the dynamic strain aging (DSA) process of solute diffusion immediately across the core of an edge dislocation. An analytical model is developed to predict the temperature- and solute-diffusion dependent strength in terms of underlying material properties. The theory was then applied to predict the strength versus temperature in a model MoNbTaW BCC HEA. Quantitative agreement with experiments is achieved if there is a fairly high non-equilibrium vacancy concentration or accelerated vacancy diffusion in the dislocation core. This should drive further studies of realistic vacancy energetics and kinetics in these complex alloys.

Chapter 9. Conclusion

The research work performed as part of this thesis allows us to gain a deeper understanding of strengthening mechanism in various BCC random alloys from very dilute to multi-component high entropy alloys. The quantitatively predictive models developed in this enable us to compute the strength of the material in terms of the underlying material parameters. The predictive models pave the way for design of novel materials with excellent mechanical strength and will greatly increase the efficiency and cost of alloy design, compared to physical experiments.

A Appendix

A.1 Standard deviation of the potential energy change

In this appendix, we derive the standard deviation of the potential energy change $\sigma_{\Delta U_{\text{tot}}}$ when a dislocation segment nucleates over a distance l_{dk} in a random field of solutes, in a dilute binary alloy. The stress-dependent total change in the nucleation barrier due to the nucleation of dislocation is

$$\Delta H^{\text{sol}}(\tau) = \sum_{i,j,k} s_{ijk} \Delta U_{ij}(a) g(z_k, \tau), \quad (\text{A.1})$$

where the site occupation variable $s_{ijk} = 1$ if a solute is at position (x_i, y_j, z_k) and 0 otherwise. Positions (x_i, y_j, z_k) refer to the atomis sites along one dislocation segment of length l_{dk} . Let $N_s = l_{dk}/b + 1$ denote the number of atomic sites along z direction at each atomic row (x_i, y_j) . Also, let label the atoms in each atomic row (x_i, y_j) by $k = 1 \dots N_s$.

The quantity of interest in the nucleation model is the standard deviation of the total energy change as defined in Eq. (4.4) which requires $\langle \Delta H^{\text{sol}} \rangle^2$ and $\langle \Delta H^{\text{sol}2} \rangle$. We can write

$$\begin{aligned} \langle \Delta H^{\text{sol}} \rangle^2 &= \sum_{i,j} \sum_k \langle s_{ijk} \rangle^2 \Delta U_{ij}^2 g(z_k, \tau)^2 \\ &+ \sum_{i,j} \sum_{k,l \neq k} \langle s_{ijk} \rangle \langle s_{ijl} \rangle \Delta U_{ij}^2 g(z_k, \tau) g(z_l, \tau) \\ &+ \sum_{i,j} \sum_{\substack{k,l \\ m,n \neq i,j}} \langle s_{ijk} \rangle \langle s_{mnl} \rangle \Delta U_{ij} g(z_k, \tau) \Delta U_{mn} g(z_l, \tau) \end{aligned} \quad (\text{A.2})$$

$$\begin{aligned}
\langle \Delta H^{\text{sol}2} \rangle &= \sum_{i,j} \sum_k \langle s_{ijk}^2 \rangle \Delta U_{ij}^2 g(z_k, \tau)^2 \\
&+ \sum_{i,j} \sum_{k,l \neq k} \langle s_{ijk} s_{ijl} \rangle \Delta U_{ij}^2 g(z_k, \tau) g(z_l, \tau) \\
&+ \sum_{i,j} \sum_{\substack{k,l \\ m,n \neq i,j}} \langle s_{ijk} \rangle \langle s_{mnl} \rangle \Delta U_{ij} g(z_k, \tau) \Delta U_{mn} g(z_l, \tau)
\end{aligned} \tag{A.3}$$

The square of the standard deviation of the potential energy change therefore equals

$$\begin{aligned}
\sigma_{\Delta H^{\text{sol}}}^2 &= \sum_{i,j} \left[\sum_k \left[\langle s_{ijk}^2 \rangle - \langle s_{ijk} \rangle^2 \right] \Delta U_{ij}^2 g(z_k, \tau)^2 \right. \\
&\left. + \sum_{k,l \neq k} \left[\langle s_{ijk} s_{ijl} \rangle - \langle s_{ijk} \rangle \langle s_{ijl} \rangle \right] \Delta U_{ij}^2 g(z_k, \tau) g(z_l, \tau) \right].
\end{aligned} \tag{A.4}$$

This result involves the variances and co-variances of the occupation variable s_{ijk} . Note that $\langle s_{ijk} \rangle = c$. We have

$$\begin{aligned}
\langle s_{ijk} s_{ijl} \rangle &= \sum_k \frac{N_s!}{k!(N_s - k)!} c^k (1 - c)^{N_s - k} \\
&\times \sum_{k_k, k_l} \frac{k!}{k_k! k_l! (k - k_k - k_l)!} \left(\frac{1}{N_s} \right)^{k_k + k_l} \left(1 - \frac{1}{N_s} \right)^{k - k_k - k_l} k_k k_l \\
&= \sum_k \frac{N_s!}{k!(N_s - k)!} c^k (1 - c)^{N_s - k} \left(\frac{1}{N_s} \right)^2 k(k - 1) \\
&= c^2 \left(1 - \frac{1}{N_s} \right),
\end{aligned} \tag{A.5}$$

with $1 \leq k \leq N_s$ and $0 \leq k_k + k_l \leq k$, and

$$\begin{aligned}
\langle s_{ijk}^2 \rangle &= \sum_k \frac{N_s!}{k!(N_s - k)!} c^k (1 - c)^{N_s - k} \\
&\times \sum_{k_k} \frac{k!}{k_k! (k - k_k)!} \left(\frac{1}{N_s} \right)^{k_k} \left(1 - \frac{1}{N_s} \right)^{k - k_k} k_k^2 \\
&= \sum_k \frac{N_s!}{k!(N_s - k)!} c^k (1 - c)^{N_s - k} \\
&\times \left[\left(\frac{1}{N_s} \right)^2 k^2 + \frac{1}{N_s} \left(1 - \frac{1}{N_s} \right) k \right] \\
&= \left(\frac{1}{N_s} \right)^2 [c^2 N_s^2 + c(1 - c) N_s] + c \left(1 - \frac{1}{N_s} \right) \\
&= c + c^2 \left(1 - \frac{1}{N_s} \right),
\end{aligned} \tag{A.6}$$

with $1 \leq k \leq N_s$ and $0 \leq k_k \leq k$. Inserting Eqs. (A.5) and (A.6) into Eq. (A.4) and neglecting the

second order terms in c ($c^2 \ll 1$), we obtain

$$\sigma_{\Delta H^{\text{sol}}}^2 = \sum_{i,j} c \Delta U_{ij}^2 \sum_k g(z_k, \tau)^2 \quad (\text{A.7})$$

Finally, by defining the $z = 0$ to be located right at the double-kink nucleus, the above equation can be rewritten as

$$\sigma_{\Delta U^{\text{sol}}}^2 = \sum_{i,j} c \Delta U_{ij}^2 \sum_{k=-N_s}^{N_s} g(kb, \tau)^2. \quad (\text{A.8})$$

Here, $N_s = l_{dk}/(2b)$.

A.2 Double-kink nucleation rate

The total double-kink nucleation rate is the sum of the rates of all N nucleation sites which can be described as

$$R = \nu_0 N \exp\left(-\frac{\Delta H^0(\tau)}{kT}\right) \int_{\Delta \bar{H}^{\text{sol}}(c, N, \tau)}^{\infty} d\Delta H P[\Delta H] \exp\left(-\frac{\Delta H}{kT}\right), \quad (\text{A.9})$$

where $P[\Delta H]$ is the probability of finding the double-kink nucleation segment with solute energy change ΔH given by Eq. (4.8). After some manipulations the above equation can be rewritten as Eq. (4.9). It is of interest to find the temperature T_0 below which the weakest link dominates and thus the rate can be expressed by 4.15. To this end, we use the following approximated form for $\text{erfc}(x)$ [77]

$$\text{erfc}(x) \approx \frac{(1 - e^{-1.98x})e^{-x^2}}{1.135\sqrt{\pi}x} \quad (\text{A.10})$$

Substituting the above relation into Eq. (4.9) and equating the resultant equation with Eq. (4.15), gives the following solution for T_0 which is the temperature at which the two representations of double-kink nucleation rate become equal

$$\frac{kT_0}{\sigma_{\Delta H^{\text{sol}}}(c, \tau)} = \left(0.35Ne^{-\frac{c_N^2}{2}} + 0.7W\left[-0.5N\exp\left(-0.5Ne^{-\frac{c_N^2}{2}} - \frac{c_N^2}{2}\right)\right] - c_N\right)^{-1} \quad (\text{A.11})$$

where $W[\cdot]$ stands for the Lambert W-function and $c_N = b_N - \gamma a_N$. This temperature is approximately $kT_0 = 0.255\sigma_{\Delta H^{\text{sol}}}$ over a wide range of N . However, since $\sigma_{\Delta H^{\text{sol}}}(c, \tau)$ depends on the applied stress τ which is not known a-priori, the exact computation of the cross-over temperature is not possible. It can be shown that, to a high approximation, T_0 can be obtained by solving the following equation

$$\Delta H_{\text{exp}}^0(\tau) = 0.255\sigma_{\Delta H^{\text{sol}}}(c, \tau) \log\left[250\frac{\dot{\epsilon}_0}{\dot{\epsilon}}\right].$$

The above equation gives the yield stress at temperature T_0 from which $\sigma_{\Delta H^{\text{sol}}}$ and thus T_0 can be computed.

A.3 Simulation details of NEB calculations for double-kink nucleation

A.3.1 Periodic array of dislocations (PAD) configuration

To model screw dislocations, we use a periodic array of dislocations (PAD) configuration (e.g. ref. [8]). Using the Fe lattice parameter, a rectangular simulation cell oriented with $[1\bar{1}2]$ along the glide direction X, $[110]$ along the glide plane normal direction Y, and $[\bar{1}11]$ along the dislocation line direction Z, was constructed. Periodic boundary conditions are imposed along X and Z directions, and Y having imposed tractions. The simulation cell has dimensions $L_1 \sim 110\text{\AA}$ and $L_2 \sim 100\text{\AA}$ and L_3 depends on the dislocation length. A screw dislocation of Burgers vector $a/2[111]$ with line direction along Z is then introduced into the center of the cell by imposing a linear displacement $u_z = -bx/l_x$ for $0 < x < l_x$ on all atoms in the upper half of the simulation cell. Atomic positions are then relaxed by using a combination of the FIRE algorithm [11] and relaxation of the cell dimensions. Convergence is achieved when the norm of the force vector fell below 10^{-6} eV/\AA and stresses σ_{XX} , σ_{XY} , and σ_{YY} fell below 0.1 MPa.

A.3.2 Nudged elastic band (NEB) calculations

To compute the minimum energy path (MEP) connecting the initial and final states, nudged elastic band (NEB) computations are performed as implemented in LAMMPS using the interatomic potential developed by [147]. To perform NEB simulations, we first construct the relaxed initial state as described above in Section A.3.1. The final state has the same structure as the initial state but shifted by a relative to the initial state as shown in Figure A.1. The constructed initial and final states are used as templates to carry out the MEP calculations in dilute alloys. In order to model the Fe-Si dilute alloys, the Fe atoms in initial state configurations were replaced randomly by Si solutes at the desired alloy concentration. Accordingly, the same Fe solutes were replaced by Si atoms in the final state. The energy of the initial and final alloy configurations were then minimized using CG and FIRE with the same tolerances on forces and stresses as specified above. NEB simulations are performed using 60 replicas. An initial path of intermediate configurations (replicas) is constructed by linearly interpolating the atomic positions between the relaxed initial and final states. The NEB inter-replica spring constant is set to 10^{-2} eV/\AA² and convergence is assumed when the maximum of the force acting on all of the atoms across all replicas is less than 1×10^{-3} eV/\AA.

The above yields us the MEP at zero applied stress. To find the MEP under applied shear stress, we follow the procedure outlined in [95] and reiterated here. The direct result of the NEB

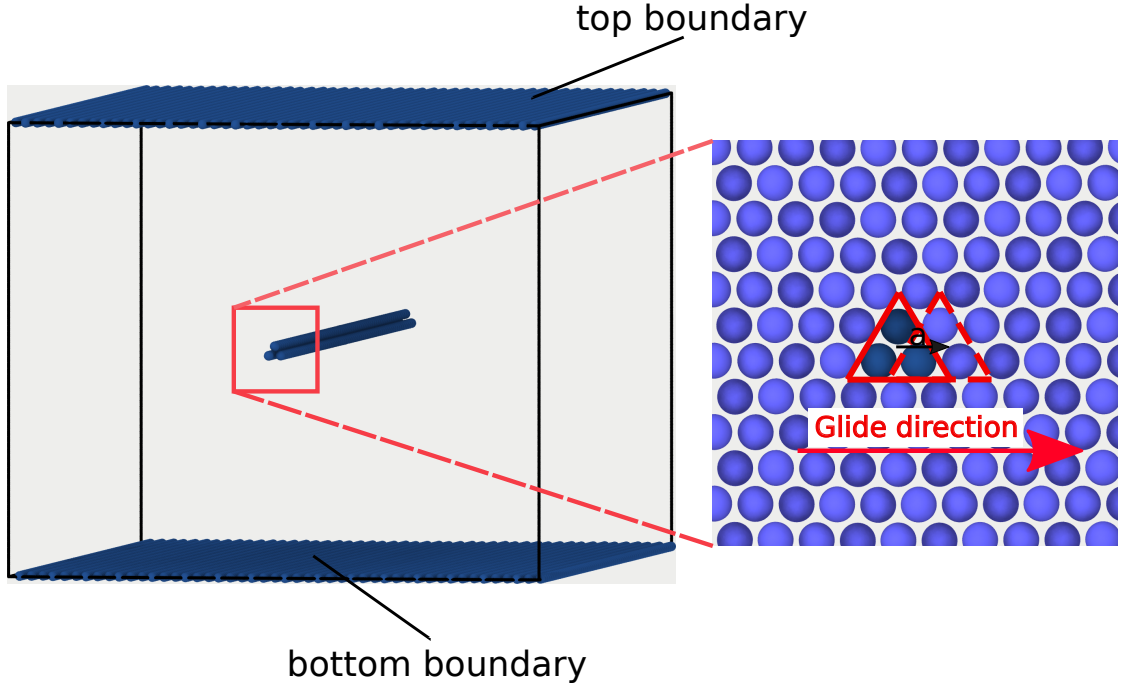


Figure A.1 – **The initial and final screw configurations in pure Fe to be used for subsequent NEB simulations of double-kink nucleation in dilute Fe-Si alloys.** The final state has the same structure as the initial state but shifted by a relative to the initial state.

calculation at each applied stress τ is the configurational energy $V^C(\tau, \xi_i)$ as a function of the reaction coordinate $\xi_i \in [0, 1]$ of replica i . The enthalpy of each replica at an applied shear stress τ can then be computed as

$$H(\tau, \xi_i) = V^C(\tau, \xi_i) - W^{ext}(\tau, \xi_i) \quad (\text{A.12})$$

where $W^{ext}(\tau, \xi_i)$ is the work done by the external stress acting on the boundary atoms given by

$$W^{ext}(\tau, \xi_i) = \mathbf{f} \cdot [\mathbf{u}_t(\xi_i) - \mathbf{u}_b(\xi_i)], \quad (\text{A.13})$$

where \mathbf{u}_b and \mathbf{u}_t are vectors containing the displacements of all atoms on the bottom and top boundary regions (see Fig. A.1), respectively, on which forces are applied.

A.4 Activation volume of kink-migration process

Here we address the activation volume V_{act} of the thermally-activated kink-migration process. V_{act} is the Burgers vector multiplied by the area swept by the dislocation during the activation process and is computed as $V_{act} = -\partial \Delta H_{km} / \partial \tau$ [171]. At the $T = 0\text{K}$ flow stress, which is the highest stress required for any kink migration, $V_{act} = 0$ is required. The activation volume from

Eq. (5.10) is

$$V_{\text{act}} = ab^2 \left(0.55 \frac{\tau}{\tau_c} + \frac{1.5}{\sqrt{L/b}} \right)^{-2}. \quad (\text{A.14})$$

This decays to zero only as $\tau \rightarrow \infty$. Due to the introduction of the correction factor, the energy barrier reaches zero at a finite τ with a finite V_{act} . This is also a flaw of the Suzuki model. However, in the present model, the activation volume at the $T = 0\text{K}$ flow stress can be computed analytically as $V^* = ab^2 \left(0.019\sqrt{L/b} - 0.59\sqrt{w/b} \right)^2$ and at typical dislocation long lengths of $L \sim 2 \times 10^3 b$, $V^* \sim 0.1abw$, which is about one tenth of that obtained by Suzuki [158].

A.5 Simulation details of NEB calculations for kink migration

To compute the minimum energy path (MEP), the initial and final states are first constructed as described in Section A.3.1 with the same sample orientations, boundary conditions, and simulation cell dimensions except that here $L_z \sim 490\text{\AA}$ remains fixed. Subsequently, two Si solutes in the proper locations, as discussed in 5.2.1, are added to the initial and final configurations (see Figure A.2). Atomic positions are then relaxed by using a combination of the FIRE algorithm [11] and relaxation of the cell dimensions. Convergence is achieved when the norm of the force vector fell below 10^{-6} eV/\AA and stresses σ_{XX} , σ_{XY} , and σ_{YY} fell below 0.1 MPa. An initial path of intermediate configurations (replicas) is constructed by linearly interpolating the atomic positions between the above relaxed initial and final states. We used 300 replicas and inter-replica spring constant was set to 10^{-2} eV/\AA^2 . Convergence was assumed when the maximum force acting on all of the atoms across all replicas was less than $1 \times 10^{-3} \text{ eV/\AA}^2$.

A.6 Simulation details of the solute/edge interaction energies

For the atomistic simulations, we use a rectangular simulation cell oriented with glide direction $X \parallel [111]$, glide plane normal $Y \parallel [101]$, and line direction $Z \parallel [121]$ with dimensions of $L_x \sim 190 \text{ \AA}$, $L_y \sim 90 \text{ \AA}$, and $L_z \sim 50 \text{ \AA}$, respectively. The surfaces normal to the Y-direction are traction-free while those along the X- and Z-directions are periodic. All Molecular Statics simulations in this study have been performed with the LAMMPS package [114] on the model NbMoTaW BCC alloy represented by the Zhou et al interatomic potentials [203]. The minimization of the system is performed with a combination of Conjugate Gradient and FIRE [11] algorithm and is continued until convergence is achieved (force tolerance $< 10^{-5} \text{ eV per atom}$).

To compute the interaction energies, the simulation cell created above is first populated with the corresponding average atom EAM potential [173] which is then minimized to find the energy of the pristine system E_{pure} . Replacing an A-atom with a solute-type n and minimizing the system yields $E_{\text{pure-sol}}^n$. An edge dislocation will then be inserted into the pure average-

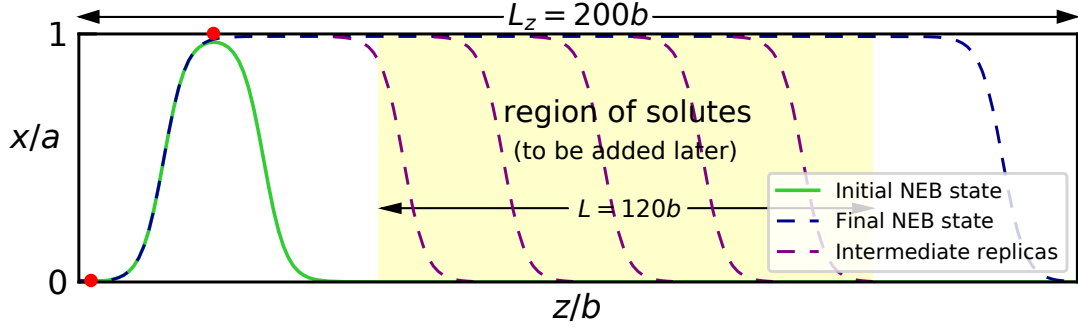


Figure A.2 – **Atomistic modeling of single kink motion.** The initial state for the NEB simulation is constructed by placing a single solute (top red dot) at the most favorable location and a second solute (bottom red dot) to inhibit motion of left sided kink. The final state of the kinked dislocation has the right kink at the far right of the sample. Executing NEB with no other solutes then generates a set of configurations (replicas) connecting the initial and final states and corresponding to kink glide. These replicas are then used as the initial path for subsequent NEB studies of the same kink motion through a field of solutes randomly distributed over the central length of $L = 120b$.

atom NbMoTaW matrix, as explained in [81], to compute the energy of the dislocated system E_{edge} . Upon substitution of the A-atom at a specific site \mathbf{x} around the core with the solute-type n and relaxation of the system, the minimized energy $E_{\text{edge-sol}}^n(\mathbf{x})$ is obtained. Finally, the interaction energy of the solute of type n at position \mathbf{x} relative to the center of the dislocation can be computed as

$$U_{\text{int}}^n(\mathbf{x}) = \left(E_{\text{edge-sol}}^n(\mathbf{x}) - E_{\text{edge}} \right) - \left(E_{\text{pure-sol}}^n - E_{\text{pure}} \right) \quad (\text{A.15})$$

In order to find the MEP between two minimum energy states we use the NEB method [63, 104, 92, 114] as implemented in LAMMPS. Details of the NEB simulations, including construction of the initial and final states can be found in Section 7.3.

A.7 Average waiting time

The analytical solution for the steady-state average waiting time is derived in [150, 151] which can be written as

$$\bar{t}_w = t_0 D_0 + t_1 D_1 + t_\infty D_\infty \quad (\text{A.16})$$

where

$$\begin{aligned}
 t_0 &= \left(\nu_0 \exp \left(-\frac{\Delta E_0}{kT} \left(1 - \frac{\tau - \Delta \tau_\infty}{\tau_0} \right)^{\frac{3}{2}} \right) \right)^{-1} \\
 t_1 &= \left(\nu_0 \left(1 + 0.12 \left(1 - \frac{\tau}{\tau_0} + 0.63 \frac{\Delta \tau_\infty}{\tau_0} \right)^{-\frac{1}{3}} \frac{\Delta \tau_\infty}{\tau_0} \frac{\Delta E_0}{kT} \right) \right. \\
 &\quad \times \exp \left(-\frac{\Delta E_0}{kT} \left(1 - \frac{\tau}{\tau_0} + 0.63 \frac{\Delta \tau_\infty}{\tau_0} \right)^{\frac{2}{3}} \right) \Big)^{-1} \\
 t_\infty &= \left(\nu_0 \exp \left(-\frac{\Delta E_0}{kT} \left(1 - \frac{\tau}{\tau_0} + \frac{\Delta \tau_\infty}{\tau_0} \right)^{\frac{2}{3}} \right) \right)^{-1}
 \end{aligned} \tag{A.17}$$

and with

$$\begin{aligned}
 D_0 &= 1 - \exp \left(-(1-k) \frac{t_d}{t_0} \right) \\
 D_\infty &= \exp \left(-(1-k) \frac{t_d}{t_0} - 2k \frac{t_d}{t_1} \right) \\
 D_1 &= 1 - D_0 - D_\infty
 \end{aligned} \tag{A.18}$$

The parameter k is a constant between 0 and 1 and t_d is given as

$$t_d = \left(2\nu_{0d} c_\nu e^{-\beta \left(\Delta H_{vm} - \frac{\Delta W}{2} \right)} \right)^{-1} \tag{A.19}$$

Bibliography

- [1] Ahmad, R. (2020). Atomic scale investigations into the origins of ductility in mg alloys. Technical report, EPFL.
- [2] Ahmad, R., Wu, Z., and Curtin, W. (2020). Analysis of double cross-slip of pyramidal $\langle c+a \rangle$ screw dislocations and implications for ductility in mg alloys. *Acta Materialia*, 183:228–241.
- [3] Ahmad, R., Yin, B., Wu, Z., and Curtin, W. (2019). Designing high ductility in magnesium alloys. *Acta Materialia*, 172:161–184.
- [4] Angsten, T., Mayeshiba, T., Wu, H., and Morgan, D. (2014). Elemental vacancy diffusion database from high-throughput first-principles calculations for fcc and hcp structures. *New J. Phys.*, 16:015018.
- [5] Argon, A. (2008). *Strengthening mechanisms in crystal plasticity*, volume 4. Oxford University Press on Demand.
- [6] Arrhenius, S. (1889). Über die reaktionsgeschwindigkeit bei der inversion von rohrzucker durch säuren. *Zeitschrift für physikalische Chemie*, 4(1):226–248.
- [7] Arsenault, R. and Lawley, A. (1967). Work hardening and dislocation structure in ta and ta-base alloys. *The Philosophical Magazine: A Journal of Theoretical Experimental and Applied Physics*, 15(135):549–565.
- [8] Bacon, D., Osetsky, Y., and Rodney, D. (2009). Dislocation–obstacle interactions at the atomic level. *Dislocations in solids*, 15:1–90.
- [9] Bechtold, J. H. (1955). Tensile properties of annealed tantalum at low temperatures. *Acta Metallurgica*, 3(3):249–254.
- [10] Bienvenu, B., Fu, C. C., and Clouet, E. (2020). Impact of magnetism on screw dislocations in body-centered cubic chromium. *Acta Materialia*, 200:570–580.
- [11] Bitzek, E., Koskinen, P., Gähler, F., Moseler, M., and Gumbsch, P. (2006). Structural relaxation made simple. *Physical review letters*, 97(17):170201.
- [12] Briggs, T. and Campbell, J. (1972). The effect of strain rate and temperature on the yield and flow of polycrystalline niobium and molybdenum. *Acta Metallurgica*, 20(5):711–724.

Bibliography

- [13] Brunner, D. and Diehl, J. (1997). The effect of atomic lattice defects on the softening phenomena of high-purity α -iron. *physica status solidi (a)*, 160(2):355–372.
- [14] Brunner, D. and Glebovsky, V. (2000). Analysis of flow-stress measurements of high-purity tungsten single crystals. *Materials letters*, 44(3-4):144–152.
- [15] Büchner, A. and Wunderlich, W. (1993). A new discussion of the interaction energy in the solid solution hardening of bcc iron alloys. *physica status solidi (a)*, 135(2):391–403.
- [16] Cai, W., Bulatov, V. V., Justo, J. F., Argon, A. S., and Yip, S. (2002). Kinetic monte carlo approach to modeling dislocation mobility. *Computational materials science*, 23(1-4):124–130.
- [17] Cai, W., Bulatov, V. V., Yip, S., and Argon, A. S. (2001). Kinetic monte carlo modeling of dislocation motion in bcc metals. *Materials Science and Engineering: A*, 309:270–273.
- [18] Caillard, D. (2013a). A tem in situ study of alloying effects in iron. i—solid solution softening caused by low concentrations of ni, si and cr. *Acta materialia*, 61(8):2793–2807.
- [19] Caillard, D. (2013b). A tem in situ study of alloying effects in iron. i—solid solution softening caused by low concentrations of ni, si and cr. *Acta materialia*, 61(8):2793–2807.
- [20] Caillard, D. and Martin, J.-L. (2003). *Thermally activated mechanisms in crystal plasticity*. Elsevier.
- [21] Chaussidon, J., Fivel, M., and Rodney, D. (2006). The glide of screw dislocations in bcc fe: atomistic static and dynamic simulations. *Acta materialia*, 54(13):3407–3416.
- [22] Chen, N. and Maddin, R. (1951). Plasticity of molybdenum single crystals. *JOM*, 3(10):937–944.
- [23] Chen, Y., Atteridge, D., and Gerberich, W. W. (1981). Plastic flow of fe-binary alloys—i. a description at low temperatures. *Acta Metallurgica*, 29(6):1171–1185.
- [24] Christian, J. (1983). Some surprising features of the plastic deformation of body-centered cubic metals and alloys. *Metallurgical transactions A*, 14(7):1237–1256.
- [25] Clouet, E., Bienvenu, B., Dezerald, L., and Rodney, D. (2021). Screw dislocations in bcc transition metals: from ab initio modeling to yield criterion. *Comptes Rendus. Physique*, 22(S3):1–34.
- [26] Clouet, E., Ventelon, L., and Willaime, F. (2009). Dislocation core energies and core fields from first principles. *Physical review letters*, 102(5):055502.
- [27] Coury, F. G., Kaufman, M., and Clarke, A. J. (2019). Solid-solution strengthening in refractory high entropy alloys. *Acta Materialia*, 175:66–81.

-
- [28] Couzinié, J.-P., Lilensten, L., Champion, Y., Dirras, G., Perrière, L., and Guillot, I. (2015). On the room temperature deformation mechanisms of a TiZrHfNbTa refractory high-entropy alloy. *Mater. Sci. Eng., A*, 645:255–263.
- [29] Couzinié, J.-P., Senkov, O., Miracle, D., and Dirras, G. (2018). Comprehensive data compilation on the mechanical properties of refractory high-entropy alloys. *Data in brief*, 21:1622–1641.
- [30] Curtin, W. A., Olmsted, D. L., and Hector, L. G. (2006). A predictive mechanism for dynamic strain ageing in aluminium–magnesium alloys. *Nature materials*, 5(11):875–880.
- [31] Dezerald, L., Proville, L., Ventelon, L., Willaime, F., and Rodney, D. (2015). First-principles prediction of kink-pair activation enthalpy on screw dislocations in bcc transition metals: V, nb, ta, mo, w, and fe. *Physical Review B*, 91(9):094105.
- [32] Domain, C. and Monnet, G. (2005). Simulation of screw dislocation motion in iron by molecular dynamics simulations. *Physical review letters*, 95(21):215506.
- [33] Dora, J. E. and Rajnak, S. (1963). Nucleation of kink pairs and the peierls’ mechanism of plastic deformation.
- [34] Duesbery, M. (1989). The dislocation core and plasticity. *Elsevier Science Publishers, Dislocations in Solids.*, 8:67–173.
- [35] Duesbery, M. a.-S. and Vitek, V. (1998). Plastic anisotropy in bcc transition metals. *Acta Materialia*, 46(5):1481–1492.
- [36] Durrett, R. (2019). *Probability: theory and examples*, volume 49. Cambridge university press.
- [37] Ehrhart, P., Jung, P., and Schultz, H. (1991). Atomic defects in metals, edited by h. ullmaier, landolt-bernstein, new series. *Group III/25, Berlin, Springer-Verlag*.
- [38] Esteban-Manzanares, G., Martínez, E., Segurado, J., Capolungo, L., and LLorca, J. (2019). An atomistic investigation of the interaction of dislocations with guinier-preston zones in al-cu alloys. *Acta Materialia*, 162:189–201.
- [39] Esteban-Manzanares, G., Santos-Güemes, R., Papadimitriou, I., Martínez, E., and LLorca, J. (2020). Influence of the stress state on the cross-slip free energy barrier in al: an atomistic investigation. *Acta Materialia*, 184:109–119.
- [40] Eyring, H. (1935). The activated complex in chemical reactions. *The Journal of Chemical Physics*, 3(2):107–115.
- [41] Farraro, R. and Mclellan, R. B. (1977). Temperature dependence of the young’s modulus and shear modulus of pure nickel, platinum, and molybdenum. *Metall. Trans. A*, 8(10):1563–1565.

Bibliography

- [42] Farraro, R. and McLellan, R. B. (1979). High temperature elastic properties of polycrystalline niobium, tantalum, and vanadium. *Metall. Trans. A*, 10(11):1699–1702.
- [43] Follansbee, P. S. (2014). *Fundamentals of strength: principles, experiment, and applications of an internal state variable constitutive formulation*. John Wiley & Sons.
- [44] Foxall, R. and Statham, C. (1970). Dislocation arrangements in deformed single crystals of niobium-molybdenum alloys and niobium-9 at.% rhenium. *Acta Metallurgica*, 18(11):1147–1158.
- [45] Frederiksen, S. L. and Jacobsen, K. W. (2003). Density functional theory studies of screw dislocation core structures in bcc metals. *Philosophical magazine*, 83(3):365–375.
- [46] George, E. P., Curtin, W., and Tasan, C. C. (2020). High entropy alloys: A focused review of mechanical properties and deformation mechanisms. *Acta Materialia*, 188:435–474.
- [47] George, E. P., Raabe, D., and Ritchie, R. O. (2019). High-entropy alloys. *Nature Reviews Materials*, 4(8):515–534.
- [48] Ghafarollahi, A. and Curtin, W. (2021). Theory of kink migration in dilute bcc alloys. *Acta Materialia*, page 117078.
- [49] Ghafarollahi, A. and Curtin, W. A. (2020). Theory of double-kink nucleation in dilute bcc alloys. *Acta Materialia*, 196:635–650.
- [50] Ghafarollahi, A. and Curtin, W. A. (2022). Screw-controlled strength of bcc non-dilute and high-entropy alloys. *Acta Materialia*, page 117617.
- [51] Ghafarollahi, A., Maresca, F., and Curtin, W. (2019). Solute/screw dislocation interaction energy parameter for strengthening in bcc dilute to high entropy alloys. *Modelling and Simulation in Materials Science and Engineering*, 27(8):085011.
- [52] Gilbert, M., Queyreau, S., and Marian, J. (2011). Stress and temperature dependence of screw dislocation mobility in α -fe by molecular dynamics. *Physical Review B*, 84(17):174103.
- [53] Gludovatz, B., George, E. P., and Ritchie, R. O. (2015). Processing, microstructure and mechanical properties of the crmnfecon high-entropy alloy. *Jom*, 67(10):2262–2270.
- [54] Gludovatz, B., Hohenwarter, A., Catoor, D., Chang, E. H., George, E. P., and Ritchie, R. O. (2014). A fracture-resistant high-entropy alloy for cryogenic applications. *Science*, 345(6201):1153–1158.
- [55] Gordon, P., Neeraj, T., Li, Y., and Li, J. (2010). Screw dislocation mobility in bcc metals: the role of the compact core on double-kink nucleation. *Modelling and Simulation in Materials Science and Engineering*, 18(8):085008.
- [56] Gordon, P., Neeraj, T., and Mendelev, M. (2011). Screw dislocation mobility in bcc metals: a refined potential description for α -fe. *Philosophical Magazine*, 91(30):3931–3945.

- [57] Gorsse, S., Miracle, D. B., and Senkov, O. N. (2017). Mapping the world of complex concentrated alloys. *Acta Materialia*, 135:177–187.
- [58] Gough, H. (1928). The behaviour of a single crystal of α -iron subjected to alternating torsional stresses. *Proceedings of the Royal Society of London. Series A, Containing Papers of a Mathematical and Physical Character*, 118(780):498–534.
- [59] Hachet, G., Ventelon, L., Willaime, F., and Clouet, E. (2020). Screw dislocation-carbon interaction in bcc tungsten: an ab initio study. *Acta Materialia*, 200:481–489.
- [60] Hänggi, P., Talkner, P., and Borkovec, M. (1990). Reaction-rate theory: fifty years after kramers. *Reviews of modern physics*, 62(2):251.
- [61] Hattendorf, H. and Büchner, A. R. (1992). A review of suzuki’s solid solution hardening theory for substitutional bcc alloys. *International Journal of Materials Research*, 83(9):690–698.
- [62] Hebda, J. and Chang, W. (2001). Niobium alloys and high temperature applications. In *Niobium science & technology: proceedings of the International Symposium Niobium*, volume 2001.
- [63] Henkelman, G. and Jónsson, H. (2000). Improved tangent estimate in the nudged elastic band method for finding minimum energy paths and saddle points. *The Journal of chemical physics*, 113(22):9978–9985.
- [64] Henkelman, G., Uberuaga, B. P., and Jónsson, H. (2000). A climbing image nudged elastic band method for finding saddle points and minimum energy paths. *The Journal of chemical physics*, 113(22):9901–9904.
- [65] Hirsch, P., Horne, R., and Whelan, M. (1956). Lxviii. direct observations of the arrangement and motion of dislocations in aluminium. *Philosophical Magazine*, 1(7):677–684.
- [66] Hoge, K. and Mukherjee, A. (1977). The temperature and strain rate dependence of the flow stress of tantalum. *Journal of Materials Science*, 12(8):1666–1672.
- [67] Hossain, M. and Marian, J. (2014). Stress-dependent solute energetics in w-re alloys from first-principles calculations. *Acta materialia*, 80:107–117.
- [68] Hu, Y.-J., Fellingner, M. R., Butler, B. G., Wang, Y., Darling, K. A., Kecskes, L. J., Trinkle, D. R., and Liu, Z.-K. (2017). Solute-induced solid-solution softening and hardening in bcc tungsten. *Acta Materialia*, 141:304–316.
- [69] Hu, Y.-J. and Liu, Z.-K. (2019). Personal communication.
- [70] Hu, Y.-J., Zhao, G., Zhang, B., Yang, C., Zhang, M., Liu, Z.-K., Qian, X., and Qi, L. (2019). Local electronic descriptors for solute-defect interactions in bcc refractory metals. *Nature communications*, 10(1):1–11.

Bibliography

- [71] Ikeda, Y., Grabowski, B., and Körmann, F. (2019). Ab initio phase stabilities and mechanical properties of multicomponent alloys: A comprehensive review for high entropy alloys and compositionally complex alloys. *Mater. Charact.*, 147:464–511.
- [72] Ismail-Beigi, S. and Arias, T. (2000). Ab initio study of screw dislocations in mo and ta: a new picture of plasticity in bcc transition metals. *Physical Review Letters*, 84(7):1499.
- [73] Itakura, M., Kaburaki, H., and Yamaguchi, M. (2012). First-principles study on the mobility of screw dislocations in bcc iron. *Acta Materialia*, 60(9):3698–3710.
- [74] Ji, R., Phan, T., Chen, H., and Xiong, L. (2020). Quantifying the dynamics of dislocation kinks in iron and tungsten through atomistic simulations. *International Journal of Plasticity*, 128:102675.
- [75] Jónsson, H., Mills, G., and Jacobsen, K. W. (1998). Nudged elastic band method for finding minimum energy paths of transitions.
- [76] Juan, C.-C., Tsai, M.-H., Tsai, C.-W., Lin, C.-M., Wang, W.-R., Yang, C.-C., Chen, S.-K., Lin, S.-J., and Yeh, J.-W. (2015). Enhanced mechanical properties of HfMoTaTiZr and HfMoNbTaTiZr refractory high-entropy alloys. *Intermetallics*, 62:76–83.
- [77] Karagiannidis, G. K. and Lioumpas, A. S. (2007). An improved approximation for the gaussian q-function. *IEEE Communications Letters*, 11(8):644–646.
- [78] Kitajima, K., Aono, Y., Abe, H., and Kuramoto, E. (1979). Solid solution hardening and softening in iron alloy single crystals between 4.2 k and 300 k. In *Strength of Metals and Alloys*, pages 965–970. Elsevier.
- [79] Kocks, U. F., AS, A., and ME, A. (1975). Thermodynamics and kinetics of slip.
- [80] Koizumi, H., Kirchner, H., and Suzuki, T. (1993). Kink pair nucleation and critical shear stress. *Acta Metallurgica et Materialia*, 41(12):3483–3493.
- [81] Kubilay, R., Ghafarollahi, A., Maresca, F., and Curtin, W. (2021). High energy barriers for edge dislocation motion in body-centered cubic high entropy alloys. *npj Computational Materials*, 7(1):1–9.
- [82] Laidler, K. J. (1984). The development of the arrhenius equation. *Journal of chemical Education*, 61(6):494.
- [83] Lee, C., Maresca, F., Feng, R., Chou, Y., Ungar, T., Widom, M., An, K., Poplawsky, J. D., Chou, Y.-C., Liaw, P. K., et al. (2021). Strength can be controlled by edge dislocations in refractory high-entropy alloys. *Nature communications*, 12(1):1–8.
- [84] Leyson, G. and Curtin, W. (2016). Solute strengthening at high temperatures. *Model. Simul. Mater. Sci. Eng.*, 24(6):065005.

-
- [85] Li, H., Wurster, S., Motz, C., Romaner, L., Ambrosch-Draxl, C., and Pippan, R. (2012a). Dislocation-core symmetry and slip planes in tungsten alloys: Ab initio calculations and microcantilever bending experiments. *Acta Materialia*, 60(2):748–758.
- [86] Li, H., Wurster, S., Motz, C., Romaner, L., Ambrosch-Draxl, C., and Pippan, R. (2012b). Dislocation-core symmetry and slip planes in tungsten alloys: Ab initio calculations and microcantilever bending experiments. *Acta materialia*, 60(2):748–758.
- [87] Li, Z., Pradeep, K. G., Deng, Y., Raabe, D., and Tasan, C. C. (2016). Metastable high-entropy dual-phase alloys overcome the strength–ductility trade-off. *Nature*, 534(7606):227–230.
- [88] Lin, D.-Y., Wang, S., Peng, D., Li, M., and Hui, X. (2013). An n-body potential for a zr–nb system based on the embedded-atom method. *Journal of Physics: Condensed Matter*, 25(10):105404.
- [89] Lüthi, B., Ventelon, L., Rodney, D., and Willaime, F. (2018). Attractive interaction between interstitial solutes and screw dislocations in bcc iron from first principles. *Computational Materials Science*, 148:21–26.
- [90] Magdon-Ismail, M., Atiya, A. F., Pratap, A., and Abu-Mostafa, Y. S. (2004). On the maximum drawdown of a brownian motion. *Journal of applied probability*, 41(1):147–161.
- [91] Mak, E., Yin, B., and Curtin, W. (2021). A ductility criterion for bcc high entropy alloys. *Journal of the Mechanics and Physics of Solids*, 152:104389.
- [92] Maras, E., Trushin, O., Stukowski, A., Ala-Nissila, T., and Jonsson, H. (2016). Global transition path search for dislocation formation in ge on si (001). *Computer Physics Communications*, 205:13–21.
- [93] Maresca, F. and Curtin, W. A. (2020a). Mechanistic origin of high strength in refractory bcc high entropy alloys up to 1900k. *Acta Materialia*, 182:235–249.
- [94] Maresca, F. and Curtin, W. A. (2020b). Theory of screw dislocation strengthening in random bcc alloys from dilute to “high-entropy” alloys. *Acta Materialia*, 182:144–162.
- [95] Maresca, F., Dragoni, D., Csányi, G., Marzari, N., and Curtin, W. A. (2018). Screw dislocation structure and mobility in body centered cubic fe predicted by a gaussian approximation potential. *npj Computational Materials*, 4(1):1–7.
- [96] Marian, J., Cai, W., and Bulatov, V. V. (2004). Dynamic transitions from smooth to rough to twinning in dislocation motion. *Nature materials*, 3(3):158–163.
- [97] Mendelev, M., Han, S., Srolovitz, D., Ackland, G., Sun, D., and Asta, M. (2003). Development of new interatomic potentials appropriate for crystalline and liquid iron. *Philosophical magazine*, 83(35):3977–3994.

Bibliography

- [98] Miracle, D. B., Miller, J. D., Senkov, O. N., Woodward, C., Uchic, M. D., and Tiley, J. (2014). Exploration and development of high entropy alloys for structural applications. *Entropy*, 16(1):494–525.
- [99] Miracle, D. B. and Senkov, O. N. (2017). A critical review of high entropy alloys and related concepts. *Acta Materialia*, 122:448–511.
- [100] Mohri, T., Chen, Y., Kohyama, M., Ogata, S., Saengdeejing, A., Bhattacharya, S. K., Wakeda, M., Shinzato, S., and Kimizuka, H. (2017). Mechanical properties of fe-rich si alloy from hamiltonian. *npj Computational Materials*, 3(1):1–14.
- [101] Mrovec, M., Nguyen-Manh, D., Elsässer, C., and Gumbsch, P. (2011). Magnetic bond-order potential for iron. *Physical review letters*, 106(24):246402.
- [102] Mrovec, M., Nguyen-Manh, D., Pettifor, D. G., and Vitek, V. (2004). Bond-order potential for molybdenum: Application to dislocation behavior. *Physical Review B*, 69(9):094115.
- [103] Nag, S. and Curtin, W. A. (2020). Effect of solute-solute interactions on strengthening of random alloys from dilute to high entropy alloys. *Acta Mater.*, 200:659–673.
- [104] Nakano, A. (2008). A space-time-ensemble parallel nudged elastic band algorithm for molecular kinetics simulation. *Computer Physics Communications*, 178(4):280–289.
- [105] Nemat-Nasser, S. and Guo, W. (2000). High strain-rate response of commercially pure vanadium. *Mechanics of Materials*, 32(4):243–260.
- [106] Nguyen-Manh, D., Horsfield, A. P., and Dudarev, S. L. (2006). Self-interstitial atom defects in bcc transition metals: Group-specific trends. *Phys. Rev. B*, 73:020101(R).
- [107] Nöhling, W. G. and Curtin, W. A. (2016). Thermodynamic properties of average-atom interatomic potentials for alloys. *Modelling and Simulation in Materials Science and Engineering*, 24(4):045017.
- [108] Nygren, K., Bertsch, K., Wang, S., Bei, H., Nagao, A., and Robertson, I. (2018). Hydrogen embrittlement in compositionally complex fcc solid solution alloy. *Current Opinion in Solid State and Materials Science*, 22(1):1–7.
- [109] Olmsted, D. L., Hector Jr, L. G., and Curtin, W. (2006). Molecular dynamics study of solute strengthening in Al/Mg alloys. *J. Mech. Phys. Solids*, 54(8):1763–1788.
- [110] Orowan, E. (1934). Plasticity of crystals. *Z. Phys*, 89(9-10):605–659.
- [111] Petukhov, B. (1971). Effects of point defects on dislocation mobility in crystals with high peierls barriers. *Sov Phys Solid State*, 13:1204–7.
- [112] Picu, R. and Zhang, D. (2004). Atomistic study of pipe diffusion in al–mg alloys. *Acta materialia*, 52(1):161–171.

-
- [113] Pink, E. (1979). Low-temperature softening in body-centered cubic alloys. *Progress in Materials Science*, 24(1):1–50.
 - [114] Plimpton, S. (1995). Fast parallel algorithms for short-range molecular dynamics. *Journal of computational physics*, 117(1):1–19.
 - [115] Polanyi, M. (1934). Lattice distortion which originates plastic flow. *Z. Phys*, 89(9-10):660–662.
 - [116] Proville, L. and Rodney, D. (2020). Modeling the thermally activated mobility of dislocations at the atomic scale. *Handbook of Materials Modeling: Methods: Theory and Modeling*, pages 1525–1544.
 - [117] Proville, L., Rodney, D., and Marinica, M.-C. (2012). Quantum effect on thermally activated glide of dislocations. *Nature materials*, 11(10):845–849.
 - [118] Raffo, P. L. (1969). Yielding and fracture in tungsten and tungsten-rhenium alloys. *Journal of the Less Common Metals*, 17(2):133–149.
 - [119] Rao, S., Akdim, B., Antillon, E., Woodward, C., Parthasarathy, T., and Senkov, O. (2019a). Modeling solution hardening in bcc refractory complex concentrated alloys: NbTiZr, Nb_{1.5}TiZr_{0.5} and Nb_{0.5}TiZr_{1.5}. *Acta Materialia*, 168:222–236.
 - [120] Rao, S., Antillon, E., Woodward, C., Akdim, B., Parthasarathy, T., and Senkov, O. (2019b). Solution hardening in body-centered cubic quaternary alloys interpreted using Suzuki's kink-solute interaction model. *Scripta Materialia*, 165:103–106.
 - [121] Rao, S. and Woodward, C. (2001). Atomistic simulations of $(a/2)\langle 111 \rangle$ screw dislocations in bcc Mo using a modified generalized pseudopotential theory potential. *Philosophical Magazine A*, 81(5):1317–1327.
 - [122] Rao, S., Woodward, C., Akdim, B., and Senkov, O. (2020). A model for interstitial solid solution strengthening of body centered cubic metals. *Materialia*, 9:100611.
 - [123] Rao, S., Woodward, C., Akdim, B., Senkov, O., and Miracle, D. (2021). Theory of solid solution strengthening of bcc chemically complex alloys. *Acta Materialia*, 209:116758.
 - [Rao] Rao, S. I. personal communication.
 - [125] Ravi, K. and Gibala, R. (1970). The strength of niobium-oxygen solid solutions. *Acta Metallurgica*, 18(6):623–634.
 - [126] Rodney, D. (2007). Activation enthalpy for kink-pair nucleation on dislocations: Comparison between static and dynamic atomic-scale simulations. *Physical Review B*, 76(14):144108.
 - [127] Rodney, D. and Bonneville, J. (2014). Dislocations. In *Physical Metallurgy*, pages 1591–1680. Elsevier.

Bibliography

- [128] Rogers, L. C. G. and Satchell, S. E. (1991). Estimating variance from high, low and closing prices. *The Annals of Applied Probability*, pages 504–512.
- [Romaner] Romaner, L. Unpublished research.
- [130] Romaner, L., Ambrosch-Draxl, C., and Pippan, R. (2010a). Effect of rhenium on the dislocation core structure in tungsten. *Physical review letters*, 104(19):195503.
- [131] Romaner, L., Ambrosch-Draxl, C., and Pippan, R. (2010b). Effect of rhenium on the dislocation core structure in tungsten. *Physical review letters*, 104(19):195503.
- [132] Sato, A. and Meshii, M. (1973). Solid solution softening and solid solution hardening. *Acta Metallurgica*, 21(6):753–768.
- [133] Schmidt, F. F. (1963). *The engineering properties of tungsten and tungsten alloys*, volume 191. Defense Metals Information Center, Battelle Memorial Institute.
- [134] Schock, G. (1980). Thermodynamics and thermal activation of dislocations. *Dislocations in solids*, 3:63–163.
- [135] Schoeck, G. (2000). Thermal activation in plastic deformation. In *Multiscale Phenomena in Plasticity: From Experiments to Phenomenology, Modelling and Materials Engineering*, pages 33–56. Springer.
- [136] Seeger, A. (1956). Lxv. on the theory of the low-temperature internal friction peak observed in metals. *Philosophical Magazine*, 1(7):651–662.
- [137] Senkov, O., Gorsse, S., and Miracle, D. B. (2019a). High temperature strength of refractory complex concentrated alloys. *Acta Mater.*, 175:394–405.
- [138] Senkov, O., Rao, S., Chaput, K., and Woodward, C. (2018a). Compositional effect on microstructure and properties of nb-ti-zr-based complex concentrated alloys. *Acta Materialia*, 151:201–215.
- [139] Senkov, O., Scott, J., Senkova, S., Meisenkothen, F., Miracle, D., and Woodward, C. (2012). Microstructure and elevated temperature properties of a refractory tanbhfzrti alloy. *Journal of Materials Science*, 47(9):4062–4074.
- [140] Senkov, O., Scott, J., Senkova, S., Miracle, D., and Woodward, C. (2011a). Microstructure and room temperature properties of a high-entropy tanbhfzrti alloy. *Journal of alloys and compounds*, 509(20):6043–6048.
- [141] Senkov, O., Senkova, S., and Woodward, C. (2014). Effect of aluminum on the microstructure and properties of two refractory high-entropy alloys. *Acta Materialia*, 68:214–228.
- [142] Senkov, O., Wilks, G., Miracle, D., Chuang, C., and Liaw, P. (2010). Refractory high-entropy alloys. *Intermetallics*, 18(9):1758–1765.

-
- [143] Senkov, O. N., Gorsse, S., and Miracle, D. B. (2019b). High temperature strength of refractory complex concentrated alloys. *Acta Mater.*, 175:394–405.
- [144] Senkov, O. N., Miracle, D. B., Chaput, K. J., and Couzinie, J.-P. (2018b). Development and exploration of refractory high entropy alloys—a review. *Journal of materials research*, 33(19):3092–3128.
- [145] Senkov, O. N., Wilks, G., Scott, J., and Miracle, D. B. (2011b). Mechanical properties of Nb₂₅Mo₂₅Ta₂₅W₂₅ and V₂₀Nb₂₀Mo₂₀Ta₂₀W₂₀ refractory high entropy alloys. *Inter-metallics*, 19(5):698–706.
- [146] Sheppard, D., Terrell, R., and Henkelman, G. (2008). Optimization methods for finding minimum energy paths. *The Journal of chemical physics*, 128(13):134106.
- [147] Shinzato, S., Wakeda, M., and Ogata, S. (2019). An atomistically informed kinetic monte carlo model for predicting solid solution strengthening of body-centered cubic alloys. *International Journal of Plasticity*, 122:319–337.
- [148] Slining, J. R. and Koss, D. (1973). Solid solution strengthening of high purity niobium alloys. *Metallurgical Transactions*, 4(5):1261–1264.
- [149] Smith, R. W. and Was, G. S. (1989). Application of molecular dynamics to the study of hydrogen embrittlement in ni-cr-fe alloys. *Physical Review B*, 40(15):10322.
- [150] Soare, M. and Curtin, W. (2008a). Single-mechanism rate theory for dynamic strain aging in fcc metals. *Acta Materialia*, 56(15):4091–4101.
- [151] Soare, M. and Curtin, W. (2008b). Solute strengthening of both mobile and forest dislocations: The origin of dynamic strain aging in fcc metals. *Acta Materialia*, 56(15):4046–4061.
- [152] Statham, C., Koss, D., and Christian, J. (1972). The thermally activated deformation of niobium-molybdenum and niobium-rhenium alloy single crystals. *Philosophical Magazine*, 26(5):1089–1103.
- [153] Stephens, J. R. (1970). Dislocation structures in single-crystal tungsten and tungsten alloys. *Metallurgical and Materials Transactions B*, 1(5):1293–1301.
- [154] Stephens, J. R. and Witzke, W. R. (1971). Alloy softening in group via metals alloyed with rhenium. *Journal of the Less Common Metals*, 23(4):325–342.
- [155] Stukowski, A. (2009). Visualization and analysis of atomistic simulation data with ovito—the open visualization tool. *Model. Simul. Mater. Sci. Eng.*, 18(1):015012.
- [156] Stukowski, A. (2012). Structure identification methods for atomistic simulations of crystalline materials. *Model. Simul. Mater. Sci. Eng.*, 20(4):045021.

Bibliography

- [157] Stukowski, A., Cereceda, D., Swinburne, T. D., and Marian, J. (2015). Thermally-activated non-schmid glide of screw dislocations in w using atomistically-informed kinetic monte carlo simulations. *International Journal of Plasticity*, 65:108–130.
- [158] Suzuki, H. (1980). Solid solution hardening in body-centred cubic alloys. *Dislocations in solids*, 4:191–217.
- [159] Szlachta, W. J., Bartók, A. P., and Csányi, G. (2014a). Accuracy and transferability of gaussian approximation potential models for tungsten. *Physical Review B*, 90(10):104108.
- [160] Szlachta, W. J., Bartók, A. P., and Csányi, G. (2014b). Accuracy and transferability of gaussian approximation potential models for tungsten. *Physical Review B*, 90(10):104108.
- [161] Tadmor, E. B. and Miller, R. E. (2011). *Modeling materials: continuum, atomistic and multiscale techniques*. Cambridge University Press.
- [162] Takeuchi, S. (1969). Solid-solution strengthening in single crystals of iron alloys. *Journal of the Physical Society of Japan*, 27(4):929–940.
- [163] Takeuchi, S., Furubayashi, E., and Taoka, T. (1967). Orientation dependence of yield stress in 4.4% silicon iron single crystals. *Acta metallurgica*, 15(7):1179–1191.
- [164] Takeuchi, S., Yoshida, H., and Taoka, T. (1968). Solid-solution strengthening in iron alloys. *Transactions of the Japan Institute of Metals, Suppl*, 9:715–719.
- [165] Taylor, G. I. (1928). Section a.-mathematical and physical sciences.-the deformation of crystals of β -brass. *Proceedings of the Royal Society of London. Series A, Containing Papers of a Mathematical and Physical Character*, 118(779):1–24.
- [166] Taylor, G. I. (1934). The mechanism of plastic deformation of crystals. part i.—theoretical. *Proceedings of the Royal Society of London. Series A, Containing Papers of a Mathematical and Physical Character*, 145(855):362–387.
- [167] Trinkle, D. R. (2005). The chemistry of deformation: How solutes soften pure metals. *Science*, 310(5754):1665–1667.
- [168] Trygubenko, S. A. and Wales, D. J. (2004). A doubly nudged elastic band method for finding transition states. *The Journal of chemical physics*, 120(5):2082–2094.
- [169] Tsai, M.-H. and Yeh, J.-W. (2014). High-entropy alloys: a critical review. *Materials Research Letters*, 2(3):107–123.
- [170] Tsuru, T. and Suzudo, T. (2018). First-principles calculations of interaction between solutes and dislocations in tungsten. *Nuclear Materials and Energy*, 16:221–225.
- [171] Varvenne, C., Leyson, G. P. M., Ghazisaeidi, M., and Curtin, W. A. (2017). Solute strengthening in random alloys. *Acta Materialia*, 124:660–683.

-
- [172] Varvenne, C., Luque, A., and Curtin, W. A. (2016a). Theory of strengthening in fcc high entropy alloys. *Acta Materialia*, 118:164–176.
- [173] Varvenne, C., Luque, A., Nöhring, W. G., and Curtin, W. A. (2016b). Average-atom interatomic potential for random alloys. *Physical Review B*, 93(10):104201.
- [174] Vegge, T., Rasmussen, T., Leffers, T., Pedersen, O. B., and Jacobsen, K. W. (2000). Determination of the of rate cross slip of screw dislocations. *Physical review letters*, 85(18):3866.
- [175] Ventelon, L. and Willaime, F. (2007). Core structure and peierls potential of screw dislocations in α -fe from first principles: cluster versus dipole approaches. *Journal of computer-aided materials design*, 14(1):85–94.
- [176] Ventelon, L., Willaime, F., Clouet, E., and Rodney, D. (2013a). Ab initio investigation of the peierls potential of screw dislocations in bcc fe and w. *Acta Materialia*, 61(11):3973–3985.
- [177] Ventelon, L., Willaime, F., Clouet, E., and Rodney, D. (2013b). Ab initio investigation of the peierls potential of screw dislocations in bcc fe and w. *Acta Materialia*, 61(11):3973–3985.
- [178] Vineyard, G. H. (1957). Frequency factors and isotope effects in solid state rate processes. *Journal of Physics and Chemistry of Solids*, 3(1-2):121–127.
- [179] Vitek, V. (1992). Structure of dislocation cores in metallic materials and its impact on their plastic behaviour. *Progress in materials science*, 36:1–27.
- [180] Wain, H., Henderson, E., and Johnstone, S. (1954). A study of the room-temperature ductility of chromium. *Journal of the Institute of Metals*, 83(4):133–142.
- [181] Wang, F., Balbus, G. H., Xu, S., Su, Y., Shin, J., Rottmann, P. F., Knipling, K. E., Stinville, J.-C., Mills, L. H., Senkov, O. N., et al. (2020). Multiplicity of dislocation pathways in a refractory multiprincipal element alloy. *Science*, 370(6512):95–101.
- [182] Warner, D., Curtin, W., and Qu, S. (2007). Rate dependence of crack-tip processes predicts twinning trends in fcc metals. *Nature materials*, 6(11):876–881.
- [183] Weertman, J. (1958). Dislocation model of low-temperature creep. *Journal of Applied Physics*, 29(12):1685–1689.
- [184] Weinan, E., Ren, W., and Vanden-Eijnden, E. (2002). String method for the study of rare events. *Phys. Rev. B*, 66(5):052301.
- [185] Weinan, E., Ren, W., and Vanden-Eijnden, E. (2007). Simplified and improved string method for computing the minimum energy paths in barrier-crossing events. *Journal of Chemical Physics*, 126(16):164103.
- [186] Weinberger, C. R., Boyce, B. L., and Battaile, C. C. (2013a). Slip planes in bcc transition metals. *International Materials Reviews*, 58(5):296–314.

Bibliography

- [187] Weinberger, C. R., Tucker, G. J., and Foiles, S. M. (2013b). Peierls potential of screw dislocations in bcc transition metals: Predictions from density functional theory. *Physical Review B*, 87(5):054114.
- [188] Woodward, C. and Rao, S. (2001). Ab-initio simulation of isolated screw dislocations in bcc mo and ta. *Philosophical Magazine A*, 81(5):1305–1316.
- [189] Woodward, C. and Rao, S. (2002). Flexible ab initio boundary conditions: Simulating isolated dislocations in bcc mo and ta. *Physical review letters*, 88(21):216402.
- [190] Wu, Z., Ahmad, R., Yin, B., Sandlöbes, S., and Curtin, W. (2018). Mechanistic origin and prediction of enhanced ductility in magnesium alloys. *Science*, 359(6374):447–452.
- [191] Wu, Z. and Curtin, W. (2015). The origins of high hardening and low ductility in magnesium. *Nature*, 526(7571):62–67.
- [192] Yang, L., Söderlind, P., and Moriarty, J. A. (2001). Accurate atomistic simulation of $(a/2)\langle 111 \rangle$ screw dislocations and other defects in bcc tantalum. *Philosophical Magazine A*, 81(5):1355–1385.
- [193] Ye, Y., Wang, Q., Lu, J., Liu, C., and Yang, Y. (2016). High-entropy alloy: challenges and prospects. *Materials Today*, 19(6):349–362.
- [194] Yin, S., Ding, J., Asta, M., and Ritchie, R. O. (2020). Ab initio modeling of the energy landscape for screw dislocations in body-centered cubic high-entropy alloys. *npj Computational Materials*, 6(1):1–11.
- [195] Yin, S., Zuo, Y., Abu-Odeh, A., Zheng, H., Li, X.-G., Ding, J., Ong, S. P., Asta, M., and Ritchie, R. O. (2021). Atomistic simulations of dislocation mobility in refractory high-entropy alloys and the effect of chemical short-range order. *Nature communications*, 12(1):1–14.
- [196] Zárubová, N. and Šesták, B. (1975). Plastic deformation of fe-3wt% si single crystals in the range from 113 to 473 k. ii. work-hardening. *physica status solidi (a)*, 30(2):479–488.
- [197] Zhang, F. and Curtin, W. (2008). Atomistically informed solute drag in Al–Mg. *Model. Simul. Mater. Sci. Eng.*, 16(5):055006.
- [198] Zhang, Y., Zuo, T. T., Tang, Z., Gao, M. C., Dahmen, K. A., Liaw, P. K., and Lu, Z. P. (2014). Microstructures and properties of high-entropy alloys. *Progress in materials science*, 61:1–93.
- [199] Zhao, Y., Dezerald, L., Pozuelo, M., Zhou, X., and Marian, J. (2020). Simulating the mechanisms of serrated flow in interstitial alloys with atomic resolution over diffusive timescales. *Nature communications*, 11(1):1–8.
- [200] Zhao, Y., Lee, D.-H., Kim, W.-J., Seok, M.-Y., Kim, J.-Y., Han, H. N., Suh, J.-Y., Ramamurty, U., and Jang, J.-i. (2018). Influence of pre-strain on the gaseous hydrogen embrittlement resistance of a high-entropy alloy. *Materials Science and Engineering: A*, 718:43–47.

-
- [201] Zhao, Y., Lee, D.-H., Seok, M.-Y., Lee, J.-A., Phaniraj, M., Suh, J.-Y., Ha, H.-Y., Kim, J.-Y., Ramamurty, U., and Jang, J.-i. (2017). Resistance of cocrfemnni high-entropy alloy to gaseous hydrogen embrittlement. *Scripta Materialia*, 135:54–58.
- [202] Zhao, Y. and Marian, J. (2018). Direct prediction of the solute softening-to-hardening transition in w-re alloys using stochastic simulations of screw dislocation motion. *Modelling and Simulation in Materials Science and Engineering*, 26(4):045002.
- [203] Zhou, X.W., J. R. and Wadley, H. (2004). Misfit-energy-increasing dislocations in vapor-deposited cofe/nife multilayers. *Physical Review B*, 69(14):144113.
- [204] Zhou, X., He, S., and Marian, J. (2021a). Cross-kinks control screw dislocation strength in equiatomic bcc refractory alloys. *Acta Materialia*, 211:116875.
- [205] Zhou, X. and Marian, J. (2021). Temperature and stress dependence of screw dislocation mobility in nb-v-ta alloys using kinetic monte carlo simulations. *Frontiers in Materials*, page 520.
- [206] Zhou, X., Tehranchi, A., and Curtin, W. A. (2021b). Mechanism and prediction of hydrogen embrittlement in fcc stainless steels and high entropy alloys. *Physical review letters*, 127(17):175501.

Alireza Ghafarollahi

PHD STUDENT

LABORATORY FOR MULTISCALE MECHANICS MODELING
INSTITUTE OF MECHANICAL ENGINEERING
COLE POLYTECHNIQUE FÉDÉRALE DE LAUSANNE
LAUSANNE, 1015, SWITZERLAND

alireza.ghafarollahi@epfl.ch | alireza.ghafarollahi@gmail.com
Webpage : [Google-Scholar](#)
(+41)786577468

EDUCATION

Ecole Polytechnique Fédérale de Lausanne, Lausanne, Switzerland

Ph.D. in Mechanical Engineering

Advisor: Prof. William Curtin

Feb 2018-Present

Sharif University of Technology, Tehran, Iran

M.S. in Civil Engineering,

Advisor: Prof. Hossein Mohammadi Shodja

2012-2014

Amirkabir University of Technology, Tehran, Iran

B.S. in Civil Engineering

2008-2012

RESEARCH INTERESTS

solid mechanics, computational materials science, dislocation mechanics, atomistic simulation, plasticity, micro/nano mechanics of defects in solids, wave propagation in elastic solids

PUBLICATIONS

A. Ghafarollahi and W. A. Curtin, The strength plateau at intermediate temperatures in BCC High-Entropy Alloys, under preparation.

A. Ghafarollahi and W. A. Curtin, Screw-controlled strength of BCC non-dilute and High-Entropy alloys, *Acta Mater.* 117617 (2022)

R. Kubilay, **A. Ghafarollahi**, F. Maresca and W. A. Curtin, High Energy Barriers for Edge Dislocation Motion in BCC High Entropy Alloys, *Npj Comput. Mater.* 7, 112 (2021)

A. Ghafarollahi and W. A. Curtin, Theory of kink migration in dilute BCC alloys, *Acta Mater.* 117078 (2021)

A. Ghafarollahi and W. A. Curtin, Theory of double-kink nucleation in dilute BCC alloys, *Acta Mater.* 196 (2020) 635-650.

A. Ghafarollahi, F. Maresca and W. A. Curtin, Solute/screw dislocation interaction energy parameter for strengthening in bcc dilute to high entropy alloys, *Modelling Simul. Mater. Sci. Eng.* 27 (2019) 085011

A. Ghafarollahi and H.M. Shodja, Scattering of transverse surface waves by a piezoelectric fiber in a piezoelectric half-space with exponentially varying electromechanical properties, *ZAMP.* 70 (2019) 1-19.

A. Ghafarollahi and H.M. Shodja, Scattering of SH-waves by an elliptic cavity/crack beneath the interface between functionally graded and homogeneous half-spaces via multipole expansion method, *J Sound Vib.* 435 (2018) 372-389.

A. Ghafarollahi and H.M. Shodja, Scattering of SH-waves by a nano-fiber beneath the interface of two bonded half-spaces within surface/interface elasticity via multipole expansion, *Int J Solids Struct.* 130 (2018) 258-279.

H.M. Shodja and **A. Ghafarollahi**, An embedded couple stress micro-/nano-obstacle with micro-inertia incident upon by SH-waves, *Acta Mech.* 229 (2018) 3333-3354.

H.M. Shodja, **A. Ghafarollahi** and C. Enzevae, Surface/interface effect on the scattering of love waves by a nano-size surface-breaking crack within an ultra-thin layer bonded to an elastic half-space, Int J Solids Struct. 108 (2017) 63-73.

RESEARCH
EXPERIENCES

Strengthening mechanisms in dilute and high-entropy BCC alloys

Advisor: Prof. William Curtin

2018-Present

Ph.D. Thesis

cole Polytechnique Fdrale de Lausanne, Lausanne, Switzerland

Surface/Interface effect on the scattering of Love waves by a surface-breaking crack within an ultra-thin layer bonded to an elastic half-space

Advisor: Prof. Hossein Mohammadi Shodja

2013-2014

M.S. Thesis

Sharif University of Technology, Tehran, Iran

RELEVANT
COURSES

- Theory of Elasticity
- Mechanics of dislocations
- Fracture Mechanics
- Micromechanics of Defects in Solids
- Advanced Engineering Mathematics
- Finite Elements Method
- Dynamics of Structure
- Statistical Mechanics

TEACHING
EXPERIENCES

Teaching Assistant, EPFL

- Advanced solid mechanics

Fall Semesters 2018,2019,2020

- Introduction to Structural Mechanics

Spring Semesters 2019,2020,2021

Teaching Assistant, SUT Tehran

- Advanced Engineering Mathematics

Fall 2014

REFERENCES
AVAILABLE TO
CONTACT

Prof. William Curtin (e-mail: william.curtin@epfl.ch; phone: +41216937366)

- Professor, Mechanical Engineering, cole polytechnique fdrale de Lausanne

Prof. Hossein Mohammadi Shodja (e-mail: shodja@sharif.edu , shodja.hossein@gmail.com)

- Professor, Civil Engineering, Sharif University of Technology

Prof. Francesco Maresca (e-mail: f.maresca@rug.nl)

- Assistant Professor, Faculty of Science and Engineering, University of Groningen

